School of Chemical Engineering and

Advanced Materials

Newcastle University UK

PEROVSKITE OXYNITRIDE

DIELECTRICS

by

Jutharat Ahchawarattaworn

A thesis submitted as a requirement for
the degree of Doctor of Philosophy
Newcastle University

January 2011

PREFACE

This thesis describes original work that has not been submitted for a degree at any other universities.

The investigations were carried out in the School of Chemical Engineering and Advanced Materials of Newcastle University, United Kingdom, during the period September 2006 to January 2011 under the supervision of Professor D.P. Thompson.

The thesis describes the synthesis, crystal structure and dielectric properties of oxynitrides of type $LnTiO_2N$ (Ln = La and Nd), $ATaO_2N$ (A = Ca, Sr and Ba) and their solid solutions

ACKNOWLEDGEMENTS

Dedicated to my father and mother

"The only greatest treasure we can give you is education"

Mum & Dad

ABSTRACT

The synthesis, crystal structures and dielectric properties of perovskite oxynitrides of the type $LnTiO_2N$ (Ln = La, Nd and mixtures) and $ATaO_2N$ (A = Ca, Sr, Ba and mixtures), have been investigated. The end-member oxynitrides and their associated $La_xNd_{1-x}TiO_2N$, $Ca_xSr_{1-x}TaO_2N$ and $Ba_xSr_{1-x}TaO_2N$ solid solutions were successfully prepared by ammonolysis of the appropriate precursor oxides at temperatures in the range 900-1200°C. The complete range of $La_xNd_{1-x}TiO_2N$ solid solution are orthorhombic perovskites, which show a small increase in unit cell parameters with increasing La content across the range. Compositions in the $Ca_xSr_{1-x}TaO_2N$ series are tetragonal for $x < 0.6$ and orthorhombic for $x > 0.6$. $Ba_xSr_{1-x}TaO_2N$ solid solutions are tetragonal for $x < 0.5$ and cubic for $x > 0.5$. It was impossible to form any perovskite solid solution in the $BaTaO_2N$-$CaTaO_2N$ series.

Attempts were made to densify these oxynitrides by hot-pressing and spark plasma sintering, but a characteristic of all these oxynitride structures is that they are stable up to relatively low temperatures (1250°C) with decomposition occurring before any sintering can be achieved. A reducing environment is necessary to prevent oxidation, but this must not be too reducing to promote conversion of the transition metal into a lower oxidation state. As a result, fully dense samples were not obtained and dielectric property measurements could not be made on these samples. As an alternative, pure single phase $LaTiO_2N$, $NdTiO_2N$ and $La_xNd_{1-x}TiO_2N$ solid solutions were prepared as $\approx$ 3 μm thick surface layers on dense pellets of the corresponding $La_2Ti_2O_7$, $Nd_2Ti_2O_7$ and $(La_xNd_{1-x})_2Ti_2O_7$) oxides by ammonolysis. The bulk dielectric properties of these

coated samples were then measured by LCR bridge techniques. The presence of an oxynitride layer significantly increased the measured dielectric constant of all samples, compared with the pure oxides, but a significantly higher dielectric loss was also observed. This lossy behaviour is believed to be due to the presence of a more conductive region of reduced $La_2Ti_2O_7$ (of typical composition $La_2Ti_{2-x}^{IV}Ti_x^{III}O_{7-z}$) situated immediately below the oxynitride layer, produced during synthesis by the presence of hydrogen in the nitriding ammonia atmosphere.

The dielectric constant of all these oxynitrides was also measured in particulate form by impedance analysis of slurries and the dielectric constant calculated by a method of mixtures. Compared with the parent oxides, the dielectric constants were noticeably larger, ranging from 100-1500. These values are in reasonable agreement with the limited amount of data available in the literature, and show that this group of materials merits further exploration, providing easier synthesis routes can be developed, which also result in low loss final materials being obtained.

CONTENTS

IX

Chapter 1 Introduction

Trends in electronic circuitry toward miniaturisation, increased functionality, enhanced performance, reduced electric power consumption and lower cost per bit have become increasingly prominent in recent years, and have followed the principle generally known as Moore's Law. It was predicted that chip complexity would grow exponentially in response to decreasing feature size, resulting in improved circuit speed, larger memory capacity and reduced cost per bit (Moore 1965 cited in Green *et al.*, 2001). Furthermore, a recent International Technology Roadmap for Semiconductors has proposed the concept of Functional Diversification "More than Moore", which has stated that devices should incorporate valuable functionalities without scaling down in size (ITRS, 2009). Dielectric materials, which constitute some of the more important parts of electronic and electrical devices, are clearly affected by these developments and the associated trends. When a component size is reduced, a lower operating voltage must be applied to maintain a constant electrical field and this requires increased capacitance in order for the device to function properly. Since capacitance is inversely proportional to thickness, the thickness must be reduced to reach a desired capacitance value. This scaling down, whilst retaining a high level of device performance requires the use of very thin dielectric films down to a certain critical thickness (≈ 1.2 nm), beyond which the tunnelling leakage current becomes unacceptable. As tunnelling current increases exponentially with decreasing thickness, it can only be kept at low levels by using thicker layers of higher-k dielectrics, designed to have the required capacitance.

Silicon dioxide, SiO_2, has been used as a gate dielectric for many decades and has many of the desired properties such as large band gap (9 eV), very high resistivity, very low leakage current, good diffusion barrier characteristics, and a well defined interface when bonded with silicon (Green *et al.*, 2001, Groner and George, 2003). In spite of these many attributes, SiO_2 has a relatively low ($k \approx 3.9$) dielectric constant (Green *et al.*, 2001). Nitrogen incorporation has been used as a method of improving the material and dielectric properties of silicon dioxide. Several studies have confirmed the benefits of this such as increased dielectric constant, higher resistance to boron penetration and an improved interface quality on a silicon substrate. Even though the resulting SiO_xN_y materials are compatible with silicon and hence with current semiconductor processing technology, they have a relatively low dielectric constant.

Various other high-k dielectric materials are under consideration as potential replacements for SiO_2 as the gate dielectric material to mitigate the leakage problem and improve performance, because using a higher k dielectric makes it possible to increase the physical thickness of the dielectric layer and still provide the same capacitance. Perovskites tend to have very large dielectric constants due to their ferroelectric behaviour at temperatures below the Curie point (Groner and George, 2003). Whereas traditional ceramic insulators have the relative permittivity in the range of 5–10, barium titanate ($BaTiO_3$) based ceramics with the perovskite structure can exhibit relative permittivities as high as 15000 (Swartz, 1990), depending on the grain size and crystal structure. In general, the structural distortion in perovskite materials from the ideal cubic arrangement to lower symmetry versions as a result of controlled cation substitution leads to

remarkable changes in material and electrical properties (Bhalla *et al.*, 2000). Additionally, anion substitution in perovskite structural materials is feasible to tailor the material and dielectric properties. Nitrogen substitution into perovskites has received considerable attention as a means of improving the dielectric properties when used in conjunction with silicon-based systems.

For many applications, not only are high dielectric constant and low leakage current required, but also the additional parameters of low dissipation factor (or dielectric loss also known as loss tangent), high breakdown voltage, good interface and thermal stability sufficient to resist the high temperature CMOS manufacturing processing must be considered. Initially, the dielectric constant of any new material should be high enough to justify the necessary research and development costs. Moreover thermodynamic stability in contact with Si is important in order to fit in with current silicon processing technology. In practice, there are many individual requirements for each application, e.g. gate dielectrics in transistors can have a much higher leakage current but the quality of the dielectric/Si bottom electrode interfacial region is critical (Groner and George, 2003). In contrast, capacitors for memories need materials with very low leakage currents ($< 10^{-8}$ A/cm^2) to allow the charge stored in the capacitor to remain large enough to be read for a relatively long time period, but the interface quality is not quite so critical as long as leakage currents are within reasonable limits (Groner and George, 2003). The required properties for new gate dielectric materials therefore include considerations of permittivity, band gap as well as mobility, thermodynamic stability, film morphology and interface quality, in addition to compatibility with current or future materials used in fabrication, process

compatibility, and good reliability. This portfolio of properties is remarkably demanding. To date, very few materials have emerged as promising candidates which combine all of the above requirements and also give good device performance. Nevertheless, attempts have been made to introduce new materials and this field of research remains very active and there are good possibilities for finding new candidates which fulfil the electrical and electronic industrial requirements.

In the present research, attempts are described to produce high-k, perovskite-type oxynitride dielectric materials in which some of the oxygen has been replaced by nitrogen. It is necessary to use higher-valence cations in either of the cation sites in order to achieve valence balance. Thus, for example, relative to $BaTiO_3$, the Ba cations can be substituted by rare earth elements (R) or alternatively, five-valent cations can be introduced on to the Ti sites to balance the increase in negative valencies as oxygen is partially substituted by nitrogen. $LnTiO_2N$ (Ln = La and Nd), $ATaO_2N$ (A = Ca, Sr and Ba) and solid solutions of $La_xNd_{1-x}TiO_2N$, $Ca_xSr_{1-x}TaO_2N$ and $Ba_xSr_{1-x}TaO_2N$ were synthesised by ammonolysis of appropriate oxide powder mixes. The crystal structures were examined by Rietveld refinement of X-ray diffraction spectra. The dielectric constants of bulk materials and thin films were studied by the LCR bridge method and the particulate dielectric constants were examined by impedance spectroscopy.

References:

Bhalla, A. S., Guo, R. and Roy, R. (2000) The perovskite structure - A review of its role in ceramic science and technology. *Materials Research Innovations,* 4**,** 3-26.

Green, M. L., Gusev, E. P., Degraeve, R. and Garfunkel, E. L. (2001) Ultrathin (< 4 nm) SiO_2 and Si-O-N gate dielectric layers for silicon microelectronics: Understanding the processing, structure, and physical and electrical limits. *Journal of Applied Physics,* 90**,** 2057-2121.

Groner, M. D. and George, S. M. (2003) High-k dielectrics grown by atomic layer deposition: Capacitor and gate applications. In Murarka, S. P., Eizenberg, M. and Sinha, A. K. (Eds.) *Interlayer Dielectrics for Semiconductor Technologies.* San Diego, Academic Press**,** 327-348.

Swartz, S. L. (1990) Topics in electronic ceramics. *IEEE Transactions on Electrical Insulation,* 25**,** 935-987.

Other reference resources:

ITRS (2009, December 11th) International Technology Roadmap for Semiconductors: Executive Summary 2009. Retrieved from http://www.itrs.net/Links/2009 ITRS/2009Chapters_2009Tables/2009_ExecSum.pdf

Chapter 2 Perovskite oxynitride dielectrics– A review

2.1 The perovskite structure

Cubic and lower symmetry perovskite materials are the most important electroceramics currently in use because of their wide diversity of electrical/electronic properties. Perovskites have the potential to display very large dielectric constants due to their unique ferroelectric behaviour. There is no net polarisation of charge above the Curie point (Groner and George, 2003) but below this temperature, cation shifts create a permanent dipole thereby giving rise to very high dielectric constants (Groner and George, 2003). However, there is evidence to show that the dielectric constant of perovskites decreases for thin films of thickness less than ≈ 1 μm and this or a low Curie temperature makes many current materials unsuitable for devices, especially those requiring high operating temperatures (Groner and George, 2003).

Perovskite is the mineral name for calcium titanium oxide, $CaTiO_3$, and is generally used to describe any substance having the same or a related crystal structure (Moulson and Herbert, 2003). As shown in Figure 2-1, the basic chemical formula of cubic perovskite is ABX_3, where A and B are cations of different sizes and X is most commonly oxygen, but can also be fluorine, chlorine, nitrogen, sulphur or carbon. In the ideal structure, large A atoms form the corners of the cubic cell, the smaller B atoms being located in the centre and the oxygen

atoms are situated in the centre of each cubic face. The crystal structure of an ideal perovskite can be described as a face centred cubic arrangement of oxygen anions with the A-cation coordinated by 12 oxygen ions and the B-cation in the octahedral interstices.
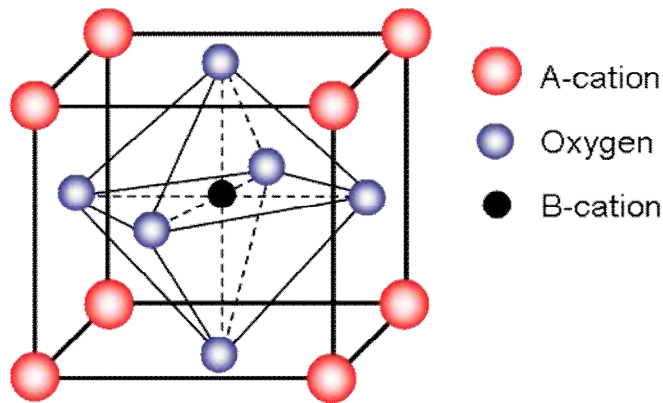
Figure 2-1 The lattice structure of a cubic perovskite (Moulson and Herbert, 2003)

This ideal structure is found in some materials (e.g. $SrTiO_3$) at room temperature. Usually the structure is modified by cation displacements as in $BaTiO_3$ or by tilting of octahedra as in $CaTiO_3$ or by a combination of both as in $NaNbO_3$ (Glazer, 1972). In the early 1920s, Goldschmidt proposed a tolerance factor (t) as given in Equation 2-1, i.e.:

$$t = \frac{R_A + R_O}{\sqrt{2} \cdot (R_B + R_O)}$$

Equation 2-1

where R_A, R_B and R_O are the ionic radii of A, B and O respectively, to study the stability of perovskites (Bhalla *et al.*, 2000, Li *et al.*, 2004, Feng *et al.*, 2008). The t value of an ideal perovskite should be 1.0; however, experimentally, the t value for most cubic perovskites is in the range 0.8–0.9 and distorted perovskites occur with a wider range and generally smaller t values. Nevertheless, for some

systems whose t is within the most favoured range (0.8–0.9), a perovskite structure is not stable (Feng *et al.*, 2008). It seems that the tolerance factor is a necessary but not sufficient condition for perovskite formation. An octahedral factor (μ) has therefore also been introduced to predict perovskite stability, defined as:

$$m = \frac{R_B}{R_O}$$

Equation 2-2

It has been found that the lowest and highest μ values for perovskite formation are 0.425 (Li *et al.*, 2004) and 0.6785, respectively (Feng *et al.*, 2008). The BO_6 octahedron is the most important basic unit in the perovskite structure. If the B-cation is too small, this unit will become unstable and a perovskite structure cannot occur. Using both the tolerance factor and the octahedral factor, perovskite structure formation can be reliably predicted (Li *et al.*, 2004). In 1943, $BaTiO_3$ was discovered to have a high dielectric constant of 1200–1500 and it has been shown by later researchers that further increases in dielectric constant can be achieved by controlled chemical substitution in the cation sites; hence, this material has been a subject of interest for numerous researchers and now has many applications (Richerson, 2006). At high temperatures, $BaTiO_3$ has the ideal cubic unit cell shown in Figure 2-1, with each barium ion surrounded by 12 oxygen ions, the oxygen ions and barium ions together forming a face centred cubic lattice, and with the titanium atoms residing in interstitial positions in oxygen-cornered octahedra. At low temperatures, the titanium ions are too small to be stable in their octahedral interstitial positions and they randomly move off-centre in the direction of any of the six oxygen ions surrounding them to

8

achieve a minimum energy configuration (Richerson, 2006). All ferroelectric materials have a transition temperature, the Curie point (T_C) (Damjanovic, 1998), such that at a temperature $T > T_C$ the crystal does not exhibit ferroelectricity, while for $T < T_C$ it is ferroelectric. If there is more than one ferroelectric phase, the temperature at which the crystal transforms from one ferroelectric phase to another provides a second transition temperature (Damjanovic, 1998). As shown in Figure 2-2, the crystal structure and polarisation characteristics of $BaTiO_3$ are strongly dependent on temperature and in regions close to each transition temperature, thermodynamic, dielectric, elastic, optical and thermal properties all show anomalous behaviour (Lines and Glass, 1979 cited in Damjanovic, 1998).
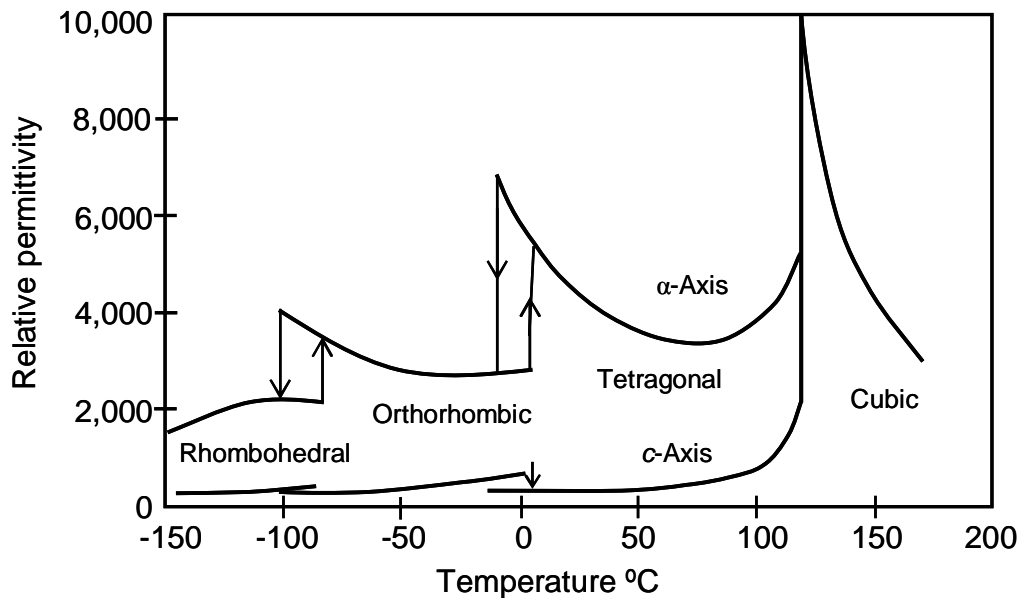
Figure 2-2 Changes in dielectric constant in $BaTiO_3$ as a function of temperature and crystallographic form (Merz 1949 cited in Richerson, 2006)

The cubic form of $BaTiO_3$ is stable only above its Curie temperature of $\approx 135°C$ (Swartz, 1990). When an electric field is applied above its Curie point, the titanium ions shift from random to aligned positions resulting in some bulk

9

polarisation but they return to their stable central position as soon as the field is removed. In this condition, the crystal is referred to as paraelectric (Richerson, 2006). $BaTiO_3$ has more than one ferroelectric phase, and on cooling from its paraelectric cubic modification it can occur in either ferroelectric tetragonal, orthorhombic or rhombohedral forms (Swartz, 1990) with transition temperatures of approximately 120℃, -10℃ and -100°C respectively (Bailey, 2003), as shown in Figure 2-2. Below 120°C (the cubic-tetragonal transition) when an electric field is applied, the octahedral site now distorts with the Ti^{4+} ion moving to an off-centre position towards one of the two oxygen ions along the long (c-) axis resulting in a permanent dipole as shown in Figure 2-3 (Richerson, 2006). Application of an electric field of opposite polarity to the original dipole will cause the Ti^{4+} ion to move through the centre of the octahedral site to an equivalent off-centre position on the other side (Richerson, 2006).
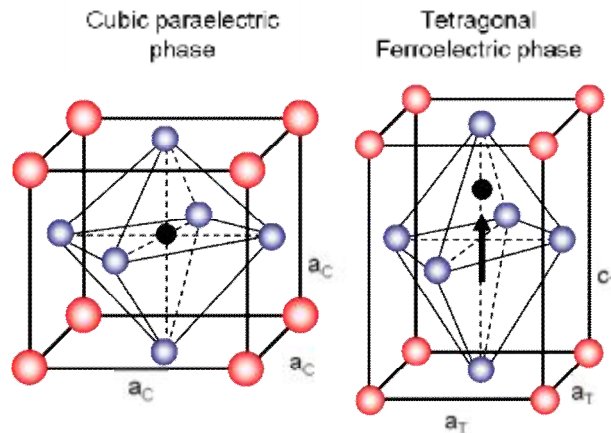
Figure 2-3 Perovskite structure for $BaTiO_3$ showing the cubic (paraelectric) and tetragonal (ferroelectric) phases (adapted from Damjanovic, 1998)

Further cooling results in conversion to an orthorhombic phase and then to a rhombohedral phase at approximately -10℃ and -100℃ respectively. The

dielectric properties of $BaTiO_3$ are not only dependent on the ferroelectric transitions between the various non-cubic phases but are also sensitive to grain size (Swartz, 1990). In large-grained $BaTiO_3$, multiple domains favourably form within a single grain and the motion of these domain walls provides a large contribution to the dielectric constant, especially at the Curie point. In contrast, each grain in fine-grained $BaTiO_3$ forms as a single domain so the domain walls are clamped by the grain boundaries, which are not free to move resulting in a lower dielectric constant at the Curie temperature. Hence, optimised properties can be achieved by appropriate control of the microstructure. The high dielectric constant of $BaTiO_3$ makes this material attractive for dielectric applications but its behaviour is temperature and microstructure dependent (Swartz, 1990). Compositional modification provided by dopants and solid solution substitutions with related perovskite compounds can shift the Curie temperature closer to room temperature and broaden the dielectric peak (Swartz, 1990, Richerson, 2006). For example, additions of $PbTiO_3$ into $BaTiO_3$ increase the Curie temperature while additions of $SrTiO_3$, $SrSnO_3$, $CaSnO_3$ or $BaSnO_3$ decrease the Curie temperature (Richerson, 2006). In high voltage applications, $SrTiO_3$ is used as a capacitor dielectric material with a dielectric constant of approximately 300 at room temperature (Bailey, 2003). $CaTiO_3$ is used in applications similar to those of $SrTiO_3$ but the dielectric constant is roughly half as big (Bailey, 2003). Dielectric constants of both $SrTiO_3$ and $CaTiO_3$ are relatively independent of electric field and temperature so they are used in solid solution with high dielectric materials to improve temperature and field stability (Bailey, 2003). Lead titanate $PbTiO_3$ is a piezoelectric material with a Curie temperature of 490°C and is often used in solid

solutions with other perovskite dielectrics to improve capacitance and stabilise the particular perovskite phase required (Bailey, 2003). Derivatives of $BaTiO_3$ formed by multiple ion substitution have been extensively explored, as shown in Figure 2-4. Because of its unique crystal structure and phase transformations, perovskite and its derivatives have been extensively investigated for many applications in the electroceramic industry.
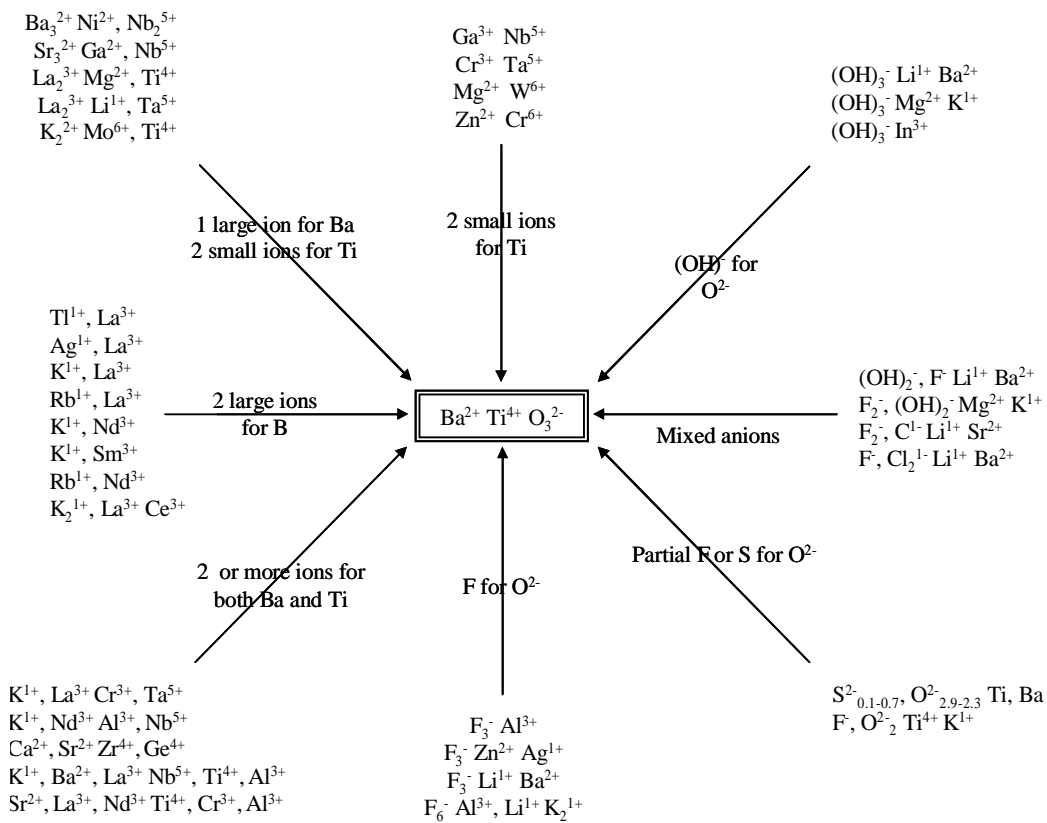
Figure 2-4 Multiple ion substitution in $BaTiO_3$-type perovskites
(Roy, 1954 cited in Bailey, 2003)

With the numerous possibilities for metal ion substitution by a variety of other cations, the physical and chemical properties can be very specifically tuned. Figure 2-5 shows the multifunctionality of these materials in their applications

within the electroceramics industry. Perovskite materials are not only of interest because of cation substitution but it is also possible to substitute into the structure anions such as nitrogen, fluorine and carbon in place of oxygen.

Capacitor High k $BaTiO_3$ $Pb_3MgNb_2O_9$	Piezoelectric $Pb^{2+}(Zr, Ti)^{4+}O_3$	Insulator $SrTiO_3$ Changes to superconductor < 4 K

Major constituent of earth $Mg^{XII}Si^{VI}O_3$	Perovskite $A^{XII}B^{VI}X_3$	High melting point $Ba_3^{2+}Mg^{2+}Ta_2^{5}O_9$

Metallic conductor $La^{3+}Cr^{3+}O_3^{2-}$	Catalysts $La^{3+}(Co, Mn)^{2-3}O_{3-n}$	Superconducors $Ba_2^{2+} Y^{3+}Cu_3^{2-3}O_{7-8}$	Magnetroresistance $La^{3+}Mn^{2-4}O_{3\pm}$
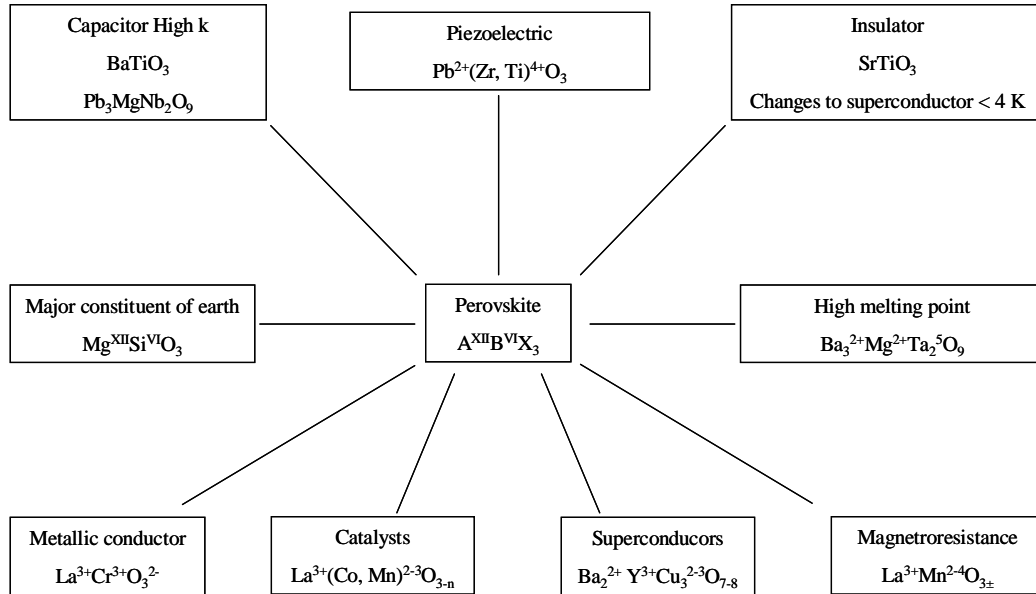
Figure 2-5 Multifunctionality of perovskite materials in the electroceramic industry (Bhalla *et al.*, 2000)

2.2 Oxynitrides

Oxynitrides are derivatives of oxides, in which oxygen is partially substituted by nitrogen (Menke *et al.*, 1998), and several of these have the perovskite structure. Though both N^{3-} and O^{2-} have similar electronic configurations and ionic radii, they differ in their formal oxidation state. Therefore, when divalent oxygen anions are substituted by trivalent nitrogen anions in ternary oxides, additional negative charges are provided by the N^{3-} ion. The additional anionic charges are possibly compensated by 3 mechanisms, i.e. oxygen vacancy formation, A- or B-site substitution with cations of higher valence (cross-substitution) and change of

13

the oxidation state of the B-site cation (Marchand *et al.*, 1991a, Logvinovich *et al.*, 2007). Although the additional charges can be compensated by replacement of three oxygen ions by two nitrogen ions, according to the electroneutrality principle, a vacancy ($\square$) is also created, i.e.:

$$2N^{3-} \equiv 3O^{2-}$$

$$3O^{2-} \equiv 2N^{3-} + 1\square$$

The perovskite structure is very flexible to accept anionic vacancies (Tessier and Marchand, 2003). By a cross substitution mechanism, the A- or B- cations can be substituted by cations of different valency (M^{n+}, $M'^{(n+1)+}$) to balance the charge in the network, i.e.:

$$O^{2-} + M^{n+} \equiv N^{3-} + M'^{(n+1)+}$$
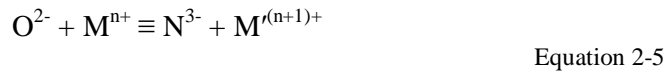
However, the introduction of rare earth and transition metal cations to balance the increasing anionic charge in the system may result in different crystal structures being formed such as scheelite, pyrochlore or fluorite (Tessier and Marchand, 2003). In some cases, the additional anionic charges can be compensated by change of oxidation state of the B-cation i.e.:

$$O^{2-} + B^{n+} \equiv N^{3-} + B^{(n+1)+}$$

For example, the introduction of nitrogen into the perovskites $LaTiO_3$ and $NdTiO_3$ would change the oxidation state of titanium from 3+ to 4+. The corresponding oxynitrides $LaTiO_2N$ and $NdTiO_2N$ have the same crystal structure as the analogous $RTiO_3$ oxides (Ln = lanthanide element) but they have insulating properties whereas $LaTiO_3$ shows metallic behaviour above -170ºC and $NdTiO_3$ is

a semiconductor at room temperature (Maclean et al., 1981 and Greedan, 1985 cited in Marchand *et al.*, 1991a). Because of the exceptional properties of $BaTiO_3$ and the envisaged advantages of incorporating nitrogen anion, there have been attempts to introduce nitrogen anions into $BaTiO_3$, but only a small amount of nitrogen can be introduced into the anion network (Bräuniger *et al.*, 2005, Müller *et al.*, 2009). Since further oxidation of Ti^{4+} is not possible, the straight addition of nitrogen is rather difficult and the increased charge can only be compensated by oxygen vacancy formation (Bräuniger *et al.*, 2005, Müller *et al.*, 2009). By exchanging Ti^{4+} by Ta^{5+} with simultaneous partial substitution of barium oxide by barium fluoride, it is possible to produce a higher nitrogen containing $BaTiO_3$ (Müller *et al.*, 2009). Nitrogen incorporation decreases the band gap and as a result, this nitrogen-containing $BaTiO_3$ shows an additional absorption band at 500 nm in the UV/visible reflectance spectrum thereby making it a candidate for photocatalytic applications (Müller *et al.*, 2009). This and other studies show that further work on the synthesis, compositional characterisation and properties of these oxynitride perovskites are needed. For example, the individual or simultaneous substitution of barium and titanium in $BaTiO_3$ by a lanthanide element and other transition metals results in oxynitride compositions of the type $RMO_{3-x}N_x$, where R represents rare earth and M a transition metal, thereby generating compounds such as $LaTiO_2N$, $NdTiO_2N$ and $LaTaON_2$ (Tessier and Marchand, 2003), where the additional charge of the nitrogen is balanced by the higher valence of the cations. After total or partial replacement of oxygen by nitrogen, the same structure type can be maintained but this cross substitution often yields significant modifications in physical and/or chemical characteristics

of the new compound (Marchand *et al.*, 1991a). The possibility for metal substitutions is potentially much larger in an oxynitride perovskite than in oxides because the exchange allows higher oxidation states for the metal atoms (Esmaeilzadeh *et al.*, 1998, Marchand *et al.*, 2001).

The increased anionic charge after nitrogen substitution results in a change and in some cases an improvement in certain properties of the oxides such as acid-base behaviour, covalent character, reducing character, and thermal and mechanical properties (Marchand *et al.*, 2001). For instance, the acid-base properties of the non-perovskite AlPON are much improved compared with $AlPO_4$ with a lower acidity and much higher reactivity in the Knowevenagel basicity test-reaction (Marchand *et al.*, 2001). The substitution of trivalent nitrogen for divalent oxygen increases the number of bonds in a glass network so the structural rigidity is greater, and in the SiAlON and PON oxynitride glass families, nitrogen introduces a significant modification to properties such as density, glass transition temperature, viscosity and refractive index, with improvements in hardness and mechanical properties such as Young's modulus, chemical durability and a decrease in the thermal expansion coefficient and ease of crystallisation (Marchand *et al.*, 2001). Similar property improvements might also be expected in the case of perovskite oxynitrides.

Certain crystalline oxynitride perovskites have been of interest for environmentally-safe pigment applications as substitutes for toxic heavy metal-based pigments because they display a wider and more controlled range of colours compared with their corresponding oxide counterparts (Jansen and Letschert,

2000). Oxynitride perovskites are stable in air, water and dilute acids at room temperature and show good stability up to quite high temperatures (Aguiar *et al.*, 2008b). The introduction of the less electronegative nitrogen in place of oxygen introduces a more covalent character and causes a reduction in the band gap energy by as much as 1 eV which can give rise to strong and different colours in the respective oxynitrides (Jansen and Letschert, 2000, Marchand *et al.*, 2001, Tessier and Marchand, 2003). In other words, the N 2p orbitals, which have a higher energy than the O 2p orbitals, increase the valence band energy and as a result, the band gap of oxynitrides is narrower than for the corresponding oxides (Fang *et al.*, 2003). The colour is determined by the position of the absorption edge of the corresponding oxynitrides that shifts towards higher wavelengths than those of the oxides and results in absorption in the visible part of spectrum (Tessier and Marchand, 2003, Marchand *et al.*, 2001). Many metal oxides have band gaps which are too wide to allow absorption in the visible region of the electromagnetic spectrum (Jansen and Letschert, 2000). The width of the band gap is affected by the extent of the overlap of the valence orbitals and by the difference between the electronegativities of the cations and anions involved (Jansen and Letschert, 2000, Aguiar *et al.*, 2008a). Reduction in the size of the A-cation is a cause of structural distortion, with the B–(O,N)–B bond angles being reduced to smaller values than the 180° in cubic perovskites while the bond distances remain almost constant (Aguiar *et al.*, 2008a). As shown in Figure 2-6, the change in B–(O,N)–B bond angles modifies the overlap between O/N-p orbitals and metal d orbitals causing a smaller band width in the conducting band, while the energetic position of the centre of the band remains almost unchanged,

17

in turn increasing the band gap (Aguiar *et al.*, 2008a). So the better overlap (i.e. bond angle closer to 180°) results in increased covalency which in turn leads to a smaller band gap. For example, the change in A-cation size in ABO_2N, when A = Ba, Sr and Ca, and B = Ta, causes a strong change in B–(O,N)–B angles while the bond distances remain almost constant for these three compounds, resulting in modification of the overlap between the O/N-p and the metal-d orbitals (Aguiar *et al.*, 2008a). Furthermore, the band gap can be adjusted by different electronegative B-cation management. The introduction of a more electronegative B-cation into oxynitride compounds decreases the energy of the conduction band without affecting its width and leads to a narrower band gap and more covalent B–O bonds as shown schematically in Figure 2-6 (Aguiar *et al.*, 2008a). For example, in ABO_2N, when A = Sr and Ba, and B = Ta and Nb, the more electronegative Nb atom changes the colour of the Sr compound from orange to brown and Ba compounds from red to black (Aguiar *et al.*, 2008a).

a) B-(O,N)-B bond angle modification   b) Different electronegativity of the B-cation modification
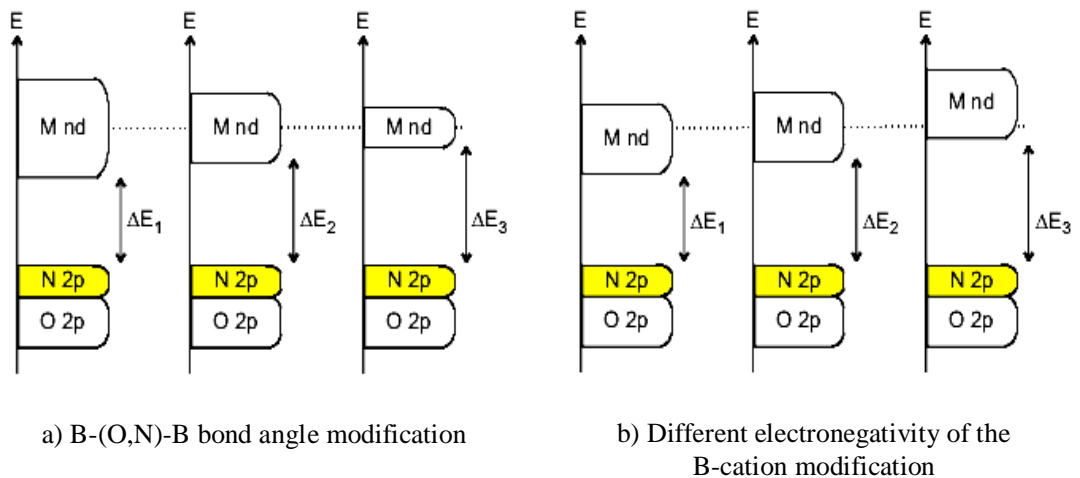
Figure 2-6 Schematic diagram of the influence of a) B–(O,N)–B bond angle modification and b) different electronegativity of the B-cation, on band gap (Aguiar *et al.*, 2008a)

The absorption edge is hence shifted from the UV to the visible part of the electromagnetic spectrum so the band gaps are smaller (Marchand *et al.*, 2001, Tessier and Marchand, 2003, Logvinovich *et al.*, 2007). Therefore, both the A-cationic size and different electronegativities of B-cation substitutions can have a significant effect on optical properties of oxynitrides. Many binary nitrides and ternary oxynitrides therefore exhibit different colours compared with their corresponding white or black oxide compounds, which make them promising candidates for inorganic pigments. Perovskite solid solutions of the type $Ca_{1-x}La_xTaO_{2-x}N_{1+x}$, for example, have been studied as a substituted pigment for cadmium sulphoselenide by simple adjustment of the O:N ratio to achieve a brilliant palette of colours ranging from yellow through orange to deep red (Jansen and Letschert, 2000). The additional benefits of high tint strength and opacity, with good dispersability, light fastness and high thermal stability make them competitive with and possibly superior to the conventional cadmium sulphoselenide pigments (Jansen and Letschert, 2000). Since oxynitrides possess narrower band gaps due to the mixing of N 2p and O 2p orbitals, many oxynitrides, for example $LaTiO_2N$ and $LaTaON_2$, have been studied as visible-light photocatalysts (Kasahara *et al.*, 2002, Kasahara *et al.*, 2003, Liu *et al.*, 2006, Zhang *et al.*, 2008). In rare earth transition metal oxynitrides, the high oxidation state of the transition metal is stabilised by the inductive effect of the rare earth element on the M–(O,N) bond whereas the transition metal in the corresponding oxides can possess a lower oxidation state such as in $LaTi^{4+}O_2N$ and $LaTi^{3+}O_3$ (Cheviré *et al.*, 2006). In this inductive effect, an electropositive element (alkaline earth or rare earth) shares some electrons with the closest transition

metal-nitrogen/oxygen bond to enhance its covalent character and the highest oxidation state of the transition metal is stabilised. From these and other considerations, it can be seen that perovskite oxynitrides are promising candidates for use as non-toxic and eco-friendly pigments in fibres, paints, plastics, and medium temperature ceramics, substituting for previously used toxic oxide pigments.

For electronic applications, many other studies have focused on silicon- or hafinium-based oxynitrides in the SiOxNy, HfON, HfSiON and HfTiON systems, for use as gate dielectrics and capacitor applications (Kang *et al.*, 2002, Visokay *et al.*, 2002, Groner and George, 2003, Choi *et al.*, 2003, Wallace and Wilk, 2003, Koike *et al.*, 2006, Ji *et al.*, 2007, Wong, 2008). Nitrogen incorporation can improve the material and electrical properties of these dielectric materials giving better resistance to high field stress, enhanced hot carrier immunity, resistance against boron penetration, high dielectric strength and higher dielectric constant, as compared with conventional SiO_2 (Albertin *et al.*, 2003, Groner and George, 2003). A few researchers have worked on other rare-earth and transition metal oxynitrides as alternative high-k dielectrics. The promising high-k lanthanum aluminium oxynitride material was reported (Hongwei *et al.*, 2003). The 8 nm film exhibited a dielectric constant of higher than 20 and a band gap of 6.6 eV and showed good thermal stability on a Si substrate and good CMOS processing compatibility up to 1000°C. The low gate leakage current was acceptable for low-power applications. Aguiar *et al.* (2007) and Le Paven-Thivet *et al.* (2007) confirmed the electrically insulating behaviour of $LaTiO_2N$; subsequently this has been explored as an alternative dielectric material. The dielectric constant of

LaTiO$_x$N$_y$ thin films deposited by reactive radio frequency (10 kHz) sputtering on SrTiO$_3$ substrates ranged from 290 to 1220 at room temperature (Ziani *et al.*, 2008). Kim and co-workers (2004) claimed high bulk dielectric constants for BaTaO$_2$N and SrTaO$_2$N, (k $\approx$ 4900 and 2900 respectively) at room temperature. Clearly from these results it can be concluded that nitrogen incorporation has the potential to improve electrical and material properties resulting in increased dielectric constant, reduced leakage current, improved resistance to boron penetration and an increased crystallisation temperature.

In many applications, oxynitride materials may be exposed to elevated temperatures so it is important to determine the temperature at which they start to oxidise and/or decompose. At room temperature, most oxynitrides are generally found to be stable in air and in a moist atmosphere (Aguiar *et al.*, 2008a). In thermal oxidation of oxynitride compounds, N$_2$ is generally the major product and a weight increase is expected according to the reaction (Aguiar *et al.*, 2008b), i.e.:

$$ABO_2N + \frac{3}{4}O_2 \rightarrow ABO_{3.5} + \frac{1}{2}N_2$$
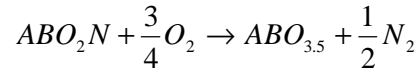
<div align="right">Equation 2-7</div>

However, a much higher weight increase than the expected value sometimes results because of the retention of nitrogen molecules within the structure during the oxidation process causing an intermediate phase consisting of ABO$_{3.5}$ and di-nitrogen molecules bonded to the cations (Aguiar *et al.*, 2008b), i.e.:

$$ABO_2N + \frac{3}{4}O_2 \rightarrow ABO_{3.5}(N_2)_x + (\frac{1}{2} - x)N_2$$

<div align="right">Equation 2-8</div>

The nitrogen is finally released from the compound as nitrogen gas at higher temperature and then the weight gain reaches its expected value (Aguiar *et al.*, 2008b), i.e.:

$$ABO_{3.5}(N_2)_x + (\frac{1}{2} - x)N_2 \rightarrow ABO_{3.5} + xN$$
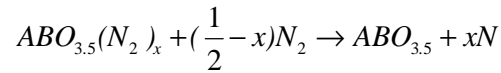
<div align="right">Equation 2-9</div>

2.3 Oxynitride formation

To produce oxynitrides, nitrogen atoms must be introduced into the anion network of binary, ternary or quaternary parent oxides and this can be done using a variety of nitrogen sources. The direct combination of elements is attractive but because of the high stability of the N_2 molecule (the enthalpy of dissociation of the N_2 molecule, 945 kJ mol^{-1}, is approximately twice as large as that of the O_2 molecule), direct reaction between oxides and nitrogen is often too difficult (Marchand *et al.*, 1991a). Other reactive nitrogen resources such as nitric oxide (NO), nitrous oxide (N_2O) and ammonia (NH_3) are therefore used.

2.3.1 Nitridation in NH₃

Thermal ammonolysis (nitridation) of stoichiometric mixtures of appropriate oxide precursors or oxide-carbonates mixtures has generally been used to synthesise nitride and oxynitride compounds at elevated temperatures in the range 900–1000°C (Marchand *et al.*, 1991b). However, not every system follows the same well-established rules, and reactions often proceed differently depending on a variety of intrinsic and extrinsic parameters (Tessier and Marchand, 2003) such as gas flow rate, temperature and reaction time, and the results often depend upon

the homogeneity and nature of the precursors and the furnace atmosphere. In high temperature ammonolysis, ammonia acts as both a reducing and a nitriding agent (Tessier and Marchand, 2003). The overall decomposition mechanism of ammonia when the reaction temperature is lower than 500ºC can be summarised by the following reaction, i.e.:

$$NH_3 \longrightarrow \frac{1}{2}N_2 + \frac{3}{2}H_2$$

<div align="right">Equation 2-10</div>

However, N_2 molecules are not effective in nitriding oxide ceramic powders, and by analogy with the nitridation of metals, a more important consideration at high temperature is the generation of active atomic nitrogen (Hellwig and Hendry, 1994), i.e.:

$$2NH_3 \longrightarrow 2NH_2 + H_2$$

<div align="right">Equation 2-11</div>

$$2NH_2 \longrightarrow 2NH + H_2$$
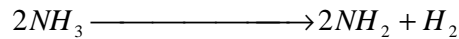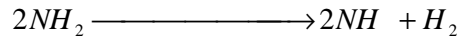
<div align="right">Equation 2-12</div>

$$2NH \longrightarrow 2N + H_2$$

<div align="right">Equation 2-13</div>

This active atomic nitrogen reacts with the sample powder on the surface. While the exchange between the oxide anions and the adsorbed nitrogen occurs, hydrogen reacts with oxygen to form water vapour molecules which are removed from the system in the flowing gas system.

In some cases, inhomogeneities in colour at opposite ends of the nitriding container are observed, and this is due to variations in nitrogen fugacity, corresponding to the temperature variation along the length of the furnace tube.

The degree of ammonia dissociation increases along the furnace tube reaching a maximum near the start of the hot zone and decreasing sharply after the hot zone (Hellwig and Hendry, 1994). In order to minimise the dissociation of ammonia into N_2 gas (which is not effective in nitriding oxide ceramics), the temperature, and also the ammonia flow rate, must be carefully controlled. Because of the difficulty of precise control of all the reaction parameters, repeated processing may be necessary to achieve single-phase oxynitride products. For example, Clarke *et al.* (2002) synthesised $LaTiO_2N$ by nitriding $La_2Ti_2O_7$ at 950°C for periods of 20, 6 and 6 hours with intermediate regrinding whereas Rachel and co-workers (2005) synthesised $BaTaO_2N$ by the same method at a reaction temperature of 1000°C for 126 hours. Using halide mineralisers (e.g. NaCl/KCl) as a flux can reduce ammonolysis temperatures and reaction times significantly (Kim *et al.*, 2004, Rachel *et al.*, 2005)**.** Also, the formation of unwanted binary (oxy)nitrides which can occur at higher temperature due to the reducing character of ammonia can be suppressed (Rachel *et al.*, 2005). With halide additions, $CaTaO_2N$, $SrNbO_2N$ and $BaNbO_2N$ were obtained by ammonolysis at 950°C in 18, 36 and 72 hours respectively compared with the halide-free route which required 36, 54 and 90 hours of reaction time respectively (Rachel *et al.*, 2005). However, the use of a hydrogen containing nitrogen source may cause a higher fixed charge density and a large number of electron traps in the dielectric film (Green *et al.*, 2001). Non-hydrogen containing nitridation gases such as nitric oxide or nitrous oxide are alternatives, providing appropriate temperatures exist at which the desired nitridation reactions can proceed.

2.3.2   NO and N$_2$O processing

Nitrogen could be incorporated into oxide targets such as SiO$_2$ by thermal nitridation in nitrous (N$_2$O) and nitric (NO) oxides. The introduction of nitrogen via nitrous oxide and/or nitric oxide is able to effectively reduce the defects which occur from the presence of hydrogen when ammonia is used (Buchanan, 1999). In both cases, it is believed that NO is responsible for nitrogen incorporation (Green *et al.*, 2001). In nitrous oxide processing, N$_2$O rapidly decomposes at high temperature to N$_2$, O$_2$, NO, and atomic O at typical reaction temperatures, 800–1100°C (Green *et al.*, 2001). NO diffuses through the interface between SiO$_2$ and the Si substrate and dissociates there; thereafter the active nitrogen nitrides the Si and the active atomic oxygen promotes some oxidation (Lu *et al.*, 2000). Basically, the amount of incorporated nitrogen progressively increases as a function of nitridation time and temperature. However, once N is incorporated, the relatively high concentration of nitrogen in the film retards the rate of further nitridation (Lu *et al.*, 1997). Furthermore, in the N$_2$O case, atomic oxygen is effective in removing nitrogen previously incorporated in the SiO$_2$ layer (Carr *et al.*, 1995). Therefore, the total concentration of nitrogen is influenced by a competition between nitrogen incorporation and removal. The electrical reliability of oxynitride gate dielectrics in metal-oxide-Si (MOS) capacitors can be significantly improved by a two-step N$_2$O nitridation i.e. rapid-thermal annealing in N$_2$O for 40 seconds at 1050°C followed by a second at lower temperature for a shorter time (850°C for 15 seconds, 850°C for 30 seconds and 900°C for 15 seconds) (Chang-Liao and Ku, 1999).   Detrimental effects such as hydrogen diffusion into and boron penetration from the Si and hot-electron induced trapped charges are significantly

suppressed by nitrogen pileup at the Si/SiO$_2$ interface, which occurs during the second step N$_2$O nitridation at lower temperatures.

2.3.3 Carbonitridation

In a carbonitriding reaction, the raw materials, generally oxygen-containing, are reduced with carbon and simultaneously nitrided. The reaction is often carried out in a horizontal alumina-tube reactor with N$_2$ gas flow. Depending on the raw materials and reaction conditions employed, it is possible to obtain a variety of nitride and oxynitride products such as Zr-Si-O-N (Mazzoni *et al.*, 2001), and Zr(C,N,O) phases (Mazzoni and Conconi, 2004). Aluminium nitride synthesised by this method shows traces of carbon and aluminium carbide which may be detrimental to the quality of the materials especially as regards thermal conductivity and the dielectric constant and loss (Marchand *et al.*, 1991a).

2.3.4 Urea as a nitrogen source

Other reactive nitrogen resources are of interest. Urea is a nitrogen-containing compound which offers a feasible route for oxynitride synthesis. Using this route, ternary metal oxynitrides (in nanoparticle size) of formulae ATaO$_2$N (A = Ca, Sr or Ba), ANbO$_2$N (A = Sr or Ba), LaTiO$_2$N and SrMoO$_{3-x}$N$_x$ have been prepared successfully by mixing metal oxides with excess urea and then heating in a N$_2$ atmosphere (Gomathi *et al.*, 2009). Urea starts decomposing giving off "active" ammonia at 523K, i.e.:

$$CO(NH_2)_2 \xrightarrow{\Delta} NH_3 + HCNO$$

Equation 2-14

26
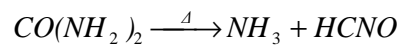
and the reaction is complete at 823 K (Gomathi *et al.*, 2009). The activity of the active ammonia is due to decomposition to give active atomic nitrogen which partially replaces oxygen in the oxide raw materials.

2.3.5 Oxide precursor preparation

In addition to optimising the conditions in the nitridation process, the nature of the starting materials used for oxynitride synthesis is very critical (Tessier and Marchand, 2003). Conventionally, solid state reaction between mixed binary oxides is the most convenient and cheap method but this has limitations as regards homogeneity and reactivity. In particular, the small specific surface area results in low reactivity and pure single phases are therefore difficult to prepare. These difficulties increase in multi-cationic stoichiometries. Generally, reactions involving liquid phases proceed more efficiently than solid reactions, and many wet chemistry-based methods have been extensively explored. Chimie douce processing (soft chemistry) and co-precipitation methods are both aqueous-based processes, which have many advantages over conventional solid state ceramic methods, and yield small particle size products, with large specific surface area, and a homogeneous composition. Appropriate ratio mixes of raw materials in solution form are reacted in a hot furnace leading to a chemically homogeneous and highly reactive oxide powder of uniform particle size and shape (Paul and Robert, 1991). Many benefits from aqueous-based processes have been reported. For example, the resulting powders for $La_2Ti_2O_7$ and $Nd_2Ti_2O_7$ (Suresh *et al.*, 2001), and $BaTa_2O_6$ (Navale *et al.*, 2007) production prepared by co-precipitation could be calcined at lower temperatures and for shorter reaction times than those

used in conventional solid state calcination. ABO_2N type oxynitrides (A= Ca, Sr, Ba; B= Ta, Nb) could be synthesised by ammonolysis of these amorphous xerogel precursors in shorter reaction times compared with crystalline oxides (Rachel *et al.*, 2005). $LaTiO_2N$ photocatalyst materials synthesised by ammonolysis of oxide precursors precipitated from solution containing lanthanum nitrate and tetrabutyl orthotitanate have been reported to have high surface area with good light absorption properties both in the ultraviolet light and the visible-light region (Zhang *et al.*, 2008). The addition of aids to optimise the medium in which reaction between the constituent oxides takes place can also increase the reactivity because of the higher mobility of reacting species, for instance using NaCl/KCl as mineralisers in $La_2Ti_2O_7$ preparation significantly reduces the temperature and reaction time (Paul and Robert, 1991). Many other aqueous-based processes have been developed to improve product quality and reactivity, however, process selection is often restricted by the solubility of the product in the solvent used.

2.4 Dielectrics and Capacitors

Dielectrics are electrically insulating materials which, when an electric field is applied, the field causes a slight shift in charges in the material to form an electrical dipole resulting in an overall polarisation (Richerson, 2006). The degree to which this polarisation occurs for a given electric field is the permittivity of the dielectric so the higher the degree of polarisation, the higher the dielectric constant and the more charge can be stored (Richerson, 2006). Figure 2-7 shows the mechanism of polarisation in a dielectric when an electric field is applied to the plates. When the material becomes polarised, an electric field

is produced inside the material in the opposite direction to the applied field resulting in the total effective electric field being less than that of the applied field.
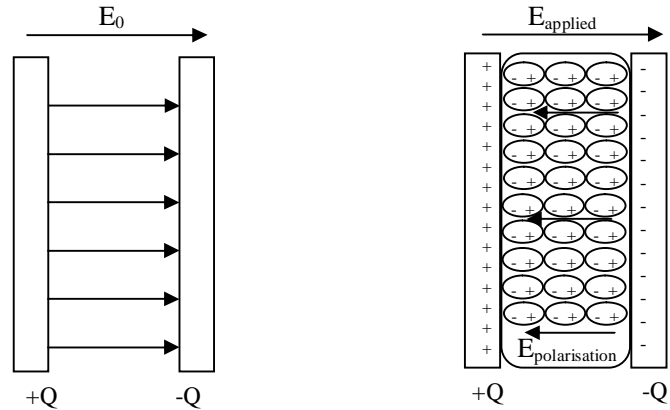
Figure 2-7 Mechanism of polarisation in dielectrics due to the applied electric field

Different mechanisms are operative; these include electronic polarisation, orientation polarisation, space charge polarisation and atomic or ionic polarisation all of which can contribute to the induced polarisation; however, only atomic or ionic polarisation involves displacement of atoms or ions within a crystal structure and this can exhibit an extremely high dielectric constant (Richerson, 2006).

The term dielectric constant (k) is often used synonymously with relative permittivity (ε_r) which is the absolute dielectric constant (ε) relative to the permittivity of free space (ε_0), as shown in Equation 2-15, i.e.:

$$e_r = \frac{e}{e_0}$$

Equation 2-15

Ideally, a dielectric material would not allow flow of electric charge, but only a displacement of charge via polarisation; however, real dielectric materials always have some energy loss when an external electric field is applied (Richerson, 2006).

The complex dielectric constant consists of a real part e_r' and an imaginary part e_r'', given by Equation 2-16, i.e.:

$$e_r = e_r' + i e_r''$$

<div align="right">Equation 2-16</div>

The real part, e_r', represents the amount of energy from the external electric field stored in the material and the imaginary part, e_r'', describes the energy loss from the AC signal as it passes through the material when an external electric field is applied.

If an ideal dielectric is placed between parallel electrodes to form a capacitor and an alternating electric field is applied, then no power would be absorbed by the dielectric, and ideally, the current would lead the voltage by a phase of 90 degrees (Richerson, 2006). Real materials always have some loss; the current phase lags δ degrees behind what it would be in the ideal material. The amount of this dissipated energy is defined as tan δ (Richerson, 2006). The dissipation factor, also known as the dielectric loss and loss tangent, is the ratio of the energy dissipated to the energy stored in the material, as expressed by Equation 2-17 (Richerson, 2006) , i.e.:

$$\tan d = \frac{e_r''}{e_r'}$$

<div align="right">Equation 2-17</div>

The dissipated energy is commonly turned into heat due to conduction of electrons flowing through the material. The degree of this energy loss is affected by many factors both intrinsic and extrinsic (Penn et al., 1997). Intrinsic losses are associated with the crystal structure such as atomic masses, atomic charges

and bond strength, and the interaction of phonons with the AC electric field. The extrinsic contributions are caused by imperfections in the crystal i.e. impurities, grain boundaries, porosity, oxygen vacancies, microstructural defects and random crystallite orientation. For simple parallel plate dielectric measurement, the dielectric material is placed between two electrodes to form a capacitor, as shown in Figure 2-8, and then energised with an AC source. Using an impedance analyser or an LCR meter, the capacitance and the dissipation factor are measured and then the dielectric constant or relative permittivity can be calculated knowing the dimensions of the dielectric material.
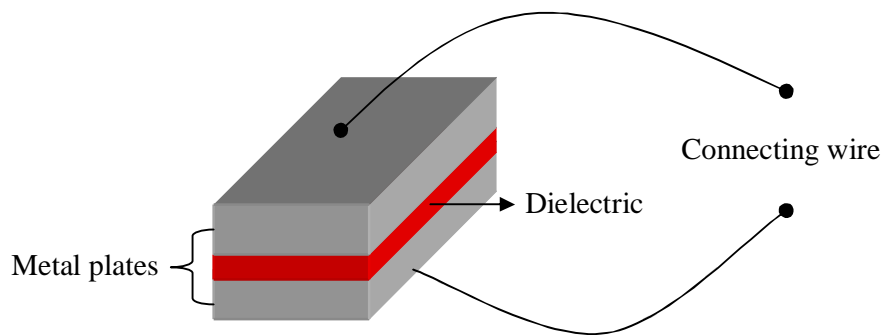

Figure 2-8 Schematic of a parallel plate dielectric capacitor

The capacitance of a set of charged parallel plates can be increased by the insertion of a dielectric layer because it is inversely proportional to the effective electric field and hence the applied voltage between the plates, according to Equation 2-18, i.e.:

$$C = \frac{Q}{V}$$

Equation 2-18

The capacitance is therefore dependent on the dielectric constant and the geometry of the capacitor. This relationship is expressed by Equation 2-19 (Swartz, 1990) , i.e.:

$$C = \frac{k\varepsilon_0 A}{d}$$

<div align="right">Equation 2-19</div>

Here k is the dielectric constant, ε_0 is the permittivity of free space (8.85×10^{-12} F/m), A is the area of the capacitor (m^2) and d is the distance between the plates (m) or the thickness of the dielectric.

According to Equation 2-19, the same charge can be obtained by using a lower voltage when the plates are closer together and/or a higher-k dielectric material is used. Clearly, a very high capacitance can be reached for a given electric field by using a very thin layer of high-k dielectric material. The higher the degree of polarisation of the dielectric material, the higher the dielectric constant and therefore more charge can be stored (Richerson, 2006). Generally, materials with a high dielectric constant come with higher dielectric loss so material selection is a compromise, i.e. a medium value of dielectric constant with acceptable dielectric loss (Bailey, 2003). One of the effective ways to maximise the capacitance is to stack many thin layers of dielectric in series and connect them electrically in parallel (Bailey, 2003). Figure 2-9 shows a structure in which many dielectric layers and internal electrodes are alternately stacked, the arrangement being referred to as a multilayer capacitor (MLCC). MLCCs give high capacitance combined with small size, high reliability and excellent high-frequency characteristics (Kishi *et al.*, 2003). The capacitance (C) of a multilayer dielectric capacitor is represented by Equation 2-20 (adapted from Kishi *et al.*, 2003), i.e.:

$$C = \frac{k\varepsilon_0(n-1)A}{d}$$

where n is the number of internal electrode layers and A is the overlap area of these electrodes. As seen from Equation 2-20, the requirements for achieving large capacitance are a high-k dielectric material, a thin dielectric layer; a large number of layers in the stack and a large overlap area of the internal electrodes.
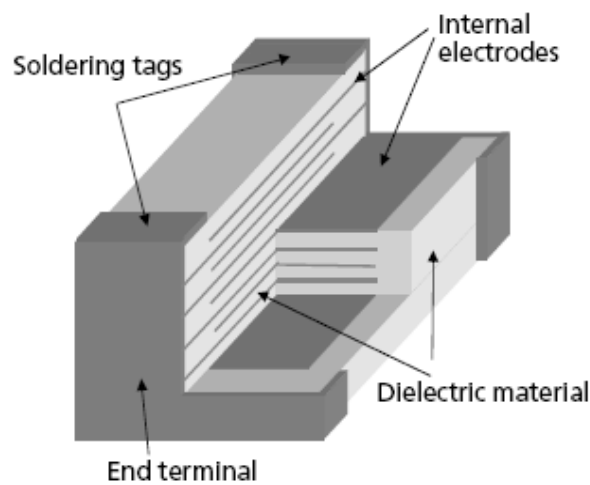
Figure 2-9 Cross section of a multilayer ceramic capacitor (Kishi *et al.*, 2003)

For small size MLCC capacitors, it is also necessary for these devices to be capable of being made with very high stacking precision (Kishi *et al.*, 2003). Since the fundamental limitation of scaling down of capacitance-operated devices, e.g. capacitors and transistors, is the exponential increase in tunnelling current with decreasing film thickness, a thicker dielectric layer than the minimum thickness is generally used; it is therefore always beneficial to use a material with a high dielectric constant.

2.5 Device principles of high-k dielectrics

Complementary Metal-Oxide-Semiconductor (CMOS) scaling has provided the means to realize higher performance with every technology node. Devices have been designed aiming at reduction in size with minimal change to the conventional CMOS processing; however, scaling down has clearly reached fundamental material limits. Hence microelectronic developments are now in an era where further reduction in the size of a device can only be realized by new materials and/or modified device architecture. In order to continue scaling down, nearly a decade of research and development has been conducted by various groups on high-k gate dielectrics to potentially replace SiON for future generation CMOS devices. Much of this work has focused on gate dielectrics in metal oxide semiconductor field electric transistors (MOSFETs) for high-performance logic CMOS technology. At the same time, high-k dielectrics are also of great interest for applications in mass storage memory devices such as NAND flash and Dynamic Random Access Memory (DRAM) as well as microwave communication devices and other CMOS devices which require a high capacitive coupling.

2.5.1 Metal oxide semiconductor field electric transistors (MOSFETs)

The basic device used in CMOS circuits is a metal oxide semiconductor field electric transistor (MOSFET). It functions as an amplifier as well as a three-terminal switch, either connecting or isolating the drain and source terminals based on the voltage applied to the controlling gate terminal (Kawamoto *et al.*, 2001). As illustrated in Figure 2-10, the gate dielectric insulates the gate electrode from the silicon substrate; boron is used as a dopant for silicon gate

electrodes to ensure reasonable conductance (Buchanan, 1999). When the gate electrode is biased above the threshold voltage, the gate dielectric enables inversion of the carrier type at the Si surface to the same type as the source and the drain and thus promotes current flow from the source to the drain.
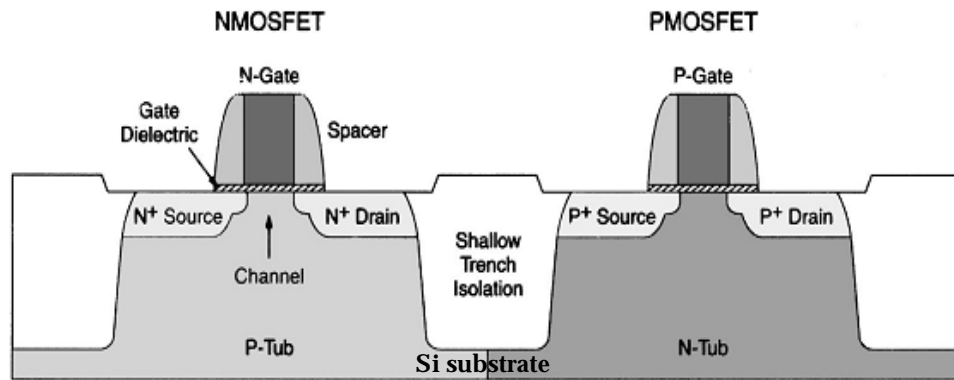
Figure 2-10 Schematic of n- and p-MOSFETs (Green *et al.*, 2001)

A MOSFET is a capacitance-operated device so the source-drain current of the MOSFET depends on the gate capacitance as expressed by Equation 2-21 (Kawamoto *et al.*, 2001), i.e.:

$$I = \frac{W}{2L} mC(V_g - V_t)^2$$

Equation 2-21

where W is the transistor width, L is the channel length, μ is the carrier mobility, C is the capacitance of the gate insulator, V_g is the gate voltage and V_t is the threshold voltage. In order to keep the saturated drive current constant, when a device is scaled down, which means that the gate voltage and channel length are reduced, the capacitance must increase and hence a high-k dielectric layer or a thinner dielectric layer is required.

Silicon dioxide has been used as a gate dielectric for MOSFETs since 1957 (Buchanan, 1999). As devices have become smaller, the SiO_2 dielectric gate has needed to become thinner; as a result, it loses its insulating property, generating a high gate leakage current which causes an increase in power consumption (Green *et al.*, 2001). With decreasing oxide thickness, boron and other dopants from the doped gate electrode and the silicon substrate diffuse rapidly through the oxide film upon thermal annealing resulting in a high concentration of boron in the channel region and hence a shift in threshold voltage (Wilk *et al.*, 2001). Nitrogen incorporation into the oxide dielectric can greatly improve the dielectric properties and reduce boron diffusion (Buchanan, 1999, Wilk *et al.*, 2001, Green *et al.*, 2001). Silicon oxynitride (SiO_xN_y) possesses a higher dielectric constant so a physically thicker film can be used for the same capacitance which consequently reduces the tunnelling current (Green *et al.*, 2001). The reduction in boron penetration results from the strong Si-O-N network bonding (Ellis and Buhrman, 1998, 1999). Additionally, SiO_xN_y is also compatible with the silicon substrate and the polycrystalline silicon gate electrode (Green *et al.*, 2001). Interfacial regions of low-k SiO_2 between either substrate or gate electrode and dielectric layer are particularly important because they can reduce the overall capacitance of the gate stack (Wilk *et al.*, 2001).

2.5.2 Capacitors for memory devices

The need to further scale down the physical dimensions of memory storage devices has driven high-k dielectrics development for both Dynamic Random Access Memory (DRAM) and flash memory devices. DRAM consists of a

capacitor as the memory storage element and a transistor as the valve for adding or removing charge from the capacitor after application of a voltage. A submicron-size capacitor represents one bit of memory for storing a given amount of charge: if the charge is present, it represents a digit one, if not then the digit is zero (Yoon *et al.*, 2002). Flash drives use Floating Gate Metal Oxide Semiconductor FETs (FGMOS) that are basically MOSFETs with an additional floating gate, as shown in Figure 2-11 (drawn from Kittl *et al.*, 2009). As with MOSFETs, all memory devices such as DRAM and flash memory are basically based on silicon technology, i.e., silicon dioxide is used as the dielectric layer in DRAM capacitors and as IPD in floating gate cells and nitride materials are used for the charge trapping layer in charge trap devices (Kittl *et al.*, 2009).
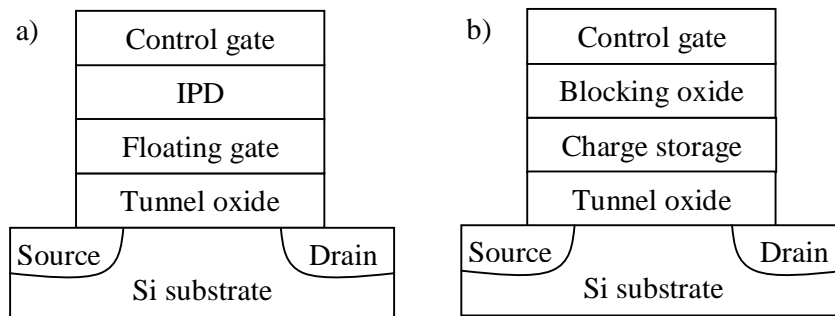
Figure 2-11 Schematic of memory flash cell: a) Floating gate and b) Charge trap
(IPD: Interlayer Polycrystalline Dielectric)

Memory capacitors require extremely low leakage currents and very high capacitance density for charge storage but the interface quality and current transport are not as critical as in MOSFETs (Wilk *et al.*, 2001). The interface is only controlled to keep capacitance high for storing charge. To improve performance and reliability, oxynitride films (SiO_xN_y) and stacked ON or ONO

(oxide-nitride-oxide) and SONOS (silicon-oxide-nitride-oxide-silicon) structures have been developed to use as the dielectric in floating gate cell memories and DRAM capacitors with many benefits (Roizin and Gritsenko, 2007). The stacked structures have much lower defect densities and suppress leakage due to charge trapping in the nitride layer (Roizin and Gritsenko, 2007). The dielectric constant of SiO_xN_y is higher than that of silicon dioxide so as a gate dielectric, the same capacitance can be obtained with a larger thickness. Due to further improvements and scaling down in microelectronics, chips are now designed to achieve the higher device density, requiring capacitors to become smaller but the amount of stored charge must remain constant and so the dielectric thickness must be decreased (Yoon *et al.*, 2002). This reduction in dielectric thickness causes charge leakage through the dielectric layer resulting in difficulties in retaining the stored charge between cycles (Yoon *et al.*, 2002). In DRAM manufacturing, in order to increase the effective area of each capacitor, this has been achieved by the development of complex high aspect ratio structures for each memory cell, involving a trenching structure and more complex stacking, or alternatively by using a high-k dielectric material (Yoon *et al.*, 2002). The scaling down has some limit due to the high cost and increasing complexity in manufacturing, and it turns out that now the materials are a key constraint. Higher-k dielectrics have been intensively explored for use as either the blocking layer for the charge trapping memories in charge trap flash cells or as IPD in floating gate applications or as the dielectric in DRAM capacitors. It is highly possible to combine the high-k dielectric with effective device structures to further improve performance and reduce power consumption.

2.5.3   High-k dielectric materials for other applications

In microwave communication devices, bulk ceramic dielectrics are used as resonators and filters for microwaves carrying the desired information as discrete components (Cava, 2001). Since the size of a resonator at any particular resonant frequency depends on the inverse of the square root of the dielectric constant, the larger the dielectric constant the smaller the components must be (Cava, 2001). Nevertheless, the dielectric behaviour of the material must not depend on temperature and it must have a low dielectric loss (Cava, 2001). The fundamental conflict for dielectric materials in microwave communication applications is that the atomic polarisation processes necessary to achieve high dielectric constant also inevitably give rise to dielectric loss and temperature dependence of the dielectric constant (Cava, 2001). Thus the development of microwave dielectric materials with high dielectric constant and suitable properties is rather limited. As portable communication devices demand further miniaturisation, there is a greater need to explore higher quality, high-k dielectric materials.

2.6   Current high-k dielectric materials

With the exponential escalation in the development of electronic devices whilst retaining improved performance, the gate dielectric thickness must also decrease to maintain values of capacitance and drive current at acceptable levels. However, since direct tunnelling increases exponentially with decreasing gate dielectric, a higher-k dielectric must be used so that a thicker dielectric layer can be used with acceptable leakage current level. Numerous alternative high-k dielectric materials have been studied.

2.6.1 Silicon oxide and oxynitride-based dielectrics

Nitrogen substitution into silicon dioxide films has been extensively studied to promote enhanced performance of these films. There is a lot of evidence to show that nitrogen increases the dielectric constant of the film (Buchanan, 1999, Wilk *et al.*, 2001, Green *et al.*, 2001). As a result, much thicker films of nitrogen incorporated dielectrics can be used which increase reliability and reduced penetration of boron implanted into the Si gate electrode, even when present in a sufficiently high dose as a dopant for the p^+ gates to ensure reasonable conductance of the gate (Buchanan, 1999, Wilk *et al.*, 2001). The reduction of boron penetration is believed to result from the more rigid Si–O–N network bonding in silicon nitride and oxynitride (Ellis and Buhrman, 1998, Green *et al.*, 2001, de Almeida and Baumvol, 2003). The side effect from preventing boron penetration is a high consumption of nitrogen which means that high nitrogen concentration is required but this cannot be too high otherwise it will severely affect reliability and electron mobility in the transition channel (de Almeida and Baumvol, 2003), with consequent threshold-voltage shifts, and mobility and transconductance degradation (Buchanan, 1999). Compared to that of SiO_2, the dielectric constant of Si_3N_4 is almost twice as high (k $\approx$ 6–7); nevertheless, it is difficult to fabricate Si_3N_4 in the form of ultrathin films without incorporating some oxygen near the interface (Green *et al.*, 2001). Since Si has a greater affinity for oxygen than for nitrogen, a low-k SiO_2 interface layer forms and decreases the overall dielectric constant of devices. Electrons travelling through a SiO_2 layer may create defects such as electron traps and interface states, which if they accumulate beyond a certain critical density, degrade the insulating

properties of the oxide (Green *et al.*, 2001). SiO_xN_y-based dielectrics are a reasonable compromise for nitrogen introduction into a Si film. The dielectric constant increases by only a small amount to a value of about 6 but the product is more compatible with silicon MOS technology and improves film properties such as resistance to high field stress, enhances hot carrier immunity, protects boron penetration and increases dielectric strength (Albertin *et al.*, 2003, Groner and George, 2003). Both high-k material selection and proper material engineering has enabled optimisation of these materials to give good dielectric performance. For example, the nitrogen profile of the film, i.e. high nitrogen concentration near the Si gate electrode/oxynitride interface and much smaller nitrogen content near the oxynitride/Si interface or alternatively using $Si_3N_4/SiO_2/Si$ and $Si_3N_4/SiO_xN_y/Si$ stacks is a way of eliminating the interface problem of Si_3N_4 (de Almeida and Baumvol, 2003). Oxynitride alloys of the type SiO_2: Si_xN_y can achieve an EOT of less than 17 Å with a leakage current of 10^{-3} A/cm^2 at 1.0 V bias which is $\approx$ 100 times lower than that for a pure SiO_2 layer of the same thickness (Yang and Lucovsky 1999 cited in Wilk *et al.*, 2001). By making an NO passivation layer, Si_xN_y films deposited via SiH_4/NH_3 reaction and further annealed in NH_3 and N_2O can achieve oxynitride layers with an EOT of 18Å and a low leakage current of 10^{-4} A/cm^2 at 1.0 V bias (Song *et al*., 1998 reviewed by Wilk *et al.*, 2001). However, the gate dielectric thickness is likely to approach 1 nm for most scaled devices in the near future and, at these thicknesses, SiO_2 and SiO_xN_y exhibit severe gate leakage current. Clearly, alternative high-k dielectric materials are necessary.

2.6.2 Metal oxide-based dielectrics

The most common metal oxides studied as alternative high-k dielectric materials are Al_2O_3, La_2O_3, Y_2O_3, Pr_2O_3 TiO_2, ZrO_2, HfO_2 and Ta_2O_5 and these have been reviewed by Wilk *et al.* (2001), Groner and George (2003) and Leskelä *et al.* (2006). As shown in Table 2-1, Al_2O_3 has many superior properties such as high band gap, thermodynamic stability with respect to Si up to high temperature and remaining amorphous under the required conditions (Wilk *et al.*, 2001). In spite of the good stability of Al_2O_3 on Si, any deposition technique typically operates under non-equilibrium conditions and undesirable phases may form. The deposition technique used must therefore be studied in detail to confirm that these are avoided.

Table 2-1 Relevant properties for high-k dielectrics (Wilk *et al.*, 2001)

Material	Dielectric constant (k)	Band gap E_G (eV)	ΔE_C to Si (eV)
SiO_2	3.9	8.9	3.2
Si_3N_4	7	5.1	2
Al_2O_3	9	8.7	2.8
Y_2O_3	15	5.6	2.3
La_2O_3	30	4.3	2.3
Ta_2O_5	26	4.5	1-1.5
TiO_2	80	3.5	1.2
HfO_2	25	5.7	1.5
ZrO_2	25	7.8	1.4

Ta_2O_5 and TiO_2 have small band gaps and correspondingly small ΔE_C values which are directly related to high leakage currents (Wilk *et al.*, 2001). La_2O_3 has a slightly higher k than HfO_2 and a far higher value than Al_2O_3 but it is very reactive to moisture (Robertson, 2004). Crystalline Pr_2O_3 epitaxially grown with molecular beam epitaxy (MBE) on Si(001) is a promising candidate for highly scaled gate insulators and has a reasonably high-k value of approximately 30, ultra-low leakage current density, good reliability and high electrical breakdown voltage (Osten *et al.*, 2003). M_2O_3 lanthanide metal oxides are interesting as high-k dielectrics because of the higher mole fraction of cations (40 mol%) present compared with MO_2 (33.3 mol%) (Wilk *et al.*, 2001). Many of these compounds show some promise as dielectric materials; nevertheless, they often exhibit significant frequency dependence, hysteresis and flat band voltage shifts as well as high oxygen diffusion and poor interface stability during high-temperature processing (Wilk *et al.*, 2001). For example, La_2O_3 tends to develop low-k interfacial layers on silicon during high temperature heat treatment above 300ºC; to improve this, Y_2O_3 has been used as a barrier layer between La_2O_3 and silicon to suppress the formation of a low-k SiO_2 interface and improve the mobility of MOSFETs (Ahmet *et al.*, 2007). Many other oxide dielectrics have been explored for dielectric applications but no simple oxide seems to have the right combination of dielectric constant, thermodynamic stability on Si and stability of the amorphous phase at reasonable processing temperatures (Green *et al.*, 2001). No doubt with appropriate materials engineering, progress could be made, but further research is needed. Several attempts have been made to optimise the desirable properties of one whilst eliminating the undesirable properties of another

by alloying mixtures of metal oxides. The resulting dielectric materials are therefore complex oxides. For example, materials in the $MgTiO_3$-$CaTiO_3$ system are widely used (Class I capacitors); BaO-$4TiO_2$ with a k of 36 finds application in ceramic capacitors; $Ba(Zn,Ta)O_3$ and $Ba(Mg,Ta)O_3$ have Q values ($Q = \frac{1}{\tan d}$) of higher than 20000 at 10 GHz; BaO-PbO-Nd_2O_3-TiO_2 compositions with k ≈ 90 have a sufficiently high Q value (≈ 5000) for use at 1 GHz; $(Zr_{0.8}Sn_{0.2})TiO_4$ materials with high-Q and good temperature stability and $Ba(Zn_{1/3}Ta_{2/3})O_3$ materials with extremely high-Q values are also currently in use (Fiedziuszko *et al.*, 2002). Pseudo-binary alloys, e.g. silicates of the type M–Si–O where M = Zr, Hf, La and Gd and aluminate of the type M–Al–O where M = Zr, made by mixing together a high-k (crystalline) metal oxide with an amorphous, stable, lower-k dielectrics such as SiO_2 or Al_2O_3 can be used to obtain a product with a morphology suitable for a CMOS gate dielectric and have been extensively studied (see the reviews by Wilk *et al.* (2001) and Hall *et al.* (2007)). Within certain ratios of SiO_2 (or Al_2O_3) and metal oxides, these alloys are thermally stable as an amorphous layer on Si, have a better oxygen diffusion resistance, a reduced growth rate of interfacial layers, and show a higher value of band gap and reduced leakage current. However, the dielectric constant of these alloys is inevitably lower than that of the pure metal oxide (Wilk *et al.*, 2001, Hall *et al.*, 2007). Incorporation of silicate layers into stacked structures, for example SiO_2/Hf_4SiO_{10}/Si_3N_4 and HfAlO/SiON insulator stacks, offers another technique for minimising the interface states by acting as a transition region between the Si substrate and the dielectric (Wilk *et al.*, 2001, Hall *et al.*, 2007). Rare earth metals can be used as effective dopants in conventional host oxides such as

TiO$_2$ and ZrO$_2$ (Leskelä *et al.*, 2006). In BaO-R$_2$O$_3$-TiO$_2$ systems especially those with molecular formulae of Ba$_{6-3x}$R$_{8+2x}$Ti$_{18}$O$_{54}$ and having the tungsten-bronze structure, rare earth oxide substitution has been found to be an effective way of improving microwave dielectric constants in the range of 80–110 with good Q factors (Q > 5000 GHz) and a low temperature coefficient near zero (Ohsato, 2001 and Nishigaki *et al.*, 1987 cited in Wang *et al.*, 2006). Lanthanum substitution into barium titanate can improve the dielectric properties (Narang *et al.*, 2006). A maximum dielectric constant of 157 was obtained although the minimum dielectric loss (0.0572) was higher than for the tungsten-bronze compounds. The dielectric properties of Ba$_{6-3x}$(Nd$_y$Sm$_{1-y}$)$_{8+2x}$Ti$_{18}$O$_{54}$ compounds with different barium: rare earth, and Nd:Sm ratios have been studied (Wang *et al.*, 2006). The results show that the dielectric constant increases with the Nd content because the large Nd^{3+} cation increases the unit cell volume leading to the larger octahedral B-sites occupied by Ti^{4+} allowing greater displacement for the Ti^{4+} ions thereby raising the ionic electronic polarisation and consequently the dielectric constant increases. The dielectric constant decreased from 91.0 to 84.2 as x increased from 0.3 to 0.7 due to the volume contraction resulting from vacancy formation, more rare earth substitution and lower electronic polarisation. Another potential high-k dielectric in temperature-compensating capacitors is Ba$_5$LnZnNb$_9$O$_{30}$ (Ln = La, Nd, Sm) which showed high dielectric constants of 310, 282 and 258, respectively for the three rare earths (Fang *et al.*, 2007). However, further reduction of the dielectric loss and temperature coefficient of these dielectric ceramics needs to be considered.

2.6.3   Hafnium-based oxynitride dielectrics

Various transition metal oxides have also been of interest for high-k dielectric applications. These simple oxides possess much poorer electrical and material properties than the conventional SiO_2; however, their properties can be improved by modifying the structure or by nitrogen incorporation (Wong, 2008). Among such candidates, HfO_2 has been considered to be the most promising because it not only has a reasonably high dielectric constant, but it is more thermodynamically stable on Si than other high-k materials and has a relatively large band gap (5.68 eV) (Albertin *et al.*, 2007). However, this material has a poor interface quality with Si and exhibits high oxygen diffusion, which results in a low-k interfacial layer growth, and a low crystallisation temperature of 500°C (Albertin *et al.*, 2007). Grain boundaries in crystalline HfO_2 provide an oxygen diffusion path, causing undesirable low-k interfacial layer growth, defect generation, threshold voltage instability and leakage current (Li *et al.*, 2008). Since the oxides HfO_2 and $HfSi_xO_y$ possess relatively high dielectric constant and are compatible with current silicon-based processing technology (Wilk *et al.*, 2001), the corresponding oxynitrides HfO_xN_y and HfSiON, have also received considerable attention as alternative high-k dielectrics. As further research has proceeded, more complex dielectrics in the HfO_xN_y, HfSiON, HfTiON, HfSiTiON and HfTaON systems have also become dominant materials under active investigation for both gate dielectric and capacitor applications (Kang *et al.*, 2002, Visokay *et al.*, 2002, Choi *et al.*, 2003, Wallace and Wilk, 2003, Koike *et al.*, 2006, Ji *et al.*, 2007, Ji *et al.*, 2008, Li *et al.*, 2008). Compared with layers of HfO_2 of the same physical thickness, HfO_xN_y films have lower equivalent oxide

thickness (EOT), much lower leakage current density and superior thermal stability (Kang *et al.*, 2002, Choi *et al.*, 2003) whilst also suppressing boron penetration (Choi *et al.*, 2003) and preventing the growth of interfacial layers at higher annealing temperatures (He *et al.*, 2006) and increasing the crystallisation temperature (Park *et al.*, 2007). The dielectric constant increases nonlinearly with increasing nitrogen content (Ino *et al.*, 2006). After post-deposition annealing, nitrogen is partially substituted by oxygen and the released nitrogen diffuses and bonds with Si at the interface forming Si_3N_4 barrier layers (He *et al.*, 2006). The presence of Si-N bonds in the dielectric film and Si interface suppresses the oxygen diffusion and hence reduces the thickness of the SiO_2 interface (Kang *et al.*, 2002, He *et al.*, 2006). Another possible reason for the reduced interfacial layer is the film being amorphous; oxygen diffusion is more difficult than in crystalline oxides (Choi *et al.*, 2003, He *et al.*, 2006). HfSiON has also been considered as a candidate for implementation as a gate dielectric in future MOS devices. Compared with HfSiO and sputtered HfON films, HfSiON has minimally low-k interfacial layers, low equivalent oxide thickness and low leakage current density (at least two order of magnitude lower than SiO_2) and also has a higher crystallisation temperature (Visokay *et al.*, 2002). Silicon plays an important role in thermal stability and acts as an amorphiser for transition and rare earth metal oxides (Neumayer and Cartier, 2001, Visokay *et al.*, 2002, Wong, 2008). Koike *et al.* (2006) fabricated HfSiON films of various atomic compositions and found that both optical and dielectric constants were enhanced as the N and Hf concentrations increased. Low interface-state density and gate leakage current combined with high reliability were reported for a HfTiON gate-

dielectric metal-oxide-semiconductor capacitor synthesised by NO nitridation (Ji *et al.*, 2007, Ji *et al.*, 2008). Surface pre-treatment by NO nitridation prior to dielectric deposition was employed and the SiON interlayer was believed to improve the electrical properties by reducing gate leakage current and thereby improving reliability (Ji *et al.*, 2007). Further work confirmed the good electrical properties of HfTiON prepared by depositing HfTiO films on Si wafers and annealing in an NO atmosphere (Ji *et al.*, 2008). The well-matched SiO_2/Si-like interface provided by HfTiSiON decreased the leakage current and improved device reliability. Titanium serves as a polarizer and produces a higher k value when it is added to other transition and rare earth metal oxides (Wong, 2008). In comparison with HfTaO compositions, the incorporated nitrogen can increase the dielectric constant of $HfTaO_xN_y$ gate dielectric films by forming a thinner SiO_x interfacial layer (Li *et al.*, 2008). Similarly, TaO_xN_y interlayers can further improve the electrical performance, giving a larger capacitance and smaller leakage currents. The formation of low-k SiO_2 layers can be suppressed by the TaO_xN_y interlayer acting as an oxygen reaction or diffusion barrier. The electrical reliability of nitrogen-incorporated $HfSiO/HfO_2/SiO_2$ gate stacks improved providing thermal stabilisation against both crystallisation and phase separation (Watanabe *et al.*, 2005). The leakage current in this nitrided film was much smaller than that through oxides stacks ($HfSiO/HfO_2$). Also, it has been found that the leakage current through $HfSiO/HfO_2$ stacks results from oxygen vacancy formation after annealing. First-principle calculations by Umezawa *et al.* (2005) showed that the oxygen vacancies in Hf-based oxides can be deactivated by incorporating nitrogen atoms. Nitrogen atoms in Hf-based dielectrics favourably

couple with oxygen vacancies and as a result the current leakage paths arising from oxygen vacancy formation are suppressed (Umezawa *et al.*, 2005). Many researchers have carried out studies on Hf- and Si-based oxynitride dielectrics using different deposition techniques and varying the composition, and have shown significant improvement in the desired final performance.

2.6.4   Perovskite oxide-based dielectrics

Barium titanate ($BaTiO_3$), strontium titanate ($SrTiO_3$) and their solid solutions $Ba_{1-x}Sr_xTiO_3$ (BST) as well as other perovskite-related oxides provide a wide range of suitable materials for capacitor dielectrics in memory devices (Kotecki *et al.*, 1999, Ouajji *et al.*, 2005), communication and microwave dielectric applications, dielectric resonators and capacitors in appliances (Bhalla *et al.*, 2000). In multilayer ceramic capacitors (MLCCs), $BaTiO_3$ dielectrics have been conventionally fabricated with noble metals such as platinum (Pt) or palladium (Pd) as the internal electrodes at high temperatures of approximately 1300ºC (Kishi *et al.*, 2003). To reduce cost, lead-based complex perovskites of the $Pb(B'B'')O_3$ with a wide range of compositions such as $Pb(Fe_{1/3}W_{2/3})O_3$, $Pb(Fe_{1/2}Nb_{1/2})O_3$, $Pb(Mg_{1/3}Nb_{2/3})O_3$, $Pb(Mg_{1/2}W_{1/2})O_3$ and $Pb(Zn_{1/3}Nb_{2/3})O_3$ were developed as low-sintering-temperature and high-k dielectrics (Kishi *et al.*, 2003). Due to the low sintering temperature, these dielectric materials enable the use of high silver content Ag-Pd alloy electrodes with excellent electrical characteristics. However, from environmental considerations, lead-free products are now preferred. $BaTiO_3$-based non-reducible dielectrics have been developed by doping with acceptor or donor elements in order to maintain a high insulation

resistance after firing in a reducing atmosphere with base metal internal electrodes composed of Ni or Cu instead of noble metals (Kishi *et al.*, 2003). Compared with many dopants, rare earth elements are regarded as the most effective acceptors/donors for $BaTiO_3$-based non-reducible dielectrics (Kishi *et al.*, 2003). It was found that using intermediate ionic size rare earth oxides such as Dy_2O_3, Ho_2O_3, Er_2O_3 and Y_2O_3 for doping $BaTiO_3$-based dielectrics could improve the reliability of Ni-MLCCs with a very thin layer of below 2 μm in thickness. The development of non-reducible dielectrics for Ni-based MLCCs has been reviewed by Kishi *et al.* (2003). The characteristics of $BaTiO_3$ dielectrics can be modified by small amounts of Nb^{5+} or Ta^{5+} dopants (Kim *et al.*, 2009). The resulting fine-grained and high density doped $BaTiO_3$ ceramic dielectrics showed good dielectric properties, a high dielectric constant of 3000 at room temperature and a lower Curie temperature than that of $BaTiO_3$. $SrTiO_3$ is another perovskite-type material which is well-known as a high-k dielectric. Its high dielectric constant makes it very attractive for high-density metal-insulator-metal capacitors (MIM) for microelectronic devices (Akedo *et al.*,1998 cited in Ouajji *et al.*, 2005). It can be used as a buffer layer for the growth of other perovskite-type ferroelectric thin films (Liu *et al.*, 2002). However, it is difficult to fabricate high quality $SrTiO_3$ dielectric gates because of the formation of a low-k SiO_x layer by Si oxidation and interdiffusion at high temperatures (Liu *et al.*, 2002). The interfacial properties of $SrTiO_3$/Si can be improved by means of a certain amount of surface nitridation (Liu *et al.*, 2002). This pre-nitridation treatment may retard the growth of low-k interfacial layers during high temperature processing and consequently decreases the EOT by 10–24%. The improved interface results in a lower leakage current.

In order to improve the crystallinity of $SrTiO_3$, SiO_2 has been added to increase its crystallization temperature (Lin *et al.*, 2007). It was found that $SrTiO_3$-SiO_2 thin films remained amorphous up to their annealing temperature of 900ºC. Furthermore, the frequency and temperature dependence of the dielectric constant of $SrTiO_3$ in the range 25–150ºC and for frequencies of 0.01 Hz–1 MHz were reported by Ouajji *et al.* (2005). Modified Ba-based perovskite compounds and their solid solutions have been intensively studied to combine desired properties. The dielectric constants of $Ba_{1-x}Sr_xTiO_3$ (BST) thin-films are in the range 200–350 with a specific capacitance exceeding 125 $fF/\mu m^2$ so they have emerged as leading contenders for dielectrics for future DRAMs (Kotecki *et al.*, 1999). The dielectric constant of BST increases with the concentration of barium because the soft mode frequency decreases (Kumar *et al.*, 2002). However, the dielectric constant is highly temperature dependent (Cava, 2001). By a mixed phase approach, the temperature dependence of BST dielectrics near room temperature can be effectively suppressed when they are mixed with $Ba_{0.5}Sr_{0.5}Nb_2O_6$ (BSN), which has an opposite temperature dependence; moreover, the dielectric constant remains the same in the mixture (Cava, 2001). Cation substitutions on the B-sites are of particular interest to modify the dielectric properties. Perovskite-$Ba(Zn_{1/3}Ta_{2/3})O_3$ dielectrics can be fabricated with exceptionally low leakage current at microwave frequencies and with low temperature coefficients although the dielectric constant is relatively low (k $\approx$ 25–30) (Cava, 2001). Another modified Ba-based-perovskite compound, $Ba(Nb_{0.15}Zr_{0.85})O_3$ (BNZ), and its solid solutions with $BaTiO_3$ have been studied (Sulepetkar and Raibagkar, 2007). BNZ exhibits a high dielectric constant of approximately 290 at 295 K and its dielectric

constant decreases further with increase of frequency. With 10% addition of $BaTiO_3$ to BNZ, the Curie temperature reduces from 295 K to 285 K which may be attributed to the formation of a disordered perovskite structure. By multiple cation substitution, dielectric properties of ordered double perovskites containing Mg^{2+} and Ta^{5+} of the type $ALaMgTaO_6$ (A= Ba, Sr, Ca) and $La_2Mg(Mg_{1/3}Ta_{2/3})O_6$ have given improved performance (Kim and Woodward, 2007). Compared with $KTaO_3$, these double perovskites have wider optical band gaps because of the electronic isolation of TaO_6 octahedra leading to a reduction in the conduction bandwidth. These compounds are insulating with dielectric constants in the range 18–23, low dielectric loss and reasonable low temperature coefficient. In particular, $BaLaMgTaO_6$ possesses a near-zero temperature dependence of capacitance. New cubic perovskites $(Na_{1/4}Bi_{3/4})(Mg_{1/4}Ti_{3/4})O_3$ (NBMT) and $(K_{1/4}Bi_{3/4})(Mg_{1/4}Ti_{3/4})O_3$ (KBMT) have been synthesised by solid-state reaction and the frequency-dependent dielectric constants vary from several hundreds to about two thousands (Wang and Cao, 2007). Clearly there is considerable scope for more complex perovskite-type materials to be further explored for dielectric applications in microelectronics.

2.6.5   High-k dielectric material selection

New gate dielectric materials must meet a variety of chemical, physical, electrical and manufacturing criteria. Apart from the dielectric properties, the most important of these requirements are band gap, morphology and interfacial quality.

In general, atoms with a large ionic radius exhibit a higher electron dipole response to an external electric field and by this electronic contribution, the

dielectric constant tends to increase (Wallace and Wilk, 2003). In contrast, the band gap is prone to decrease with increasing atomic number. A small band gap results in a small conduction band offset ΔE_c, which might provide an insufficient energy barrier height to gate leakage currents (Wallace and Wilk, 2003). In perovskite materials, uniform displacements of the moving ion, for example Ti in $(Ba,Sr)TiO_3$, causes a large polarisation which gives rise to a very large dielectric constant (Wallace and Wilk, 2003). The ionic contribution to the dielectric constant can therefore be larger than the electronic part but this will begin to decrease at very high frequencies (typically in the infrared range of $\approx 10^{12}$ Hz) because ions respond to an applied electric field more slowly than electrons (Wallace and Wilk, 2003). A high-k dielectric constant with a large band gap is rare so there often needs to be a compromise between a reasonable k value and the proper band gap. Most binary metal oxides tend to crystallise at rather low temperatures (typically $\approx 800°C$) and grain boundaries in fully or partially crystallised materials can act as pathways for oxygen or dopant diffusion (Wilk *et al.*, 2001, Choi *et al.*, 2003). In these cases, a low-k interface is formed which causes a higher leakage current, dielectric breakdown and long-term reliability degradation (Wilk *et al.*, 2001, Watanabe *et al.*, 2005). However, with care, the interfacial region can be designed to achieve the desired properties by serving as a transition region between the Si substrate and the dielectric. For example, TaO_xN_y interlayers can further improve the electrical characteristics to give large capacitance and small leakage current in $HfTaO_xN_y$ capacitors (Li *et al.*, 2008) and HfO_2/TaO_xN_y stack gate dielectrics (Xu *et al.*, 2008). Achieving good high-k dielectric performance is seemingly difficult; it is often better to consider

dielectrics that have only a moderate dielectric constant but also provide a sufficient tunnelling barrier and high quality interface when deposited on silicon.

2.7 Perovskite oxynitride-based dielectrics

From the previous sections it is clear that the idea of combining the high-k dielectric constant of an oxide such as $BaTiO_3$ with some of the advantages of nitrogen incorporation, requiring the simultaneous substitution of rare earth elements (R) or alkaline earth metals (A) on the barium site and transition metals (M) on titanium sites is a promising line of new research for finding alternative high-k dielectric materials. In multilayer ceramic capacitors (MLCCs), the Ni and Cu electrodes and the $BaTiO_3$ dielectric materials have to be co-sintered in a reducing atmosphere; however, conventional dielectrics are readily reduced under such conditions and become semiconductive (Kishi *et al.*, 2003). Perovskite-type oxynitrides can be sintered in a reducing atmosphere which would therefore allow internal electrodes to be made successfully using less noble and less expensive metals. Marchand *et al.* (1986) first reported the possibility of perovskite oxynitrides being used as dielectric materials. High dielectric constants for $BaTaO_2N$ and $BaNbO_2N$ powders over a wide range of temperature regardless of frequency were reported though the values were not confirmed due to the relatively poor reliability of the measurement methods. Also, this study showed that these ceramic dielectrics were stable at high temperatures under neutral or reducing atmosphere so making perovskite oxynitrides possible candidates for use in multiple ceramic capacitors with low-cost metal electrodes. The dielectric characteristics of $BaTaO_2N$ were also investigated by comparing the infrared

reflection spectrum with that of $BaTiO_3$ by Gouin *et al.* (1995). It was claimed that $BaTaO_2N$ does not show a polar soft mode which is a part of the origin of the ferroelectric properties of $BaTiO_3$ so the dielectric response of $BaTaO_2N$ should not reach very high values. This was explained as being due to the stronger Ta–N bond so that the Ta^{5+} atomic displacement was less compared with other oxide perovskites. However, Kim *et al.* (2004) claimed that $BaTaO_2N$ and $SrTaO_2N$ possessed high bulk dielectric constants of 4,900 and 2,900 respectively at room temperature but these measurements were made on compacted powder with densities less than 60% of theoretical. Upon introducing Sc into $BaTaO_2N$, the resulting $BaSc_{0.05}Ta_{0.95}O_2N$ ceramic had a higher bulk-dielectric constant (k = 7300) with an even higher dielectric constant at the grain boundary region (Kim and Woodward, 2007a). This was possibly because Sc-containing oxides like $BaSc_2O_4$ formed as an internal barrier layer in these capacitors (Kim and Woodward, 2007a). Epitaxial thin films of $BaTaO_2N$ were grown on a conducting $SrRuO_3$ buffer layer deposited on a (100)-cut $SrTiO_3$ single-crystal substrate (Kim *et al.*, 2007). The dielectric constant of this epitaxial structure ranged from 200–240 depending on frequency with a minimal variation with temperature and a smaller dielectric loss than had been reported for the 55% dense $BaTaO_2N$ ceramic. Some discrepancy in the dielectric characteristics between bulk ceramics and thin films would be expected. Factors such as interfacial dead layer effects and epitaxial strain can be causes of reduced dielectric constant in thin films (Kim *et al.*, 2007). The microstructure, e.g. grain boundaries as well as extended and point defects play an important role in determining the dielectric loss (Kim *et al.*, 2007). Aguiar *et al.* (2007) reported good electrical insulating

properties for $La_xSr_{(1-x)}Ti(O,N)_3$ thin films. These films were deposited by spin coating polymeric precursor solutions on (100) $SrTiO_3$ substrates. The films exhibited electrical insulating properties for $LaTiO_2N$ to semiconducting properties for N-doped $SrTiO_3$. Consistently, Le Paven-Thivet *et al.* (2007) deposited $LaTiO_xN_y$ on (001) $SrTiO_3$ substrates by reactive radio frequency sputtering from a $LaTiO_2N$ target in mixed argon-nitrogen gas and confirmed the insulating behaviour of the films. High nitrogen content in the deposition atmosphere promoted high nitrogen content in the films. It was also found that band gap energies are gradually decreased with increasing nitrogen content because the top level of the valence band of an oxynitride is dominated by the N 2p orbitals which have higher energies than those of an oxide having only O 2p orbitals. From the viewpoint of electronic applications, these oxynitrides behave as semiconducting materials. The effect of nitrogen content on the properties of these $LaTiO_xN_y$ thin films has been studied by Ziani *et al.* (2008). The results confirmed that the band gap values are inversely proportional to nitrogen content in the film. The films have high values of dielectric constant ranging from 290 to 1220 at room temperature and 10 kHz, depending on the nitrogen content and increasing with %N. It is unclear what effect the nitrogen has on the dielectric properties but it was found that more nitrogen made the film more polycrystalline. A polycrystalline microstructure enhances the presence of defects at grain boundaries and lowers the cooperative dipole alignment resulting in a decrease in dielectric constant. Synthesis and dielectric characterisation of Eu-based oxynitrides $EuTaO_2N$ and $EuNbO_2N$ were studied by Jorge *et al.* (2008). $EuMO_2N$ perovskites were synthesised by ammonolysis of $EuMO_4$ precursors at

950ºC. While Ta compounds tended to be nitrogen-rich with a mixture of Eu^{3+}/Eu^{2+}, i.e. $(Eu^{2+}_{1-x}Eu^{3+}_{x})Ta^{5+}O_{2-x}N_{1+x}$ with $0 < x < 0.20$, due to the ease of niobium reduction, $Eu^{2+}(Nb^{5+}_{1-y}Nb^{4+}_{y})O_{2+y}N_{1-y}$ with $y = 0–0.14$ tended to be nitrogen deficient under the same conditions. Very highly insulating $EuTaO_2N$ materials showed a dielectric constant of only 37 at low temperature with small frequency dependence while the corresponding value for $EuNbO_2N$ was of the order of 10^4 at a temperature of 150 K, decreasing with increasing frequency.

2.8 Conclusions

Dielectric materials form some of the most important parts of electronic and electrical devices. They are used as gate dielectrics in MOSFETs and as the dielectric layer in capacitors and multilayer capacitors. Silicon dioxide has been used as a gate dielectric for decades and the well-known perovskite $BaTiO_3$ has been used as a high-k dielectric layer in capacitors. Since silicon dioxide gate dielectrics have a relatively low dielectric constant of 3.9, nitrogen has been incorporated to increase the dielectric constant and improve the interface quality. Although relatively small increases in dielectric constant can be achieved, the incorporated nitrogen can also improve other properties such as boron penetration resistance, narrower band gap, and improved interfacial layer quality. Additionally, hafnium-based materials such as in HfON, HfSiON, HfTiON and HfTaON systems have been introduced as alternative high-k dielectric materials. They can be used in conjunction with silicon technology because they produce a good interface quality with the silicon substrate. The microelectronic revolution is still exponentially increasing and could be beyond the limits of silicon-based

technology in the near future. Hence, alternative high-k dielectric materials are being extensively explored for use with both current silicon technology and the future beyond silicon. Because of the feasibility of multi-ion substitution in perovskite structural materials, a variety of new complex perovskite oxynitrides have emerged as interesting dielectric materials because they combine many of the desired properties. It is hoped that it will be possible to integrate the high-k dielectric potential of perovskite-materials with the improved dielectric properties arising from nitrogen incorporation. The right amount of nitrogen is critical for achieving the desired dielectric properties. Up to now, a considerable amount of work has been carried out on the synthesis, structural characterisation and physical and chemical properties of perovskite oxynitrides; however, very few studies have been made of dielectric characterisation of these materials and their potential for use in high-k dielectric applications.

2.9   References

Aguiar, R., Logvinovich, D., Weidenkaff, A., Rachel, A., Reller, A. and Ebbinghaus, S. G. (2008a) The vast colour spectrum of ternary metal oxynitride pigments. *Dyes and Pigments,* 76**,** 70-75.

Aguiar, R., Logvinovich, D., Weidenkaff, A., Reller, A. and Ebbinghaus, S. G. (2008b) Thermal oxidation of oxynitride perovskites in different atmospheres. *Thermochimica Acta,* 471**,** 55-60.

Aguiar, R., Weidenkaff, A., Schneider, C. W., Reller, A. and Ebbinghaus, S. G. (2007) Synthesis and properties of oxynitrides (La,Sr)Ti(O,N)$_3$ thin films. *Progress in Solid State Chemistry,* 35**,** 291-298.

Ahmet, P., Kakushima, K., Tsutsui, K., Sugii, N., Hattori, T. and Iwai, H. (2007) La-based oxides for high-k gate dielectric application. *ICSICT-2006: 2006 8th International Conference on Solid-State and Integrated Circuit Technology, Proceedings.* Shanghai**,** 408-411.

Albertin, K. F., Pereyra, I. and Alayo, M. I. (2003) MOS capacitors with PECVD SiO_xN_y insulating layer. *Materials Characterization,* 50**,** 149– 154.

Albertin, K. F., Valle, M. A. and Pereyra, I. (2007) Study of MOS Capacitors with TiO_2 and SiO_2/TiO_2 Gate Dielectric. *Journal Integrated Circuites and Systems,* 2**,** 89-93.

Bailey, A. E. (2003) Ceramics and glasses. In Harper, C. A. (Ed.) *Electronic materials and processes handbook.* 3rd ed. New York, McGraw-Hill**,** 3.1-3.81.

Bhalla, A. S., Guo, R. and Roy, R. (2000) The perovskite structure - A review of its role in ceramic science and technology. *Materials Research Innovations,* 4**,** 3-26.

Buchanan, D. A. (1999) Scaling the gate dielectric: materials, integration, and reliability. *IBM Journal of Research and Development,* 43**,** 245-264.

Carr, E. C., Ellis, K. A. and Buhrman, R. A. (1995) N depth profiles in thin SiO_2 grown or processed in N_2O: The role of atomic oxygen. *Applied Physics Letters***,** 1492-1494.

Cava, R. J. (2001) Dielectric materials for applications in microwave communications. *Journal of Materials Chemistry,* 11**,** 54-62.

Chang-Liao, K.-S. and Ku, J.-M. (1999) Improvement of oxynitride reliability by two-step N_2O nitridation. *Solid-State Electronics,* 43**,** 2057-2060.

Cheviré, F., Fessier, F. and Marchand, R. (2006) Optical properties of the perovskite solid solution $LaTiO_2N$-$ATiO_3$ (A= Sr, Ba). *Eur. J. Inorg. Chem***,** 1223-1230.

Choi, C. H., Jeon, T. S., Clark, R. and Kwong, D. L. (2003) Electrical properties and thermal stability of CVD HfO_xN_y gate dielectric with poly-Si gate electrode. *IEEE Electron Device Letters,* 24**,** 215-217.

Clarke, S. J., Guinot, B. P., Michie, C. W., Calmont, M. J. C. and Rosseinsky, M. J. (2002) Oxynitride Perovskites: Synthesis and Structures of $LaZrO_2N$, $NdTiO_2N$ and $LaTiO_2N$ and Comparison with Oxide Perovskites. *Chem. Mater.,* 14**,** 288-294.

Damjanovic, D. (1998) Ferroelectric, dielectric and piezoelectric properties of ferroelectric thin films and ceramics. *Rep. Prog. Phys.,* 61**,** 1267-1324.

de Almeida, R. M. C. and Baumvol, I. J. R. (2003) Reaction-diffusion in high-k dielectrics on Si. *Surface Science Reports,* 49**,** 1-114.

Ellis, K. A. and Buhrman, R. A. (1998) Boron diffusion in silicon oxides and oxynitrides. *Journal of the Electrochemical Society,* 145**,** 2068-2074.

Ellis, K. A. and Buhrman, R. A. (1999) Time-dependent diffusivity of boron in silicon oxide and oxynitride. *Applied Physics Letters,* 74**,** 967-969.

Esmaeilzadeh, S., Grins, J. and Hörlin, T. (1998) Synthesis and ionic conductivity properties of oxynitride perovskites $A_xLa_{2/3}Ta_2O_{6-x}N_x$ (A=Na, Li) with $La_{2/3}Ta_2O_6$ type structure and a new Ruddlesden-Popper phase $Li_2LaTa_2O_6N$. In Hampshire, S. and Pomeroy, M. J. (Eds.) *Proceedings of the Second International Symposium on Nitrides.* Limerick, Irelnad, Trans Tech Publications Ltd**,** 11-16.

Fang, C. M., De Wijs, G. A., Orhan, E., De With, G., De Groot, R. A., Hintzen, H. T. and Marchand, R. (2003) Local structure and electronic properties of $BaTaO_2N$ with perovskite-type structure. *Journal of Physics and Chemistry of Solids,* 64**,** 281-286.

Fang, L., Yu, Q., Hu, C.-Z. and Zhang, H. (2007) High dielectric constant and low-loss dielectric ceramics of $Ba_5LnZnNb_9O_{30}$ (Ln = La, Nd and Sm). *Materials Letters,* 61**,** 4140-4143.

Feng, L. M., Jiang, L. Q., Zhu, M., Liu, H. B., Zhou, X. and Li, C. H. (2008) Formability of ABO_3 cubic perovskites. *Journal of Physics and Chemistry of Solids,* 69**,** 967-974.

Fiedziuszko, S. J., Hunter, I. C., Itoh, T., Kobayashi, Y., Nishikawa, T., Stitzer, S. N. and Wakino, K. (2002) Dielectric materials, devices, and circuits. *IEEE Transactions on Microwave Theory and Techniques,* 50**,** 706-720.

Glazer, A. (1972) The classification of tilted octahedra in perovskites. *Acta Crystallographica Section B,* 28**,** 3384-3392.

Gomathi, A., Reshma, S. and Rao, C. N. R. (2009) A simple urea-based route to ternary metal oxynitride nanoparticles. *Journal of Solid State Chemistry,* 182**,** 72-76.

Gouin, X., Marchand, R., Laurent, Y. and Gervais, F. (1995) Infrared dielectric response of $BaTaO_2N$. *Solid State Communications,* 93**,** 857-859.

Green, M. L., Gusev, E. P., Degraeve, R. and Garfunkel, E. L. (2001) Ultrathin (< 4 nm) SiO_2 and Si-O-N gate dielectric layers for silicon microelectronics: Understanding the processing, structure, and physical and electrical limits. *Journal of Applied Physics,* 90**,** 2057-2121.

Groner, M. D. and George, S. M. (2003) High-k dielectrics grown by atomic layer deposition: Capacitor and gate applications. In Murarka, S. P., Eizenberg, M. and Sinha, A. K. (Eds.) *Interlayer Dielectrics for Semiconductor Technologies.* San Diego, Academic Press**,** 327-348.

Hall, S., Buiu, O., Mitrovic, I. Z., Lu, Y. and Davey, W. M. (2007) Review and perspective of high-k dielectrics on silicon. *Journal of telecommunications and information technology***,** 33-43.

He, G., Fang, Q. and Zhang, L. D. (2006) Structural and interfacial properties of high-k HfO_xN_y gate dielectric films. *Materials Science in Semiconductor Processing,* 9**,** 870-875.

Hellwig, A. and Hendry, A. (1994) Formation of barium-tantalum oxynitrides. *Journal of Materials Science,* 29**,** 4686-4693.

Hongwei, Z., Xiaoping, W., Bich-Yen, N., Rai, R., Prabhu, L., Jack, J., Kaushik, V., Scheaffer, J., Zavala, M., Duda, E., Ran, L., Zonner, S., Hradsky, B., Fejes, P., Theodore, D., Edwards, G., Gregory, R., Wang, R., Hak, Y., Jimmy, Y., Huibin, L., Zhenghao, C., Xubing, L. and Zhiguo, L. (2003) High-k LAON for gate dielectric application. *Electron Devices and Solid-State Circuits, 2003 IEEE Conference on.* 357-360.

Ino, T., Kamimuta, Y., Suzuki, M., Koyama, M. and Nishiyama, A. (2006) Dielectric constant behavior of Hf-O-N system. *Japanese Journal of Applied Physics, Part 1: Regular Papers and Short Notes and Review Papers,* 45**,** 2908-2913.

Jansen, M. and Letschert, H. P. (2000) Inorganic yellow-red pigments without toxic metals. *Nature,* 404**,** 980-982.

Ji, F., Xu, J., Zhang, H., Lai, P., Li, C. and Guan, J. (2008) Influence of natridation annealing of HfTiO on electrical properties of MOS device. *Guti Dianzixue Yanjiu Yu Jinzhan/Research and Progress of Solid State Electronics,* 28**,** 330-333.

Ji, F., Xu, J. P., Lai, P. T., Li, C. X. and Guan, J. G. (2007) Electrical properties of HfTiON gate-dielectric metal-oxide-semiconductor capacitors with different Si-surface nitridations. *Applied Physics Letters,* 91**,** 052902-052904.

Jorge, A. B., Oró-Solé, J., Bea, A. M., Mufti, N., Palstra, T. T. M., Rodgers, J. A., Attfield, J. P. and Fuertes, A. (2008) Large coupled magnetoresponses in $EuNbO_2N$. *Journal of the American Chemical Society,* 130**,** 12572-12573.

Kang, C. S., Cho, H. J., Onishi, K., Nieh, R., Choi, R., Gopalan, S., Krishnan, S., Han, J. H. and Lee, J. C. (2002) Bonding states and electrical properties of ultrathin HfO_xN_y gate dielectrics. *Applied Physics Letters,* 81**,** 2593.

Kasahara, A., Nukumizu, K., Hitoki, G., Takata, T., Kondo, J. N., Hara, M., Kobayashi, H. and Domen, K. (2002) Photoreactions on $LaTiO_2N$ under visible light irradiation. *Journal of Physical Chemistry A,* 106**,** 6750-6753.

Kasahara, A., Nukumizu, K., Takata, T., Kondo, J. N., Hara, M., Kobayashi, H. and Domen, K. (2003) $LaTiO_2N$ as a visible-light ($\leq$600 nm)-driven photocatalyst (2). *Journal of Physical Chemistry B,* 107**,** 791-797.

Kawamoto, A., Cho, K. and Dutton, R. (2001) Perspective paper: First principles modeling of high-k gate dielectrics. *Journal of Computer-Aided Materials Design,* 8**,** 39-57.

Kim, Y.-I., Woodward, P. M., Baba-Kishi, K. Z. and Tai, C. W. (2004) Characterization of the structural, optical, and dielectric properties of oxynitride perovskites AMO_2N (A = Ba, Sr, Ca; M = Ta, Nb). *Chemistry of Materials,* 16**,** 1267-1276.

Kim, Y. I., Si, W., Woodward, P. M., Sutter, E., Park, S. and Vogt, T. (2007) Epitaxial thin-film deposition and dielectric properties of the perovskite oxynitride $BaTaO_2N$. *Chemistry of Materials,* 19**,** 618-623.

Kim, Y. I. and Woodward, P. M. (2007) Crystal structures and dielectric properties of ordered double perovskites containing Mg^{2+} and Ta^{5+}. *Journal of Solid State Chemistry,* 180**,** 2798-2807.

Kishi, H., Mizuno, Y. and Chazono, H. (2003) Base-metal electrode-multilayer ceramic capacitors: Past, present and future perspectives. *Japanese Journal of Applied Physics, Part 1: Regular Papers and Short Notes and Review Papers,* 42**,** 1-5.

Kittl, J. A., Opsomer, K., Popovici, M., Menou, N., Kaczer, B., Wang, X. P., Adelmann, C., Pawlak, M. A., Tomida, K., Rothschild, A., Govoreanu, B., Degraeve, R., Schaekers, M., Zahid, M., Delabie, A., Meersschaut, J., Polspoel, W., Clima, S., Pourtois, G., Knaepen, W., Detavernier, C., Afanas'ev, V. V., Blomberg, T., Pierreux, D., Swerts, J., Fischer, P., Maes, J. W., Manger, D., Vandervorst, W., Conard, T., Franquet, A., Favia, P., Bender, H., Brijs, B., Van Elshocht, S., Jurczak, M., Van Houdt, J. and Wouters, D. J. (2009) High-k dielectrics and metal gates for future generation memory devices. *ECS Transactions.* 1 ed. San Francisco, CA**,** 29-40.

Koike, M., Ino, T., Kamimuta, Y., Koyama, M., Kamata, Y., Suzuki, M., Mitani, Y. and Nishiyama, A. (2006) Dielectric properties of noncrystalline HfSiON. *Physical Review B - Condensed Matter and Materials Physics,* 73**,** 1-6.

Kotecki, D. E., Baniecki, J. D., Shen, H., Laibowitz, R. B., Saenger, K. L., Lian, J. J., Shaw, T. M., Athavale, S. D., Cabral Jr, C., Duncombe, P. R., Gutsche, M., Kunkel, G., Park, Y. J., Wang, Y. Y. and Wise, R. (1999) $(Ba,Sr)TiO_3$ dielectrics for future stacked-capacitor DRAM. *IBM Journal of Research and Development,* 43**,** 367-382.

Kumar, A., Naithani, U. C. and Semwal, B. S. (2002) Dielectric behaviour of $Ba_xSr_{1-x}TiO_3$ perovskites. *Sri Lankan Journal of Physics,* 3**,** 63-73.

Le Paven-Thivet, C., Le Gendre, L., Le Castrec, J., Cheviré, F., Tessier, F. and Pinel, J. (2007) Oxynitride perovskite LaTiO$_x$N$_y$ thin films deposited by reactive sputtering. *Progress in Solid State Chemistry,* 35**,** 299-308.

Leskelä, M., Kukli, K. and Ritala, M. (2006) Rare-earth oxide thin films for gate dielectrics in microelectronics. *Journal of Alloys and Compounds,* 418**,** 27-34.

Li, C., Soh, K. C. K. and Wu, P. (2004) Formability of ABO$_3$ perovskites. *Journal of Alloys and Compounds,* 372**,** 40-48.

Li, C. X., Zhang, X. F., Xu, J. P. and Lai, P. T. (2008) Enhanced performance of Si MOS capacitors with HfTaO$_x$N$_y$ gate dielectric by using AlO$_x$N$_y$ or TaO$_x$N$_y$ interlayer. *2008 IEEE International Conference on Electron Devices and Solid-State Circuits, EDSSC.* Hong Kong**,** 1-4.

Lin, C. C., Lai, L. W., Lin, C. Y. and Tseng, T. Y. (2007) SrTiO$_3$-SiO$_2$ oxide films for possible high-k gate dielectric applications. *Thin Solid Films,* 515**,** 8005-8008.

Liu, C. Y., Lue, H. T. and Tseng, T. Y. (2002) Effects of nitridation of silicon and repeated spike heating on the electrical properties of SrTiO$_3$ gate dielectrics. *Applied Physics Letters,* 81**,** 4416-4418.

Liu, M., You, W., Lei, Z., Takata, T., Domen, K. and Li, C. (2006) Photocatalytic water splitting to hydrogen over a visible light-driven LaTaON$_2$ catalyst. *Chinese Journal of Catalysis,* 27**,** 556-558.

Logvinovich, D., Börger, A., Döbeli, M., Ebbinghaus, S. G., Reller, A. and Weidenkaff, A. (2007) Synthesis and physical chemical properties of Ca-substituted LaTiO$_2$N. *Progress in Solid State Chemistry,* 35**,** 281-290.

Lu, H. C., Gusev, E. P., Garfunkel, E., Busch, B. W., Gustafsson, T., Sorsch, T. W. and Green, M. L. (2000) Isotopic labeling studies of interactions of nitric oxide and nitrous oxide with ultrathin oxynitride layers on silicon. *Journal of Applied Physics,* 87**,** 1550-1555.

Lu, H. C., Gusev, E. P., Gustafsson, T., Brasen, D., Green, M. L. and Garfunkel, E. (1997) Compositional and mechanistic aspects of ultrathin oxynitride film growth on Si(100). *Microelectronic Engineering,* 36**,** 29-32.

Marchand, R., Laurent, Y., Guyader, J., L'Haridon, P. and Verdier, P. (1991a) Nitrides and oxynitrides: Preparation, crystal chemistry and properties. *Journal of the European Ceramic Society,* 8**,** 197-213.

Marchand, R., Pors, F., Laurent, Y., Regreny, O., Lostec, J. and Haussonne, J. M. (1986) Perovskites oxynitrures utilises en tant que materiaux dielectriques. *Journal de Physique (Paris), Colloque* 47**,** 901-905.

Marchand, R., Pors, F. and Y.Laurent (1991b) Nouvelles perovskites oxynitrures de stoechiometrie ABO_2N (A = lanthanide, B = Ti) et $ABON_2$ (A = lanthanide, B = Ta ou Nb) *Annales des Chimie, France,* 16**,** 553-560.

Marchand, R., Tessier, F., Le Sauze, A. and Diot, N. (2001) Typical features of nitrogen in nitride-type compounds. *International Journal of Inorganic Materials,* 3**,** 1143-1146.

Mazzoni, A. D. and Conconi, M. S. (2004) Study of carbonitriding reactions of zirconia. Synthesis of $Zr(C,N,O)$ phases and β-type zirconium oxynitrides. *Ceramics International,* 30**,** 23-29.

Mazzoni, A. D., Conconi, M. S. and Aglietti, E. F. (2001) Synthesis of Zr-Si-O-N phases by carbonitriding reaction. Characterization of crystalline phases using the rietveld method *Materials Research,* 4**,** 107-111.

Menke, Y., Baron, V., Lemercier, H. and Hampshire, S. (1998) Influence of the atmosphere on the oxidation state of the Eu-Ion in a SiAlO(N) gass and glass-ceramic. In Hampshire, S. and Pomeroy, M. J. (Eds.) *Proceedings of the Second International Symposium on Nitrides.* Limerick, Ireland, Trans Tech Publications Ltd**,** 277-282.

Moulson, A. J. and Herbert, J. M. (2003) *Electroceramics,* West Sussex, John Wiley & Sons Ltd

Narang, S. B., Kaur, D. and Bahel, S. (2006) Dielectric properties of lanthanum substituted barium titanate microwave ceramics. *Materials Letters,* 60**,** 3179-3182.

Navale, S. C., Samuel, V., Gaikwad, A. B. and Ravi, V. (2007) A co-precipitation technique to prepare $BaTa_2O_6$. *Ceramics International,* 33**,** 297-299.

Osten, H. J., Bugiel, E. and Fissel, A. (2003) Epitaxial praseodymium oxide: A new high-K dielectric. *Solid-State Electronics,* 47**,** 2161-2165.

Ouajji, H., Sylvestre, A., Defay, E., Raouadi, K. and Jomni, F. (2005) Dielectric properties in thin film $SrTiO_3$ capacitor. *Electronic Packaging Technology Conference, 2005. EPTC 2005. Proceedings of 7th.* 740-743.

Park, J. H., Hyun, J. S., Kang, B. C. and Boo, J. H. (2007) Electrical properties of HfO_xN_y thin films deposited by PECVD. *Surface and Coatings Technology,* 201**,** 5336-5339.

Paul, A. F. and Robert, E. N. (1991) $La_2Ti_2O_7$ Ceramics. *Journal of the American Ceramic Society,* 74**,** 2876-2881.

Penn, S. J., Alford, N. M., Templeton, A., Wang, X., Xu, M., Reece, M. and Schrapel, K. (1997) Effect of porosity and grain size on the microwave dielectric properties of sintered alumina. *Journal of the American Ceramic Society,* 80**,** 1885-1888.

Rachel, A., Ebbinghaus, S. G., Güngerich, M., Klar, P. J., Hanss, J., Weidenkaff, A. and Reller, A. (2005) Tantalum and niobium perovskite oxynitrides: Synthesis and analysis of the thermal behaviour. *Thermochimica Acta,* 438**,** 134-143.

Richerson, D. W. (2006) Dielectric, magnetic, and optical behavior. *Modern Ceramic Engineering: properties, processing, and use in design.* 3rd ed. Boca Raton, FL CRC Taylor & Francis, 2006.**,** 323-341.

Robertson, J. (2004) High dielectric constant oxides. *EPJ Applied Physics,* 28**,** 265-291.

Roizin, Y. and Gritsenko, V. (2007) ONO structures and oxynitrides in modern microelectronics: Material science, characterization and application. In Baklanov, M., Green, M. and Maex, K. (Eds.) *Dielectric Films for Advanced Microelectronics.* Chichester, England ; Hoboken, NJ, John Wiley & Sons**,** 251-295.

Sulepetkar, S. T. and Raibagkar, R. L. (2007) Ferroelectric properties of modified Ba-based perovskite compound and its solid solution with $BaTiO_3$. *Journal of Materials Science: Materials in Electronics,* 18**,** 671-675.

Suresh, M., Prasadarao, A. V. and Komarneni, S. (2001) Mixed hydroxide precursors for $La_2Ti_2O_7$ and $Nd_2Ti_2O_7$ by homogeneous precipitation. *Journal of Electroceramics,* 6**,** 147-151.

Swartz, S. L. (1990) Topics in electronic ceramics. *IEEE Transactions on Electrical Insulation,* 25**,** 935-987.

Tessier, F. and Marchand, R. (2003) Ternary and higher order rare-earth nitride materials: Synthesis and characterization of ionic-covalent oxynitride powders. *Journal of Solid State Chemistry,* 171**,** 143-151.

Umezawa, N., Shiraishi, K., Ohno, T., Watanabe, H., Chikyow, T., Torii, K., Yamabe, K., Yamada, K., Kitajima, H. and Arikado, T. (2005) First-principles studies of the intrinsic effect of nitrogen atoms on reduction in gate leakage current through Hf-based high- k dielectrics. *Applied Physics Letters,* 86**,** 1-3.

Visokay, M. R., Chambers, J. J., Rotondaro, A. L. P., Shanware, A. and Colombo, L. (2002) Application of HfSiON as a gate dielectric material. *Applied Physics Letters,* 80**,** 3183-3185.

Wallace, R. M. and Wilk, G. D. (2003) High-k dielectric materials for microelectronics. *Critical Reviews in Solid State and Materials Sciences,* 28**,** 231-285.

Watanabe, H., Kamiyama, S., Umezawa, N., Shiraishi, K., Yoshida, S., Watanabe, Y., Arikado, T., Chikyow, T., Yamada, K. and Yasutake, K. (2005) Role of nitrogen incorporation into Hf-based high-& gate dielectrics for

termination of local current leakage paths. *Japanese Journal of Applied Physics, Part 2: Letters,* 44**,** 1333-1336.

Wilk, G. D., Wallace, R. M. and Anthony, J. M. (2001) High-k gate dielectrics: Current status and materials properties considerations. *Journal of Applied Physics,* 89**,** 5243-5275.

Wong, H. (2008) Properties of high-dielectric constant complex materials based on transition and rare-earth metal oxides. *International Conference on Solid-State and Integrated Circuits Technology Proceedings, ICSICT.* Beijing**,** 761-764.

Xu, J. P., Zhang, X. F., Li, C. X., Lai, P. T. and Chan, C. L. (2008) Improved electrical properties of Ge p-MOSFET with HfO_2 gate dielectric by using TaO_xN_y interlayer. *IEEE Electron Device Letters,* 29**,** 1155-1158.

Yoon, D. S., Roh, J. S., Baik, H. K. and Lee, S. M. (2002) Future direction for a diffusion barrier in future high-density volatile and nonvolatile memory devices. *Critical Reviews in Solid State and Materials Sciences,* 27**,** 143-226.

Zhang, H., Li, Y., Zhang, Q. and Wang, H. (2008) Preparation of high surface area $LaTiO_2N$ photocatalyst. *Materials Letters,* 62**,** 2729-2732.

Ziani, A., Le Paven-Thivet, C., Le Gendre, L., Fasquelle, D., Carru, J. C., Tessier, F. and Pinel, J. (2008) Structural and dielectric properties of oxynitride perovskite $LaTiO_xN_y$ thin films. *Thin Solid Films,* 517**,** 544-549.

Chapter 3 Experimental procedures

3.1 Introduction

In this study, oxynitride samples were prepared by ammonia heat treatment of mixtures of oxide and carbonate powders at an appropriate reaction temperature for each desired composition. In some cases, oxide precursors needed to be preprepared and these were made by reacting mixed powders, which were then heated in ammonia afterwards. Oxynitride samples were densified either by careful hot-pressing or by spark plasma sintering. X-ray diffraction was used to confirm the correct final composition and to identify phase purity. Both bulk and particulate dielectric properties of the selected oxynitrides were studied. The dielectric properties of bulk and thin film were measured by the LCR bridge method. Particulate dielectric constants were investigated by measuring the dielectric constants of the powders in slurry form.

3.2 Starting powders

The carbonate and oxide powders used as starting materials for preprepared oxide and final oxynitride sample preparation are listed in Table 3-1. During heat treatment either in air or in ammonia atmosphere, the carbonates were decomposed into their oxides, which reacted with other constituents to form the desired final product (Smart and Moore, 2005).

Table 3-1 Starting chemical powders and specifications

Chemical	Specification
Lanthanum oxide (La_2O_3)	Sigma 99.9%
Neodymium oxide (Nd_2O_3)	Sigma 99.9%
Samarium oxide (Sm_2O_3)	Sigma 99.9%
Dysprosium oxide (Dy_2O_3)	Aldrich 99.9%
Ytterbium oxide (Yb_2O_3)	Aldrich 99.9%
Yttrium oxide (Y_2O_3)	HCST grade A standard
Calcium carbonate ($CaCO_3$)	Sigma-Aldrich 99.0%
Strontium carbonate ($SrCO_3$)	Aldrich 98+%
Barium carbonate ($BaCO_3$)	BDH AnalaR ® 99.0%
Titanium dioxide (TiO_2)	BDH $\geq$98%
Zirconium dioxide (ZrO_2)	BDH
Tantalum (V) oxide (Ta_2O_5)	Aldrich 99%
Zirconyl chloride octahydrate ($ZrOCl_2 \cdot 8H_2O$)	Aldrich 98%
Zirconium (IV) propoxide $Zr(OCH_2CH_2CH_3)_4$	Aldrich 70 wt% solution in 1-propanol
Titanium (IV) propoxide $Ti(OC_3H_7)_4$	Aldrich 98%
Polyvinyl alcohol	BDH max. impurities: ash 0.7%
Nitric acid (HNO_3)	BDH GPR 69%
Hydrochloric acid (HCl)	BDH GPR sp.gr. 1.18
Iso-propanol (propane-2-ol)	
Carbon black powder	Cabot grade Monarch 1000
Ammonia gas (NH_3)	BOC 99.98% pure with minimal levels of moisture (<200 ppm) and other impurities (<5ppm oil)

3.3 Powder processing

Small quantities of the appropriate chemical powders ($\approx$ 5 g) were thoroughly hand mixed in an agate pestle and mortar in isopropanol. The slurry was stirred under an infra-red lamp to evaporate the isopropanol for 15–20 minutes depending on the particle size. The constituents needed to be very well mixed and finely ground to give a uniform small particle size, thereby maximising surface contact area and minimising diffusion distance of reactants (Smart and Moore, 2005). The most commonly use technique of ball-milling was avoided because it causes contamination from the inevitably abraded milling media (Moulson and Herbert, 2003). Also in this research, samples were prepared in small amounts (less than 5 g) so that they could be effectively mixed and ground manually. Isopropanol was chosen as the mixing medium because it is not reactive towards any of the carbonate or oxide starting materials; it is also easily evaporated at low temperatures. In the case of oxide precursors, after well mixing and grinding, the mixed powders were compacted into pellets and then calcined in air (see Sections 3.4 and 3.5); in other cases they were directly heated in flowing ammonia gas. It was noted that La_2O_3 is sensitive to moisture present in the air which hydrolyses it to $La(OH)_3$. Therefore, the powder was pre-dried at 900ºC for 16 hours before using it as a starting material.

3.4 Powder compaction

Powder mixes were green compacted by applying uniaxial pressure of up to 30 MPa in steel dies 1 cm in diameter to give cylindrical pellets of thickness ≤ 0.5 cm. Density variations throughout the green compact are undesirable because these can cause warpage, distortion, or cracking during firing (Richerson, 2006). One of the sources of density differential across the green compact is friction between the die wall and the powder particles, and also between individual powder grains (Richerson, 2006).
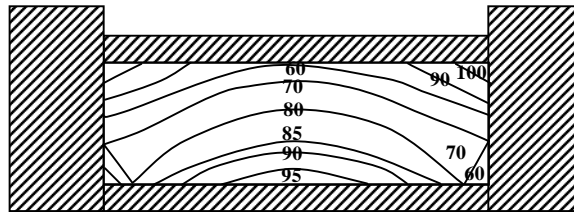
a) L:D = 0.45
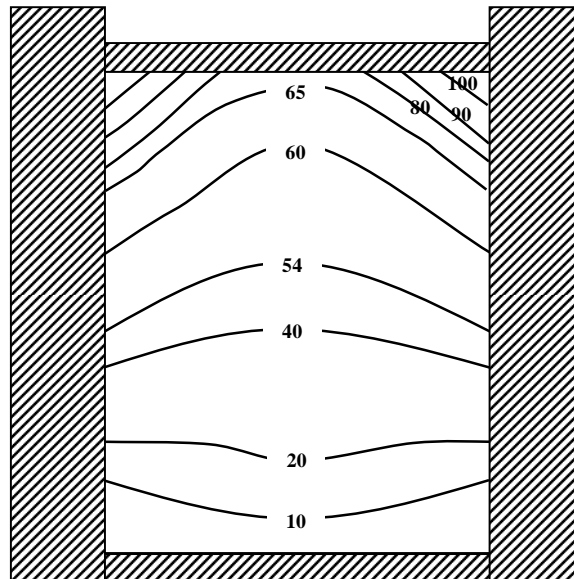
b) L:D = 1.75

Figure 3-1 Pressure differential in uniaxial pressing and length:diameter (L:D) effect (Richerson, 2006)

Figure 3-1 shows the pressure variation as a percentage across the compact in uniaxial pressing for (a) thick and (b) thin sample pellets. It can be seen that the ratio of the length to the diameter of the pellet (L:D) strongly affects the pressure variation, i.e. the pressure variation increases with increasing L:D ratio. This pressure differential throughout the pellet results in non-uniform density and layered cracking of the pellet during compaction (Kamm *et al*., 1949 cited in Yu, 2000); also, during firing, the lower density areas are not densified completely and experience more shrinkage than surrounding areas, causing flaws or defects in the fired product (Richerson, 2006). This effect can be minimised by maintaining a low L:D ratio for cylindrical pellets (Kingery, 1958 cited in Yu, 2000); also, the use of binders or lubricants can reduce friction (Richerson, 2006). Variations in density can also be caused by non-uniform stacking of the loaded powder (Richerson, 2006). A large pile of powder in the stack is compacted to a higher density than that of surrounding regions. Another possible source of density variation is the presence of hard agglomerates (Richerson, 2006). These clusters of particles are shielded by the surrounding soft powder from exposure to the maximum pressure causing pore clusters and reduction in strength of product parts. As can be appreciated, non-uniform density is more associated with the condition of the powder loaded into the pressing die rather than with the pressing operation itself. However, from practical experience, the powder should be gradually pressed and repeatedly compacted by uniaxial pressure till it reaches the desired pressure and retained at this pressure for a short time.

71

3.5 Oxide precursor preparation

Solid state sintering is the term used to describe the process that occurs by solid-state diffusion of atoms, that is, by the motion of individual atoms along the surface of grains or through the bulk of a powder sample when heated (Richerson, 2006). The constituents must be well mixed and ground before heating to a temperature at which they react by inter-diffusion of the ions (Moulson and Herbert, 2003). As a rule of thumb, the correct firing temperature should be about two-thirds of the average melting temperature of the solid constituents to enable atomic diffusion to proceed (Smart and Moore, 2005). In order to achieve a homogeneous composition, it is necessary to have a high surface area of grains in direct contact with one another and a short inter-grain diffusion distance. A compacted pellet increases the chance of surface interaction compared with loose powder (Smart and Moore, 2005). Reaction occurs initially at grain surfaces resulting in a layer of product round the grains, which ionic reactants need to diffuse through in order to continue the reaction (Smart and Moore, 2005). Therefore, intermediate regrinding is beneficial to open up fresh surfaces for contact and so speed up the reaction.

In this research, relevant oxide precursors of oxynitrides were preprepared by the solid state method. To prepare $Ln_2Ti_2O_7$ (Ln = La, Nd, Sm, Dy, Yb and Y), $A_2Ta_2O_7$ (A = Ca, Sr) and solid solutions of La and Nd oxides, and Ca and Sr oxides, the starting reagents for sample preparation consisted of stoichiometric amounts of La_2O_3, Nd_2O_3, Sm_2O_3, Dy_2O_3, Yb_2O_3, Y_2O_3, CeO_2, $CaCO_3$, $SrCO_3$, TiO_2 and Ta_2O_5 powders, which were mixed and ground in isopropanol in an

agate mortar as described in Section 3.3. After grinding, the mixture was compacted into a pellet; the details and the care needed during this process were described in Section 3.4. Afterwards, the green compact was calcined in air at an appropriate temperature for a reasonable reaction time (from practical experience typically not less than 10 hours) followed by a repeated heat treatment cycle with intermediate regrinding which was often necessary to achieve the single phase oxide precursor product. The intended reactions taking place are given by Equation 3-1 and Equation 3-2, i.e.:

$$Ln_2O_3 \ + \ 2TiO_2 \rightarrow \ Ln_2Ti_2O_7 \ ; Ln = La, Nd, \ldots$$

Equation 3-1

$$2ACO_3 \ + \ Ta_2O_5 \rightarrow A_2Ta_2O_7 \ + \ 2CO_2 \ ; A = Ca, Sr$$

Equation 3-2
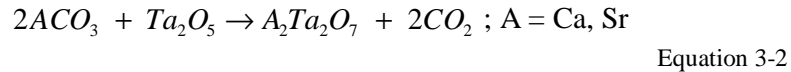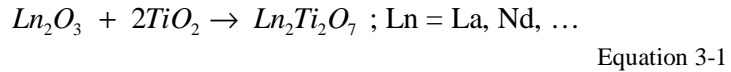
Since in the $BaO\text{-}Ta_2O_5$ system, a compound of the type $A_2Ta_2O_7$ does not exist, the above reaction leads to mixtures of $Ba_5Ta_4O_{15}$ and $BaTa_2O_6$ being produced (Rachel *et al.*, 2005); the oxynitride compounds of Ba were therefore prepared by direct ammonolysis nitridation of the mixed reagents as described in Section 3.6.

Solid solutions of the type $(La_xNd_{1-x})_2Ti_2O_7$ and $(Ca_xSr_{1-x})_2TaO_7$, x = 0, 0.2, 0.4, 0.5, 0.6, …, 2 were also processed using the same conditions as those for $Ln_2Ti_2O_7$ and $A_2Ta_2O_7$, as shown in Equation 3-3 and Equation 3-4, i.e.:

$$xLa_2O_3 \ + \ (1\text{-}x)Nd_2O_3 \ + \ 2TiO_2 \ \rightarrow \ (La_xNd_{(1\text{-}x)})_2Ti_2O_7$$

Equation 3-3

$$2xCaCO_3 \ + \ 2(1\text{-}x)SrCO_3 \ + \ Ta_2O_5 \ \rightarrow \ (Ca_xSr_{(1\text{-}x)})_2Ta_2O_7 \ + \ 2CO_2$$

Equation 3-4
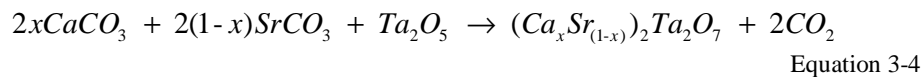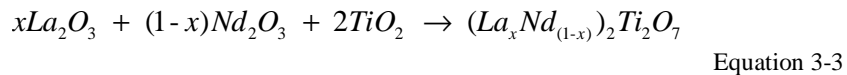
3.6 Ammonolysis Nitridation

Ammonolysis is a nitriding process used to introduce nitrogen into oxide samples at elevated temperature as described in Section 2.3.1. At a temperature higher than 500ºC, ammonia readily decomposes to give active atomic nitrogen which congregates on the surface of powder grains. An exchange then occurs between the oxide anions and the adsorbed nitrogen, and simultaneously hydrogen reacts with oxygen to form water vapour which is removed from the system. Simple and complex oxynitride powders were prepared by nitridation of oxide precursors or oxide/carbonate mixes at high temperature in hot anhydrous flowing ammonia as schematically illustrated in Figure 3-2.
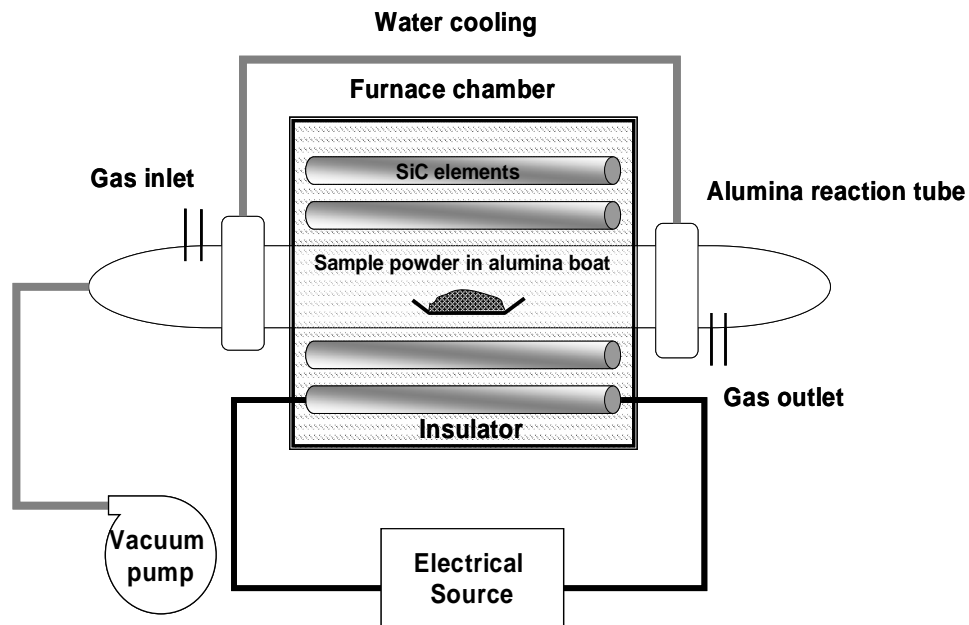
Figure 3-2 Schematic showing the essential elements of the ammonia nitriding furnace

Since the effectiveness of nitridation in the ammonolysis process depends critically upon the diffusion of atomic nitrogen into oxide grains, the reactants are generally heated in loose powder form to facilitate gas access. Typically, for each composition, approximately 3 g of starting material was heated at a rate of 10°C/min to the target temperature and held at that temperature for 16 hours before cooling down to room temperature at a rate of 10°C/min. After completion of the 16 hour-reaction, the samples were cooled down to 350°C in an ammonia atmosphere in order to avoid thermal oxidation of oxynitride products. Thereafter, the samples were kept in desiccators containing silica gel to protect them from oxidation in air. At room temperature, oxynitride compositions are stable, as confirmed by X-ray diffraction. The nitriding process was repeated with intermediate regrinding to open up fresh reactive surfaces until a single phase of the desired oxynitride product had been achieved.

When the $Ln_2Ti_2O_7$ and $A_2Ta_2O_7$ oxide precursors were nitrided in ammonia at elevated temperature, the intended chemical reactions were:

$$Ln_2Ti_2O_7 \;+\; 2NH_3 \;\rightarrow\; 2LnTiO_2N \;+\; 3H_2O$$

Equation 3-5

$$A_2Ta_2O_7 \;+\; 2NH_3 \;\rightarrow\; 2ATaO_2N \;+\; 3H_2O$$
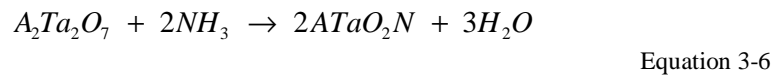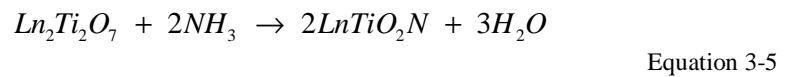
Equation 3-6

Since $Ba_2Ta_2O_7$ phase does not exist, a mixture of $BaCO_3$ and Ta_2O_5 powder was directly nitrided in the ammonia furnace at high temperature for several hours as given by Equation 3-7, i.e.:

$$2BaCO_3 \;+\; Ta_2O_5 \;+\; 2NH_3 \;\rightarrow\; 2BaTaO_2N \;+\; 3H_2O \;+\; 2CO_2$$

Equation 3-7
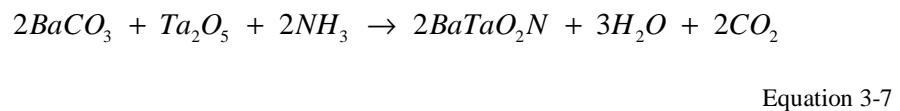
Solid solutions of the type $La_xNd_{1-x}TiO_2N$, $Ca_xSr_{1-x}TaO_2N$, $Ca_xBa_{1-x}TaO_2N$ and $Ba_xSr_{1-x}TaO_2N$ were produced by ammonolysis of appropriate oxide constituents under the same conditions as their parent rare earth oxynitrides. Since a Ca compound of the type $A_2Ta_2O_7$ does exist whereas the equivalent Ba compound does not, both direct nitridation of stoichiometric mixtures of $CaCO_3$, $BaCO_3$ and Ta_2O_5 and nitridation of intermediate oxide mixtures were tried out experimentally to prepare $Ca_xBa_{1-x}TaO_2N$ solid solutions. Since $SrTaO_2N$ could be synthesised by direct ammonia treatment of $SrCO_3/Ta_2O_5$ mixtures, direct nitridation of mixed $BaCO_3$, $SrCO_3$ and Ta_2O_5 powders was chosen to synthesise $Ba_xSr_{1-x}TaO_2N$ solid solutions.

3.7   Sintering

Sintering is achieved in the case of oxide materials by heating a consolidated mass of particles to a temperature ranging between 50 and 80% of the melting temperature (Rahaman, 2008). Under these conditions, the powders do not melt but instead join together and the porosity is reduced by atomic diffusion in the solid state. In polycrystalline ceramics, the requirements of correct phase, full density and a controlled microstructure are often difficult to achieve simultaneously.

3.7.1   Sintering parameters

Many factors affect the sintering behaviour of ceramic compacts. These include particle size, particle size distribution, packing within the green body, heating schedule and sintering atmosphere (Rahaman, 2008). Finer particles can speed up the sintering rate at low sintering temperature because there is more surface area

in contact with other grains. A homogenous distribution of fine particles is best, but in practice a mixture of particle sizes is always found. The densification of finer particles proceeds faster than coarser ones (Rahaman, 2008). This difference in behaviour affects the overall density of the final product. A wide distribution of coarser and finer particles can improve the final density because the smaller particles fit within the interstitices of the larger particles (Rahaman, 2008). Though low-density green powder compacts or loose powders can be sintered, well-compacted green pellets with a density of 50–60% of theoretical are much more likely to reach a high sintered density rather than low density green compacts or loose powders (Rahaman, 2008). Another parameter which affects sintering behaviour is particle shape although this has less effect. It is found that spherical or equiaxed particles give a lower packing density and homogeneity while acicular or elongated grains can be sintered to high density if the particles are aligned and well packed (Rahaman, 2008). The sintering atmosphere can have an important effect on densification and microstructure; hence, different gas atmospheres with varied oxygen partial pressures may be selected for sintering (Rahaman, 2008). It is rather difficult to simultaneously achieve a high density ceramic with the required microstructure (and properties) because to achieve a high density requires a high densification energy that may also cause grain growth and/or decomposition. The use of additives or dopants provides a very effective approach for sintering ceramics to high density at lower temperature because it can control grain growth (Rahaman, 2008). The selection of an efficient sintering additive is an issue based on experience rather than on theory so it is not easy to predict suitable additives especially when a new phase is being prepared. Many

parameters must be considered for reaching the required high density, taking into account other required characteristic of the final product.

In this research, prior to measuring dielectric properties of bulk oxynitride samples, sample powders had to be densified by a method which avoided decomposition and oxidation of the samples. Each oxynitride phase required different conditions of temperature and gas atmosphere and densification mechanisms were not always identical for different oxynitrides. Hot-pressing, spark plasma sintering and pressureless sintering were selected as the techniques to be used for densification and the appropriate conditions to suit each oxynitride compound were determined.

3.7.2 Hot-pressing

Hot-pressing is a technique used to densify powder samples by the simultaneous application of pressure and heat to a green compact or loose powder (Rahaman, 2008). Hot-pressing is typically conducted at approximately half the average melting point of the powders concerned, which is a lower temperature than pressureless sintering (Richerson, 2006). The applied pressure accelerates the kinetics of densification by increasing the contact stress between particles and thereby rearranging particle positions and improving particle packing (Richerson, 2006). The densification energy is greater than for pressureless sintering, providing several advantages such as reduced grain growth and a higher strength for the final product, these occurring because the applied pressure provides the major part of the driving force to reduce porosity and the temperature can be kept at a lower level at which grain growth is very slow (Richerson, 2006). Heat can

be employed either directly by induction or resistance heating or indirectly by convection or radiation; however, inductive heating is advantageous over resistive heating because insulation of the hot-pressing zone is much easier with the former (Bengisu, 2001b). Pressure is applied statically or dynamically to the heated component in one or both opposing directions along a single axis by a hydraulic press in the pressure range 5 to 50 MPa (Bengisu, 2001b). Many kinds of materials can be used as a die for hot-pressing as shown in Table 3-2.

Table 3-2 Die materials for Hot-pressing

Material	Temperature (°C)	Pressure (MPa)	Comments
Nimonic alloys	1100	High	Creep and erode at high T
Mo or alloys	1100	20	Oxidises unless protected
W	1500	25	Oxidises unless protected
Al_2O_3	1400	200	Brittle, non-conducting
BeO	1000	100	Brittle, non-conducting
SiC	1500	275	Brittle
TaC	1700	55	Brittle
WC, TiC	1400	70	Brittle
TiB_2	1200	100	Brittle
Standard graphite	2500	40	Severe oxidation > 1200°C in air
Special graphite	2500	100	Severe oxidation > 1200°C in air

The die must be able to withstand the temperature, transient thermal stresses, high hot-pressing loads, and be chemically inert to the material being hot pressed and for non-conducting samples must itself be conducting (Richerson, 2006). Graphite is normally used as the die and piston material for hot-pressing alumina-based compositions, nitrides and carbides and for this purpose, the inner surfaces are coated with BN or Al_2O_3 to prevent reaction with the sample powder (Bengisu, 2001b). Although graphite is commonly used as the die, it has certain limitations (Rahaman, 2008). At temperatures above 1200°C, an inert or reducing atmosphere is needed because graphite is oxidised easily at these temperatures. Also, the pressure should not exceed 40 MPa for standard graphite and at higher pressures, special graphite is necessary. Refractory metal dies such as molybdenum, molybdenum alloys or tantalum have been used in certain cases but these are expensive, highly reactive and easily deformed at high temperatures (Richerson, 2006). Ceramic dies such as Al_2O_3 and SiC have reasonably low thermal expansion, are non-reactive and exhibit high resistance to abrasion and thereby can be used in hot-pressing up to temperatures of 1200°C and 1400°C, respectively (Richerson, 2006). A vacuum-controlled or protective gas atmosphere is beneficial at high temperatures to prevent samples reacting with air; however, this depends on the material being pressed (Rahaman, 2008). Direct loading of loose powder into the hot-pressed die is the most common procedure; however, loose powder has a lower thermal conductivity than pre-compacted powder so the region in contact with the dies may heat up and consolidate faster than the interior causing a non-uniformity of heat distribution resulting in a density (and hence strength) gradient especially for long cylinders or thick and intricate shapes

(Bengisu, 2001b, Richerson, 2006). However, shape and size were not problems in the present research because the samples were disk shaped approximately 1 cm in diameter and 0.5 cm thick. A densification aid or a grain growth inhibitor could have been added to improve density and minimise grain size (Rahaman, 2008) but this procedure was not adopted in the present work.
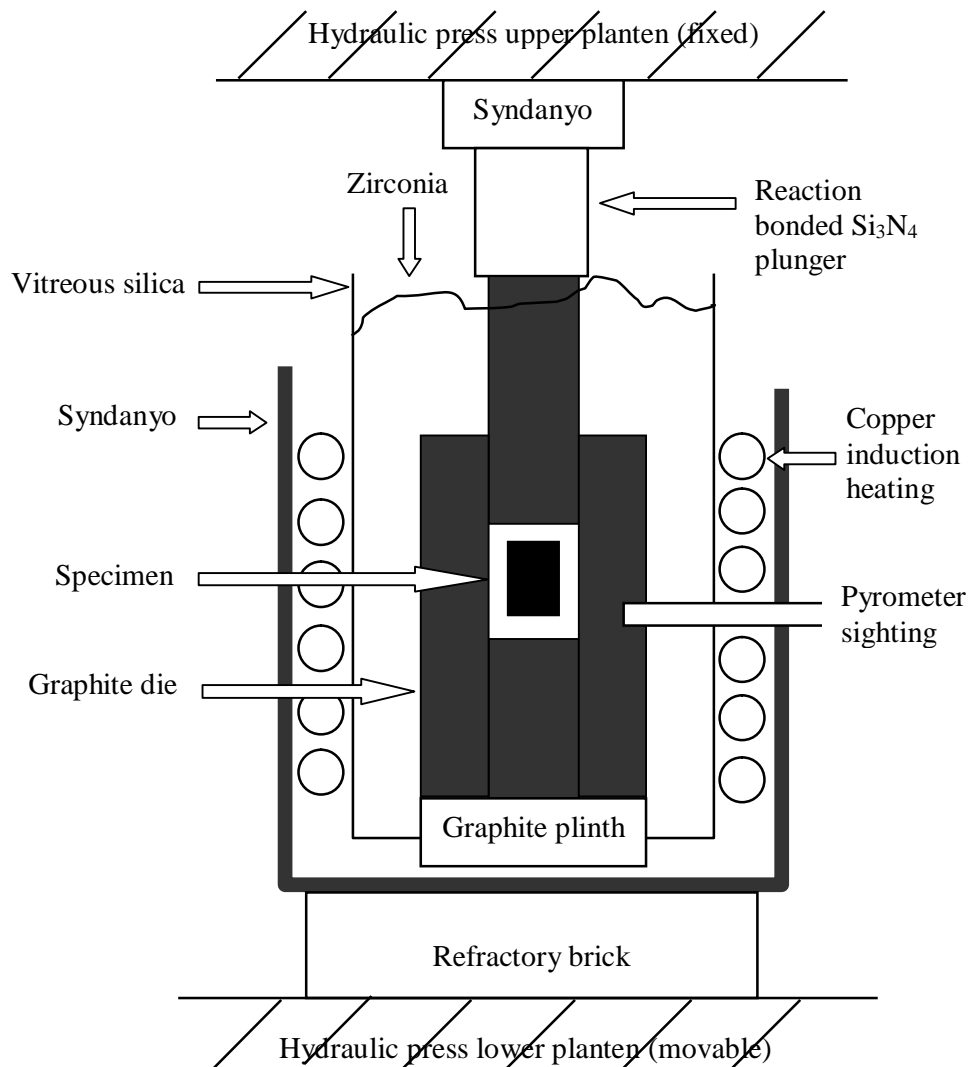
Figure 3-3 Schematic diagram of the hot-pressing apparatus used in this research
(Yu, 2000)

Uniaxial hot-pressing was used to prepare dense samples and the set-up used is shown in Figure 3-3. Standard and special graphite dies were used at temperatures of up to 1200ºC and pressures up to 2.5 MPa as indicated on the gauge on the apparatus. However, the sample size is approximately 1 cm diameter so the actual pressure on the sample is higher than the figure of 2.5 MPa shown on the gauge. From calculations based on sample size, the actual pressure is about 70 MPa. Loose powder samples were loaded into the graphite die which had been coated with boron nitride to prevent reaction with carbon at high temperature. The graphite die was enclosed inside a sillimanite cylinder and surrounded by closely packed granules of fused zirconia which acted as a thermal and electrical insulator and also protected the graphite die from oxidation. A water cooled copper induction coil powered by the radio frequency induction generator (Radyne 150E, 15 kW Max, 500 kHz) was arranged around the cylinder. The die rested on a graphite block placed on refractory bricks and the whole assembly was contained in a SINDANYO asbestos box on refractory bricks. During the hot-pressing operation, pressure was maintained at the required level manually and the desired temperature was monitored by a disappearing filament infrared pyrometer (accurate to ±20ºC) sighting through an open ended alumina tube on to the die liner wall. The samples were held at the desired temperature and pressure for 1 hour and then cooled down to room temperature.

3.7.3 Spark plasma sintering

Spark Plasma Sintering (SPS) is a high speed powder consolidation technique. A high amperage DC pulsed current is passed through the powder compact in a die made of an electrically conducting material under an applied pressure of 30–50 MPa for normal graphite and up to 100 MPa for special graphite (Rahaman, 2008). Since the current passes through the die and the specimen at the same time, the overall specimen is homogeneously heated, and also benefits from the self-heating action caused by spark discharges generated in the voids between particles; these combined effects promote material transfer and allow full densification to take place rapidly (Shen and Nygren, 2001). Spark discharges in the voids momentarily cause local high temperatures resulting in some vaporisation and melting at the surface of particles, which facilitates neck formation around the contact area between them, resulting in a highly sintered compact (Aalund, 2010). Grain growth is minimised due to the remarkably high densification rate (and hence the very short times needed) in SPS. As seen in Figure 3-4 the compacted powder sample is placed between the die and the punches in the central region of the chamber and pressure is applied. The high energy, low voltage DC pulse current is then switched on for a short time—typically 0–20 minutes. The atmosphere can be either vacuum or inert gas and can be tailored for samples likely to be sensitive to air at high temperatures.

Because of the many advantages of SPS, this method was chosen to densify the oxynitride powders produced in the present work. The fast heating at high temperature for a short time was expected to limit any oxynitride decomposition

in the densification process. The sample powders were loaded in the special graphite die and sintered at temperatures above 1000ºC for 5–10 minutes under pressures of approximately 100 MPa.
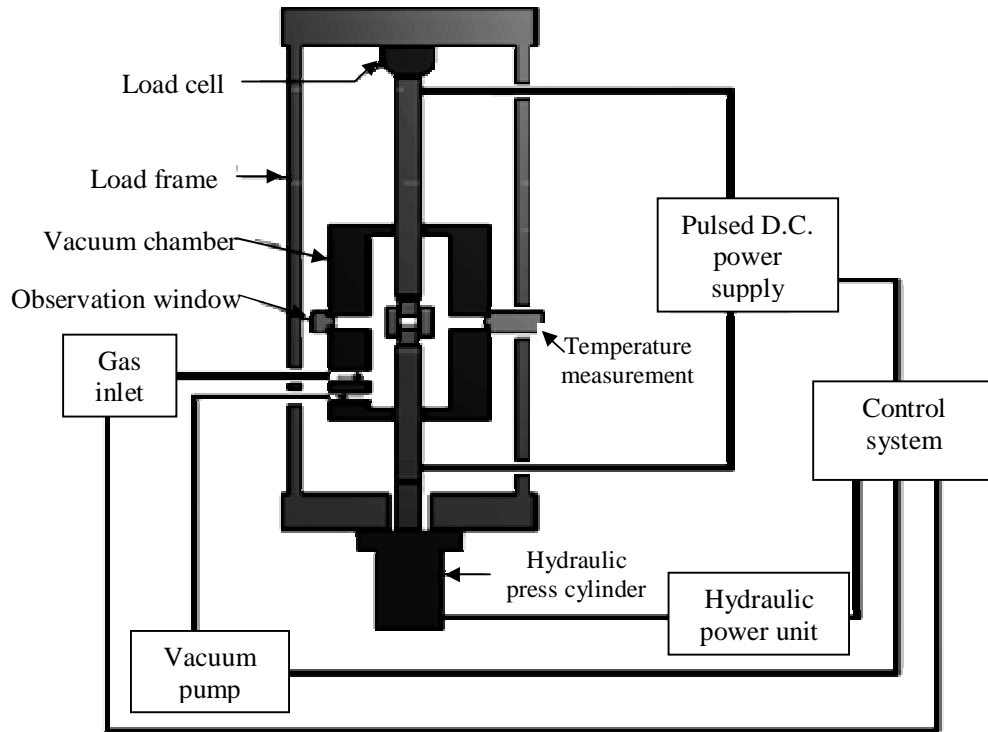
Figure 3-4 Schematic of a Spark Plasma Sintering (SPS) apparatus (Aalund, 2010)

3.7.4 Pressureless sintering

Since many of the oxynitride compounds prepared here were sensitive to air at the high temperatures needed for reaction and densification, attempts were made to densify them by pressureless sintering in either an ammonia atmosphere or in vacuum. Ammonia gas was selected because it maintains a higher partial pressure of nitrogen around the samples. Oxynitride powders were green compacted and heated in ammonia at temperatures in the range 1000–1500ºC. $LaTiO_2N$, $CaTaO_2N$ and $BaTaO_2N$ were the samples sintered by this method.

3.8 Density measurement

For making high density samples, the theoretical density of a crystalline material (ρ_c) is often used as a standard to compare with the actual bulk density achieved after sintering. Relative density (ρ_r) is defined as $r_r = \dfrac{r_m}{r_c}$ where ρ_m is the measured density of the sample and ρ_c is the calculated density of the crystalline material—here taken as being the same as that of the pure dense sample (Bengisu, 2001b). ρ_c is calculated from Equation 3-8, i.e.:

$$r_c = \frac{Z \times FW}{N_a \times V_{uc}}$$

Equation 3-8

where Z is the number of formula units per unit cell, FW is the formula weight, N_a is Avogadro's number and V_{uc} is the unit cell volume (Richerson, 2006).

Bulk density can be measured by several techniques. In this research, bulk densities of sintered bodies were measured by using a mercury displacement balance as shown in Figure 3-5. This method gives an accurate measurement of bulk volume. The balance operates on the principle of a hydrometer, that is, the bulk volume is determined by measuring the upthrust exerted by the mercury on the sample immersed in it (Ashworth 1969 cited in Yu, 2000). Firstly the pointer is adjusted to be exactly in contact with the surface of the mercury then the balance is re-set to zero and allowed to equilibrate. Next, the sample is placed on the surface of the mercury under the brass pin and immersed by screwing up the support frame until the pointer just touches the surface of the mercury. Weights (W_l) are added to re-submerge the sample. This weight (W_l) plus the weight of

the sample in air (W$_s$) gives the upthrust weight of the mercury on the specimen and the bulk volume of the sample is then equal to the volume of mercury displaced; therefore,

$$\frac{Weight\ of\ sample\ (Ws)}{Bulk\ density\ of\ sample\ (r_m)} = \frac{Upthrust\ weight\ of\ mercury\ (W_l + W_s)}{density\ of\ mercury\ (13.56\ g\ /\ cm^3)}$$

and

$$Bulk\ density\ of\ sample\ (r_m)\ = \frac{W_s \times 13.56}{W_l + W_s}\ g\ /\ cm^3$$

<div align="right">Equation 3-9</div>
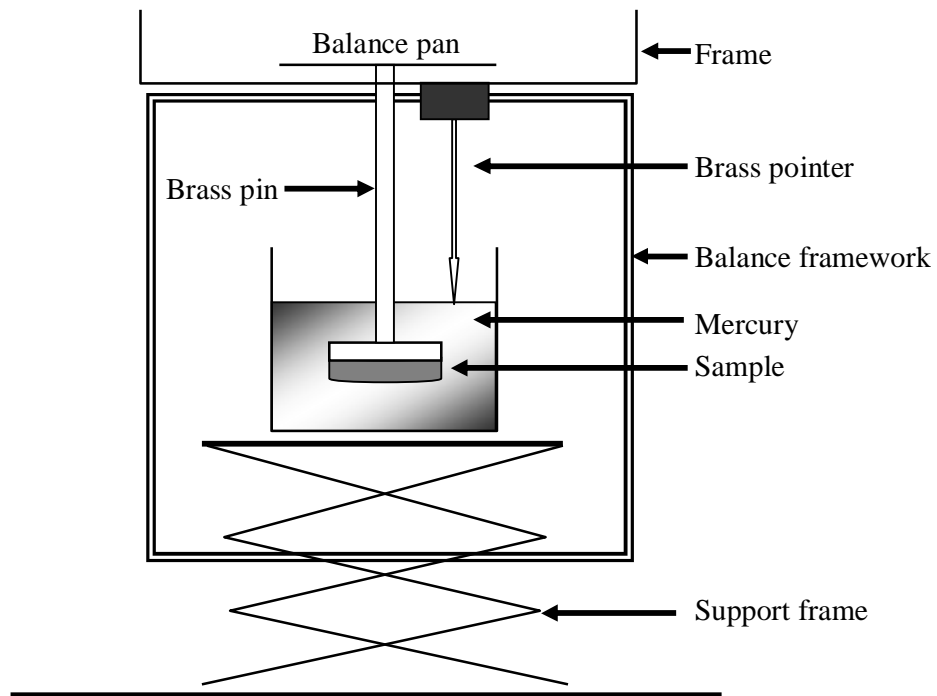
Figure 3-5 Schematic diagram of bulk density measurement apparatus (Yu, 2000)

3.9 Characterisation

3.9.1 X-ray diffraction

X-ray diffraction is a versatile non-destructive technique used to analyse phase composition and the crystalline structure of natural and manufactured materials. It uses a collimated beam of X-rays which is then diffracted by crystallographic planes in the sample (Bengisu, 2001b).
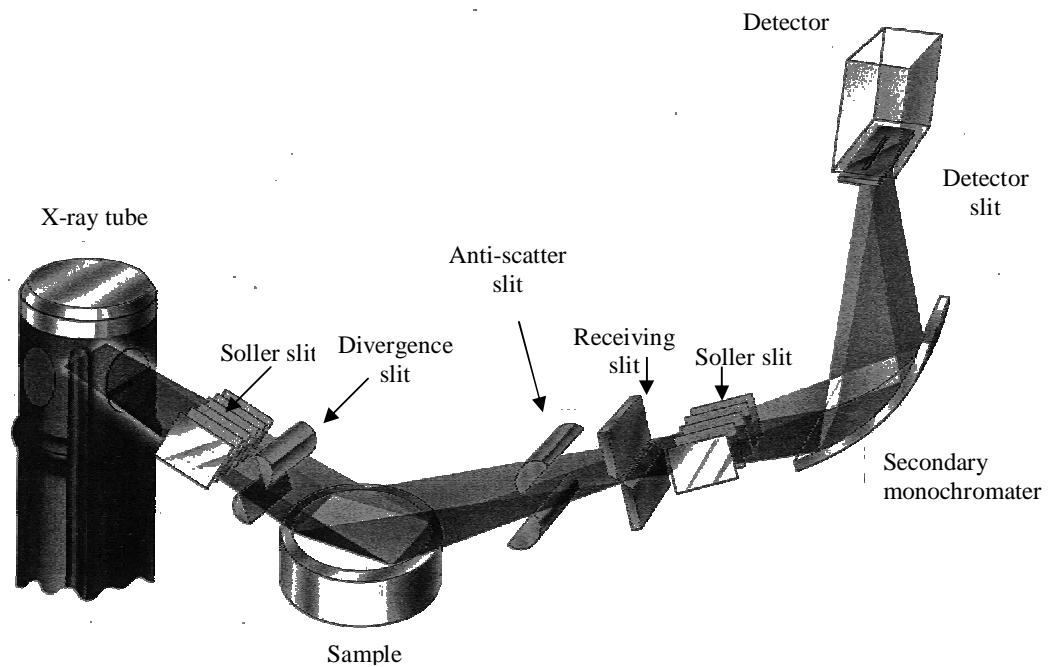
Figure 3-6 Principle of an X-ray Diffractometer (PANalytical B.V.)

The incident X-ray beam of wavelength λ is projected on to the sample over a range of angles of incidence θ, and then diffracted beams are given off at angles θ when the Bragg's Law is satisfied (Cullity, 1978)—see Figure 3-7. The X-rays are diffracted by adjacent atomic planes inclined at an equal angle θ to the incident beam and the spacing between successive atomic planes is d. Ray 1 and

Ray 2 scatter from the upper and the lower atomic planes respectively at an equal

angle θ. However, Ray 2 travels a distance of ML + LN farther than Ray 1.
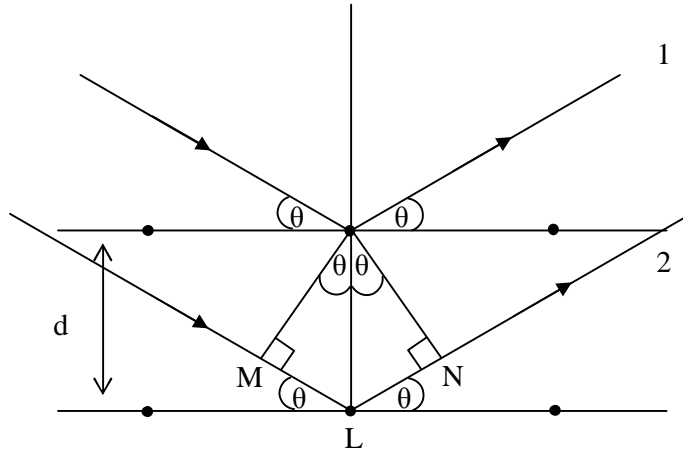
Figure 3-7 Diffraction of X-rays by a crystal (adapted from Cullity, 1978)

A strong diffracted beam occurs only if this distance is equal to an integral number

of wavelengths (nλ); under these circumstances Rays 1 and 2 constructively interfere

(they are in phase) and combine to reinforce one another to give a strong diffracted

beam. From Figure 3-7, ML + LN = 2dsinθ and   ML + LN = nλ; therefore, Bragg's

Law is expressed as Equation 3-10, i.e.:

$$nl \ = \ 2d\sin q$$

Equation 3-10

where n is the order of the Bragg reflection, λ is the wavelength of the X ray

employed (for Cu-Kα radiation, typically used for routine analysis, λ = 1.544 Å),

d is the interplanar distance, and θ is the angle of inclination of the incident

X-ray beam. In practice, n is always combined with d, so for example, instead

of using n=2 for the d_{111} plane, the *d*-spacing of the (222) plane (d_{222}) is used,

since $d_{222} = d_{111}/2$.

A typical diffraction spectrum consists of a plot of reflected intensities versus the detector angle 2θ. Where a mixture of different phases is present, the resultant diffracted pattern is formed by addition of the individual patterns. From Bragg's Law, the angular positions of peaks in the diffracted pattern are measured and used to calculate the corresponding interplanar distances (d-spacings), which are a characteristic of the particular phase. The calculations of d-spacing, lattice parameter(s) and Miller indices are done by the computer programme specifically written for the particular X-ray diffraction equipment used. Besides the interplanar distance, the intensities of the peaks (Guinebretière, 2007b) and the number of peaks (Geselbracht, 2010) are also characteristic features of the diffraction pattern which define a unique fingerprint for every crystalline material. The number of observed peaks is related to the symmetry of the unit cell, with higher symmetry generally giving fewer peaks (Geselbracht, 2010). The intensities of the peaks on an X-ray diffraction pattern are determined from the scattering power and positions of the atoms in the unit cell (Guinebretière, 2007b). The light atoms scatter X-rays weakly, whilst heavy atoms scatter X-rays more strongly.

In this research, a Phillips X'Pert X-ray diffractometer was used with Cu-Kα radiation and data were collected with an X'Pert Data Collector (X'celerator version 2.2) in the interval range 5–70° of 2θ with step size and counting time 0.033° and 100s, respectively. The sample powder was loaded into a sample holder from the back so that the top surface was flat, smooth and homogeneous. Only crystallites having reflecting planes parallel to the specimen surface contribute to the reflected intensities, and it is therefore important to have a

random distribution of grain orientations so that the distribution of hkl planes is also random, and back-loading reduces the effect of preferred orientation of crystallites (Guinebretière, 2007b). Phase identification was implemented by X'Pert HighScore Plus software version 2.2d (2.2.4). The list of relative intensities and interplanar distances were compared with those of known crystalline phases from the data base of the International Centre for Diffraction Data (ICDD).

3.9.2 Rietveld refinement

The Rietveld refinement method was used for determining the crystal structure of the analysed powder sample. It refines all variable parameters that control the intensity distribution of the X-ray pattern by minimising the difference between the experimental diffracted pattern and a model based on hypothesised crystal structure, also taking into account various instrumental parameters (Guinebretière, 2007a). In order to perform a Rietveld refinement, a high quality experimental diffraction pattern and structure data for all phases present in the sample are needed. It is suggested that not too many parameters should be refined at once in the early stages because some parameters affect each other. The following guideline for Rietveld refinement was suggested by Speakman (2010). A good refinement should start with the best fitting of background, peak positions and peak profile. The peak profile parameters (W, V and U respectively) will be refined one at a time. To finish the refinement, multiple profile parameters are refined at the same time. However, the fitting should be as good as possible before multiple parameter refinement because they all influence each other and

this prevents anomalous refinement minima being achieved. The quality of a Rietveld refinement can be determined from the agreement indicators or R factors such as profile R (R_p), weighted profile R (R_{wp}), expected R (R_{exp}) and goodness-of-fitting (GOF) (McCusker *et al.*, 1999 and Speakman, 2010), i.e.:

Profile R (R_p) defines the difference between the observed and calculated intensities (*y_i(obs)* and *y_i(cal)*, respectively) on a point-by-point (*i*). It is expressed by Equation 3-11, i.e.:

$$R_p = \frac{\sum_i |y_i(obs) - y_i(cal)|}{\sum_i y_i(obs)}$$

<div align="right">Equation 3-11</div>

Weighted profile R factor (R_{wp}) determines the residual after the fitting of the observed and calculated data, where w_i is the weight at step *i*. It is defined as Equation 3-12, i.e.:

$$R_{wp} = \sqrt{\frac{\sum_i w_i [y_i(obs) - y_i(cal)]^2}{\sum_i w_i [y_i(obs)]^2}}$$

<div align="right">Equation 3-12</div>

The expected R factor (R_{exp}) evaluates the quality of the data. It is defined by Equation 3-13, where *N* is the number of observation and *P* the number of parameters, i.e.:

$$R_{exp} = \sqrt{\frac{(N-P)}{\sum_i^N w_i y_i(obs)^2}}$$

<div align="right">Equation 3-13</div>

Goodness-of-fitting (GOF or χ^2) is a ratio between the weighted profile R factor (R_{wp}) and the expected R factor (R_{exp}):

$$c^2 = \frac{R_{wp}}{R_{exp}}$$

Equation 3-14

These agreement indices are automatically calculated by the instrument software. Ideally, the R_{wp} value after refinement should approach the statistically expected R value (R_{exp}) and as a result, the expected GOF should be close to 1 (McCusker *et al.*, 1999). In general, R_p and R_{wp} are required to be less than 10% (Speakman, 2010). R indices evaluate the quality of the entire refinement but the profile plots are much more informative.

3.9.3   Morphology and microstructure

Scanning electron microscopy was used to carry out microstructural analysis at high magnification. Electrons are accelerated through a high voltage field in vacuum, and when they reach the sample, they are either scattered (as back-scattered electrons) or they interact with the sample, producing X-rays and secondary electrons (Bengisu, 2001a). Back-scattered electrons are used for distinguishing grains of phases containing elements with substantially different atomic numbers and the secondary electron mode yields topographic information (Bengisu, 2001a). Interactions between the sample and the electron beam result in the emitted signal, which is detected and reconstructed into a virtual image.

In the present case, optical microscopy and Scanning Electron Microscopy (FEI XL30 ESEM-FEG model) were used to determine topographic information such

as grain shape and size, the presence of pores and other surface defects. For SEM, sample pellets were coated with either gold or carbon to improve the surface conductivity and reduce the effects of charging under the electron beam (Bengisu, 2001a).
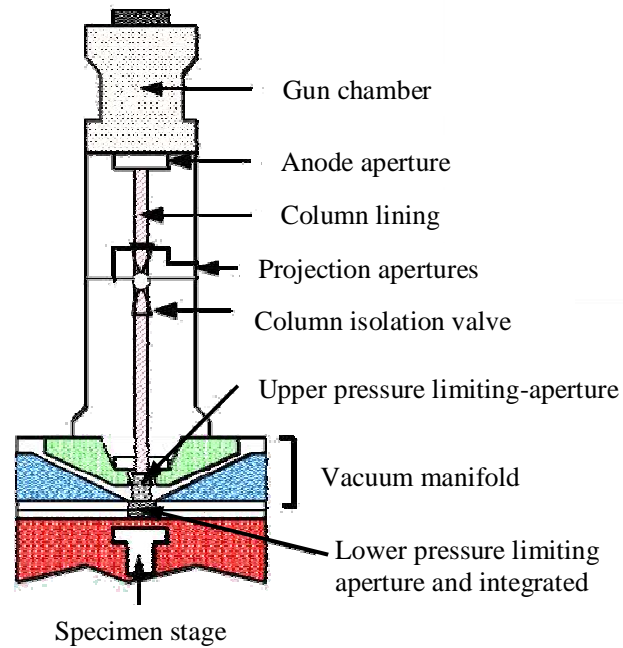
Figure 3-8 Schematic diagram of environmental scanning electron microscope
(Department of Physics, University of Cambridge, 2010)

3.10 Bulk dielectric measurement

Fundamentally, dielectric constant and dielectric loss can be estimated by measuring the voltage and the current between a pair of electrodes in order to determine the conductance and capacitance of the material between these electrodes. Conductance is a measure of the energy transmitted and dissipated through the material, while capacitance is a measure of the ability of the material to store energy. From the relation between capacitance and dielectric constant (see Section 2.4), the dielectric constant can be calculated. Both conductance and

capacitance depend on the geometry of the electrodes, i.e. their shape, width and separation distance, and the dielectric material between the electrodes.

There are many techniques to measure dielectric constant (or effective dielectric constant) of a material such as lumped circuit, resonance cavities, transmission line, free space, parallel plate and open-ended coaxial probe methods. Figure 3-9 summarises an application list provided by Agilent Technologies Inc. (Agilent-Technologies, 2010) which compares some of the current dielectric measurement methods.

Coaxial probe		Broadband convenient, non-destructive Best for lossy MUTs: liquid or semisolids
Transmission line		Broadband convenient Best for lossy to low loss MUTs; machineable solids
Free space		Non-contacting Best for high temperature; flat samples
Resonant cavity		Accurate Best for low loss MUTs; small samples
Parallel plate		Accurate Best for low frequencies; thin flat sheets
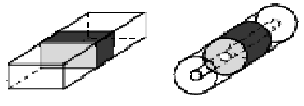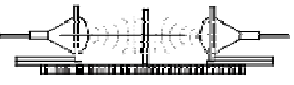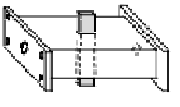
Figure 3-9 Summary of the dielectric measurement techniques

Most of these techniques are widely used but each technique has its own limitations. Factors such as accuracy, convenience, and the material shape and form are important in selecting the most appropriate measurement technique. Variables affecting dielectric constant include (in decreasing order of importance) frequency, temperature, pressure and the intensity of the applied electric field;

however, the choice of method is determined principally by frequency and temperature (Vaughan, 1969). Special methods are required for measurement at high pressures and high electric field strengths but these were not used in this research.

The parallel plate technique was used in the present work and sample discs were gold coated by sputtering to give the parallel electrodes of the capacitor. The thickness of the coating was about 50 nm. A Hewlett Packard (4284 A) LCR bridge was used to determine capacitance and dielectric loss at room temperature from frequencies of 10^2 Hz to 10^6 Hz. The dielectric constant was then calculated (see Section 2.4).

3.11 Particulate dielectric measurements

Studies of the dielectric properties of powders base the theory on that of a two-phase system, i.e. powder and matrix, and theoretical models based on mixing rules. The general procedure consists of three steps as follows:

(i)   The dielectric powder is dispersed in a liquid host.

(ii)   The complex impedance ($Z = Z' + jZ''$) of the composite specimen consisting of the powder and liquid is measured.

(iii)   A model for the composite specimen is applied to analyse the capacitance and then calculate the dielectric constant of the powder and the liquid host.

Sample preparation has been described in a previous report (Petrovsky *et al.*, 2008). 20% by volume of powder was loaded into > 99% butoxyethanol ($\varepsilon = 10$)

and then ultrasonically dispersed for 10 minutes. An electrochemical cell with stainless steel electrodes (electrode diameter: 44 mm and distance between electrodes: 1.1 mm) was used as a sample holder. Impedance was collected by an automated Solartron system (1255b Frequency Response Analyzer and 1470 Cell Tester, Farnborough, Hampshire, UK).

A typical impedance spectrum of a two-phase system consists of two semicircles—the first semicircle is attributed the liquid host response at high frequency and the second one is from the particle response at low frequency—as shown in Figure 3-10 a) (Jasinski *et al.*, 2010).
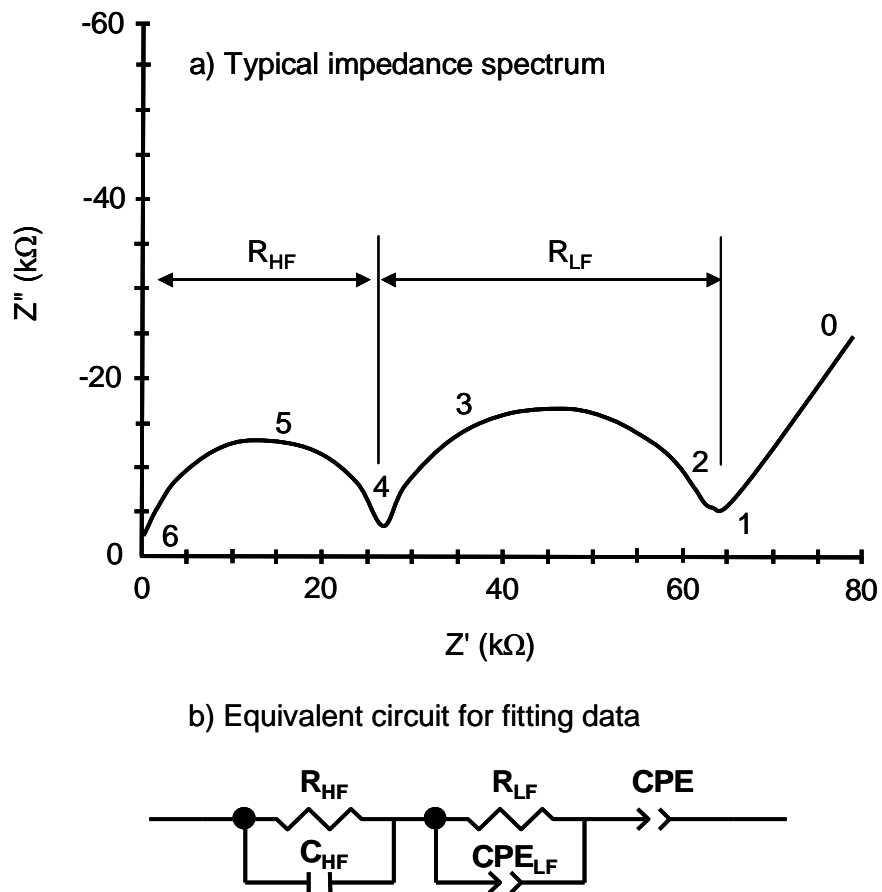
Figure 3-10 a) Typical impedance spectra of a two-phase system, and b) two parallel RC equivalent circuits connected in series (Jasinski *et al.*, 2010)

The two semicircles may overlap depending on the difference in dielectric constants of the powder and the liquid host (Petrovsky *et al.*, 2006). The low frequency tail is related to the double layer capacitance at the electrodes (Jasinski *et al.*, 2010) and is not of interest here. The Z-View software supplied by Scribner Inc. (Southern Pines, NC) was used to fit the impedance spectrum from the experiment to the calculated one by considering 2 parallel RC circuits individually connected in series, as shown in Figure 3-10 b).

The use of CPE (Constant Phase Element) instead of capacitance in the equivalent circuit is necessary because at low frequencies, the semicircle, for which the centre would be expected to lie exactly on the Z' axis, is slightly depressed to a lower position (Jasinski *et al.*, 2010). This can be explained by a number of phenomena related to the system being investigated, such as distribution in values of some physical properties of the system.
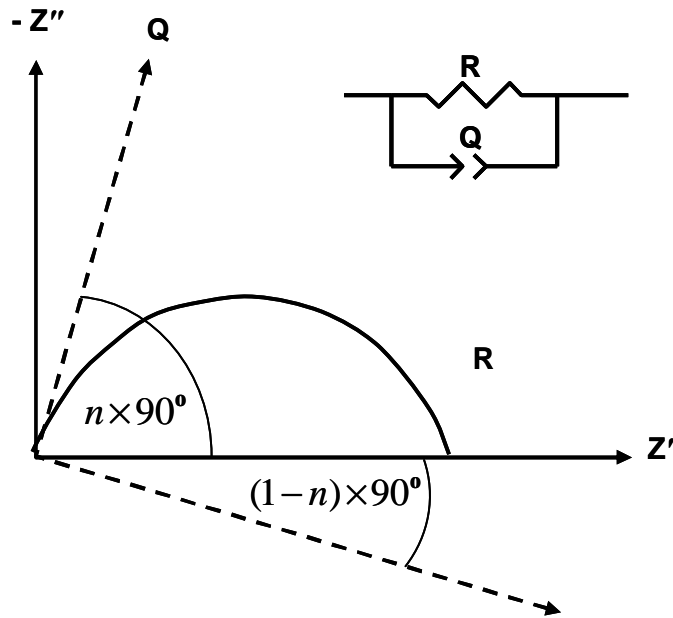
Figure 3-11 Depressed impedance spectrum
(http://www.consultrsr.com/resources/eis/cpe1.htm)

97

Figure 3-11 shows a typical depressed semicircle from impedance analysis. The Q axis is given by the depressed semicircle making an angle of $n \times 90°$ to original Z' axis, where $0 \leq n \leq 1$. The capacitance corresponding to the low frequency semicircle C_{LF} is calculated from CPE parameters (Q and n) by Equation 3-15 (Kidner *et al.* 2008 and Macdonald 1987 cited in Jasinski *et al.*, 2010), i.e.:

$$C_{LF} = (Q_{LF})^{1/n} (R_{LF})^{(1-n)/n}$$

<div align="right">Equation 3-15</div>

where Q and n are parameters associated with CPE, which are obtained from the fitting of the spectrum, and R_{LF} is the resistance.

The dielectric constants of the liquid host and the dielectric powder were then calculated from Equation 3-16 and Equation 3-17, respectively (Jasinski *et al.*, 2010), i.e.:

$$e_{HF} = \frac{C_{HF}}{e_0} \cdot \frac{d}{A}$$

<div align="right">Equation 3-16</div>

$$e_{LF} = \frac{C_{LF}}{e_0} \cdot \frac{d}{A}$$

<div align="right">Equation 3-17</div>

where e_{HF}, e_{LF} and C_{HF}, C_{LF} are the dielectric constants and capacitances at high and low frequency, respectively, A represents the electrode area and d is the distance between the electrodes.

3.12 References

Bengisu, M. (2001a) Characterisation. In Bengisu, M. (Ed.) *Engineering Ceramics.* New York, Springer**,** 363-406.

Bengisu, M. (2001b) Production of Ceramic Bodies. In Bengisu, M. (Ed.) *Engineering ceramics.* New York, Springer**,** 85-208.

Cullity, B. D. (1978) Diffraction I: Direction of Diffracted Beams. In Cullity, B. D. (Ed.) *Elements of X-ray diffraction.* 2nd ed. Reading, Messachusetts, Addison-Wesley publishing Co., Inc.**,** 81-106.

Guinebretière, R. (2007a) Data Processing, Extracting Information. In Guinebretière, R. (Ed.) *X-ray diffraction by polycrystalline materials.* Chippenham, Wiltshire, Antony Rowe Ltd.**,** 127-153.

Guinebretière, R. (2007b) Interpreting the Results. In Guinebretière, R. (Ed.) *X-ray diffraction by polycrystalline materials.* Chippenham, Wiltshire, Antony Rowe Ltd. **,** 155-193.

Jasinski, P., Petrovsky, V. and Dogan, F. (2010) Impedance spectroscopy of BaTiO3 cubes suspended in lossy liquids as a physical model of two-phase system. *Journal of Applied Physics,* 108**,** 074111-074118.

McCusker, L. B., Von Dreele, R. B., Cox, D. E., Louer, D. and Scardi, P. (1999) Rietveld refinement guidelines. *Journal of Applied Crystallography,* 32**,** 36-50.

Moulson, A. J. and Herbert, J. M. (2003) Processing of Ceramics. In Moulson, A. J. and Herbert, J. M. (Eds.) *Electroceramics: materials, properties, applications.* 2nd ed. Chichester, Wiley**,** 95-134.

Petrovsky, V., Manohar, A. and Dogan, F. (2006) Dielectric constant of particles determined by impedance spectroscopy. *Journal of Applied Physics,* 100**,** 014102-014105.

Rachel, A., Ebbinghaus, S. G., Gᴣᴧngerich, M., Klar, P. J., Hanss, J., Weidenkaff, A. and Reller, A. (2005) Tantalum and niobium perovskite oxynitrides: Synthesis and analysis of the thermal behaviour. *Thermochimica Acta,* 438**,** 134-143.

Rahaman, M. N. (2008) Sintering process variables and sintering practice. In Rahaman, M. N. (Ed.) *Sintering of Ceramics.* Boca Raton, FL, CRC Press**,** 305-365.

Richerson, D. W. (2006) Densification. In Richerson, D. W. (Ed.) *Modern ceramic engineering: properties, processing, and use in design.* 3rd ed. Boca Raton, FL, CRC Press**,** 477-527.

Shen, Z. and Nygren, M. (2001) Kinetic aspects of superfast consolidation of silicon nitride based ceramics by spark plasma sintering. *Journal of Materials Chemistry,* 11**,** 204-207.

Smart, L. E. and Moore, E. A. (2005) Preparative methods. In Smart, L. E. and Moore, E. A. (Eds.) *Solid state chemistry: an introduction.* 3rd ed. Boca Raton, FL, CRC press**,** 125-154.

Vaughan, W. E. (1969) Experimental methods. In Sugden, T. M. (Ed.) *Dielectric properties and moleculare behaviour.* 1st ed. London UK, Butler & Tanner Ltd.**,** 108-190.

Yu, Z. (2000) *Monolithic and composite Li-α SIALON ceramics.* PhD Thesis, University of Newcastle upon Tyne, Newcastle upon Tyne UK.

Other reference resources:

Agilent-Technologies (2010, November 23rd) *Application Note: Basics of measuring the dielectric properties of material.* Retrieved from http://www3.imperial.ac.uk/pls/portallive/docs/1/11949698.PDF

Aalund, R. (2010, October 15th) Spark plasma sintering. Retrieved from http://www.ceramicindustry.com/Articles/Feature_Article/BNP_GUID_9-5-2006_A_10000000000000321084.

Department of Physics, University of Cambridge (2010, July 20th). Environmental Scanning Electron Microscopy. Retrieved from http://www.phy.cam.ac.uk/research/bss/bsspictures/esem.jpg

Geselbracht, M. (2010, January 20th) Introduction to Powder X-ray Diffraction. Retrieved from https://www.ionicviper.org/lab-experiment/introduction-powder-x-ray-diffraction.

PANalytical B.V (2010). X-ray diffractometer (Poster).

Speakman, S. A. (2010, October 26th). Fundamental of Rietveld Refinement I, II and III. Retrieved from http://prism.mit.edu/xray/tutorials.htm

The constant phase element (2010, November 15th). Retrieved from http://www.consultrsr.com/resources/eis/cpe1.htm

Chapter 4 Synthesis and dielectric characterisation of bulk LnTiO₂N (Ln = La, Nd), ATaO₂N (A = Ca, Sr, Ba) and their solid solutions

4.1 Introduction

Of the various new materials available for development as high-k dielectrics, perovskite oxynitrides are some of the more interesting candidates, and of these, the rare earth and alkaline earth-based oxynitrides have received most attention. Marchand *et al.* (1986a) were the first to explore the possibility of incorporating nitrogen into the anion network of an ABO_3 perovskite. For example when nitrogen is introduced into barium titanate, $BaTiO_3$, the increased anionic charge can be compensated by the replacement of Ti in oxidation state +4 by an element in oxidation state +5 such as tantalum or niobium, with the change:

$$Ti^{+4} + O^{-2} \equiv Ta^{+5} + N^{-3}$$
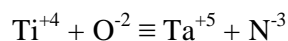
This cross substitution maintains electrical neutrality and results in perovskite-type oxynitrides such as $BaTaO_2N$, $BaNbO_2N$ and $SrTaO_2N$, and $CaTaO_2N$. These were synthesised by the reaction between ammonia and the appropriate oxide derivatives at 900–1000℃ (Marchand *et al.*, 1986a) and were considered to be potential high-k dielectrics with especially $BaTaO_2N$ and $BaNbO_2N$ exhibiting high dielectric constants over a wide range of temperature and frequency (Marchand *et al.*, 1986b). Nevertheless, Gouin *et al.* (1995) claimed that by

comparison with the infrared reflection spectrum of $BaTiO_3$, $BaTaO_2N$ did not show a polar soft mode so the dielectric response of $BaTaO_2N$ should not reach high values. This was explained as being due to the stronger Ta–N bond, resulting in less atomic displacement compared with related oxide perovskites. Later work by Kim *et al.* (2004)used powdered samples compacted by cold isostatic pressing to only 55% of their theoretical density and found high bulk-dielectric constant values of 2900 and 4900 for $SrTaO_2N$ and $BaTaO_2N$ respectively at room temperature.   For these materials, the temperature coefficients of permittivity were higher than those of medium-k oxide dielectric materials but smaller than those of ferroelectrics. $CaTaO_2N$ was found to have a fairly low dielectric constant more typical of an oxide perovskite (k ≈ 30) with lower conductivities than most Ta^{5+}-containing oxides by several orders of magnitude. These workers also observed metallic conductivity for $BaNbO_2N$, which most likely originated from partial reduction of niobium in oxidation state +5 to +3 thereby leading to the introduction of carriers into the conduction band.

When the barium in $BaTiO_3$ is replaced by a lanthanide (Ln^{3+}= La, Nd…) cation, the increased charge of the Ln cation can be compensated by the introduction of nitrogen, allowing the titanium to remain in oxidation state +4, resulting in an overall $LnTiO_2N$ stoichiometry, as given by the change:

$$Ba^{+2} + O^{-2} \rightarrow Ln^{+3} + N^{-3}$$
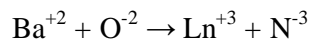
Lanthanide-based perovskite oxynitrides of the type $LnTiO_2N$ and $LnTaON_2$ were synthesised by conventional ammonolysis of their ternary oxide powders at a temperature of 950ºC (Marchand *et al.*, 1991, Clarke *et al.*, 2002). Repeated

ammonolysis was needed following intermediate regrinding to produce a pure product.

No previous work has been reported in the literature on the synthesis, characterisation and dielectric properties of $La_xNd_{1-x}TiO_2N$, $Ba_xSr_{1-x}TaO_2N$ and $Ca_xSr_{1-x}TaO_2N$ and $Ca_xBa_{1-x}TaO_2N$ solid solutions. In this research, $LnTiO_2N$ (Ln = La, Nd,..) and $ATaO_2N$ (A = Ca, Sr, Ba) and their solid solutions were therefore synthesised by ammonolysis of their corresponding oxide precursors and in the case of barium-based compounds, they were synthesised directly by ammonolysis of mixed oxide and carbonate powders. Product phases were identified by X-ray diffraction (XRD) and the morphology of the resulting powders was observed by scanning electron microscopy (SEM). Hot-pressing (HP) and spark plasma sintering (SPS) were explored as densification methods. The capacitance of the resulting materials was measured by the LCR bridge method and dielectric constants calculated.

4.2 Synthesis of $LnTiO_2N$ (Ln = La, Nd,..) and $La_xNd_{1-x}TiO_2N$

4.2.1 $LnTiO_2N$ (Ln = La, Nd,…)

Ternary $Ln_2Ti_2O_7$, (Ln = La, Ce, Nd, Sm, Dy Yb and Y) oxide precursor powders were prepared by solid-state reaction between lanthanide oxides (Ln_2O_3) and titanium dioxide (TiO_2) at temperatures of 1200°C for 5 hours and then, after regrinding and pelletising, at 1350°C for a further 16 hours. Since La_2O_3 and Nd_2O_3 are moderately sensitive to moisture, a pre-dry at temperatures of 900°C was necessary. Pure $La_2Ti_2O_7$, $Nd_2Ti_2O_7$, $Sm_2Ti_2O_7$, $Dy_2Ti_2O_7$, $Yb_2Ti_2O_7$ and

$Y_2Ti_2O_7$ were successfully obtained under these conditions; $Ce_2Ti_2O_7$ could not be produced because CeO_2 is highly thermodynamically stable when heated in air or an oxidising atmosphere (Preuss and Gruehn, 1994). When mixed powders of CeO_2 and TiO_2 were heated in vacuum at temperatures of 1350ºC for a total of 10 hours with intermediate regrinding, X-ray diffraction patterns (Figure 4-1) indicated that some $Ce_2Ti_2O_7$ had been obtained but additional unknown peaks were also present. The reaction occurring is given by Equation 4-1 and Equation 4-2 as:

$$2CeO_2 \quad \boldsymbol{f} \quad Ce_2O_3 + \tfrac{1}{2}O_2$$

Equation 4-1

and
$$Ce_2O_3 + 2TiO_2 \rightarrow Ce_2Ti_2O_7$$

Equation 4-2
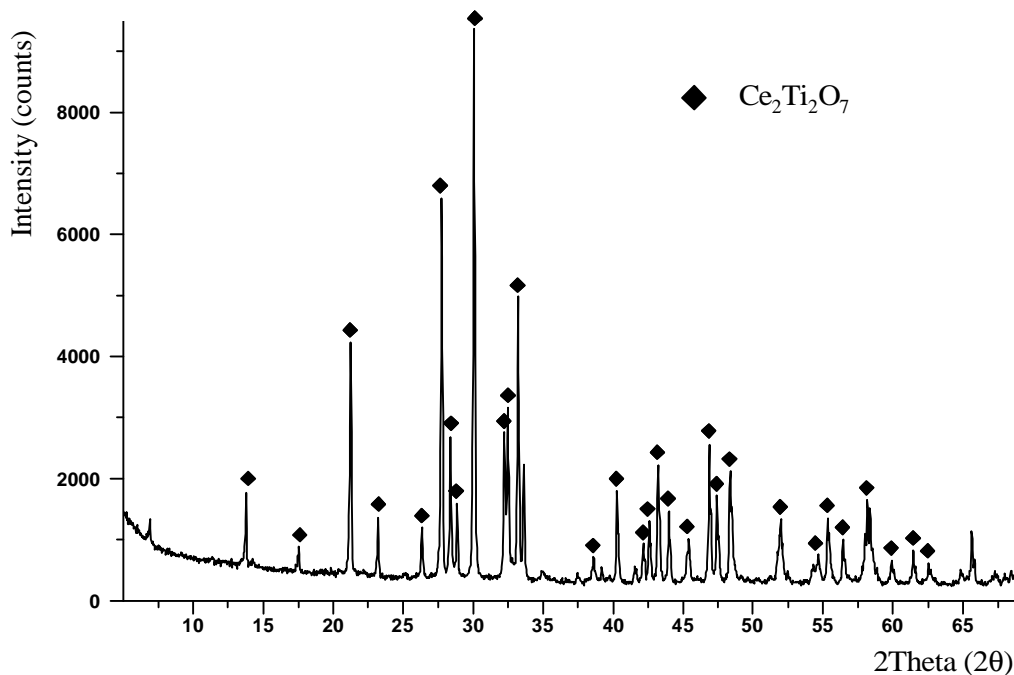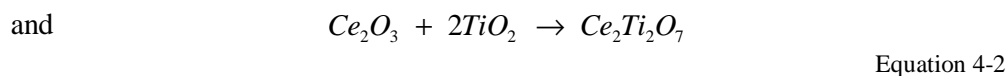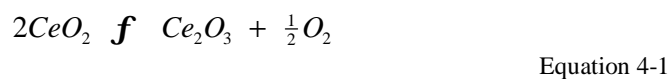
Figure 4-1 X-ray diffraction pattern of $Ce_2Ti_2O_7$ after calcination of mixed CeO_2 and TiO_2 powder in vacuum at 1350ºC for up to 10 hours

Pure single phase $Ce_2Ti_2O_7$ could not be achieved because of the relative instability of Ce^{3+} compounds compared with Ce^{4+}, as a result of which the very stable CeO_2 always remained in the products (Preuss and Gruehn, 1994). An alternative route to be explored might be to synthesise $Ce_2Ti_2O_7$ via Ce^{4+}/Ti^{3+} reaction to promote the change:

$$Ce^{4+} + Ti^{3+} \rightarrow Ce^{3+} + Ti^{4+}$$

Equation 4-3

The reaction being:

$$2CeO_2 + Ti_2O_3 \rightarrow Ce_2Ti_2O_7$$

Equation 4-4
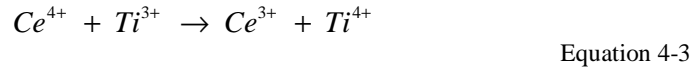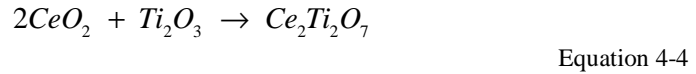
All other $Ln_2Ti_2O_7$ powders were nitrided in ammonia at 950°C for 16 hours as described in the previous work of Marchand *et al.* (1991). Repeated nitridation with intermediate regrinding was needed to expose fresh surface and achieve single phase oxynitride products. As shown in Figure 4-2 and Figure 4-3, spectra of pure $LaTiO_2N$ and $NdTiO_2N$ phases were observed after ammonolysis of $La_2Ti_2O_7$ and $Nd_2Ti_2O_7$ using the above conditions. However, even after several repeated nitridations of $Sm_2Ti_2O_7$, $Dy_2Ti_2O_7$, $Yb_2Ti_2O_7$, and $Y_2Ti_2O_7$ powders, X-ray diffraction patterns did not show any peaks of perovskite-type oxynitride products. In the case of $Sm_2Ti_2O_7$, $Dy_2Ti_2O_7$ and $Yb_2Ti_2O_7$, the ternary precursors remained with trace amounts of unreacted binary oxides.
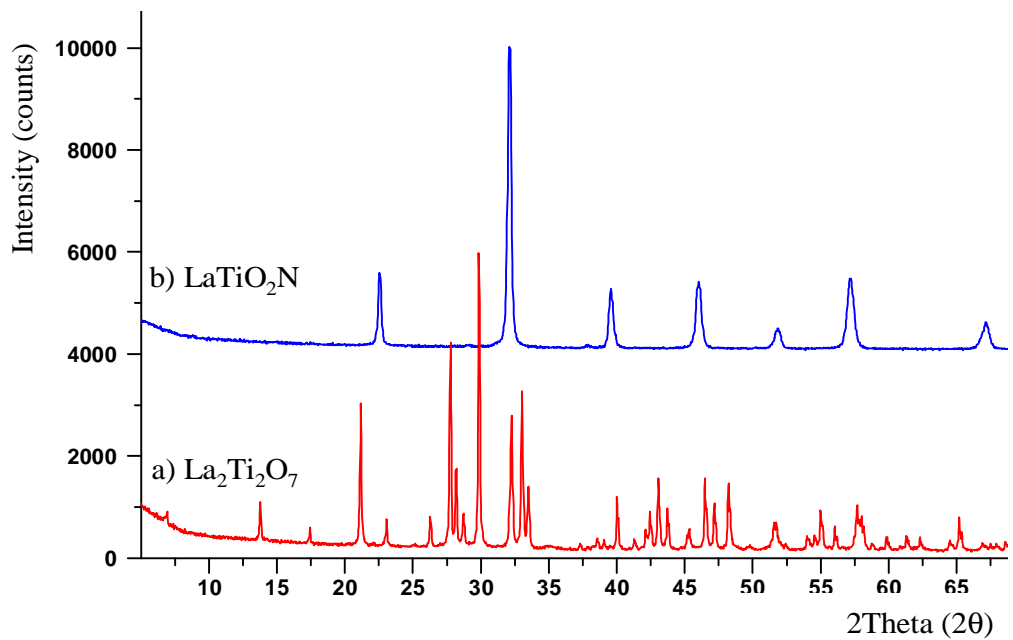
Figure 4-2 X-ray diffraction patterns of a) $La_2Ti_2O_7$ and b) $LaTiO_2N$
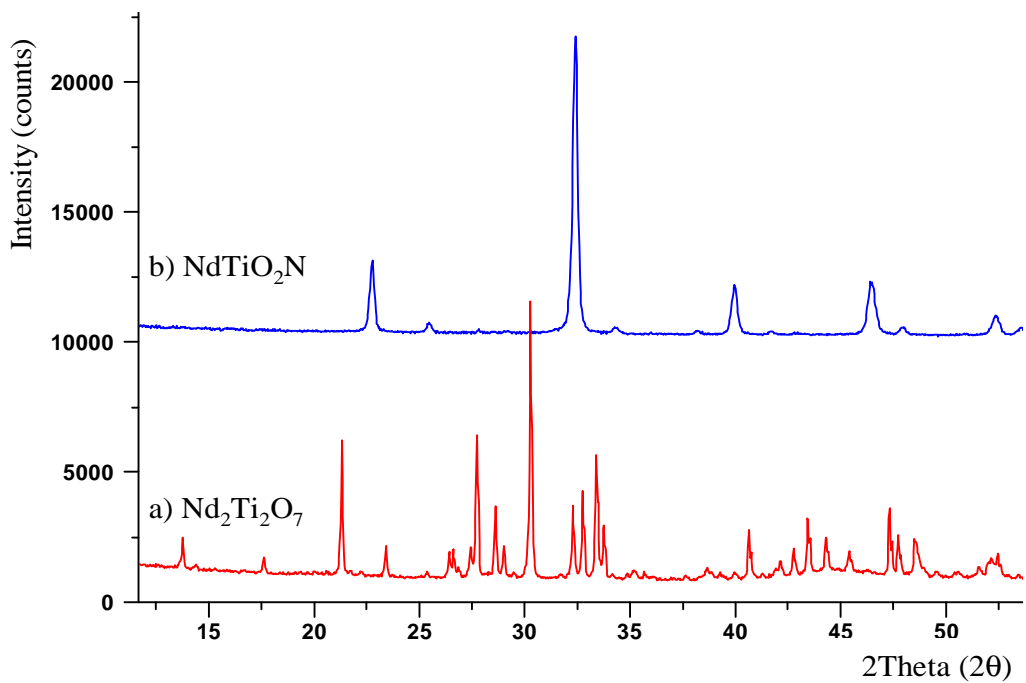
Figure 4-3 X-ray diffraction patterns of a) $Nd_2Ti_2O_7$ and b) $NdTiO_2N$

After ammonolysis, $Y_2Ti_2O_7$ partially decomposed into Y_2O_3 and TiO_2, the latter reacting with nitrogen to form TiN. When the impure $Ce_2Ti_2O_7$ powder was nitrided (at a temperature of 1350ºC up to 16 hours), it decomposed into CeO_2 and

TiO$_2$, the latter converting to TiN. As discussed above, cerium-based compounds are more thermodynamically stable in the Ce^{4+} oxidation state, so again the ammonolysis route did not lead to a CeTiO$_2$N product, even at the higher temperatures used.

In an attempt to increase the reactivity of lanthanide-based titanates in the ammonolysis reaction, carbon black powder was used as a reducing agent. Carbon generates a highly reducing atmosphere which assists the removal of oxygen atoms as either carbon monoxide or carbon dioxide. In this way, the reaction time for pure LaTiO$_2$N production was significantly reduced from 16 hours to 4 hours. Figure 4-4 shows X-ray diffraction patterns for the resulting LaTiO$_2$N when 1 wt% of carbon powder was included as the reducing additive.
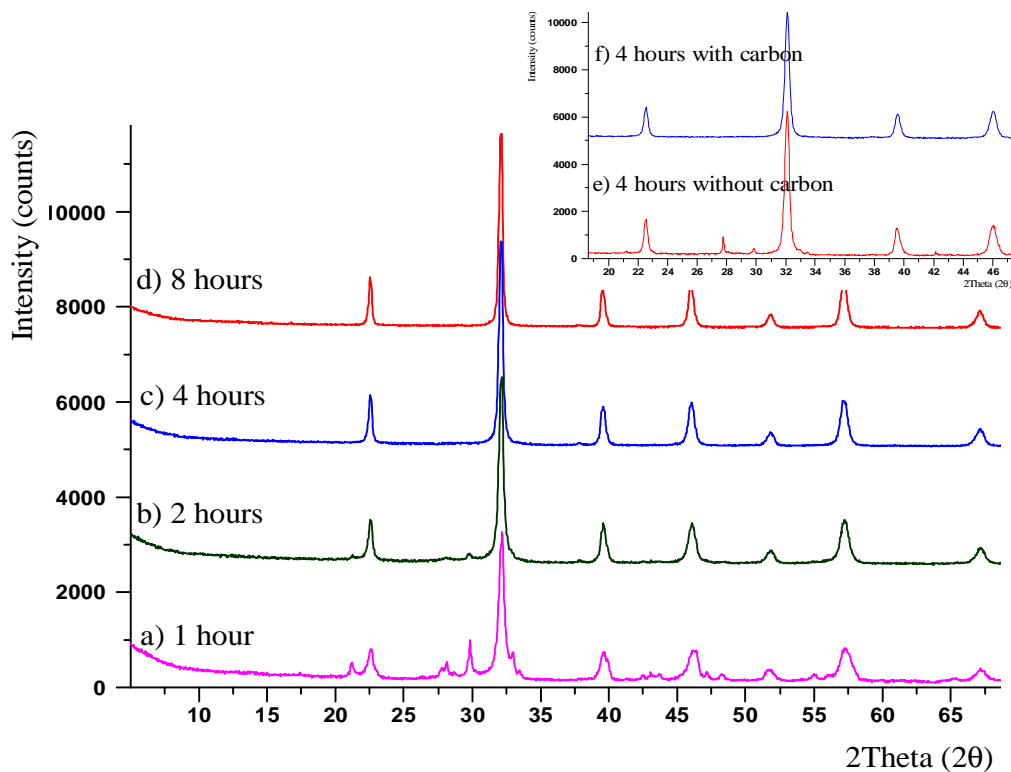
Figure 4-4 X-ray diffraction pattern of LaTiO$_2$N with 1%wt. carbon additive

In this experiment, LaTiO$_2$N peaks started to appear within the first 2 hours of nitridation and a pure single phase product could be obtained after 4 hours. The X-ray diffraction patterns shown in the inset of Figure 4-4 compare LaTiO$_2$N formation after 4 hours of nitridation with and without carbon additive. In contrast, carbon additions were not found to be beneficial for the synthesis of LnTiO$_2$N phases in other Ln systems. Seemingly, NdTiO$_2$N needed a much longer reaction time to achieve the single phase product. After nitridation of Sm$_2$Ti$_2$O$_7$ with 1 wt% of carbon black, X-ray diffraction showed no perovskite oxynitride, the pattern consisting only of Sm$_2$Ti$_2$O$_7$ plus some unreacted Sm$_2$O$_3$.

4.2.2 La$_x$Nd$_{1-x}$TiO$_2$N solid solutions

Single phase compositions of the type La$_x$Nd$_{1-x}$TiO$_2$N (x = 0, 0.2, 0.4,…1.0) were also achieved by ammonolysis of preprepared (La$_x$Nd$_{1-x}$)$_2$Ti$_2$O$_7$ samples at 950ºC for 16 hours. These oxide precursors were prepared as before by solid-state reaction between the corresponding Ln$_2$O$_3$ and TiO$_2$ powders. The colour of the resulting powder ranged from the dark greenish brown of NdTiO$_2$N through to the dark brown of LaTiO$_2$N. For Nd-rich compositions, longer reaction times were needed. After regrinding, powders were re-nitrided to achieve a single phase of each composition. This is the first time that a complete oxynitride solid solution has been reported for this system. Figure 4-5 and Figure 4-6 are X-ray diffraction patterns which confirm the existence of single-phase (La$_x$Nd$_{1-x}$)$_2$Ti$_2$O$_7$ and La$_x$Nd$_{1-x}$TiO$_2$N phases, respectively.
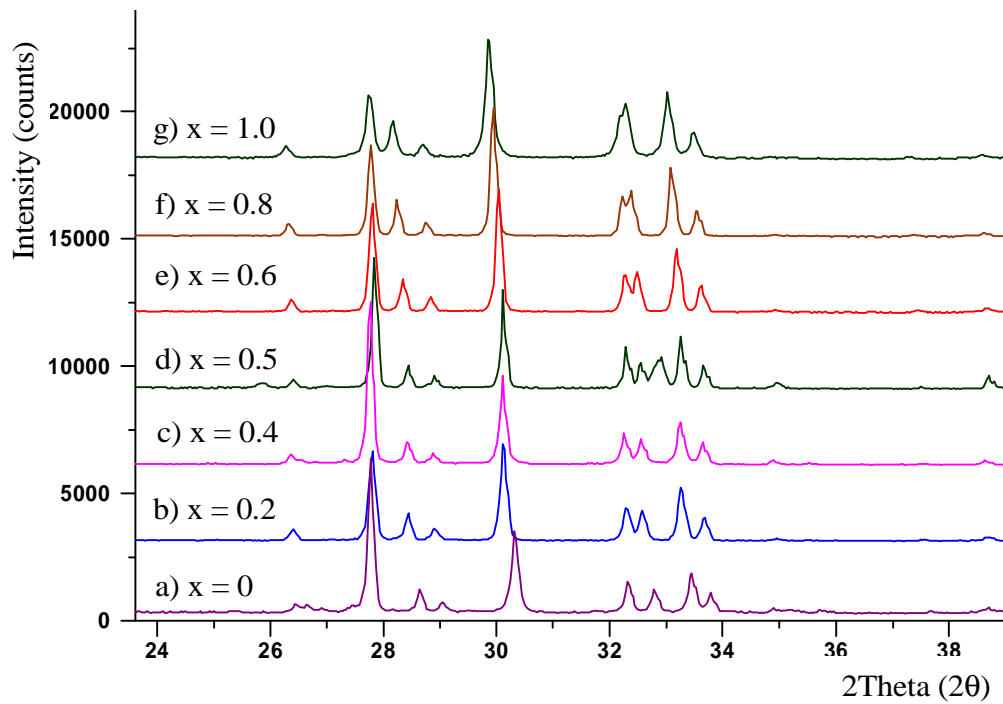
Figure 4-5 X-ray diffraction patterns of $(La_xNd_{1-x})_2Ti_2O_7$ solid solutions
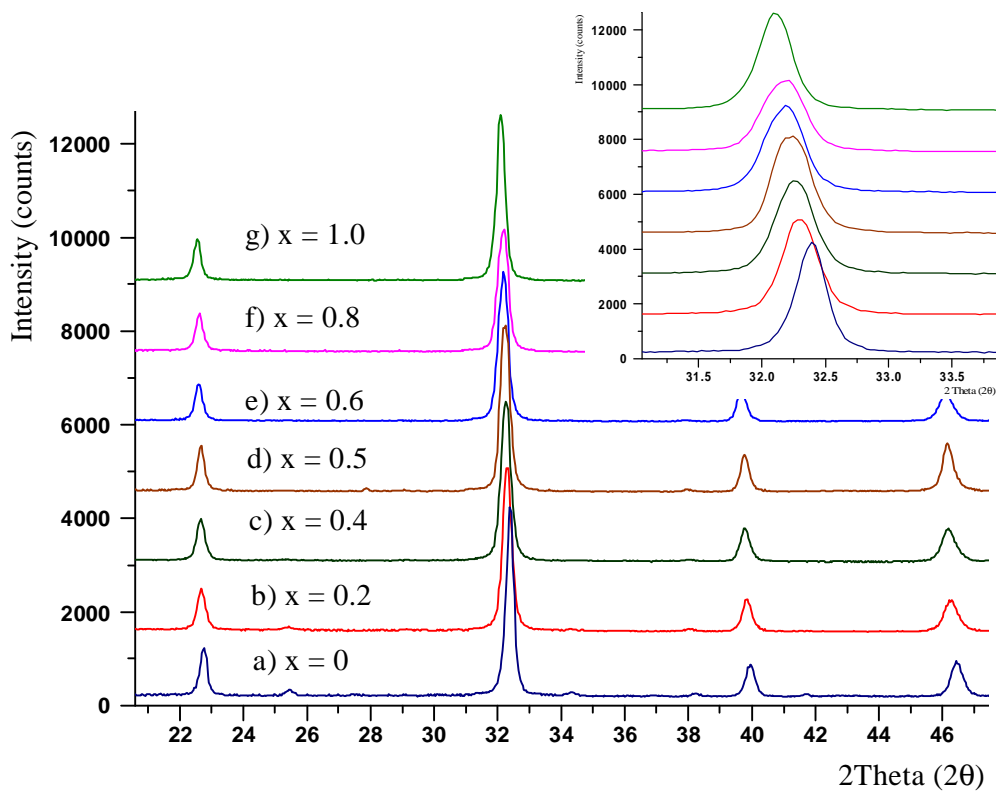
Figure 4-6 X-ray diffraction patterns of $La_xNd_{1-x}TiO_2N$ solid solutions

4.3 Synthesis of ATaO$_2$N and their solid solutions (A = Ca, Sr, Ba)

4.3.1 ATaO$_2$N (A = Ca, Sr and Ba)

As with LaTiO$_2$N and NdTiO$_2$N, Ta^{5+} based oxynitride perovskites of the type ABO$_2$N (A = Ca, Sr, Ba) were synthesised by ammonolysis of oxide precursors. The oxide precursors Ca$_2$Ta$_2$O$_7$ and Sr$_2$Ta$_2$O$_7$ were prepared by solid-solid reaction at temperatures above 1000ºC as described in Chapter 3 and X-ray diffraction showed that pure Ca$_2$Ta$_2$O$_7$ and Sr$_2$Ta$_2$O$_7$ were formed after heat treatment at 1200ºC for 16 hours followed by regrinding and pelletising at 1400ºC for a further 3 hours, as shown in Figure 4-7.
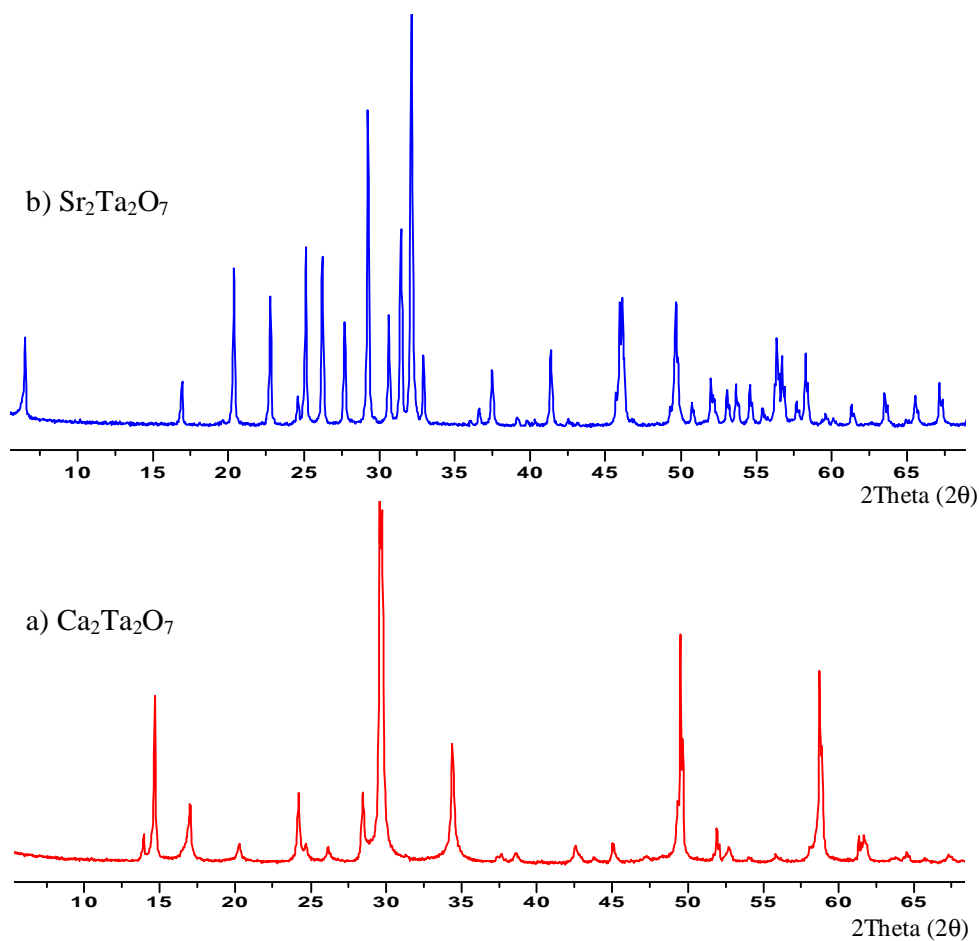
Figure 4-7 X-ray diffraction patterns of a) Ca$_2$Ta$_2$O$_7$ and b) Sr$_2$Ta$_2$O$_7$

These $Ca_2Ta_2O_7$ and $Sr_2Ta_2O_7$ powders were then nitrided in ammonia at temperatures in excess of 1000ºC for several hours as described in Chapter 3. Pure $CaTaO_2N$ and $SrTaO_2N$ were achieved at temperatures of 1150ºC within 16 hours as the X-ray diffraction patterns show in Figure 4-8.
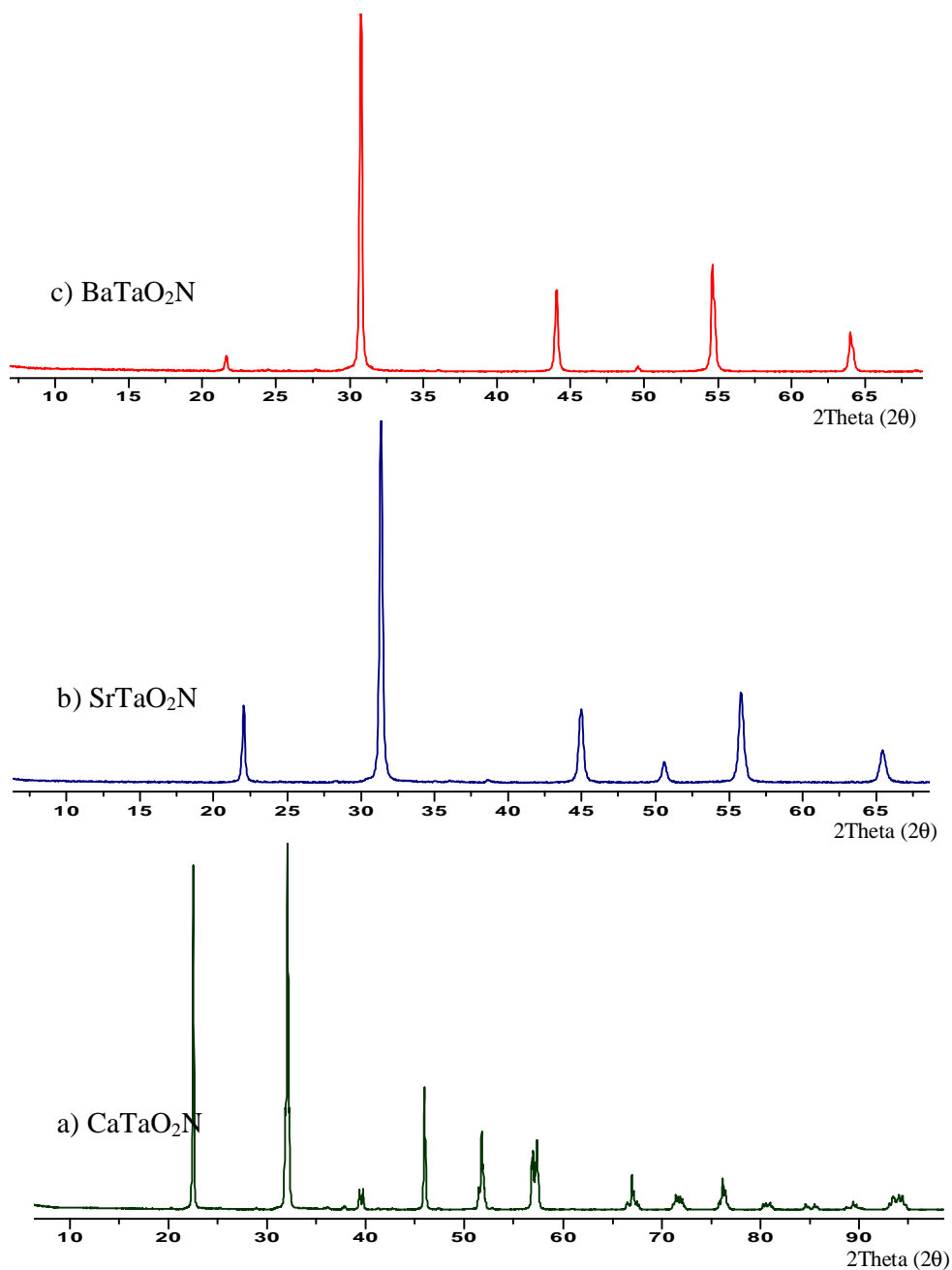
Figure 4-8 X-ray diffraction patterns of a) $CaTaO_2N$, b) $SrTaO_2N$ and c) $BaTaO_2N$

For $BaTaO_2N$, since a precursor Ba-compound of the type $A_2Ta_2O_7$ does not exist, synthesis was achieved by direct nitridation of $BaCO_3$ and Ta_2O_5 powders mixed in the appropriate ratio. The X-ray diffraction pattern (Figure 4-8) shows that pure $BaTaO_2N$ was achieved by heating in ammonia at 1100ºC for 16 hours. $SrTaO_2N$ could also be prepared by direct nitridation of $SrCO_3$ and Ta_2O_5 powders; however, this latter method could easily result in generating tantalum nitride as an impurity, and this possibility was avoided in the nitridation of $Sr_2Ta_2O_7$ route.

4.3.2   ATaO₂N solid solutions (A = Ca, Sr, Ba)

Binary solid solutions of $CaTaO_2N$, $BaTaO_2N$ and $SrTaO_2N$ with different ratios of calcium, barium and strontium were synthesised in a similar way as in the previous experiments by nitridation of the corresponding mixed oxide and/or carbonate powders at temperatures above 1000°C.

$Ca_xSr_{1-x}TaO_2N$ solid solutions with x = 0, 0.2, 0.4…, 1.0 were synthesised by nitridation of $(Ca_xSr_{1-x})_2Ta_2O_7$ powders at temperatures up to 1150°C. These mixed oxides were prepared in the same way and using the same conditions as those described above for end member $Ca_2Ta_2O_7$ and $Sr_2Ta_2O_7$ oxides. Figure 4-9 shows X-ray diffraction patterns for the full range of $(Ca_xSr_{1-x})_2Ta_2O_7$ compositions. The $(Ca_xSr_{1-x})_2Ta_2O_7$ powders were nitrided in flowing ammonia at temperatures of 1150°C for 16 hours and yielded a complete oxynitride solid solution range of the type $Ca_xSr_{1-x}TaO_2N$, for $0 \leq x \leq 1.0$, as shown in Figure 4-10. The colours of these solid solution powders ranged from yellow to green. This is

the first reported preparation of this series of compounds, and details of the crystal

structures will be given in Chapter 5.
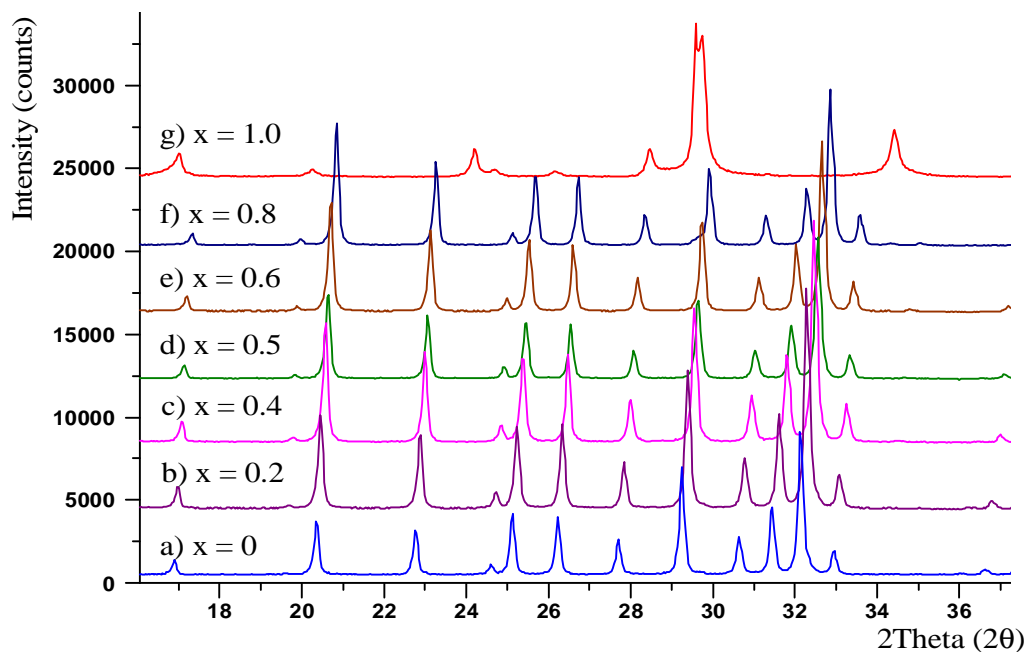
Figure 4-9 X-ray diffraction patterns of $(Ca_xSr_{1-x})_2Ta_2O_7$ (x = 0, 0.2, 0.4,…, 1.0)
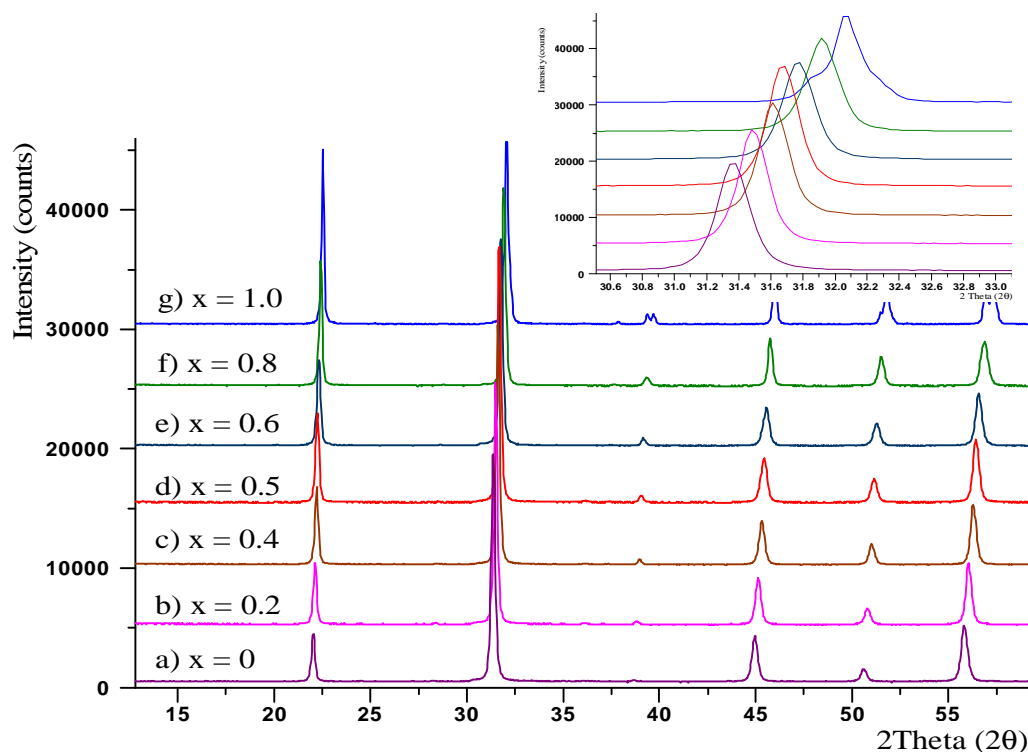
Figure 4-10 X-ray diffraction patterns of $Ca_xSr_{1-x}TaO_2N$, x= 0, 0.1, 0.2,…, 1.0

As $Ba_2Ta_2O_7$ does not exist (Rachel *et al.*, 2005), Ba oxynitride compounds were directly synthesised by nitridation of Ta_2O_5 and $BaCO_3$ mixtures, and, consistent with previous results (Pors *et al.*, 1988), $Ba_xSr_{1-x}TaO_2N$ solid solutions were obtained by reacting stoichiometric amounts of $BaCO_3$, $SrCO_3$ and Ta_2O_5 powders and directly nitriding in ammonia at a temperature of 1100°C for 16 hours. Figure 4-11 shows the X-ray diffraction peaks of the pure phase of the full ranges of $Ba_xSr_{1-x}TaO_2N$ solid solutions with $0 \leq x \leq 1.0$.
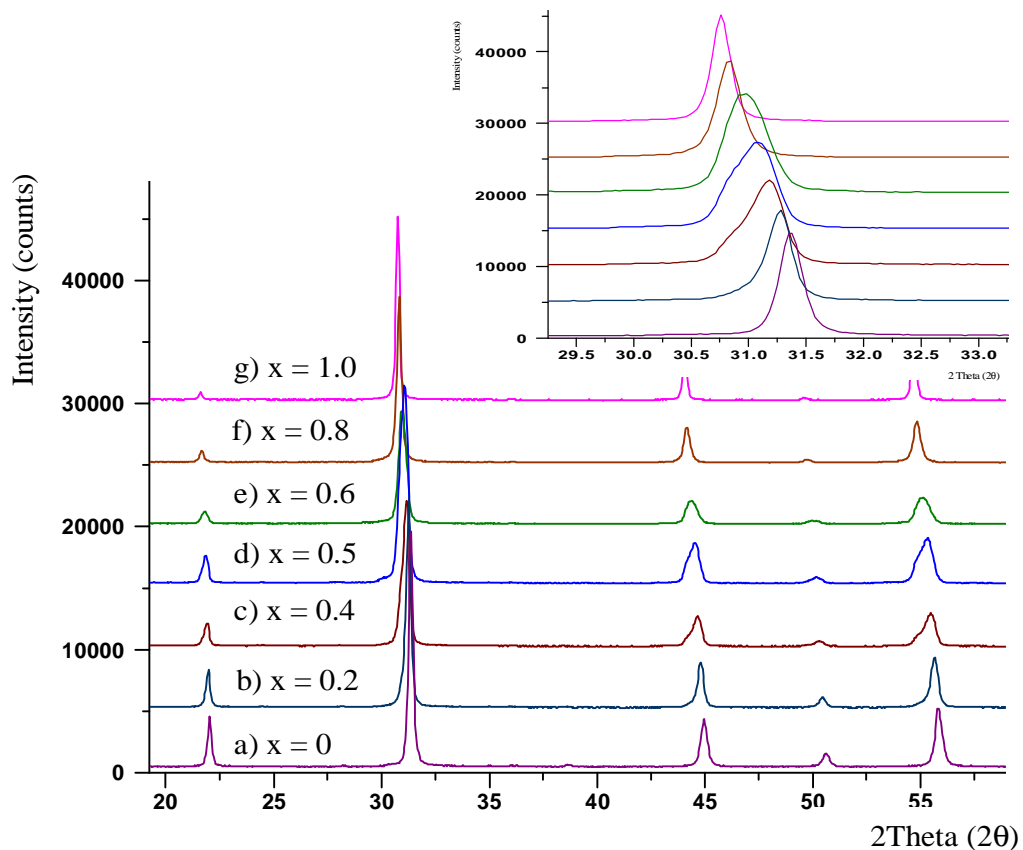
Figure 4-11 X-ray diffraction patterns of $Ba_xSr_{1-x}TaO_2N$ solid solutions

In the case of $Ca_xBa_{1-x}TaO_2N$, however, a $Ca_2Ta_2O_7$ phase needed to be preprepared and then oxide precursors of the type $(Ca_xBa_{1-x})_2Ta_2O_7$ were prepared by solid state reaction between $CaCO_3$, $BaCO_3$ and Ta_2O_5 using the same conditions as for $(Ca_xSr_{1-x})_2Ta_2O_7$ formation. X-ray diffraction patterns showed a

variety of calcium tantalates, barium tantalate and calcium barium tantalates (but not the $A_2Ta_2O_7$ form). These intermediate oxide precursors were then nitrided in flowing ammonia at 1150°C for 16 hours.
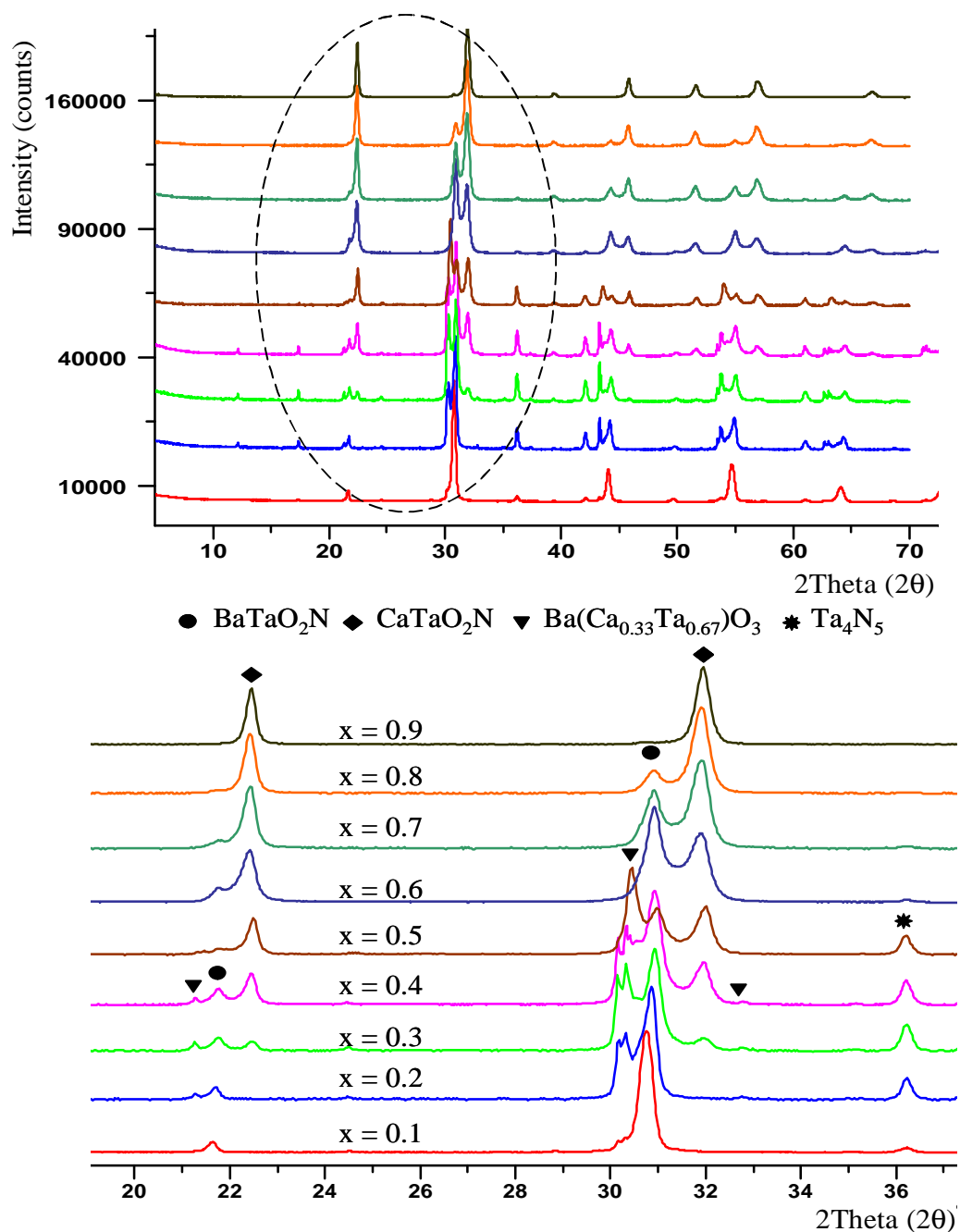
Figure 4-12 X-ray diffraction spectra of $(Ca_x Ba_{1-x})_2Ta_2O_7$ intermediate oxide precursors nitrided in ammonia at 1150ºC for 16 hours

Figure 4-12 shows X-ray diffraction spectra of the $(Ca_x\ Ba_{1-x})_2Ta_2O_7$ intermediate oxide precursors after nitriding at 1150ºC for 16 hours. The nitrided products were mixtures of $CaTaO_2N$, $BaTaO_2N$, $Ba(Ca_{0.33}Ta_{0.67})O_3$ and Ta_4N_5.

For comparison, the $Ca_{0.5}Ba_{0.5}TaO_2N$ solid solution composition was prepared by direct nitridation of stoichiometric mixtures of binary oxides and carbonates using the same nitriding conditions. X-ray diffraction showed very high intensity peaks of Ta_4N_5 plus some $Ba(Ca_{0.33}Ta_{0.67})O_3$, compared with those from the nitrided $(Ca_{0.5}Ba_{0.5})_2Ta_2O_7$ sample, as shown in Figure 4-13 d).
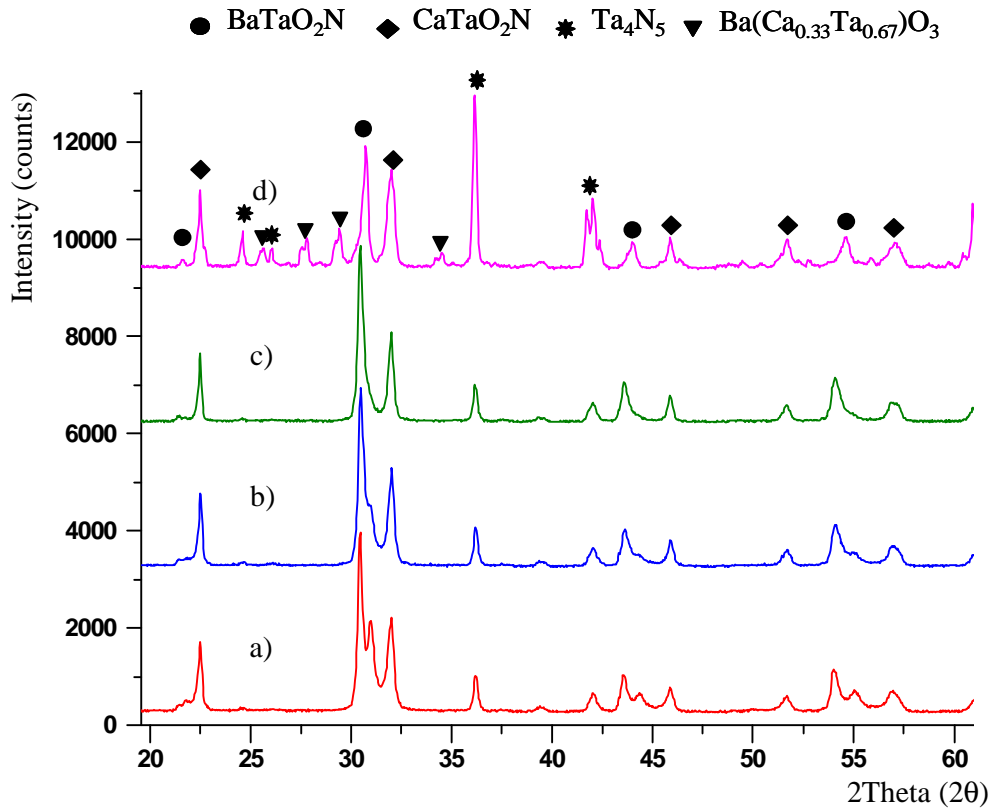
Figure 4-13 X-ray diffraction patterns of nitrided $CaBaTa_2O_7$ at 1150ºC for
a) 16 hours; b) 32 hours; c) 48 hours, and d) direct nitridation

Neither method was successful in producing pure single phase $Ca_xBa_{1-x}TaO_2N$ products even when samples were repeatedly nitrided or nitrided for longer periods of time. For example, nitridation of intermediate $CaBaTa_2O_7$ was repeatedly carried out for 16, 32 and 48 hours with regrinding but no X-ray diffraction spectra convincingly showed a solid solution of $Ca_{0.5}Ba_{0.5}TaO_2N$ had been formed. Instead, X-ray diffraction showed mixtures of $BaTaO_2N$, $CaTaO_2N$ and Ta_4N_5 plus some other barium calcium tantalates. It appears that the Ca^{2+} (r = 0.99 Å) ion is too small to be stable in the very large cationic site of Ba^{2+} (r = 1.35 Å). Attempts to produce oxynitrides in the $Ca_xBa_{1-x}TaO_2N$ system were therefore not successful by these means.

4.4 Densification

The main aim of the work described in this section was to prepare dense oxynitride samples suitable for dielectric measurement. Le Paven-Thivet *et al.* (2007) attempted to prepare dense $LaTiO_2N$ by cold-pressing the powder into pellets and thereafter pressureless sintering at 1100ºC for 10 hours in flowing ammonia; however, only 56% of theoretical density (i.e. almost no additional densification from green compacting) was obtained. This value is too low for measuring bulk dielectric properties, and highlighted a key limitation of these materials, namely that their dissociation temperatures are in general considerably below densification temperatures.

Pressureless sintering is always the most desirable densification method because it is the easiest, and this was explored in the present case by sintering either in ammonia or in vacuum. The sintering of $LaTiO_2N$, $BaTaO_2N$ and $Ba_{0.5}Sr_{0.5}TaO_2N$ powders

was carried out by green compaction and sintering in ammonia or in vacuum at temperatures in the range 1100–1250ºC for 8 hours. The samples sintered in vacuum showed no densification at all even at 1250ºC (the onset of dissociation). In an ammonia atmosphere, samples were more stable, but again no significant densification was observed. The sintered samples were powdery on the outer surface and the density was approximately only 50% of theoretical density for all samples. Pressureless sintering was clearly not a successful route for making dense samples, and therefore alternative methods were considered which involved the use of pressure in addition to temperature. Hot-Pressing (HP) was the obvious choice, and this was carried out in the Newcastle laboratory; Spark Plasma Sintering (SPS) is a newer and often very successful method, and selected samples were SPSed in the Arrhenius laboratory of the Inorganic Chemistry department in Stockholm University, in collaboration with Professor Z. Shen.

Experiments to densify $LaTiO_2N$ powder were carried out by hot-pressing at temperatures of 1200ºC and 1300ºC in graphite dies coated with boron nitride powder, with the pressure maintained at up to 70 MPa. The sample was held at this temperature and pressure for 1 hour and then cooled down to room temperature. The observed densities are given in Table 4-1. Only $\approx$ 60% of theoretical density ($\approx$ 6.3 g/cm^3) was achieved; the $LaTiO_2N$ was partially decomposed and after the relatively slow cooling down to room temperature, the products showed mainly undissociated $LaTiO_2N$, but also some La_2O_3 and TiN, as shown in Figure 4-14. Hot-pressing was also carried out at the lower temperature of 1150ºC at $\approx$ 70 MPa but small amounts of dissociation products were still observed.

Table 4-1 LaTiO$_2$N densification by hot-pressing and spark plasma sintering

No.	Densification	ρ_{exp} (g/cm^3)	% ρ_c	Comments
1	HP/1150ºC/70 MPa/1 hr	3.76	59%	All samples
2	HP/1250ºC/70 MPa/1 hr	3.93	62%	densified by both
3	SPS/1150ºC/75 MPa/5min	4.17	66%	hot-pressing (HP)
4	SPS/1100ºC/100 MPa/5min	3.99	63%	and spark plasma
5	SPS/1150ºC/100 MPa/5min	4.34	69%	sintering (SPS)
6	SPS/1200ºC/100 MPa/5min	4.94	69%	decomposed to
7	SPS/1250ºC/125 MPa/5min	4.87	78%	La$_2$O$_3$ and TiN

ρ_{exp} = experimental density, ρ_c = calculated density of LaTiO$_2$N = 6.3 g/cm^3
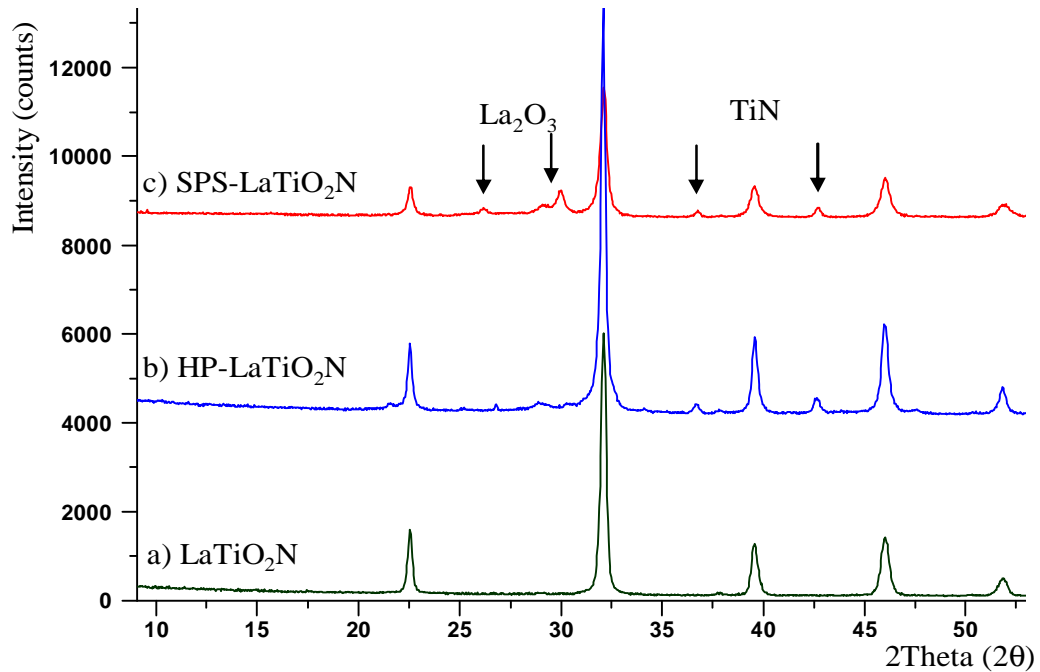
Figure 4-14 X-ray diffraction patterns of LaTiO$_2$N after hot-pressing b) and spark plasma sintering c) in comparison with the initial LaTiO$_2$N spectrum a)

The combined high temperature and fast-heating sinter process of SPS was expected to reduce the chance of lanthanum oxide and titanium nitride formation by $LaTiO_2N$ densification, but still give a final product of high density. Samples were SPSed at temperatures above 1100ºC for 5 min at pressures of up to 125 MPa. A slight vacuum drop was detected in the temperature range 950–1100ºC, which might indicate the onset of densification, but could also indicate decomposition. As shown in Figure 4-14, X-ray diffraction confirmed that some dissociation had occurred.

Attempts were also made to densify $NdTiO_2N$ by hot-pressing, in the same way as described above for $LaTiO_2N$ but at lower temperatures because previous experiments in the ammonia nitriding furnace had suggested that this compound started to dissociate at temperatures just above 1000ºC. However, when the $NdTiO_2N$ powder was hot-pressed at 1000ºC appreciable dissociation was observed, with no indication of any densification having occurred and therefore further hot-pressing (and SPS) experiments were not carried out.

$CaTaO_2N$ and $BaTaO_2N$ powders were also densified by hot-pressing and spark plasma sintering. For $CaTaO_2N$, after hot-pressing at temperatures of 1100ºC under a pressure of 70 MPa for 1 hour the samples had small cracks inside and boron nitride penetrated into the samples via the cracks so the density could not be measured. Up to 80% of theoretical density was achieved by spark plasma sintering at temperatures of up to 1250ºC and pressures of 100–125 MPa for 5–10 minutes (see Table 4-2).

Table 4-2 Densified $CaTaO_2N$ and $BaTaO_2N$

	Densification	ρ_{exp} (g/cm^3)	% ρ_c	Comments
$CaTaO_2N$	PLS/Vacuum 1150ºC/8 hr	3.90	54%	Decomposed
	PLS/Ammonia 1150ºC/8 hr	3.94	55%	Some decomposition
	SPS/1250ºC 100MPa/5 min	5.83	81%	Decomposed to Ta_3N_5 and XRD showed some unidentified peaks and structural transformation
	SPS/1200ºC 100MPa/10 min	5.51	76%	
	SPS/1200ºC 125MPa/10 min	5.58	77%	
$BaTaO_2N$	SPS/1250ºC 100MPa/5 min	6.86	79%	XRD peaks shifted compared with before SPS
	SPS/1200ºC 100MPa/10 min	6.53	75%	

PLS = Pressureless sintering, SPS = Spark plasma sintering, ρ_{exp} = experimental density, ρ_c = calculated density of $CaTaO_2N$ = 7.20 g/cm^3 (Günther *et al.*, 2000) and of $BaTaO_2N$ = 8.69 g/cm^3 (Kim *et al.*, 2004)

Although the density is rather low for reliable dielectric measurements, the mechanical strength was sufficient. It was suspected that the sintered sample pellets might have acquired some carbon contamination from the graphite die which might significantly affect the dielectric measurements and therefore the outer surface was removed before making X-ray diffraction and dielectric measurements. However, X-ray diffraction of the sintered $CaTaO_2N$ shown in Figure 4-15 indicated peaks of tantalum nitride and trace amounts of other unidentified phases present in low intensity. Additionally, it was noticed that after

densification, multiple peaks of orthorhombic-CaTaO$_2$N slightly merged into single peaks. This suggested that some dissociation had taken place.
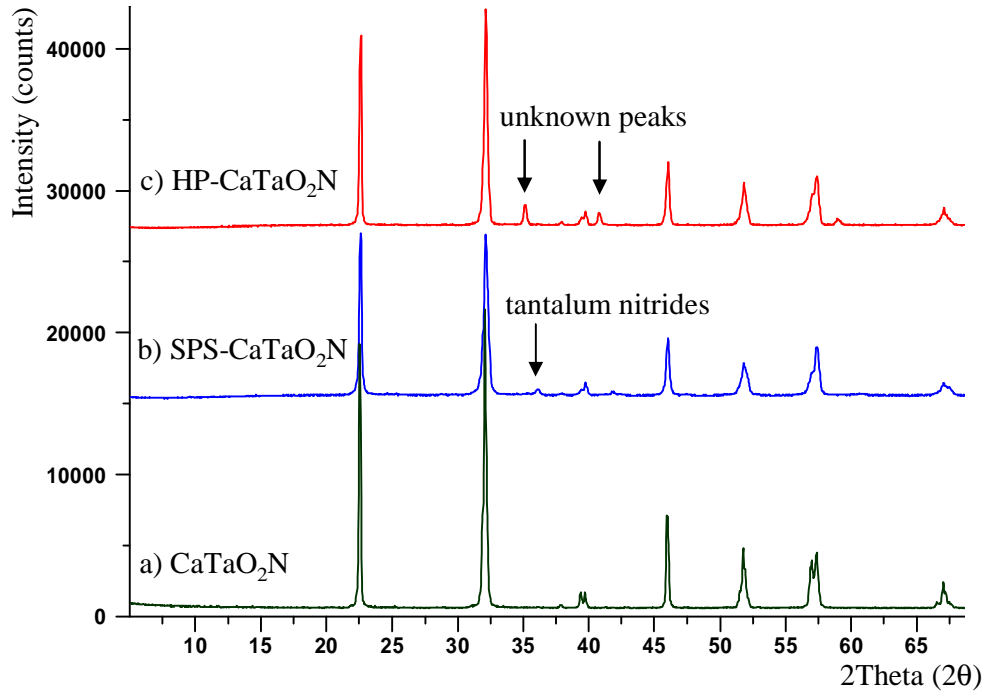
Figure 4-15 X-ray diffraction pattern of CaTaO$_2$N by hot-pressing (HP) and spark plasma sintering (SPS)

The initial CaTaO$_2$N is yellow in colour but after hot-pressing and spark plasma sintering it changed to dark green. The outer surface of SPSed samples was polished off deeper than for normal X-ray diffraction sample preparation and Figure 4-16 shows the resulting spectrum, compared with those of the starting and SPSed samples. Clearly the SPSed CaTaO$_2$N peaks have shifted away from the initial ones and after polishing off the surface, the X-ray diffraction spectrum is closer to that of the sample before SPS.
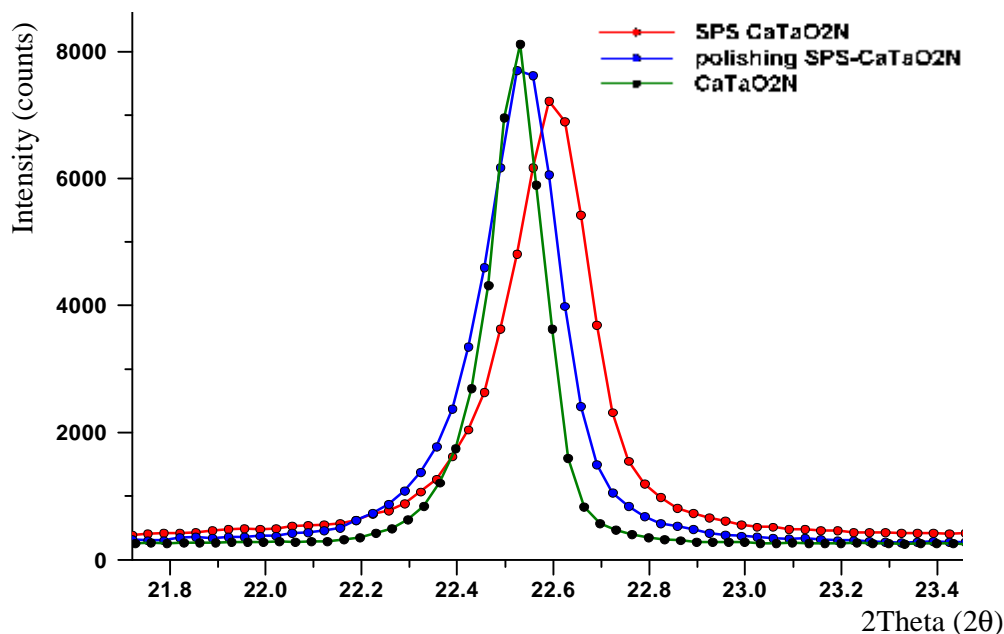
Figure 4-16 X-ray diffraction spectrum of CaTaO$_2$N after SPS and polishing off the surface in comparison with the starting CaTaO$_2$N

The densities of SPSed BaTaO$_2$N samples were approximately 80% of theoretical, as summarised in Table 4-2. Figure 4-17 shows X-ray diffraction patterns of the resulting samples. Very low intensity peaks of TaO were observed (this may not be clear from the X-ray diffraction image due to the low magnification) and the main BaTaO$_2$N peaks were also obviously shifted to smaller d-spacings. The HPed and SPSed BaTaO$_2$N samples were darker in colour compared with those before densification. The SPSed samples were polished to remove the outer surface, which was believed to have been contaminated from the densification environment. As shown in Figure 4-17 inset, after polishing off the outer surface, the BaTaO$_2$N spectrum shifted to give peaks very close in position to those before SPS. The darker colour plus the shifted X-ray diffraction peaks to smaller d-spacings is convincing evidence for the appearance of mixed-valency tantalum ions (Ta^{4+} and Ta^{5+}).
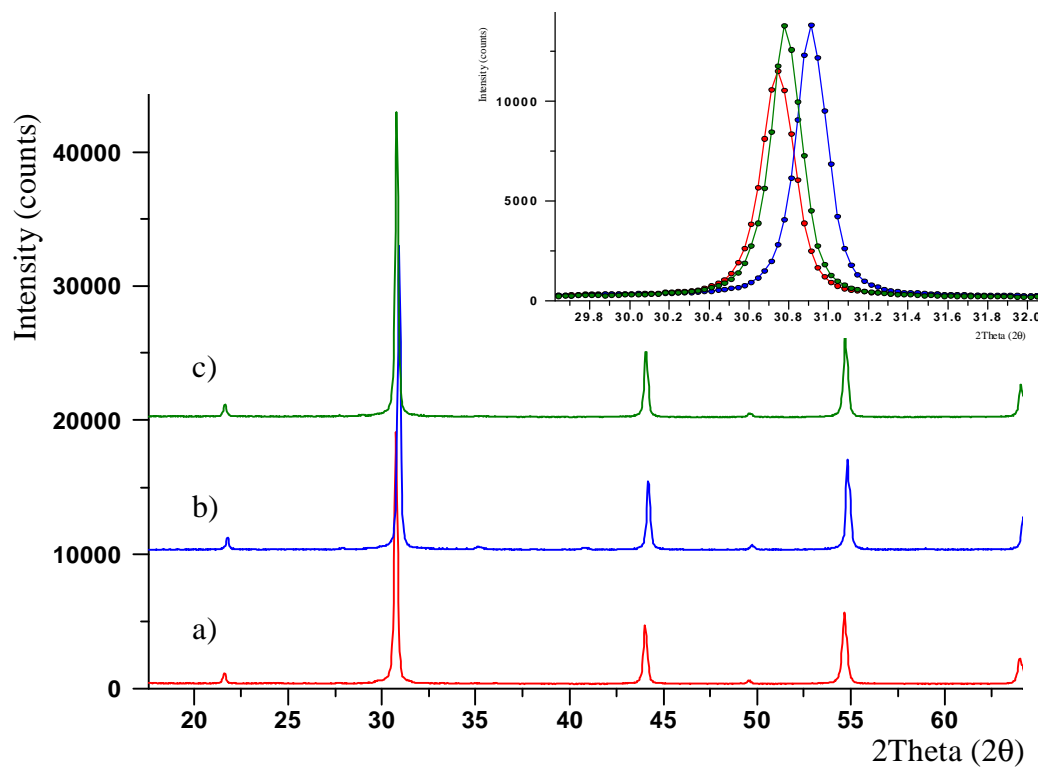
Figure 4-17 X-ray diffraction spectrum of BaTaO$_2$N after spark plasma sintering b) and the polished off outer surface of SPSed BaTaO$_2$N c) in comparison with the initial BaTaO$_2$N spectrum a)
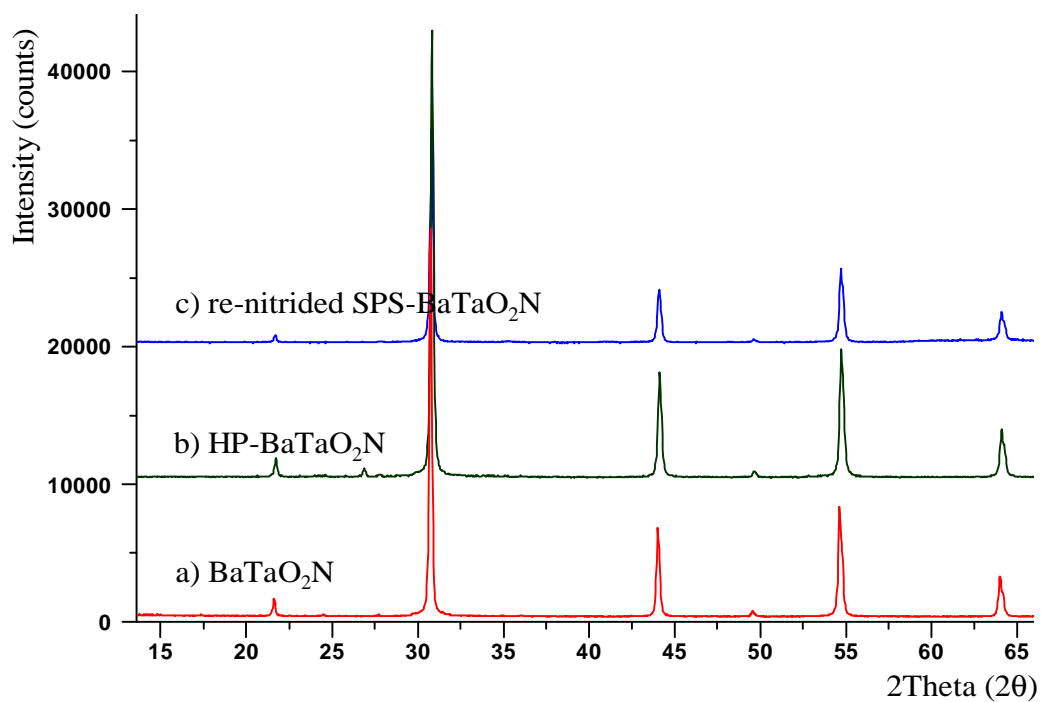
Figure 4-18 X-ray diffraction pattern of BaTaO$_2$N a) after hot-pressing b) and re-nitrided SPSed sample c)

The TaO lines disappeared after re-nitriding and the $BaTaO_2N$ peaks also shifted back very closely to their positions before SPS, as shown in Figure 4-18. These samples were also densified by hot-pressing but the hot-pressed samples showed a tendency to crumble and clearly did not have enough mechanical strength to use for dielectric measurements.

Because of the limitations of time, it was not possible to pursue these densification studies further in order to prepare a wider range of oxynitride samples of high density. However, it was felt that the HP-sintered $LaTiO_2N$, SPS-sintered $CaTaO_2N$ and $BaTaO_2N$ samples were of adequate purity and had enough mechanical strength to be used for making dielectric measurements. This work was carried out in the School of Materials in Manchester University, in collaboration with Professor R. Freer and Dr. F. Azough.

4.5 Dielectric measurements

Dielectric measurements were made using a Hewlett Packard (4284 A) LCR bridge at room temperature with frequencies ranging from 100 Hz to 1 MHz. Capacitance and dielectric loss were measured for each sample and the dielectric constant calculated. For comparison, the dielectric constant of a 90% dense $La_2Ti_2O_7$ sample was measured, as shown in Figure 4-19. These results are in good agreement with the literature (Paul and Robert, 1991)—the measured value being approximately 49—frequency independent, and showing dielectric loss values below 0.01.

Figure 4-19 Dielectric measurement of 90% dense $La_2Ti_2O_7$ ceramic

Takahashi *et al.* (1993) produced the same sample by coprecipitation and the dielectric constant of this oxide at 95–97% of theoretical density was 47 while Shao *et al.* (2010) prepared this oxide sample by sol-gel and the dielectric constant of a bulk sample with a density in the range of 86–95% of theoretical was approximately 12 at frequency of 1 MHz, clearly much lower than values obtained by other researchers. The true value for fully dense materials may be not easy to measure but it is possible to calculate this assuming the sample to be a two-phase of dielectric material and porosity (see Section 4.6).

However, the hot-pressed $LaTiO_2N$ sample showed metallic conductivity, rather than dielectric behaviour. This is probably due to the conductive behaviour of TiN which appeared in the sample in trace amounts after hot-pressing. The X-ray diffraction spectrum of the hot-pressed sample showed very low intensity of TiN

peaks, as shown in Figure 4-20. Even though the actual percentage of TiN must have been very small, it is believed that it may well have been present as a dispersion of very small grains in the grain boundaries, forming a more or less continuous electrical path through the specimen. Clearly there still remains a challenge to produce pure, fully dense LaTiO$_2$N samples suitable for dielectric measurement.
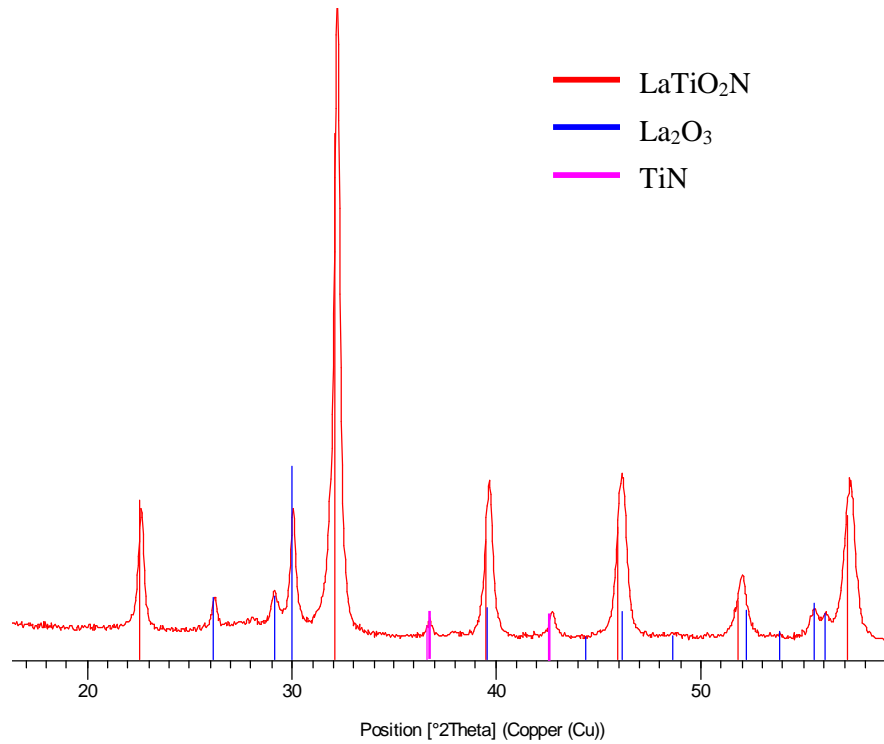
Figure 4-20 X-ray diffraction spectrum of LaTiO$_2$N hot-pressed
at 1150ºC and 70 MPa for 1 hour

The dielectric constants of both the SPSed-BaTaO$_2$N and -CaTaO$_2$N samples come out very high—35000 and 4000 at 100 Hz respectively, but the dielectric losses were also very high (1 and 0.8 for BaTaO$_2$N and CaTaO$_2$N respectively) even at the high frequency of 1 MHz. The loss values are clearly too large for practical applications, and indicate that even though X-ray diffraction showed more or less 100% phase purity, the sample either still contained some residual

conducting phase in trace amounts, or the reducing atmosphere of the SPS system had in some other way affected the sample (e.g. by causing some Ta in the 5+ state to be reduced to 4+ or 3+). Before SPS, the $CaTaO_2N$ sample was bright yellow and $BaTaO_2N$ reddish brown but after SPS both were obviously darkened to dark green and dark brown, respectively. A darkened colour has often been observed for oxynitrides formed by ammonolysis at high temperatures, and for example, thermally ammonolysed rare earth tantalum oxide ($RTaO_4$; R = Dy, Er, Yb and Y) previously reported that as being due to mixed-valent Ta (Maillard *et al.* 2005 cited in Motohashi *et al.*, 2009). In the present case, the oxynitride powders were spark plasma sintered in a graphite die to minimise nitrogen loss but apparently, under these conditions, Ta^{5+} ions have been partially reduced to Ta^{4+} or Ta^{3+} in the sintered samples causing the high loss. From the dielectric loss equation, $\tan d = \dfrac{e'}{e''} = \dfrac{1}{wRC}$ (ω= angular frequency, R= resistance and C= capacitance), a low dielectric loss can be obtained only when a solid possesses both high resistance and high capacitance. Therefore, any low resistance phase can result in a high value of dielectric loss. The loss data reported by Kim *et al.* (2004) for their $BaTaO_2N$ sample was much lower than in the present case, but only corresponded to that for compacted powder, whereas the present samples had been heated to high temperatures in a carbon atmosphere, which is much more likely to promote chemical changes which can lead to the high losses observed.

4.6 Effect of porosity on dielectric measurements

Due to the difficulties of oxynitride densification, mathematical models can be used to calculate bulk dielectric properties using measurement made on porous samples. Several mathematical models based on mixing rules have been proposed, assuming a two-phase composite system of dielectric phase and porosity (Penn *et al.*, 1997). Capacitance measurements conducted on the porous sample allow the effective dielectric constant e_{eff} and hence the bulk dielectric constant e_m to be calculated from Equation 4-5, i.e.:

$$e_{eff} = e_m \left(1 - \frac{3P(e_m - 1)}{2e_m + 1} \right)$$

Equation 4-5

where *P* is the fractional porosity.

When Equation 4-5 is applied to the sample of bulk $La_2Ti_2O_7$ (90% of theoretical density) discussed earlier, for which the measured dielectric constant was 49, the value for fully dense $La_2Ti_2O_7$ came out to be 57.

In addition, the dielectric loss can also be calculated by theoretical models based on mixing rules. In principle, dielectric loss is directly proportional to the porosity but in reality the dielectric loss of the fully dense material is not zero (Penn *et al.*, 1997) and the porosity contributes an additional term to the loss. The dielectric loss of porous samples is measured in term of the effective tan δ and the dielectric loss of the fully dense material, tan δ_0 is calculated by Equation 4-6 (Penn *et al.*, 1997):

$$\tan d = (1 - P) \tan d_0 + A'P \left(\frac{P}{1 - P} \right)^{2/3}$$

<div align="right">Equation 4-6</div>

where P is fractional porosity and A' is a constant for the material.

Nevertheless, the calculations of dielectric constant and dielectric loss from mathematical models give only guidelines for dielectric properties. In fact, several other parameters, e.g. random grain orientation, and grain boundaries, can have an effect on bulk dielectric properties.

4.7 Discussion and conclusions

Perovskite-type $LnTiO_2N$ oxynitrides (Ln = La and Nd), $ATaO_2N$ (A = Ca, Sr and Ba) and their solid solutions were successfully produced by solid state reaction of the corresponding oxide precursors under hot ammonia flow consistent with previous work (Marchand *et al.*, 1986a, Marchand *et al.*, 1991, Kim *et al.*, 2004). For the lanthanide series of compositions, only the La and Nd endmembers could be prepared; alternative methods may be needed to prepare the remaining members of the series. The present work is the first recorded observation of $La_xNd_{1-x}TiO_2N$ and $Ca_xSr_{1-x}TaO_2N$ solid solutions, with the range extending across the entire system. Whereas Pors *et al.* (1988) reported the existence of $Ba_{1-x}Sr_xTaO_2N$ phases corresponding to $0 < x < 0.44$, in the present work the full $0 < x < 1$ range of $Ba_xSr_{1-x}TaO_2N$ compositions was prepared. In the work of Pors *et al.* (1988), mixed powders were nitrided in flowing ammonia at a temperature of 950°C for 15 hours while in the present studies, samples were heated in ammonia flow at both 950°C and higher temperatures. A full range of

$Ba_xSr_{1-x}TaO_2N$ solid solutions has also been demonstrated in the $BaTaO_2N$-$SrTaO_2N$ system, significantly assisted by the use of higher reaction temperatures, which were needed to achieve the required higher reactivity. Attempts were also made to synthesise $Ca_xBa_{1-x}TaO_2N$ solid solutions but no evidence was found for their existence. After repeated nitridation, X-ray diffraction showed patterns corresponding to the Ba- and Ca- rich end members along with some additional unidentified phases.

In order to make dielectric measurements on bulk material, attempts were made to densify powdered samples of the oxynitrides described above by pressureless sintering in vacuum and in ammonia, in addition to the techniques of hot-pressing and spark plasma sintering. Although the samples were more stable in ammonia than in vacuum, in neither case was any densification achieved by pressureless sintering; final densities $\approx$ 50% of theoretical were far too low to be used for making any reliable dielectric measurements. $LaTiO_2N$ powder was densified by hot-pressing (to approximately 65% of theoretical) and the sample retained good mechanical integrity. However, dielectric measurements on this sample showed it to be conducting, and careful X-ray diffraction measurements showed that this was most likely due to a fine dispersion of TiN particles in the grain boundaries. Similar attempts made to densify $NdTiO_2N$ by hot-pressing were unsuccessful, and even at lower temperatures (1000ºC) dissociation of $NdTiO_2N$ into other phases occurred.

The alternative technique of Spark Plasma Sintering was also used for densification and dense samples of $LaTiO_2N$, $CaTaO_2N$ and $BaTaO_2N$ of approximately 80% of theoretical density were produced in this way. However, some dissociation of the $LaTiO_2N$ occurred. A significant amount of conductive TiN was present and the dielectric measurements of SPSed $LaTiO_2N$ had to be discarded. For the $CaTaO_2N$ and $BaTaO_2N$ samples, dielectric constants in the range of ten thousands were measured for these samples, linked also to very high dielectric loss. Again, these results are believed to be due to the presence of conducting phases—either a fine dispersion of nitride particles in the grain boundaries, or some reduction of the primary phase (e.g. via Ta^{5+} to Ta^{4+} or Ta^{3+}), with possible simultaneous loss of oxygen. Neither hot-pressing nor spark plasma sintering proved satisfactory techniques to give fully dense, single-phase products of the right composition. Kim *et al.* (2004) measured dielectric properties on $\approx 50\%$ dense bulk $CaTaO_2N$, $SrTaO_2N$ and $BaTaO_2N$ prepared by cold isostatic pressing of the oxynitride powders. The dielectric constant measured for $CaTaO_2N$ was low ($k \approx 30$, typical of many oxide perovskites) whilst $SrTaO_2N$ and $BaTaO_2N$ gave very high dielectric constants of about 4900 and 2900, respectively. However, the dielectric loss was still several orders higher than the desired level for practical applications. This may well have been due to chemical changes at the surface of the powder grains, leading to enhanced conductivity. In principle, in order to achieve fully dense materials, high temperature and high pressure are compulsory; however oxynitride compounds are relatively sensitive to oxidation at temperatures even at low temperatures. Aguiar *et al.* (2008) studied the oxidation of $LaTiO_2N$, $SrNbO_2N$ and $SrTaO_2N$ in different

atmospheres, and found that oxidation started at approximately 400ºC in air with the oxidation rate significantly increasing with oxygen content in the densification atmosphere and also with temperature. During all processing steps, protecting the samples from oxygen attack is therefore critically significant. Since the temperatures needed for densification would appear from the present study to be at least ≈ 1000ºC, protection against oxidation is especially important during sintering. Since the present results have shown that densification routes may also involve contact with carbon (which can also create difficulties due to possible reduction), defining the exact conditions for successful densification of these materials remains a demanding challenge. Mathematically, the dielectric constant and the loss of low density materials can be calculated by equations based on a two-phase system—phase one is the material and the other is porosity.

Because of the difficulties of achieving dense samples, as an alternative method, oxynitride dielectrics have also been studied as thin films. An added advantage of this route is that non-stoichiometric compounds can be produced, and these often display more interesting properties than their more stoichiometric counterparts. A good example of this is provided by the $LaTiO_xN_y$ system. In a series of experiments, thin layers of $LaTiO_2N$ were deposited on $SrTiO_3$ substrates by reactive radio frequency (10 kHz) magnetron sputtering with varying nitrogen: argon ratio in plasma (Ziani *et al.*, 2008). These films exhibited high dielectric constant ranging from 290 to 1220 with very high tan δ at room temperature. It was found that the dielectric constant and band gap energy decreased with increasing $\%N_2$ in the plasma (and hence increasing N content in the films). The high dielectric loss in this case may be caused by the highly reducing atmosphere

during ammonolysis resulting in Ti^{4+} being reduced to conductive Ti^{3+} ions, as happened in the present study. However, compared with equivalent oxides, e.g. metallic $LaTiO_3$ and lower-dielectric constant $La_2Ti_2O_7$ (k ≈ 40–60) (Paul and Robert, 1991), it would appear that nitrogen incorporation significantly improved the dielectric properties. In the present study, techniques were not available to produce thin films in the way described by the above authors, but alternative routes involving deposition of thin surface layers on dense oxide samples were employed (see Chapter 6). As a completely different method, particulate dielectric constants were measured on powder dispersed in slurry form, and the results are presented in Chapter 7.

4.8 References

Aguiar, R., Logvinovich, D., Weidenkaff, A., Reller, A. and Ebbinghaus, S. G. (2008) Thermal oxidation of oxynitride perovskites in different atmospheres. *Thermochimica Acta,* 471**,** 55-60.

Clarke, S. J., Guinot, B. P., Michie, C. W., Calmont, M. J. C. and Rosseinsky, M. J. (2002) Oxynitride perovskites: Synthesis and structures of $LaZrO_2N$, $NdTiO_2N$ and $LaTiO_2N$ and comparison with oxide perovskites. *Chem. Mater.,* 14**,** 288-294.

Gouin, X., Marchand, R., Laurent, Y. and Gervais, F. (1995) Infrared dielectric response of $BaTaO_2N$. *Solid State Communications,* 93**,** 857-859.

Günther, E., Hagenmayer, R. and Jansen, M. (2000) strukturuntersuchungen an den Oxidnitriden $SrTaO_2N$, $CaTaO_2N$ und $LaTaON_2$ mittels Neutronen- und Röntgenbeugung. *Z. Anorg. Allg. Chem. ,* 626**,** 1519-1525.

Kim, Y.-I., Woodward, P. M., Baba-Kishi, K. Z. and Tai, C. W. (2004) Characterization of the structural, optical, and dielectric properties of oxynitride perovskites AMO_2N (A = Ba, Sr, Ca; M = Ta, Nb). *Chemistry of Materials,* 16**,** 1267-1276.

Le Paven-Thivet, C., Le Gendre, L., Le Castrec, J., Cheviré, F., Tessier, F. and Pinel, J. (2007) Oxynitride perovskite $LaTiO_xN_y$ thin films deposited by reactive sputtering. *Progress in Solid State Chemistry,* 35**,** 299-308.

Marchand, R., Pors, F. and Laurent, Y. (1986a) Préparation et caractérisation de nouveaux oxynitrures à structure perovskite. *Rev. Int. Hautes Tempér. Réfract. Fr.,* 23**,** 11-15.

Marchand, R., Pors, F., Laurent, Y., Regreny, O., Lostec, J. and Haussonne, J. M. (1986b) Perovskites oxynitrures utilises en tant que materiaux dielectriques. *Journal de Physique (Paris), Colloque* 47**,** 901-905.

Marchand, R., Pors, F. and Y.Laurent (1991) Nouvelles perovskites oxynitrures de stoechiometrie ABO_2N (A = lanthanide, B = Ti) et $ABON_2$ (A = lanthanide, B = Ta ou Nb) *Annales des Chimie, France,* 16**,** 553-560.

Motohashi, T., Hamade, Y., Masubuchi, Y., Takeda, T., Murai, K. i., Yoshiasa, A. and Kikkawa, S. (2009) Structural phase transition in the perovskite-type tantalum oxynitrides, $Ca_{1-x}Eu_xTa(O,N)_3$. *Materials Research Bulletin,* 44**,** 1899-1905.

Paul, A. F. and Robert, E. N. (1991) $La_2Ti_2O_7$ Ceramics. *Journal of the American Ceramic Society,* 74**,** 2876-2881.

Penn, S. J., Alford, N. M., Templeton, A., Wang, X., Xu, M., Reece, M. and Schrapel, K. (1997) Effect of porosity and grain size on the microwave dielectric properties of sintered alumina. *Journal of the American Ceramic Society,* 80**,** 1885-1888.

Pors, F., Bacher, P., Marchand, R., Laurent, Y. and Roult, G. (1988) Etude structurale par diffraction neutronique de la pérovskite oxyazotée $SrTaO_2N$ et de la solution solide $Ba_{1-x}Sr_xTaO_2N$ *Rev. Int. Hautes Tempér. Réfract. Fr.,* 24**,** 239-246.

Preuss, A. and Gruehn, R. (1994) Preparation and Structure of Cerium Titanates Ce_2TiO_5, $Ce_2Ti_2O_7$, and $Ce_4Ti_9O_{24}$. *Journal of Solid State Chemistry,* 110**,** 363-369.

Rachel, A., Ebbinghaus, S. G., Güngerich, M., Klar, P. J., Hanss, J., Weidenkaff, A. and Reller, A. (2005) Tantalum and niobium perovskite oxynitrides: Synthesis and analysis of the thermal behaviour. *Thermochimica Acta,* 438**,** 134-143.

Shao, Z., Saitzek, S., Roussel, P., Mentré, O., Prihor Gheorghiu, F., Mitoseriu, L. and Desfeux, R. (2010) Structural and dielectric/ferroelectric properties of $(La_{1-x}Nd_x)_2Ti_2O_7$ synthesized by sol-gel route. *Journal of Solid State Chemistry,* 183**,** 1652-1662.

Takahashi, J., Kageyama, K. and Kodaira, K. (1993) Microwave dielectric properties of lanthanide titanate ceramics. *Japanese Journal of Applied Physics, Part 1: Regular Papers and Short Notes and Review Papers,* 32**,** 4327-4331.

Ziani, A., Le Paven-Thivet, C., Le Gendre, L., Fasquelle, D., Carru, J. C., Tessier, F. and Pinel, J. (2008) Structural and dielectric properties of oxynitride perovskite LaTiO$_x$N$_y$ thin films. *Thin Solid Films,* 517**,** 544-549.

Chapter 5 Structural characterisation of $La_xNd_{1-x}TiO_2N$, and $A_xSr_{1-x}TaO_2N$ (A= Ca and Ba) solid solutions

5.1 Introduction

Previous work on the oxynitrides $BaTaO_2N$, $SrTaO_2N$, $CaTaO_2N$, $LaTiO_2N$ and $NdTiO_2N$ was summarised in Chapter 2, and information on their preparation has been given in Chapter 4. The current chapter looks into their structural characterization, and especially examines changes observed when going along solid solutions between the above end-members.

From powder X-ray diffraction studies, Marchand *et al.* (1986, 1991) considered $LaTiO_2N$ to have a simple cubic perovskite cell ($a_{cub} \approx 4$ Å) whereas $NdTiO_2N$ was clearly non-cubic and these authors reported it as having an orthorhombic ($GdFeO_3$-type) superlattice of the simple cubic cell, with a_{ortho} and $c_{ortho} \approx a_{cub} \sqrt{2}$ and $b_{ortho} \approx 2a_{cub}$ (Marchand *et al.*, 1991). From neutron diffraction studies, Clarke *et al.* (2002) confirmed the orthorhombic structure of $NdTiO_2N$ (space group *Pnma* with a = 5.52901, b = 7.8017, c = 5.5492 Å) but in the case of $LaTiO_2N$, these authors and also Logvinovich *et al.* (2009) believed it to be triclinic (space group $P\bar{1}(I\bar{1})$). More recently however, Yashima *et al.* (2010) prepared $LaTiO_2N$ by a NaCl flux method to obtain a high-purity, highly crystalline product, and from electron diffraction studies favoured an orthorhombic cell. They refined the structure in space group *Imma* by Rietveld analysis using data

collected by both neutron and synchrotron X-ray powder diffraction. The final crystallographic parameters refined satisfactorily (R_{wp} = 2.87%). From a comparison of the neutron diffraction results, it is believed that the Clarke *et al.* (2002) refinement is the more accurate, and that the structure of $LaTiO_2N$ is indeed triclinic. However, it can be seen from their refined triclinic unit cell dimensions (a = 5.6097 Å, b = 7.8719 Å, c = 5.5752 Å; α = 90.199°, β = 90.154°, γ = 89.988°, that not only are the three angles extremely close to 90° and the a, b and c values almost identical with those given by Yashima *et al.* (2010) but when the a and c dimensions are divided by $\sqrt{2}$ and the b dimension by 2, the resulting values (3.967, 3.936, 3.943 Å) give very similar values for the basic perovskite sub-cell. The multiple overlaps of the principle reflections generated by the triclinic cell would therefore almost precisely overlap, and in the present case could not be distinguished on X-ray diffraction spectra, especially since the crystallinity of the samples is relatively poor, which would result in additional broadening of the reflections. It was therefore decided in the present work to use Yashima *et al.* (2010)'s orthorhombic unit cell (*Imma* with a = 5.57137, b = 7.8790, c = 5.60279 Å) as well as the *Pnma* $NdTiO_2N$ orthorhombic unit cell in refinement of these and associated solid solution perovskite compounds.

In contrast to the original work on $SrTaO_2N$ and $CaTaO_2N$ (Marchand *et al.*, 1986), Günther *et al.* (2000) refined the structures of $SrTaO_2N$ and $CaTaO_2N$ by Rietveld analysis using both X-ray and neutron powder diffraction data, concluding that $SrTaO_2N$ was tetragonal and $CaTaO_2N$ orthorhombic. $Ba_xSr_{1-x}TaO_2N$ solid solutions and their crystal structures were reported previously by Pors *et al.* (1988), who found that when synthesised by

ammonolysis at 950ºC for 15 hours, a cubic solid solution range extended up to x = 0.56 with the same structure as the cubic end-member, $BaTaO_2N$. Logvinovich *et al.* (2007) synthesised perovskite-type $La_{1-x}Ca_xTiO_{2+x}N_{1-x}$ compounds by ammonolysis of appropriate oxide precursors (the latter using a soft chemistry route). By carefully controlling the reaction parameters (time, temperature and ammonia flow rate), single phase perovskite-type products were obtained for all compositions. With increasing Ca content, the lattice parameter decreases resulting in the band gap correspondingly increasing because of decreasing N^{3-} which increases the ionicity of the chemical bonds (Logvinovich *et al.*, 2007). Motohashi *et al.* (2009) studied structural phase transitions in the perovskite-type $Ca_{1-x}Eu_xTa(O,N)_3$ series. The structures of these oxynitrides are apparently orthorhombic for x < 0.4 and cubic for x ≥ 0.4. The ratio of oxygen to nitrogen is 2:1, independent of Eu content.

There is no previous work in the literature on synthesis and structural phase transitions in $La_xNd_{1-x}TiO_2N$, $Ca_xSr_{1-x}TaO_2N$ and $Ca_xBa_{1-x}TaO_2N$ solid solutions. In this research, these and the related $Ba_xSr_{1-x}TaO_2N$ (x= 0, 0.2, 0.4,.., 1.0) solid solutions were prepared by thermal ammonolysis as described in Chapters 3 and 4. However, no evidence was found for the existence of $Ca_xBa_{1-x}TaO_2N$ solid solution and so no structural studies could be performed. Crystal structure determinations were carried out in the other series using Rietveld refinement of powder X-ray diffraction data.

5.2 $La_xNd_{1-x}TiO_2N$

Recently, the $(La_xNd_{1-x})_2Ti_2O_7$ precursors needed for this study were reported by Shao *et al.* (2010), who carried out structural characterisation, morphology and dielectric properties. The complete solid solution range adopts a monoclinic (pyrochlore) structure in space group *P2₁* with a and b parameters decreasing with increasing neodymium content whilst the c parameter remains almost unaffected. SEM showed no significant change in grain shape as a function of composition. The $(La_xNd_{1-x})_2Ti_2O_7$ precursors used in the present study (made as described in Chapter 4) showed identical X-ray diffraction patterns to those reported by Shao *et al.* (2010) (see Figure 5-1).
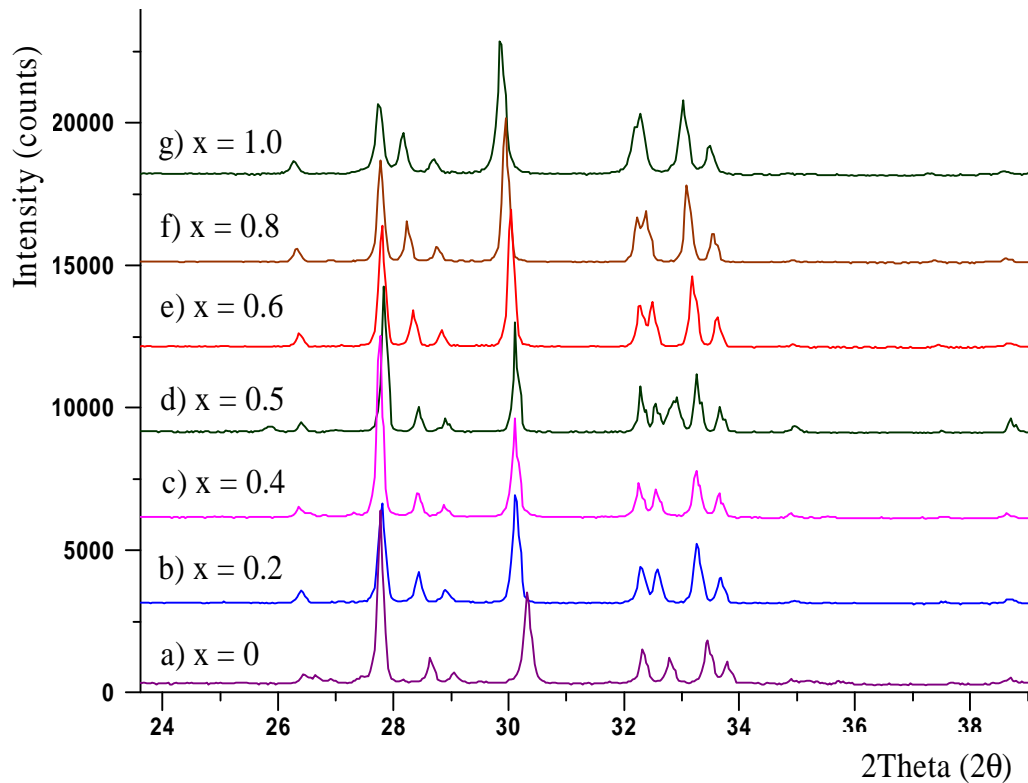
Figure 5-1 X-ray diffraction patterns of $(La_xNd_{1-x})_2Ti_2O_7$, $0 \leq x \leq 1.0$

These compositions were then nitrided in ammonia (also described in Chapter 4) to form the corresponding $La_xNd_{1-x}TiO_2N$ oxynitrides and a complete range of perovskite solid solution was observed across the entire $0 \leq x \leq 1.0$ range without any evidence of second phases, as shown in Figure 5-2.
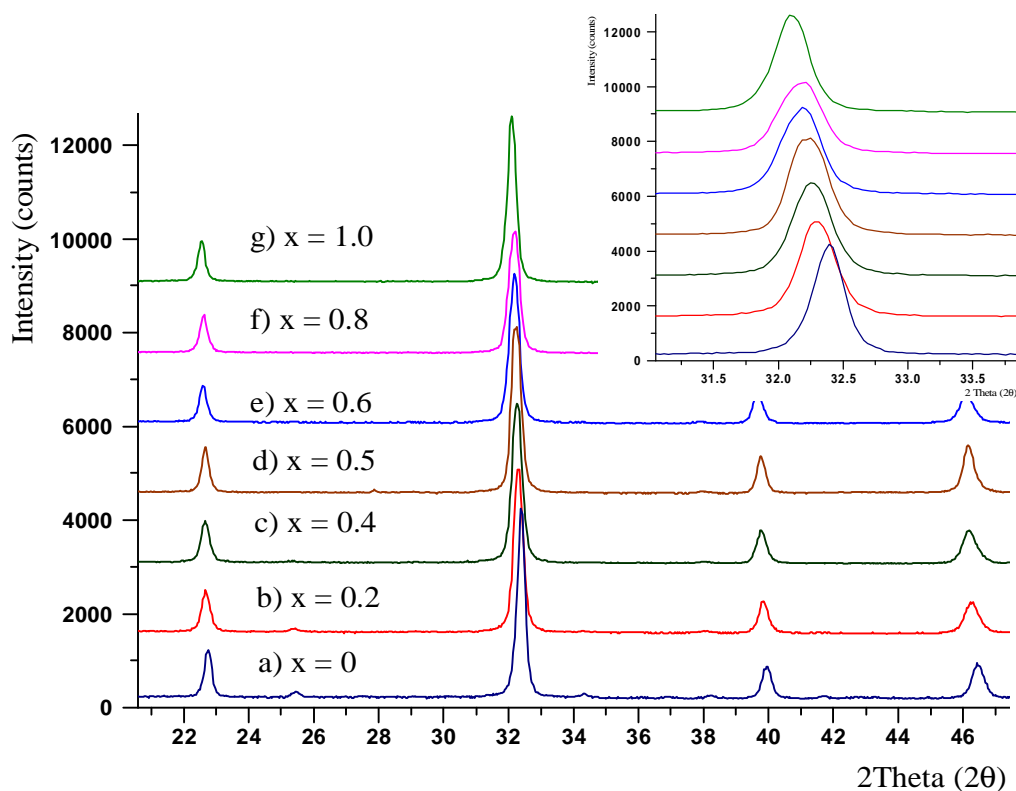
Figure 5-2 X-ray diffraction patterns of $La_xNd_{1-x}TiO_2N$, $0 \leq x \leq 1$

When comparing the *Pnma* and *Imma* space groups, clearly, the *Imma* space group has the higher symmetry, and relative to this, there is only one unique octahedron in the structure. In contrast, the lack of body-centering in *Pnma* gives more freedom for the atoms to move, and means that there are now two distinct sets of octahedra. Both space groups *Imma* and *Pnma* were used for the structure refinement of $La_xNd_{1-x}TiO_2N$ in this study (starting parameters listed in Table 5-1).

Table 5-1 Initial unit cell dimensions and crystallographic parameters for structure refinements of $La_xNd_{1-x}TiO_2N$ (after Clarke *et al.*, 2002, Yashima *et al.*, 2010)

Atom	Wyckoff	x	y	z	s.o.f.
Based on *Imma* $LaTiO_2N$[1]					
La/Nd	4e	0	¼	1.0010	*x/1-x*
Ti	4b	0	0	½	1.0
O/N (1)	4e	0	¼	0.551	0.67/0.33
O/N (2)	8g	¼	0.0325	¼	0.67/0.33
Based on *Pnma* $NdTiO_2N$[2]					
La	4c	0.03175	¼	0.9955	*x/1-x*
Ti	4b	½	0	0	1.0
O/N (1)	4c	0.4853	¼	0.0755	0.67/0.33
O/N (2)	8d	0.2850	0.03934	0.7161	0.67/0.33

[1] a = 5.57137, b = 7.8790 and c = 5.60279 Å, and $\alpha = \beta = \gamma = 90°$ (Yashima *et al.*, 2010).

[2] a = 5.5492, b = 7.8017 and c = 5.52901Å, and $\alpha = \beta = \gamma = 90°$ (Clarke *et al.*, 2002)

It is clear that in Clarke *et al.* (2002) and Yashima *et al.* (2010) refinements, the La/Nd atom has shifted negligibly from z = 0 (its cubic perovskite value), whereas there has been slightly more movement in the O/N positions, corresponding to some rotation of the octahedra. In the case of space group *Pnma*, the x and z parameters of La,Nd are free to move and most of the O/N parameters can and have adjusted, with most change being observed for the O/N(1) position. In the present case, the profile fits for the two end members of $LaTiO_2N$ and $NdTiO_2N$ are shown in Figure 5-3 and Figure 5-4, respectively. Though the R_{wp} of both are at acceptable levels < 10, small differences between the observed profile and the calculated one can easily be seen from the X-ray diffraction spectra.
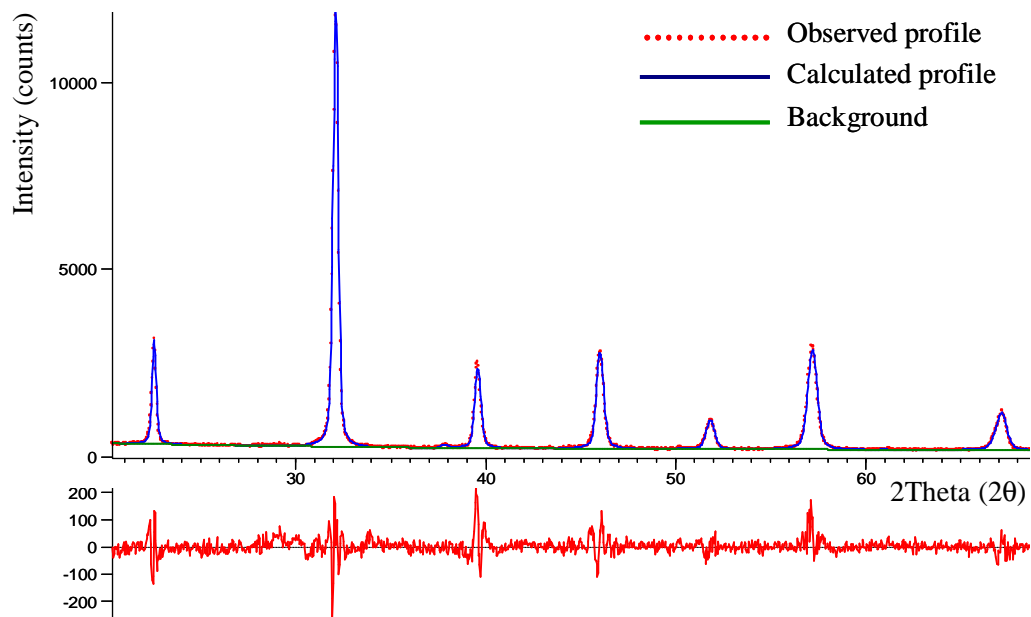
Figure 5-3 Observed and calculation profiles (top) and difference plot (bottom) of *Imma*
LaTiO$_2$N refined by Rietveld analysis
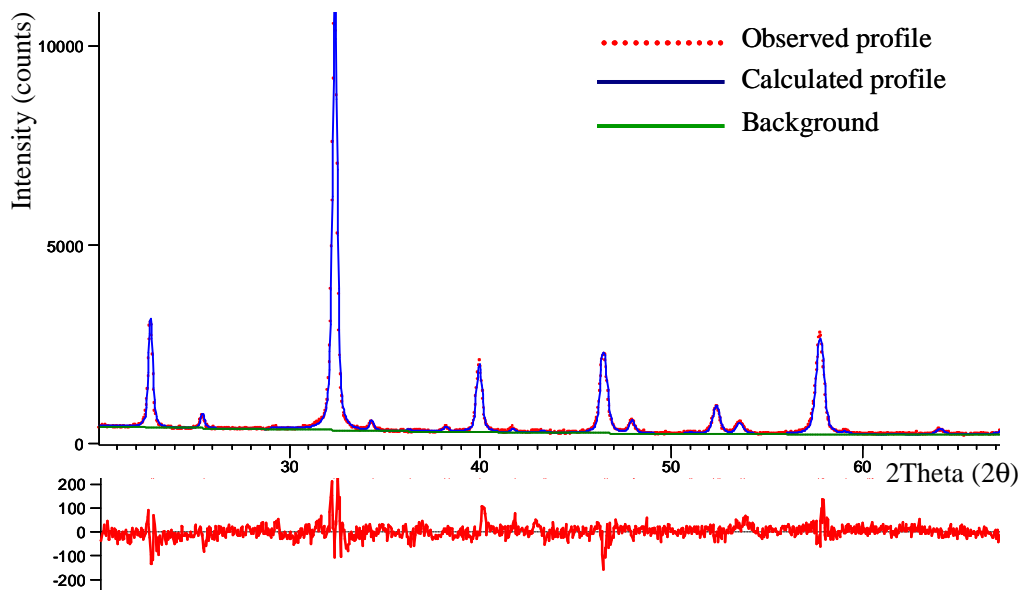
Figure 5-4 Observed and calculation profiles (top) and difference plot (bottom) of *Pnma*
NdTiO$_2$N refined by Rietveld analysis

La$_x$Nd$_{1-x}$TiO$_2$N structural refinement in *Imma* and *Pnma* results are shown in Table 5-2 and Table 5-3, NdTiO$_2$N structural refinement in the *Imma* space group showed an unsatisfactory R factor higher than 10, meaning that the observed spectra did not fit well with the calculated ones and the results are not shown here. Similarly, the R factor for LaTiO$_2$N refinement in space group *Pnma* was above acceptable levels so the refined unit cell parameters were not reliable and are not given here. It was expected that when comparing the *Pnma* and *Imma* refinements there would be a point across the series where one space group would be preferred rather than the other. Whereas *Pnma* clearly gives the lower R$_e$, R$_p$ and R$_{wp}$ and GOF factors for the NdTiO$_2$N composition, the increase in these with %La content is not strong. However, it is noticeable that the x = 0.8 composition has appreciably higher R$_p$ and R$_{wp}$ and GOF factors.

Table 5-2 Refined unit cell dimensions for La$_x$Nd$_{1-x}$TiO$_2$N solid solutions in space group *Pnma*

x	0.0	0.2	0.4	0.5	0.6	0.8
%R$_e$	4.43	4.73	4.57	4.87	4.73	4.58
%R$_p$	3.95	4.43	4.54	4.53	4.86	6.36
%R$_{wp}$	5.11	5.75	5.87	5.86	6.33	8.09
GOF	1.33	1.48	1.65	1.45	1.79	3.12
a/ Å	5.5498(4)	5.5533(7)	5.5565(6)	5.5575(7)	5.5572(7)	5.5658(9)
b/ Å	7.7989(6)	7.8238(8)	7.8241(9)	7.8300(8)	7.865(1)	7.878(2)
c/ Å	5.5236(4)	5.5568(5)	5.5552(5)	5.5623(6)	5.5565(5)	5.5645(5)
V (10^6 pm^3)	239.08	241.43	241.51	242.04	242.87	243.99

Reliability factors in Rietveld analysis: R$_e$ = R (expected), R$_p$ = R (profile), R$_{wp}$ = R (weighed profile) and GOF = Goodness of fit; V = unit cell volume; numbers in parenthesis are estimated standard deviations.

Table 5-3 Refined unit cell dimensions for La$_x$Nd$_{1-x}$TiO$_2$N solid solutions in space group *Imma*

x	0.2	0.4	0.5	0.6	0.8	1.0
%R$_e$	4.74	4.57	4.88	4.74	4.59	4.65
%R$_p$	5.31	5.17	4.94	4.99	6.14	3.86
%R$_{wp}$	6.98	6.82	6.70	6.48	7.88	5.12
GOF	2.17	2.22	1.89	1.87	2.95	1.21
a/ Å	5.5551(6)	5.5620(7)	5.5579(5)	5.5639(7)	5.5711(8)	5.5723(4)
b/ Å	7.8336(7)	7.832(1)	7.8390(7)	7.868(1)	7.884(1)	7.8676(8)
c/ Å	5.571(1)	5.5594(6)	5.5774(8)	5.5624(5)	5.5696(5)	5.6006(6)
V (10^6 pm^3)	242.45	242.17	243.00	243.50	244.64	245.53

Reliability factors in Rietveld analysis: R$_e$ = R (expected), R$_p$ = R (profile), R$_{wp}$ = R (weighed profile) and GOF = Goodness of fit; V = unit cell volume; numbers in parenthesis are estimated standard deviations.

Similarly, when examining the *Imma* data, the LaTiO$_2$N composition gives the lowest R$_p$ and R$_{wp}$ and GOF factors, but there is no systematic trend with %Nd content. Across the series, the refinement results showed a slightly non-linear variation in unit cell parameters as a function of La content (see Figure 5-5) but it will be seen that the R$_{wp}$ factors are still relatively high for both *Imma* and *Pnma* refinements. This is probably due to the multiply overlapped nature of the reflections, but may also be due to the fact that whereas the compositions are believed to be fairly close to their stated values, the breadths of the X-ray diffraction peaks were quite large and showed some variation across the range. This may be because of variations in O:N ratio, but also to variations in crystallinity of the oxynitride layer as a function of La:Nd ratio. The most likely conclusion that could be inferred from these refinements is that the *Pnma* space

group applies up to approximately x = 0.6, with *Imma* space group preferred at higher x values.
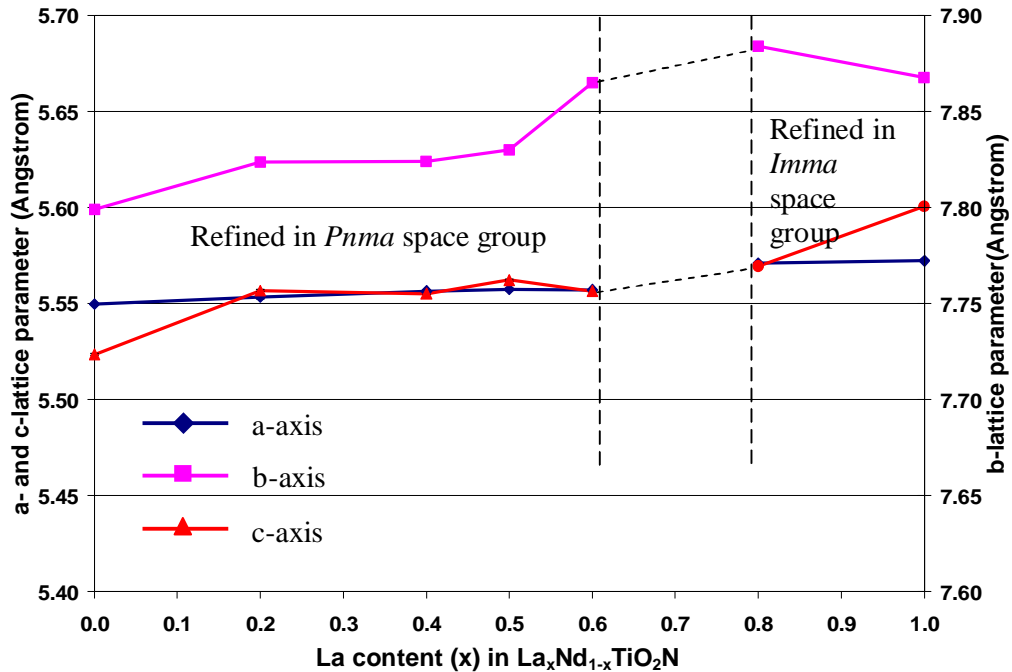
Figure 5-5 Variation of unit cell parameter of $La_xNd_{1-x}TiO_2N$ compounds

Some information might also have been expected from the variation in x, y, z parameters (Table 5-4). For *Pnma* data, the x and z parameters for the La/Nd atom systematically decrease and increase, respectively; trends in O/N parameters are not clear. For *Imma* data, there are no clear trends. This is also enhanced by the structure diagrams drawn from the above data (see Figure 5-6). Diagrams for $0 \leq x \leq 0.6$ have been constructed using *Pnma* data and the two final x = 0.8 and 1.0 diagrams from *Imma* data. It is impossible to see any significant different between the two space groups, showing that rotation of the octahedra in all these compounds is very similar. Further work to study this in more detail would need to be carried out using neutron diffraction, as used by Clark *et al.* (2002) and Yashima *et al.* (2010).

Table 5-4 Refined atomic coordinates of $La_xNd_{1-x}TiO_2N$ in space group *Pnma* at $0 \leq x \leq 0.6$ and *Imma* at $0.8 \leq x \leq 1.0$

Atom	Wyckoff	s.o.f.	x	y	z
x = 0					
Nd	4c	1	0.0298(3)	¼	0.9919(7)
Ti	4b	1.0	½	0	0
O/N (1)	4c	0.67/0.33	0.491(3)	¼	0.073(6)
O/N (2)	8d	0.67/0.33	0.309(3)	0.030(3)	0.736(4)
x = 0.2					
La/Nd	4c	0.2/0.8	0.0175(4)	¼	0.9950(5)
Ti	4b	1.0	½	0	0
O/N (1)	4c	0.67/0.33	0.523(4)	¼	0.078(3)
O/N (2)	8d	0.67/0.33	0.214(8)	0.014(5)	0.720(4)
x = 0.4					
La/Nd	4c	0.4/0.6	0.0182(4)	¼	0.9972(7)
Ti	4b	1.0	½	0	0
O/N (1)	4c	0.67/0.33	0.533(4)	¼	0.085(3)
O/N (2)	8d	0.67/0.33	0.224(9)	0.007(4)	0.727(6)
x = 0.5					
La/Nd	4c	0.5/0.5	0.0163(4)	¼	0.9931(5)
Ti	4b	1.0	½	0	0
O/N (1)	4c	0.67/0.33	0.524(5)	¼	0.057(5)
O/N (2)	8d	0.67/0.33	0.210(9)	0.012(4)	0.727(7)
x = 0.6					
La/Nd	4c	0.6/0.4	0.0130(6)	¼	0.9988(8)
Ti	4b	1.0	½	0	0
O/N (1)	4c	0.67/0.33	0.520(6)	¼	0.060(6)
O/N (2)	8d	0.67/0.33	0.23(1)	0.036(4)	0.740(7)
x = 0.8					
La/Nd	4e	0.8/0.2	0	¼	0.9962(8)
Ti	4b	1.0	0	0	½
O/N (1)	4e	0.67/0.33	0	¼	0.505(9)
O/N (2)	8g	0.67/0.33	¼	0.045(2)	¼
x = 1.0					
La	4e	1.0	0	¼	0.001(1)
Ti	4b	1.0	0	0	½
O/N (1)	4e	0.67/0.33	0	¼	0.581(3)
O/N (2)	8g	0.67/0.33	¼	0.018(3)	¼
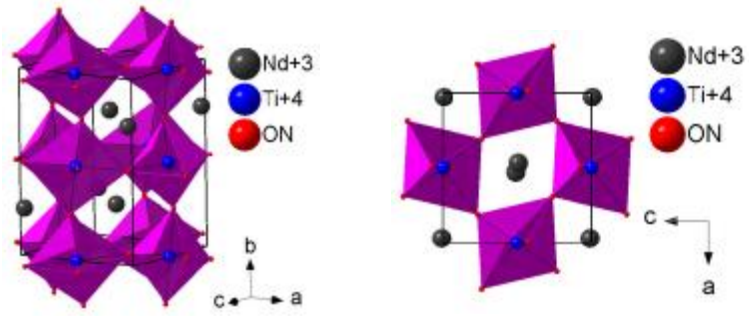
NdTiO$_2$N

La$_{0.2}$Nd$_{0.8}$TiO$_2$N
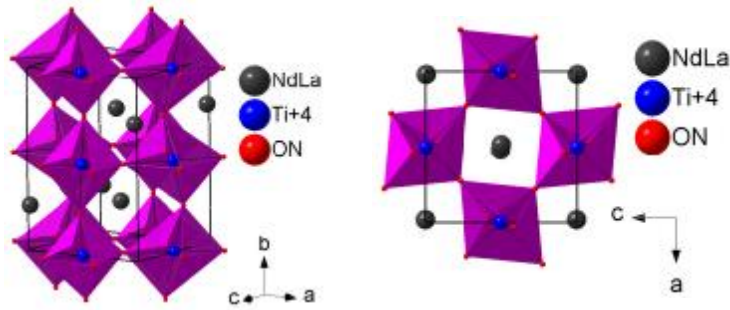
La$_{0.4}$Nd$_{0.6}$TiO$_2$N
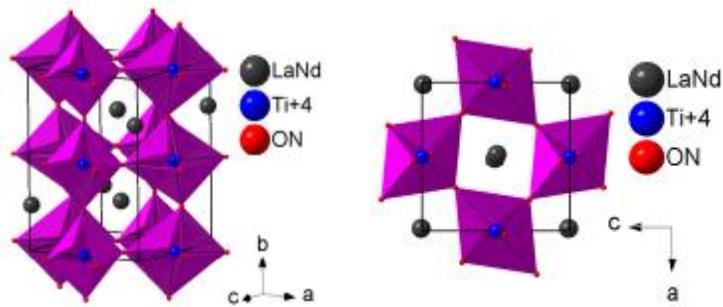
La$_{0.5}$Nd$_{0.5}$TiO$_2$N

Figure 5-6 Crystal structure of orthorhombic La$_x$Nd$_{1-x}$TiO$_2$N in *Pnma* space group at
$0 \leq x \leq 0.6$ and *Imma* space group at $0.8 \leq x \leq 1.0$

La$_{0.6}$Nd$_{0.4}$TiO$_2$N

La$_{0.8}$Nd$_{0.2}$TiO$_2$N

LaTiO$_2$N
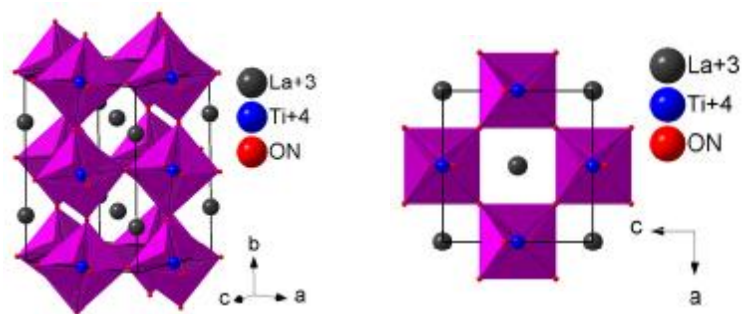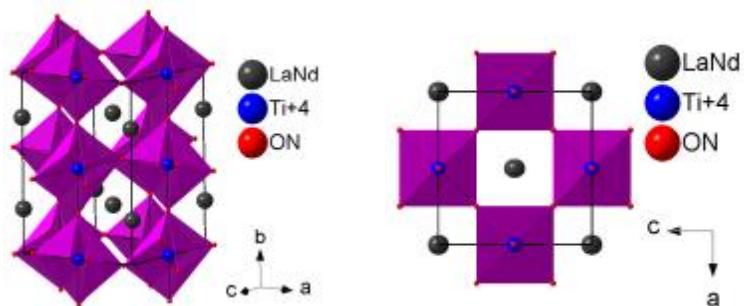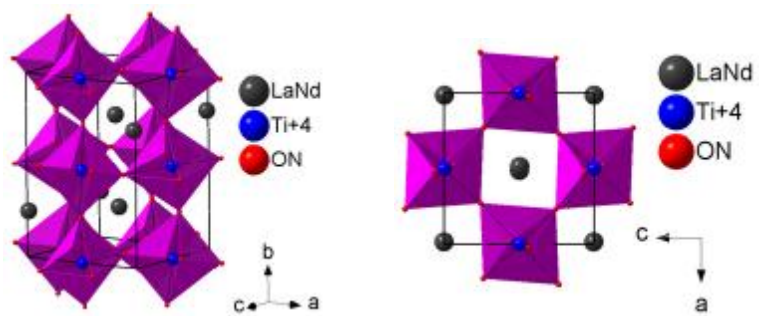
Figure 5-6 Crystal structure of orthorhombic La$_x$Nd$_{1-x}$TiO$_2$N in

Pnma space group at $0 \leq x \leq 0.6$ and *Imma* space group at $0.8 \leq x \leq 1.0$ (continued)

5.3 $Ca_xSr_{1-x}TaO_2N$

The present work is the first recorded study of $Ca_xSr_{1-x}TaO_2N$ solid solutions, with the range extending across the entire system. These were synthesised by nitriding their corresponding intermediate oxides in hot flowing ammonia, as described in Chapter 4. X-ray diffraction spectra of the oxide precursors are shown in Figure 5-7. After nitriding, X-ray diffraction patterns shown in Figure 5-8 confirmed the existence of $Ca_xSr_{1-x}TaO_2N$ solid solutions for the complete range ($0 \leq x \leq 1.0$), with no trace of second phases.
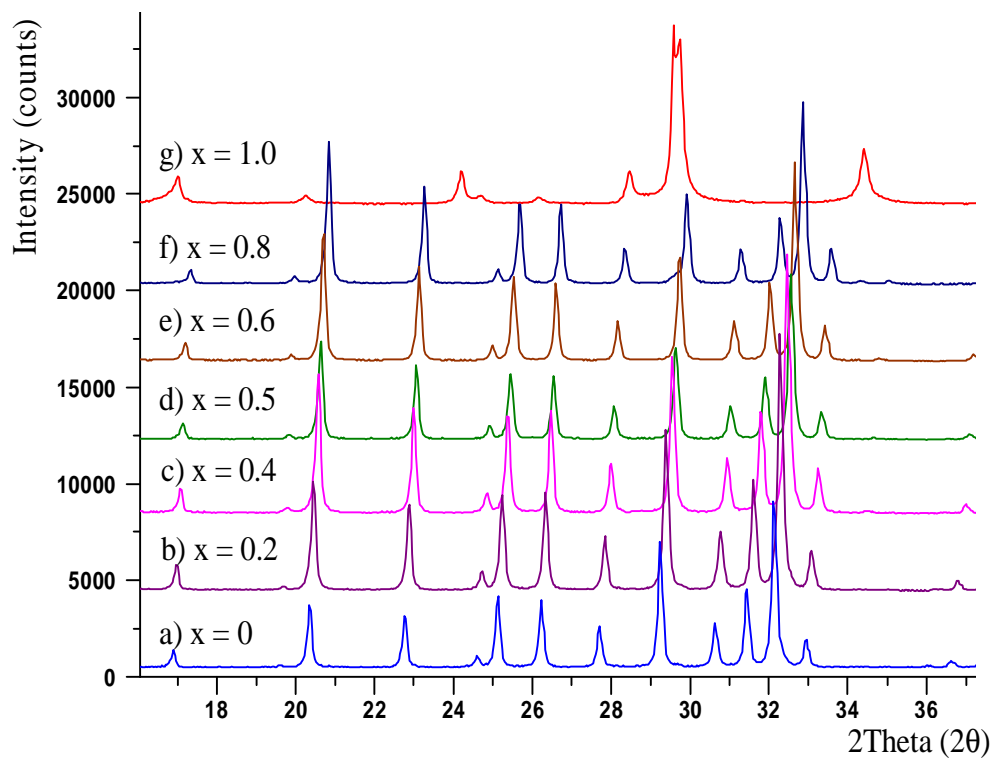
Figure 5-7 X-ray diffraction patterns for $(Ca_xSr_{1-x})_2Ta_2O_7$, x= 0, 0.2, 0.4,…, 1.0
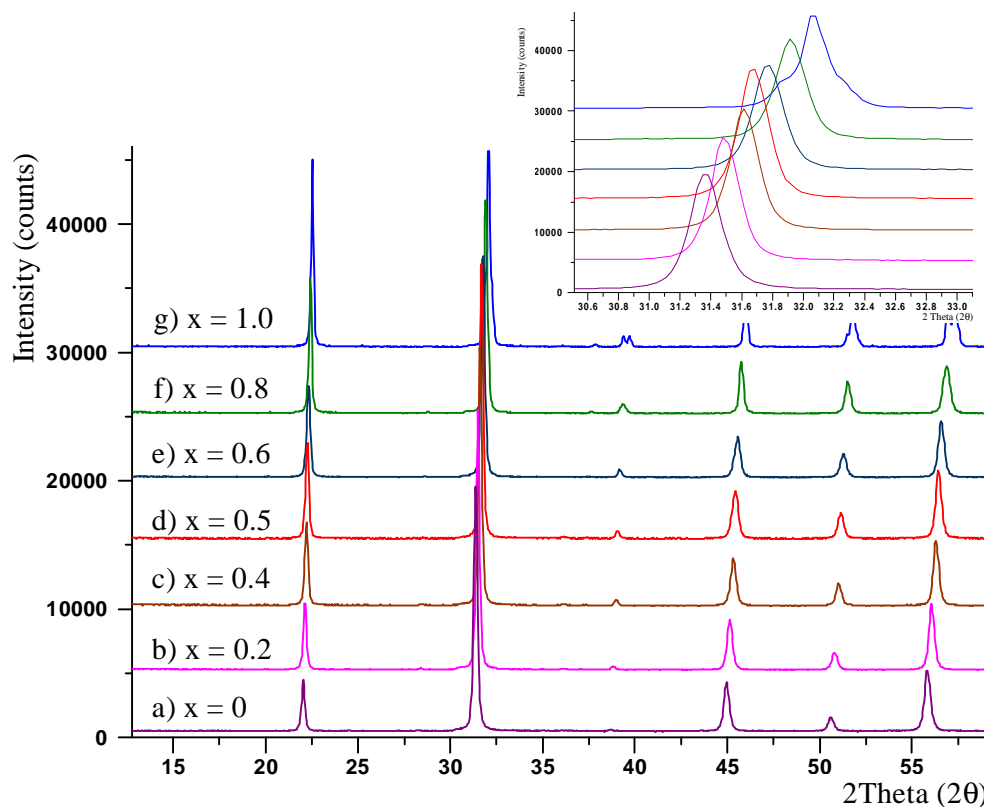
Figure 5-8 X-ray diffraction patterns for $Ca_xSr_{1-x}TaO_2N$, x= 0, 0.2, 0.4,…, 1.0

The two end members of these solid solutions, $CaTaO_2N$ and $SrTaO_2N$, have been previously studied and the crystal structures determined as orthorhombic and tetragonal, respectively (Günther *et al.*, 2000). In Ca-rich compositions, it was expected that the orthorhombic type of structure of $CaTaO_2N$ would predominate and the tetragonal type of structure at the Sr-rich end. Upon Ca substitution at x > 0.6, diffraction peaks tend to split into more peaks; this is close to the point where the tetragonal Sr-rich structure changes to the orthorhombic form for Ca-rich compositions (see Figure 5-9).
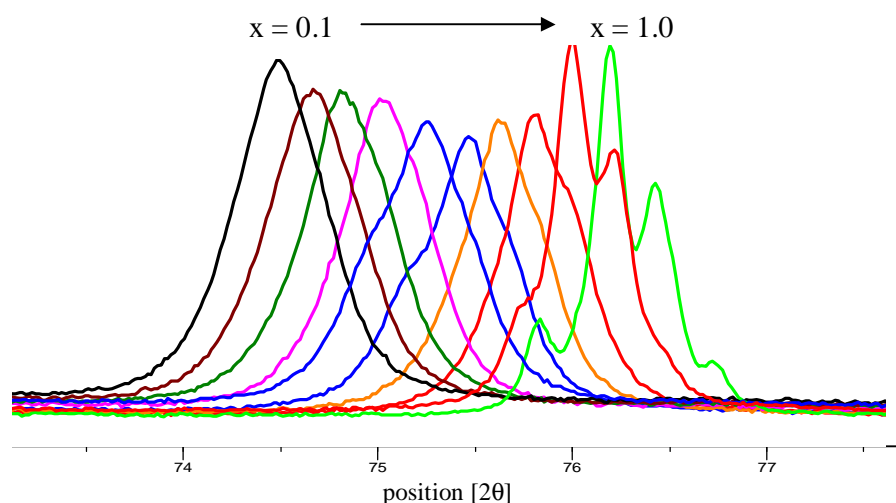
Figure 5-9 X-ray diffraction patterns showing an increasing tendency for orthorhombic distortion in Ca-rich $Ca_xSr_{1-x}TaO_2N$ compositions for x= 0.1, 0.2,…, 1.0

To confirm this, structural characterisation of these solid solutions was studied by Rietveld refinement. The orthorhombic *Pnma* and tetragonal *I4/mcm* space groups were used for structure determination in these series, and the details are shown in Table 5-5.

Table 5-5 Atomic parameters of end members used for $Ca_xSr_{1-x}TaO_2N$ structural refinement (after Günther *et al.*, 2000)

Atom	Wyck.	x	y	z	s.o.f.
I4/mcm $SrTaO_2N$[1]					
Ca/Sr	4b	0	½	¼	*x/1-x*
Ta	4c	½	½	0	1.0
O/N(1)	8h	0.7721	½+x	0	0.67/0.33
O/N(2)	4a	0	0	¼	0.67/0.33
Pnma $CaTaO_2N$[2]					
Ca/Sr	4c	0.0307	¼	-0.003	*x/1-x*
Ta	4b	0	0	½	1.0
O/N(1)	4c	0.4824	¼	0.0764	0.67/0.33
O/N(2)	8d	0.2937	0.0409	0.7079	0.67/0.33

[1]a = 5.7049 and c = 8.0499 Å, and [2]a = 5.6239, b = 7.8954 and c = 5.5473 Å; (Günther *et al.*, 2000)

Figure 5-10 and Figure 5-11 show the profile fitting results of the observed spectra and the calculated ones of $SrTaO_2N$ and $CaTaO_2N$, respectively. The refinement indicators and unit cell dimensions for $Ca_xSr_{1-x}TaO_2N$ in tetragonal *I4/mcm* and orthorhombic *Pnma* are summarised Table 5-6 and Table 5-7.
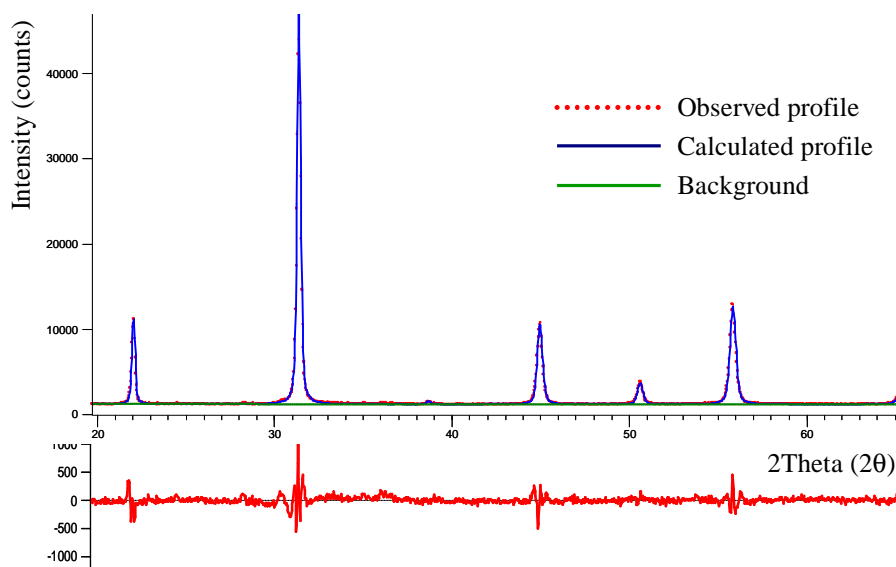
Figure 5-10 Observed and calculated profiles (top) and difference plot (bottom) of *I4/mcm* $SrTaO_2N$ by Rietveld analysis
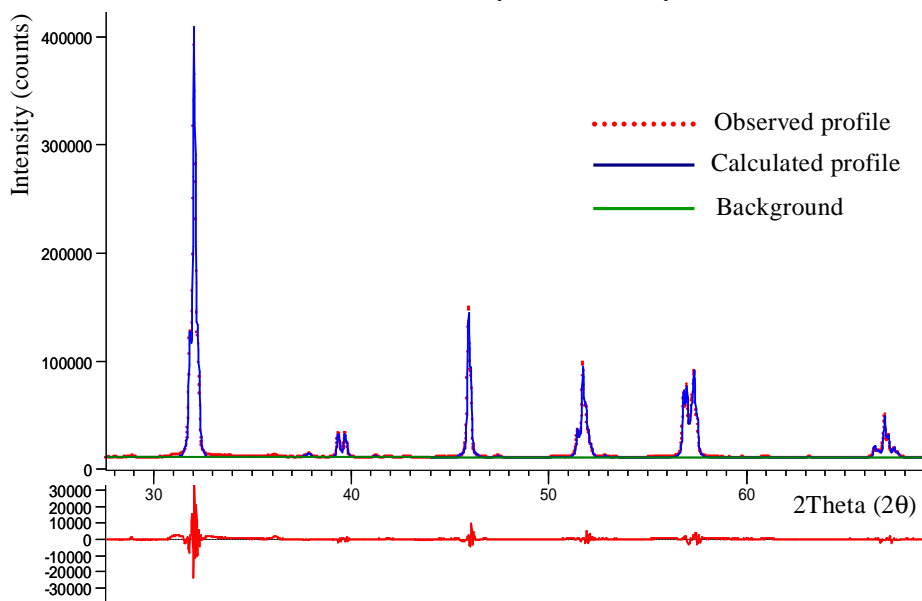

Figure 5-11 Observed and calculated profiles (top) and difference plot (bottom) of *Pnma* $CaTaO_2N$ by Rietveld analysis

Table 5-6 Refined parameters for $Ca_xSr_{1-x}TaO_2N$ in tetragonal space group *I4/mcm*

x	0	0.1	0.2	0.3	0.4	0.5	0.6	0.7
%R_e	2.34	0.77	0.78	0.78	0.79	0.78	0.80	0.80
%R_p	2.43	2.04	2.11	2.24	2.28	2.34	2.42	2.12
%R_{wp}	3.18	3.01	3.11	3.27	3.48	3.60	3.76	3.11
GOF	1.85	15.25	16.06	17.46	19.37	21.46	22.05	14.96
a/ Å	5.7085(2)	5.7019(1)	5.6925(1)	5.6812(1)	5.6669(1)	5.6618(1)	5.6482(1)	5.6264(2)
c/ Å	8.0519(5)	8.0428(3)	8.0278(3)	8.0135(3)	7.9915(2)	7.9781(2)	7.9612(2)	7.9696(5)
V (10^6 pm^3)	262.39	261.48	260.13	258.64	256.64	255.75	253.98	252.29

Reliability factors in Rietveld analysis: R_e = R (expected), R_p = R (profile), R_{wp} = R (weighed profile) and GOF = Goodness of Fit; V = unit cell volume; numbers in the parenthesis are estimated standard deviations.

Table 5-7 Refined parameters for $Ca_xSr_{1-x}TaO_2N$ in orthorhombic space group *Pnma*

x	0.6	0.7	0.8	0.9	1.0
%R_e	0.80	0.80	0.81	0.78	0.80
%R_p	1.92	1.84	1.84	2.09	2.80
%R_{wp}	2.71	2.79	2.84	3.26	4.46
GOF	11.49	12.08	12.40	17.38	30.96
a/ Å	5.6265(4)	5.6327(2)	5.6264(1)	5.62029(7)	5.61935(7)
b/ Å	7.9879(2)	7.9342(2)	7.9235(2)	7.9100(1)	7.8939(1)
c/ Å	5.6204(3)	5.6124(1)	5.5905(1)	5.57020(8)	5.54957(7)
V (10^6 pm^3)	252.60	250.82	249.23	247.63	246.17

Reliability factors in Rietveld analysis: R_e = R (expected), R_p = R (profile), R_{wp} = R (weighed profile) and GOF = Goodness of Fit; V = unit cell volume; numbers in the parenthesis are estimated standard deviations.

From the Rietveld refinement results, a-, b- and c-axis lengths were plotted as a function of Ca content (x) according to the tetragonal *I4/mcm* and orthorhombic *Pnma* model space group, as shown Figure 5-12 and Figure 5-13, respectively. Sr-rich $Ca_xSr_{1-x}TaO_2N$ compounds were refined on a tetragonal model in space group *I4/mcm* up to x = 0.7 because at x ≥ 0.7 the refined structures are not stable and the unit cell parameters departed from a linear trend line. Similarly, in the case of orthorhombic refinements, at x ≤ 0.6, the refinement results were not stable and did not fit a linear trend line. From X-ray diffraction spectra and structure refinement, $Ca_xSr_{1-x}TaO_2N$ solid solutions adopt the tetragonal *I4/mcm* space group like $SrTaO_2N$ at x ≤ 0.6 and the orthorhombic space group *Pnma* at x > 0.6. The structural transition takes place somewhere between x = 0.6 and x = 0.7, as summarised in Figure 5-14.

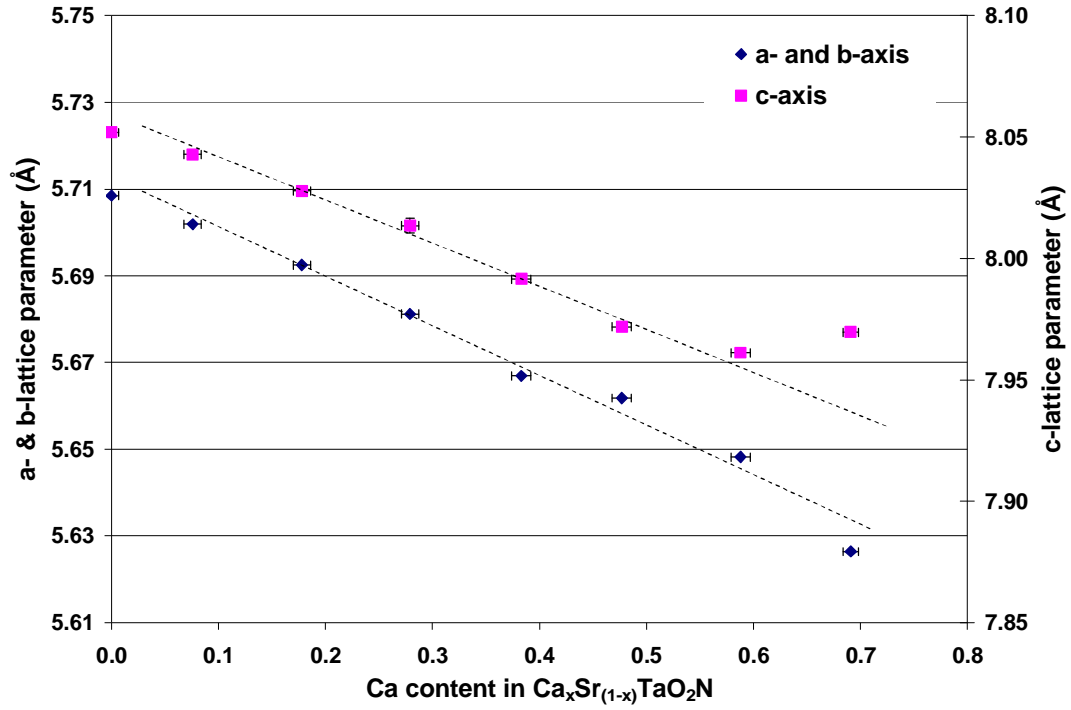Figure 5-12 Variation in unit cell parameters of Ca$_x$Sr$_{1-x}$TaO$_2$N compositions
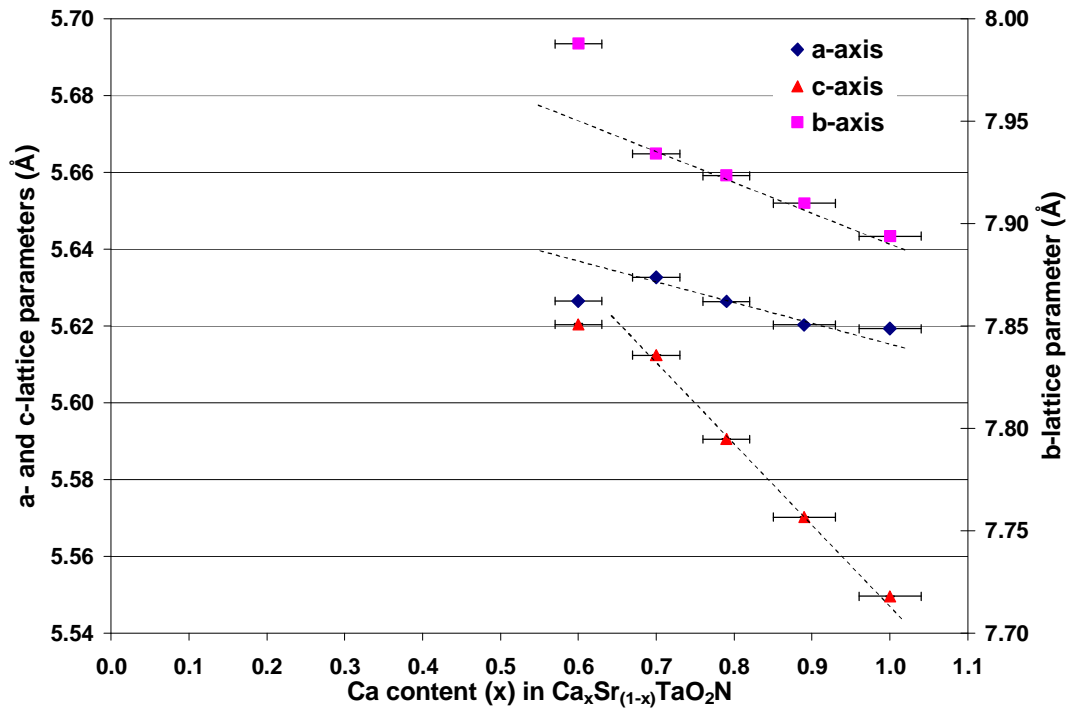
versus Ca content in the case of a tetragonal model

Figure 5-13 Variation in unit cell parameters of Ca$_x$Sr$_{1-x}$TaO$_2$N compositions
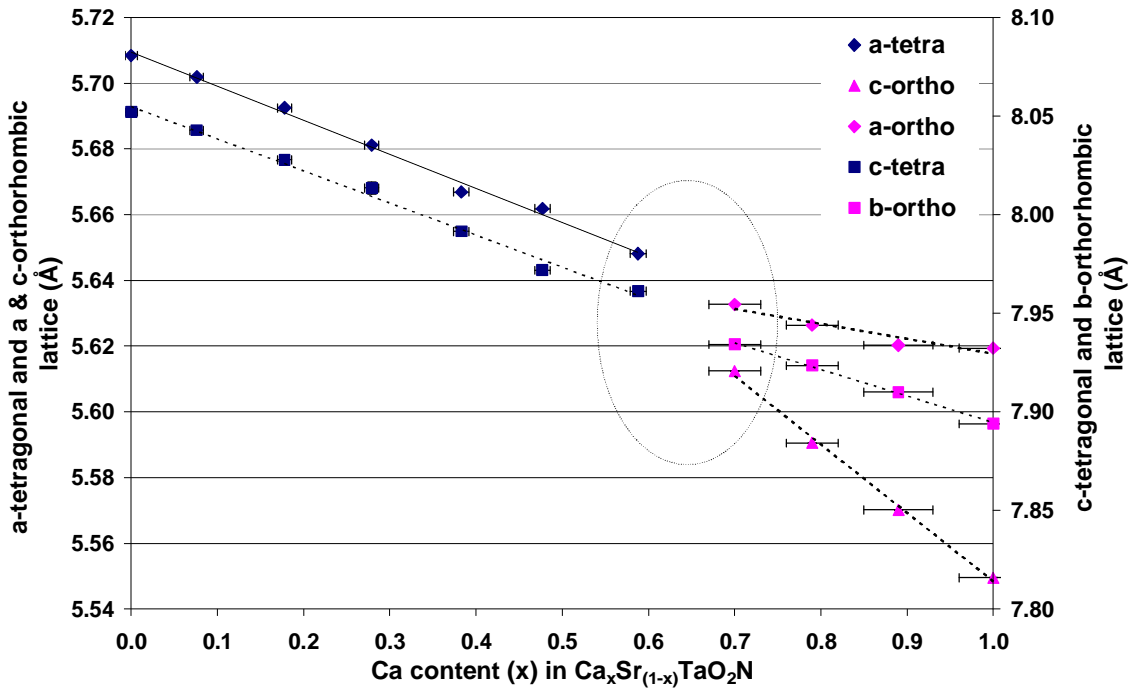
versus Ca content in the case of orthorhombic structures

Figure 5-14 Structure transition in the $Ca_xSr_{1-x}TaO_2N$ series from tetragonal Sr-rich to orthorhombic Ca-rich solid solutions

Atomic positions are not shifted very much from their starting values for the tetragonal model (Table 5-8) and the 7 diagrams in Figure 5-15 (i.e. up to x = 0.6) all appear identical as regards octahedral distortion. A satisfactory feature of the refinement is that site occupation factors for the Ca, Sr site refined to values within ± 0.02 of the starting values. Even though the orthorhombic structures (0.6 < x < 1.0) show more variation in atomic parameters (see Table 5-9), this is not clearly apparent from the last 4 diagrams in Figure 5-15. However, careful study of the refined atomic coordinates in Table 5-9 (and neglecting the x = 0.6 data as being on the tetragonal: orthorhombic border) show that the x-coordinate of Ca/Sr systematically increases as also do the x- and z- coordinates of O/N1 (slightly) and the x-, y- and z-coordinates of O/N2.

Table 5-8 Refined atomic coordinates of $Ca_xSr_{1-x}TaO_2N$ in compositions with $0 \leq x \leq 0.7$ in space group $I4/mcm$

Atom	Wyckoff	s.o.f.	x	y	z
x = 0					
Sr	4b	1.000(7)	0	½	¼
Ta	4c	1.0	½	½	0
O/N1	4a	1.0	0	0	¼
O/N2	8h	1.0	0.775(2)	0.275(2)	0
x = 0.1					
Ca/Sr	4b	0.076(8)/0.924(8)	0	½	¼
Ta	4c	1.0	½	½	0
O/N1	4a	1.0	0	0	¼
O/N2	8h	1.0	0.777(1)	0.277(1)	0
x = 0.2					
Ca/Sr	4b	0.178(8)/0.822(8)	0	½	¼
Ta	4c	1.0	½	½	0
O/N1	4a	1.0	0	0	¼
O/N2	8h	1.0	0.776(1)	0.276(1)	0
x = 0.3					
Ca/Sr	4b	0.279(8)/0.721(8)	0	½	¼
Ta	4c	1.0	½	½	0
O/N1	4a	1.0	0	0	¼
O/N2	8h	1.0	0.782(1)	0.282(1)	0
x = 0.4					
Ca/Sr	4b	0.383(9)/0.617(9)	0	½	¼
Ta	4c	1.0	½	½	0
O/N1	4a	1.0	0	0	¼
O/N2	8h	1.0	0.781(2)	0.281(2)	0
x = 0.5					
Ca/Sr	4b	0.477(9)/0.523(9)	0	½	¼
Ta	4c	1.0	½	½	0
O/N1	4a	1.0	0	0	¼
O/N2	8h	1.0	0.783(2)	0.283(2)	0
x = 0.6					
Ca/Sr	4b	0.588(9)/0.412(9)	0	½	¼
Ta	4c	1.0	½	½	0
O/N1	4a	1.0	0	0	¼
O/N2	8h	1.0	0.788(1)	0.288(1)	0
x = 0.7					
Ca/Sr	4b	0.691(7)/0.309(7)	0	½	¼
Ta	4c	1.0	½	½	0
O/N1	4a	1.0	0	0	¼
O/N2	8h	1.0	0.8004(6)	0.3004(6)	0

Table 5-9 Refined atomic coordinates of $Ca_xSr_{1-x}TaO_2N$ in compositions with $0.6 \leq x \leq 1.0$ in space group *Pnma*

Atom	Wyckoff	s.o.f.	x	y	z
x = 0.6					
Ca/Sr	4c	0.63(3)/0.37(3)	0.0151(9)	¼	0.9924(9)
Ta	4b	1.0	0	0	½
O/N1	4c	0.67/0.33	0.509(5)	¼	0.072(3)
O/N2	8d	0.67/0.33	0.295(3)	0.003(4)	0.714(2)
x = 0.7					
Ca/Sr	4c	0.70(3)/0.30(3)	0.989(1)	¼	0.998(5)
Ta	4b	1.0	0	0	½
O/N1	4c	0.67/0.33	0.462(4)	¼	0.062(6)
O/N2	8d	0.67/0.33	0.275(3)	0.033(3)	0.708(3)
x = 0.8					
Ca/Sr	4c	0.79(3)/0.21(3)	0.0190(7)	¼	0.998(3)
Ta	4b	1.0	0	0	½
O/N1	4c	0.67/0.33	0.466(3)	¼	0.077(3)
O/N2	8d	0.67/0.33	0.280(2)	0.031(2)	0.709(2)
x = 0.9					
Ca/Sr	4c	0.89(4)/0.11(4)	0.0288(6)	¼	0.995(2)
Ta	4b	1.0	0	0	½
O/N1	4c	0.67/0.33	0.485(3)	¼	0.076(2)
O/N2	8d	0.67/0.33	0.282(2)	0.041(1)	0.713(2)
x = 1.0					
Ca	4c	1.00(4)	0.0347(7)	¼	0.994(2)
Ta	4b	1.0	0	0	½
O/N1	4c	0.67/0.33	0.478(3)	¼	0.080(2)
O/N2	8d	0.67/0.33	0.281(2)	0.046(1)	0.713(2)

Tetragonal *I4/mcm* space group
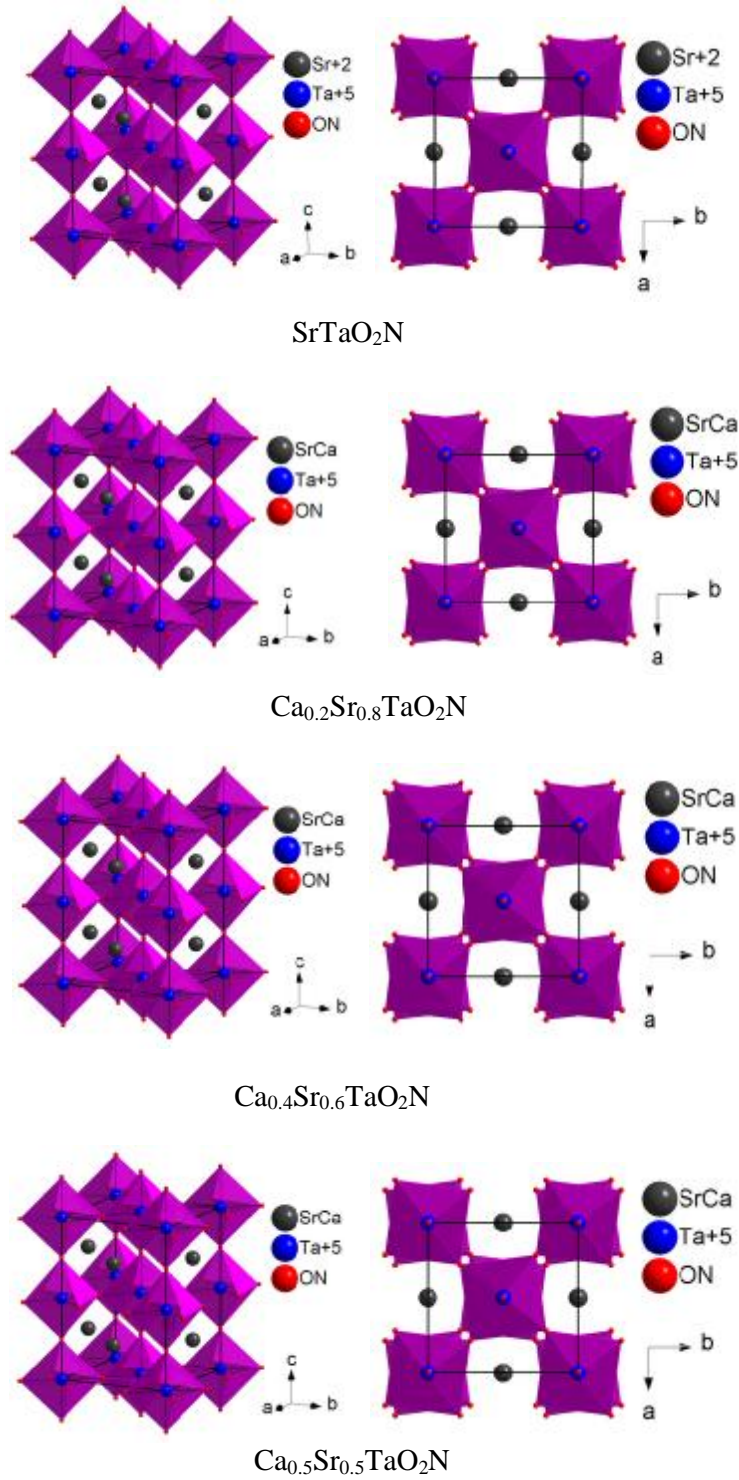
SrTaO$_2$N

Ca$_{0.2}$Sr$_{0.8}$TaO$_2$N

Ca$_{0.4}$Sr$_{0.6}$TaO$_2$N

Ca$_{0.5}$Sr$_{0.5}$TaO$_2$N

Figure 5-15 Crystal structure variation across the Ca$_x$Sr$_{1-x}$TaO$_2$N series illustrating the very slight changes in octahedral rotation

$Ca_{0.6}Sr_{0.4}TaO_2N$
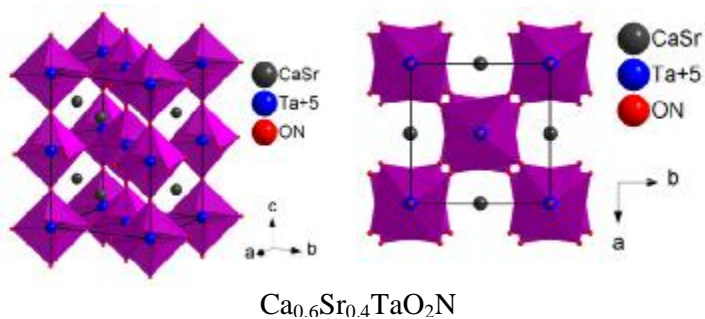
Orthorhombic *Pnma* space group
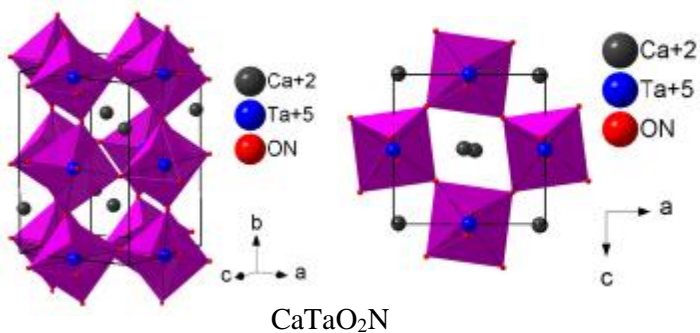
$Ca_{0.8}Sr_{0.2}TaO_2N$

$CaTaO_2N$

Figure 5-15 Crystal structure variation across the $Ca_xSr_{1-x}TaO_2N$ series illustrating the very slight changes in octahedral rotation (continued)

These changes mainly move the atom further from their perfect perovskite positions, consistent with the observed transition to lower (orthorhombic) symmetry. However, as mentioned above, the atomic displacements are very small. There is good agreement with expected values for the site occupation factors.

5.4 $Ba_xSr_{1-x}TaO_2N$

Consistent with the work of Pors *et al.* (1988), X-ray diffraction confirmed the existence of $Ba_xSr_{1-x}TaO_2N$ solid solutions prepared by direct nitridation of oxide and carbonate mixed powders, as shown in Figure 5-16.
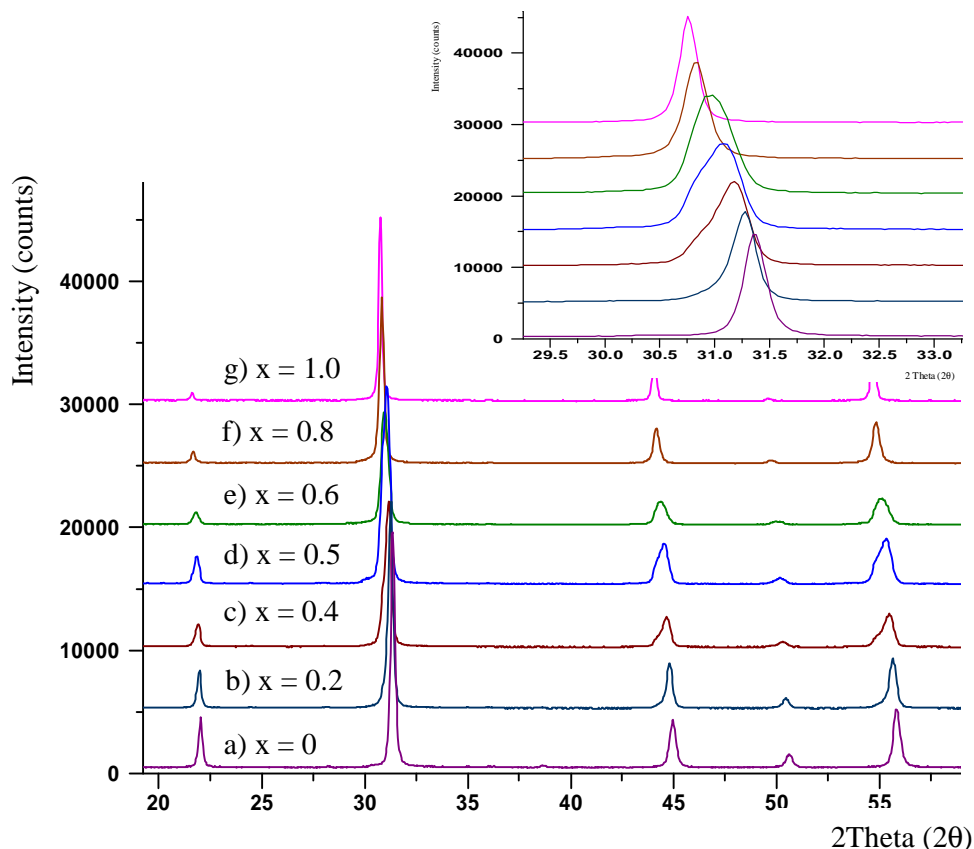
Figure 5-16 X-ray diffraction pattern of $Ba_xSr_{1-x}TaO_2N$, $0 \leq x \leq 1$

From previous work, the crystal structures of $SrTaO_2N$ and $BaTaO_2N$ have been established as tetragonal (space group *I4/mcm*) and cubic (*Pm3m*), respectively (Günther *et al.*, 2000, Pors *et al.*, 1988). In the present study, it was impossible from visual examination to identify differences in peak shape when comparing structures which were clearly tetragonal or clearly cubic. The broad and slightly asymmetric-shaped peaks for all reflections clearly consisted of overlapping

peaks as well as being affected by the $K_{\alpha 1}/ K_{\alpha 2}$ splitting. So it was not possible to identify the difference between tetragonal and cubic structures visually. In order to see whether more information could be obtained, the structures of $Ba_xSr_{1-x}TaO_2N$ series were characterised by Rietveld analysis using as starting parameters the previous crystal structure models of Günther *et al.* (2000) and Pors *et al.* (1988). For Sr-rich compositions, the tetragonal *I4/mcm* structure of $SrTaO_2N$ was expected to be appropriate and the cubic *Pm3m* symmetry for Ba-rich $Ba_xSr_{1-x}TaO_2N$ solid solutions. Starting parameters used for the Rietveld refinement are given in Table 5-10.

Table 5-10 starting parameters used for Rietveld analysis of $Ba_xSr_{1-x}TaO_2N$ compositions

Atom	Wyckoff	x	y	z	s.o.f.
Based on tetragonal *I4/mcm* SrTaO₂N[1]					
Ba/Sr	4b	0	½	¼	*x/1-x*
Ta	4c	½	½	0	1.0
O/N(1)	8h	0.7721	½+x	0	0.67/0.33
O/N(2)	4a	0	0	¼	0.67/0.33
Based on cubic *Pm3m* BaTaO₂N[2]					
Ba/Sr	1a	0	0	0	*x/1-x*
Ta	1b	½	½	½	1.0
O/N	3c	0	½	½	0.67/0.33

[1]a = b = 5.7049 Å, c = 8.0499 Å, $\alpha = \beta = \gamma = 90°$ (Günther *et al.*, 2000) and [2]a = 4.1128 Å, $\alpha = \beta = \gamma = 90°$ (Pors *et al.*, 1988)

Table 5-11 and Table 5-12 show final refinement indices and unit cell dimensions for compositions in the $Ba_xSr_{1-x}TaO_2N$ series assuming either a tetragonal or a cubic structure, respectively. The refinements are all satisfactory; both tetragonal *I4/mcm* and cubic *Pm3m* models gave similar R_{wp} values in the acceptable range (R_{wp} < 10%). The fact that such good refinements can be obtained in both cubic and tetragonal systems shows that the departure from perfect cubic symmetry into tetragonal is not very great. Figure 5-17 and Figure 5-18 show the result of fitting profile between the observed and calculated of $SrTaO_2N$ and $BaTaO_2N$ as a tetragonal and a cubic structure, respectively.
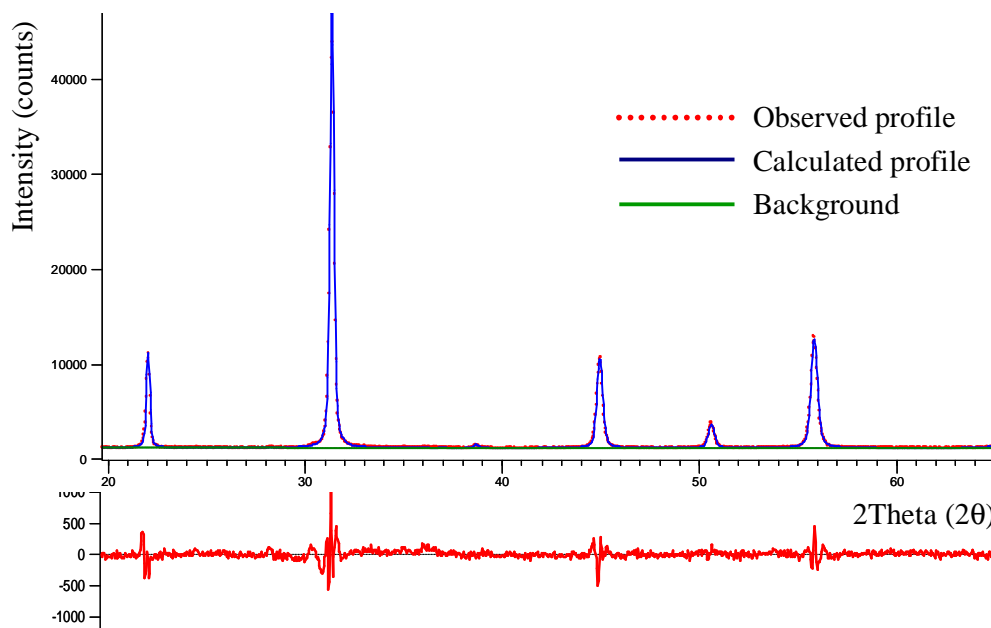
Figure 5-17 Observed and calculated profiles (top) and difference plot (bottom) of *I4/mcm* $SrTaO_2N$ after Rietveld refinement
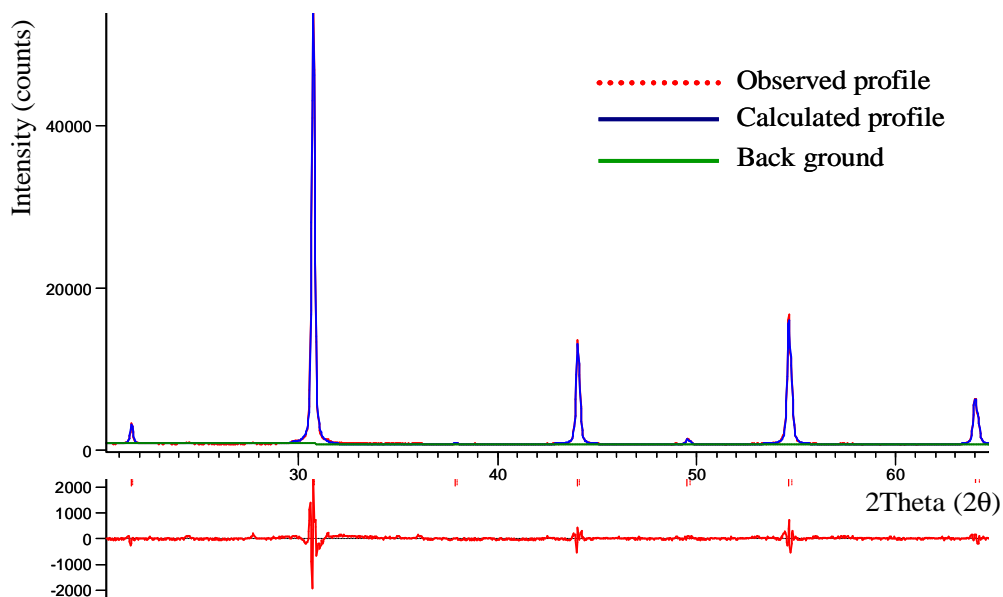
Figure 5-18 Observed and calculated profiles (top) and difference plot (bottom) of
*Pm*3*m* BaTaO$_2$N after Rietveld refinement

When the unit cell dimensions are plotted on versus Ba content (Figure 5-19 for
tetragonal; Figure 5-20 for cubic), it is clear that the unit cell variations are not
linear, and there is a discontinuity at approximately x = 0.6. This was the most
convincing evidence that compositions in the range $0 \leq x < 0.6$ are tetragonal,
whereas those in the range $0.6 \leq x \leq 1.0$ are cubic. This conclusion is in good
agreement with the previous work of Pors *et al.* (1988) who reported cubic solid
solutions for x > 0.56. The more definitive plot of cell dimensions is therefore
as shown in Figure 5-21 in which it is assumed that there is a region of mixed
tetragonal/cubic structures in the $0.5 < x < 0.6$ region.

Table 5-11 Rietveld refinement results for $Ba_xSr_{1-x}TaO_2N$ composition assuming a tetragonal crystal structure with space group *I4/mcm*

x	0	0.1	0.2	0.3	0.4	0.5	0.6	0.7	0.8	0.9	1.0
$\%R_e$	2.34	2.41	2.45	2.48	2.57	2.74	2.79	2.91	2.99	3.10	2.83
$\%R_p$	2.43	3.30	4.54	4.93	4.58	2.37	5.22	4.06	3.22	2.74	3.46
$\%R_{wp}$	3.17	4.23	5.90	6.53	5.89	3.25	7.05	5.45	4.23	3.62	4.51
GOF	1.84	3.09	5.80	6.95	5.25	1.41	6.38	3.50	2.00	1.36	2.54
a/ Å	5.7084(2)	5.7160(5)	5.7253(9)	5.7369(8)	5.7511(9)	5.7597(4)	5.7765(9)	5.7854(7)	5.789(1)	5.7968(6)	5.8054(5)
c/ Å	8.0520(5)	8.073(1)	8.088(2)	8.102(2)	8.116(2)	8.1328(9)	8.148(2)	8.168(2)	8.189(3)	8.204(2)	8.207(1)
V (10^6 pm^3)	262.38	263.78	265.10	266.65	268.42	269.80	271.89	273.39	274.48	275.66	276.58

Table 5-12 Rietveld refinement results of $Ba_xSr_{1-x}TaO_2N$ crystal structure as cubic structure with space group *Pm3m*

x	0	0.1	0.2	0.3	0.4	0.5	0.6	0.7	0.8	0.9	1.0
$\%R_e$	2.34	2.39	2.43	2.48	2.57	2.74	2.79	2.92	2.99	3.10	2.83
$\%R_p$	2.57	3.30	4.55	4.90	4.54	2.46	5.18	4.06	3.19	2.79	3.52
$\%R_{wp}$	3.33	4.22	5.90	6.48	5.82	3.36	7.03	5.41	4.21	3.69	4.59
GOF	2.02	3.12	5.88	6.83	5.12	1.51	6.34	3.44	1.98	1.41	2.63
a/ Å	4.02886(9)	4.0405(1)	4.0479(2)	4.0565(2)	4.0665(3)	4.0741(1)	4.0881(3)	4.0957(2)	4.1013(1)	4.10715(8)	4.11174(7)
V (10^6 pm^3)	65.40	65.96	66.33	66.75	67.25	67.62	68.32	68.71	68.99	69.28	69.51

Reliability factors in Rietveld analysis: R_e = R (expected), R_p = R (profile), R_{wp} = R (weighed profile) and GOF = Goodness of Fit; V = unit cell volume; numbers in parenthesis are estimated standard deviations.
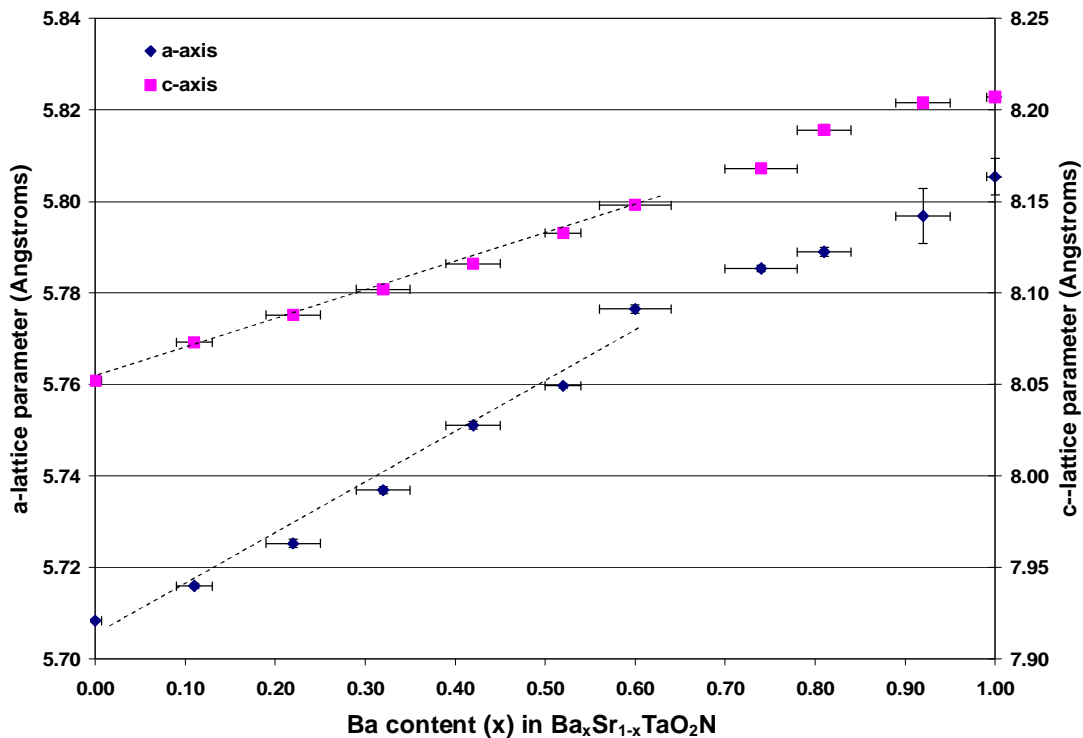
Figure 5-19 Variation in unit cell parameters of $Ba_xSr_{1-x}TaO_2N$ versus Ba content on
the assumption of a tetragonal structure model
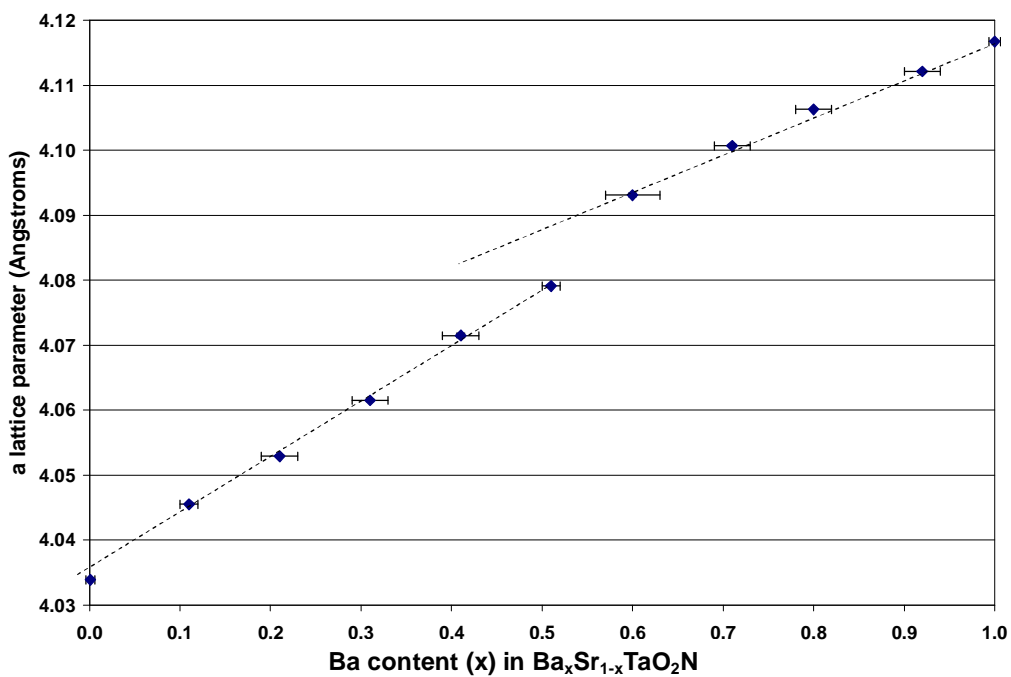
Figure 5-20 Variation in unit cell parameters of $Ba_xSr_{1-x}TaO_2N$ versus Ba content on
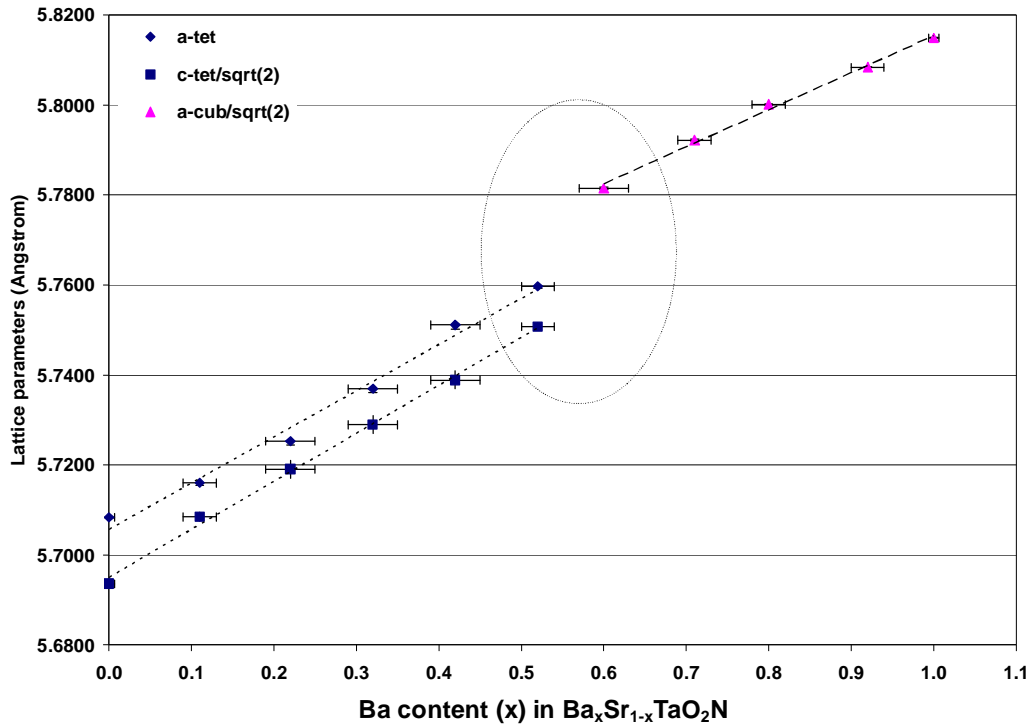the assumption of a cubic structure model

Figure 5-21 Structure transition of $Ba_xSr_{1-x}TaO_2N$ from tetragonal in Sr-rich to cubic in Ba-rich solid solutions

The crystal structures of $Ba_xSr_{1-x}TaO_2N$ as being tetragonal for x < 0.5 and cubic for x > 0.6 are shown in Figure 5-22 and the related atomic coordinates for $Ba_xSr_{1-x}TaO_2N$ solid solution compositions with $0 \leq x \leq 1.0$ are given in Table 5-13. Consistently, all structures are very similar; no octahedral distortion was significantly observed. .

Table 5-13 Atomic coordinates movement of $Ba_xSr_{1-x}TaO_2N$ in tetragonal model

Atom	Wyckoff	s.o.f.	x	y	z
x = 0					
Sr	4b	1.000(7)	0	0.5	0.25
Ta	4c	1.0	0	0	0
O/N1	4a	1.0	0	0	0.25
O/N2	8h	1.0	0.769(2)	0.269(2)	0
x = 0.2					
Ba/Sr	4b	0.22(3)/0.78(3)	0	0.5	0.25
Ta	4c	1.0	0	0	0
O/N1	4a	1.0	0	0	0.25
O/N2	8h	1.0	0.771(5)	0.271(5)	0
x = 0.4					
Ba/Sr	4b	0.42(3)/0.58(3)	0	0.5	0.25
Ta	4c	1.0	0	0	0
O/N1	4a	1.0	0	0	0.25
O/N2	8h	1.0	0.774(5)	0.274(5)	0
x = 0.5					
Ba/Sr	4b	0.52(2)/0.48(2)	0	0.5	0.25
Ta	4c	1.0	0	0	0
O/N1	4a	1.0	0	0	0.25
O/N2	8h	1.0	0.776(2)	0.276(2)	0
x = 0.6					
Ba/Sr	4b	0.60(4)/0.40(4)	0	0.5	0.25
Ta	4c	1.0	0	0	0
O/N1	4a	1.0	0	0	0.25
O/N2	8h	1.0	0.778(4)	0.278(4)	0
x = 0.8					
Ba/Sr	4b	0.81(3)/0.19(3)	0	0.5	0.25
Ta	4c	1.0	0	0	0
O/N1	4a	1.0	0	0	0.25
O/N2	8h	1.0	0.778(3)	0.278(3)	0
x = 1.0					
Ba	4b	1.000(9)	0	0.5	0.25
Ta	4c	1.0	0	0	0
O/N1	4a	1.0	0	0	0.25
O/N2	8h	1.0	0.771(3)	0.271(3)	0

Tetragonal *I4/mcm* space group
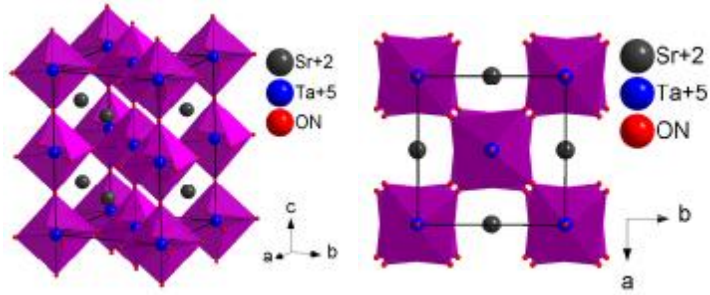
SrTaO$_2$N
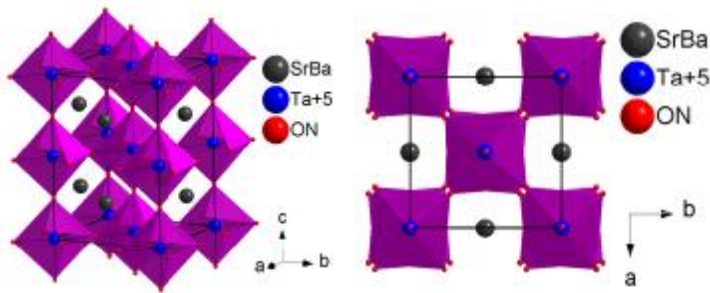
Ba$_{0.2}$Sr$_{0.8}$TaO$_2$N
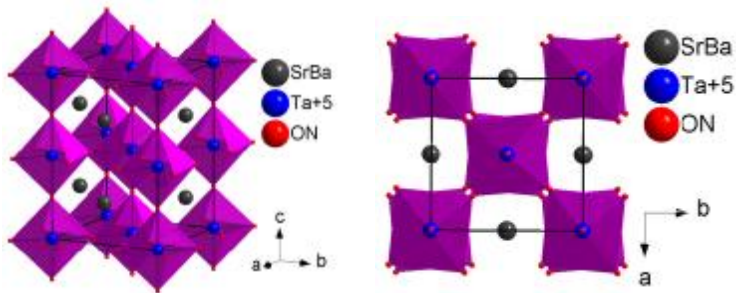
Ba$_{0.4}$Sr$_{0.6}$TaO$_2$N
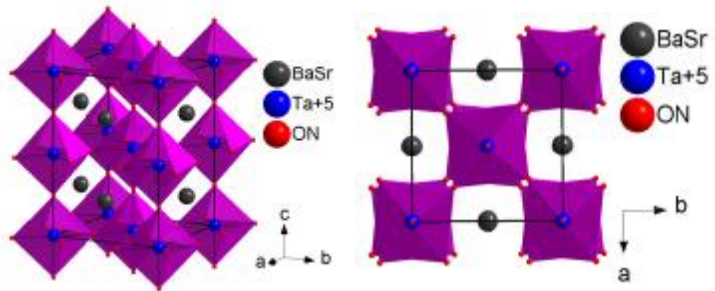
Ba$_{0.5}$Sr$_{0.5}$TaO$_2$N

Figure 5-22 Crystal structure of Ba$_x$Sr$_{1-x}$TaO$_2$N illustrating the octahedral distortions

Cubic *Pm*3*m* space group
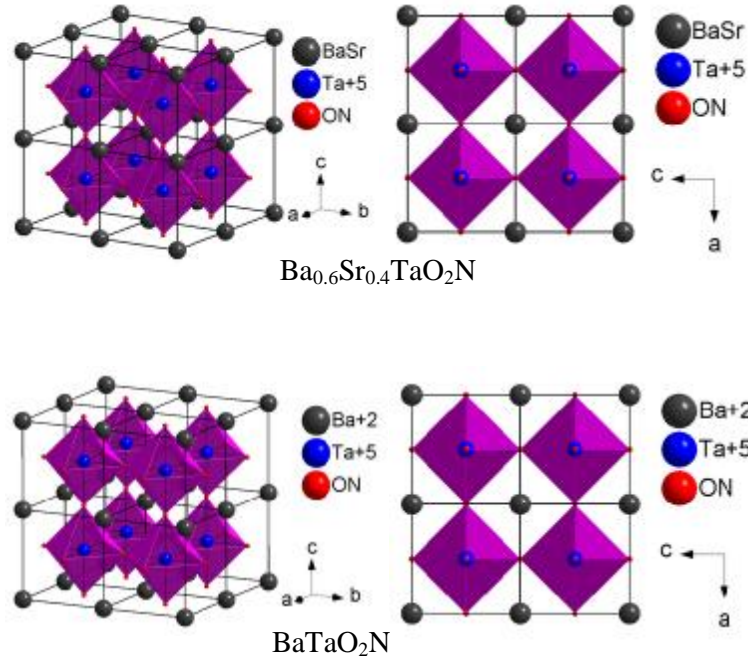
Ba$_{0.6}$Sr$_{0.4}$TaO$_2$N

BaTaO$_2$N

Figure 5-22 Crystal structure of Ba$_x$Sr$_{1-x}$TaO$_2$N illustrating the octahedral distortions

(continued)

5.5   Discussion and conclusions

Complete ranges of perovskite oxynitride solid solution were observed across the series La$_x$Nd$_{1-x}$TiO$_2$N, Ca$_x$Sr$_{1-x}$TaO$_2$N and Ba$_x$Sr$_{1-x}$TaO$_2$N and structure refinements were successfully carried out by means of Rietveld procedures. La$_x$Nd$_{1-x}$TiO$_2$N solid solutions with high x values were indexed as orthorhombic *Pnma* and with low x values as orthorhombic *Imma*. A systematic variation in a-, b- and c- axis lengths and Ti-(O,N) octahedral distortion was observed with increasing La substitution.   When Ca is substituted for Sr in Ca$_x$Sr$_{1-x}$TaO$_2$N solid solutions, the lattice parameters decrease with increasing Ca content. For x ≤ 0.6, the crystal structures of Ca$_x$Sr$_{1-x}$TaO$_2$N compositions are tetragonal with the SrTaO$_2$N-type of structure, whilst those with x > 0.6 prefer an

orthorhombic structure. However, the octahedral distortions are very small. Consistent with work of Pors *et al.* (1988), the crystal structures of $Ba_xSr_{1-x}TaO_2N$ solid solutions retained cubic symmetry like-$BaTaO_2N$ for $x > 0.6$ and the remainder are tetragonal like $SrTaO_2N$.

Based on the Goldschmidt tolerance factor, oxynitrides such as $CaTaO_2N$, $SrTaO_2N$ and $BaTaO_2N$ should form cubic perovskite structures (Wolff and Dronskowski, 2008). However, the simple cubic perovskite can be achieved only when M–O and M–N bonds have the same lengths, which is not the case. M–N bonds tend to be shorter than M–O bonds due to the covalent character of nitrogen (Fang *et al.*, 2003). All perovskite oxynitrides generally show lower crystal symmetry than cubic. $BaTaO_2N$ was previously determined as having a cubic perovskite structure (Marchand *et al.*, 1986) and a very high dielectric constant (Kim *et al.*, 2004). Since high-k dielectric materials often exhibit polar behaviour and display phase transitions to lower symmetry structures (Page *et al.*, 2007), the behaviour of $BaTaO_2N$ is uncommon. Previously, Fang *et al.* (2003) reported that the local symmetry of $BaTaO_2N$ should be lower than *m3m* due to the replacement of oxygen by nitrogen in the crystal structure, compared with the cubic perovskite $BaTiO_3$. From first-principles electronic-structure calculations, molecular-dynamic simulations suggested that a lower local symmetry such as tetragonal (*I4/mcm*) or orthorhombic (*Pnma*) would be more stable for $BaTaO_2N$ rather than cubic (Fang *et al.*, 2003, Wolff and Dronskowski, 2008). From density-functional theory calculations, a *Pbmn* orthorhombic structure was predicted as being the most stable for $SrTaO_2N$ (Page *et al.*, 2007). The classification of $BaTaO_2N$ as cubic is justified from the empirical point of view, as evidence from X-ray and neutron diffraction find

difficulties in differentiating the small differences in unit cell parameters. Wolff and Dronskowski (2008) concluded that alkaline-earth-based tantalum and niobium oxynitrides with perovskite-type structures should favourably crystallise with distorted Ta–(O/N) octahedra in tetragonal or orthorhombic systems. The type of crystal structure observed for oxynitrides may also depend upon the synthesis routes and processing conditions. In the present study, it was not possible to determine whether $SrTaO_2N$ and $BaTaO_2N$ would be more energetically stable if they had orthorhombic structures. X-ray diffraction spectra and Rietveld analysis showed that the most likely structures for $Ba_xSr_{1-x}TaO_2N$ oxynitrides would be tetragonal or possible cubic. However, it should be recognised that the structural results presented here require further more detailed work using neutron diffraction to confirm these conclusions.

5.6   References

Clarke, S. J., Guinot, B. P., Michie, C. W., Calmont, M. J. C. and Rosseinsky, M. J. (2002) Oxynitride perovskites: Synthesis and structures of $LaZrO_2N$, $NdTiO_2N$ and $LaTiO_2N$ and comparison with oxide perovskites. *Chem. Mater.,* 14**,** 288-294.

Fang, C. M., De Wijs, G. A., Orhan, E., De With, G., De Groot, R. A., Hintzen, H. T. and Marchand, R. (2003) Local structure and electronic properties of $BaTaO_2N$ with perovskite-type structure. *Journal of Physics and Chemistry of Solids,* 64**,** 281-286.

Günther, E., Hagenmayer, R. and Jansen, M. (2000) strukturuntersuchungen an den Oxidnitriden $SrTaO_2N$, $CaTaO_2N$ und $LaTaON_2$ mittels Neutronen- und Röntgenbeugung. *Z. Anorg. Allg. Chem. ,* 626**,** 1519-1525.

Kim, Y.-I., Woodward, P. M., Baba-Kishi, K. Z. and Tai, C. W. (2004) Characterization of the structural, optical, and dielectric properties of oxynitride perovskites AMO_2N (A = Ba, Sr, Ca; M = Ta, Nb). *Chemistry of Materials,* 16**,** 1267-1276.

Logvinovich, D., Bocher, L., Sheptyakov, D., Figi, R., Ebbinghaus, S. G., Aguiar, R., Aguirre, M. H., Reller, A. and Weidenkaff, A. (2009)

Microstructure, surface composition and chemical stability of partly ordered LaTiO$_2$N. *Solid State Sciences,* 11**,** 1513-1519.

Logvinovich, D., Börger, A., Döbeli, M., Ebbinghaus, S. G., Reller, A. and Weidenkaff, A. (2007) Synthesis and physical chemical properties of Ca-substituted LaTiO$_2$N. *Progress in Solid State Chemistry,* 35**,** 281-290.

Marchand, R., Pors, F. and Laurent, Y. (1986) Préparation et caractérisation de nouveaux oxynitrures à structure perovskite. *Rev. Int. Hautes Tempér. Réfract. Fr.,* 23**,** 11-15.

Marchand, R., Pors, F. and Y.Laurent (1991) Nouvelles perovskites oxynitrures de stoechiometrie ABO$_2$N (A = lanthanide, B = Ti) et ABON$_2$ (A = lanthanide, B = Ta ou Nb) *Annales des Chimie, France,* 16**,** 553-560.

Motohashi, T., Hamade, Y., Masubuchi, Y., Takeda, T., Murai, K. i., Yoshiasa, A. and Kikkawa, S. (2009) Structural phase transition in the perovskite-type tantalum oxynitrides, Ca$_{1-x}$Eu$_x$Ta(O,N)$_3$. *Materials Research Bulletin,* 44**,** 1899-1905.

Page, K., Stoltzfus, M. W., Kim, Y. I., Proffen, T., Woodward, P. M., Cheetham, A. K. and Seshadri, R. (2007) Local atomic ordering in BaTaO2N studied by neutron pair distribution function analysis and density functional theory. *Chemistry of Materials,* 19**,** 4037-4042.

Pors, F., Bacher, P., Marchand, R., Laurent, Y. and Roult, G. (1988) Etude structurale par diffraction neutronique de la pérovskite oxyazotée SrTaO$_2$N et de la solution solide Ba$_{1-x}$Sr$_x$TaO$_2$N   *Rev. Int. Hautes Tempér. Réfract. Fr.,* 24**,** 239-246.

Shao, Z., Saitzek, S., Roussel, P., Mentré, O., Prihor Gheorghiu, F., Mitoseriu, L. and Desfeux, R. (2010) Structural and dielectric/ferroelectric properties of (La$_{1-x}$Nd$_x$)$_2$Ti$_2$O$_7$ synthesized by sol-gel route. *Journal of Solid State Chemistry,* 183**,** 1652-1662.

Wolff, H. and Dronskowski, R. (2008) First-principles and molecular-dynamics study of structure and bonding in perovskite-iype oxynitrides ABO$_2$N (A = Ca, Sr, Ba; B = Ta, Nb). *Journal of Computational Chemistry,* 29**,** 2260-2267.

Yashima, M., Saito, M., Nakano, H., Takata, T., Ogisu, K. and Domen, K. (2010) Imma perovskite-type oxynitride LaTiO$_2$N: Structure and electron density. *Chemical Communications,* 46**,** 4704-4706.

Chapter 6 Synthesis and dielectric properties of thin layered (La,Nd)TiO$_2$N perovskites

6.1 Introduction

The major problem hindering the measurement of dielectric properties of perovskite oxynitrides is their sinterability, which so far has prevented the preparation of high-quality bulk samples, and the few researchers who have tackled this problem have had to be content with lower density materials. Kim *et al.* (2004) prepared compacted, low-density pellets of ATaO$_2$N (A = Ba, Sr, Ca) and BaNbO$_2$N by uniaxial pressing (30 kpsi) followed by cold isostatic pressing (60 kpsi) of their oxynitride powders, heated under flowing ammonia at 1020ºC for 2 hours. Le Paven-Thivet *et al*. (2007) densified LaTiO$_2$N by cold-pressing the powder followed by pressureless sintering at 1100ºC for 10 hours under flowing ammonia but only 50% of the theoretical density was achieved. Obtaining a sample with > 95% of the theoretical density is essential for obtaining meaningful measurement of dielectric properties.

In the present work, the results shown in Chapter 4 demonstrated that pressureless sintering was not a successful route for obtaining dense samples of LaTiO$_2$N principally because the temperatures required for atomic diffusion in this material are in excess of the decomposition temperature, which is approximately 1250ºC (in a reducing environment). Sintering additives were not used because these generally result in the presence of secondary (grain-boundary) phases, and previous

work on nitrides and oxynitrides has shown that even small amounts of a grain boundary phase can dominate the overall electrical performance, completely masking the behaviour of the main phase. The alternative process of hot-pressing was also explored, and even though it was possible to obtain quite high densities (85% of theoretical) at temperatures above 1000ºC, the reducing atmosphere of the hot-press (graphite dies were used, but the sample was partially protected by surrounding with boron nitride) generally resulted in the presence of trace amounts of TiN in the final product. This resulted in the sample being electrically conducting and therefore the true dielectric properties of $LaTiO_2N$ could not be measured.

An alternative strategy was therefore developed. It is much easier to obtain dense oxide materials than their corresponding oxynitrides, and nitriding these bulk samples would be expected to result in the formation of a thin and dense surface layer of oxynitride (see Figure 6-1).

Oxynitride Layer

a) Oxide pellet   b) Cross section of   c) Removed oxynitride
                      coated oxynitride   side coat
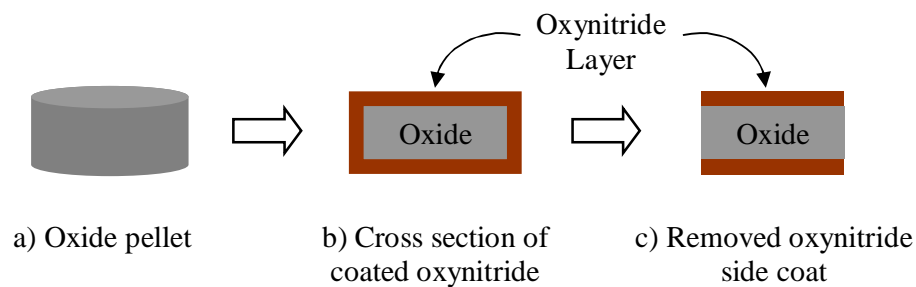
Figure 6-1 Coating with a thin surface layer of oxynitride

Even though it is well established that nitriding of bulk oxide pellets results in only thin surface layers, it was expected that by using thin starting samples of dense oxide, the thickness of the oxynitride layer could reach a significant proportion of the total thickness, and knowing the dielectric constant of the bulk

176

oxide, measurement of the overall dielectric constant would enable a reasonably accurate value of the permittivity of the oxynitride to be calculated by a subtraction procedure. The dielectric properties of the whole coated oxynitride pellet and with the side oxynitride coating removed were studied in comparison.

Initial experiments were carried out using $La_2Ti_2O_7$ as the starting oxide. $La_2Ti_2O_7$ is an excellent high temperature dielectric in its own right (Curie temperature ≈ 1500°C), displaying strong ferroelectric behaviour (Fasquelle *et al.*, 2005), and having a dielectric constant 48.8 for a dense oxide (99% of theoretical density) (Paul and Robert, 1991), a low temperature coefficient of permittivity and low dielectric loss at medium frequencies (100 kHz–1MHz) (Fasquelle *et al.*, 2005, Zhang *et al.*, 2007). Because of the good dielectric properties of $La_2Ti_2O_7$, a surface thin film of oxynitride on $La_2Ti_2O_7$ would be expected to produce a material with possibly better high-k dielectric properties in its own right, avoiding any mismatch between the dielectric layer and the substrate. It was therefore of interest to study the dielectric performance of the coated sample in addition to using this as a method of determining the dielectric properties of $LaTiO_2N$ itself.

In the early part of this study, it was found that nitriding $Ln_2Ti_2O_7$ powders to produce $LnTiO_2N$ oxynitrides was relatively easy when the rare earth element was lanthanum, but the process became significantly more difficult as the atomic number of the rare earth element increased, because the reactivity of rare earth elements decreases with increasing atomic number. The procedure outlined above was therefore extended to neodymium but not to higher rare earth elements. Cerium was not used because initial experiments had showed that because of the

variable valency of Ce, it was more difficult to produce a $CeTiO_2N$ phase containing trivalent cerium and tetravalent titanium during the nitriding step. Only $La_2Ti_2O_7$ and $Nd_2Ti_2O_7$ pellets were therefore chosen to prepare the coated oxynitride films. Takahashi *et al.* (1993) prepared $La_2Ti_2O_7$ by a coprecipitation technique. It was found that substitution of La^{3+} by the smaller sized Nd^{3+} ion (La:Nd = 1:1) caused the dielectric constant to decrease from 47 of $La_2Ti_2O_7$ to 42 of $La_{0.5}Nd_{0.5}Ti_2O_7$ and 36 of $Nd_2Ti_2O_7$ with the lower dielectric loss. Recently, $(La_xNd_{1-x})_2Ti_2O_7$ solid solutions have been synthesised by sol-gel techniques and structural, dielectric and ferroelectric properties measured (Shao *et al.*, 2010). These oxide solid solutions exhibited dielectric constant in the ranges 10-80 and were almost frequency independent in the range $1–10^6$ Hz. In the present work, dense $(La_xNd_{1-x})_2Ti_2O_7$ ($0 \leq x \leq 1$) oxide compositions were therefore produced and films of solid $La_xNd_{1-x}TiO_2N$ deposited on the surface of the oxide precursor by ammonia nitridation. The technique was also extended to include the formation of thin films of $ATaO_2N$ (A = Ca and Sr) on dense samples of their respective oxides.

6.2 Deposition of oxynitride films on dense oxide ceramics

$Ln_2Ti_2O_7$ (Ln = La and Nd) and $A_2Ta_2O_7$ (A = Ca and Sr) powders were prepared by solid state reaction. Appropriate weights of oxide and carbonate starting powders were mixed and ground in iso-propanol and compacted into pellets as described in Chapter 3. The pellets were calcined in air at 1200°C for 5 hours and then, after regrinding and pelletising, heated at 1350°C for 16 hours to reach the single phase product of $Ln_2Ti_2O_7$. Dense oxide pellets were prepared by a

subsequent pressureless sintering step at 1500°C for 3 hours in the case of $La_2Ti_2O_7$, and 1400°C for 3 hours for $Nd_2Ti_2O_7$. Approximately, 85–90% of theoretical density was achieved (see Table 6-1). In order to improve powder compaction, 1–2 drops of 15% polyvinyl alcohol (PVA) solution was used as a binder (Wang *et al.*, 2006). The powders were well mixed and pressed into disk-shaped compacts and then heated at 550°C for 2 hours to evaporate the PVA, and subsequently pressureless sintered at 1500°C for 3 hours.

Table 6-1 Densities of sintered $La_2Ti_2O_7$

Oxide	[1]Theoretical density (ρ_c) (g/cm^3)	Experimental density (ρ) (g/cm^3)	% ρ_c
$La_2Ti_2O_7$	5.78	5.25	90%
$La_2Ti_2O_7$+PVA	5.78	5.41	94%

[1] X-ray diffraction database ICDD number: 00-028-00517

With the PVA addition, the density was slightly improved from 90 to 94% of the theoretical density. However, X-ray diffraction showed that the $La_2Ti_2O_7$ peaks shifted to smaller *d*-spacings possibly corresponding to $La_2Ti_2O_{7-x}$ with some unidentified peaks. Therefore, PVA binder was not explored further as an aid for $Ln_2Ti_2O_7$ densification. Thereafter, the pressureless sintered oxide pellets were nitrided in flowing ammonia at 950°C for increasing reaction times. For samples of $La_2Ti_2O_7$ nitrided for 4, 8 and 12 hours, X-ray diffraction revealed mainly the oxynitride peaks for $LaTiO_2N$ with very weak peaks of unreacted $La_2Ti_2O_7$ also present. For longer reaction times (16, 20 and 24 hours), X-ray diffraction gave only the peaks of pure, single phase $LaTiO_2N$, as shown in Figure 6-2. A

scanning electron micrograph of the top surface of the LaTiO$_2$N pellet after ammonia nitriding at 950ºC for 16 hours is shown in Figure 6-3.
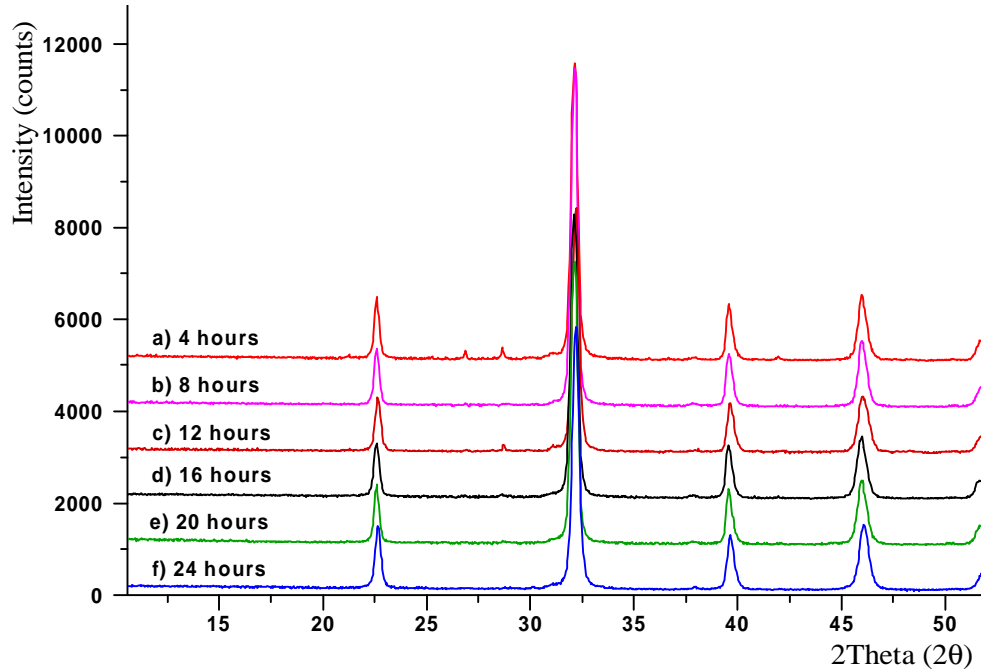
Figure 6-2 X-ray diffraction patterns of LaTiO$_2$N formed as a surface layer on dense La$_2$Ti$_2$O$_7$ by ammonia nitridation for increasing lengths of time at 950ºC
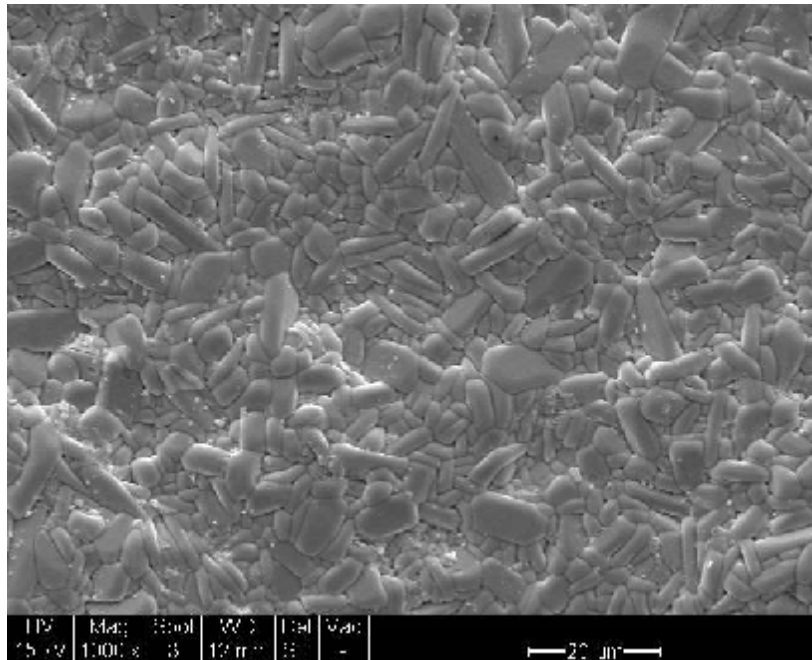
Figure 6-3 SEM image of the top surface of the La$_2$Ti$_2$O$_7$ pellet nitrided at 950ºC 16 hours
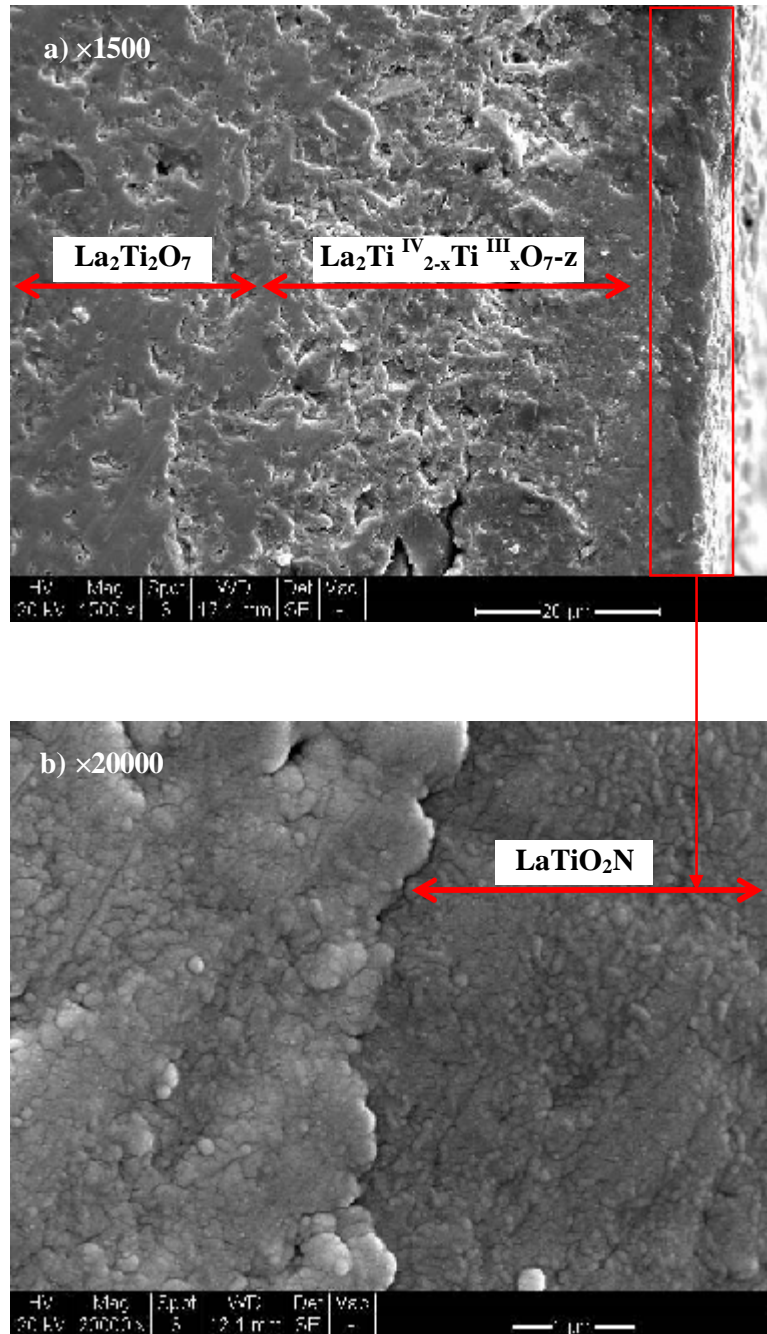
Figure 6-4 SEM images of cross sections of the $La_2Ti_2O_7$ pellet nitrided at 950ºC 16 hours

The microstructure shows a reasonably dense interlocked mesh of slightly elongated rectangular grains, exhibiting lengths of up to 10 µm and breadths of up to 5 µm. Clearly the procedure of depositing an oxynitride layer on top of a dense oxide substrate successfully produces a dense surface layer of the oxynitride.

Scanning electron micrographs of the cross section of the nitrided pellets confirmed the sandwich-like structure of oxynitride layers on the top and bottom of the sample with unreacted oxide layer in the middle, as shown in Figure 6-4. After 16-hours of nitridation, the micrograph shows that an approximately 4 μm thick film of $LaTiO_2N$ had been produced. Below the oxynitride layer, it was expected that the starting $La_2Ti_2O_7$ would be unchanged even though some variation in contrast was observed.
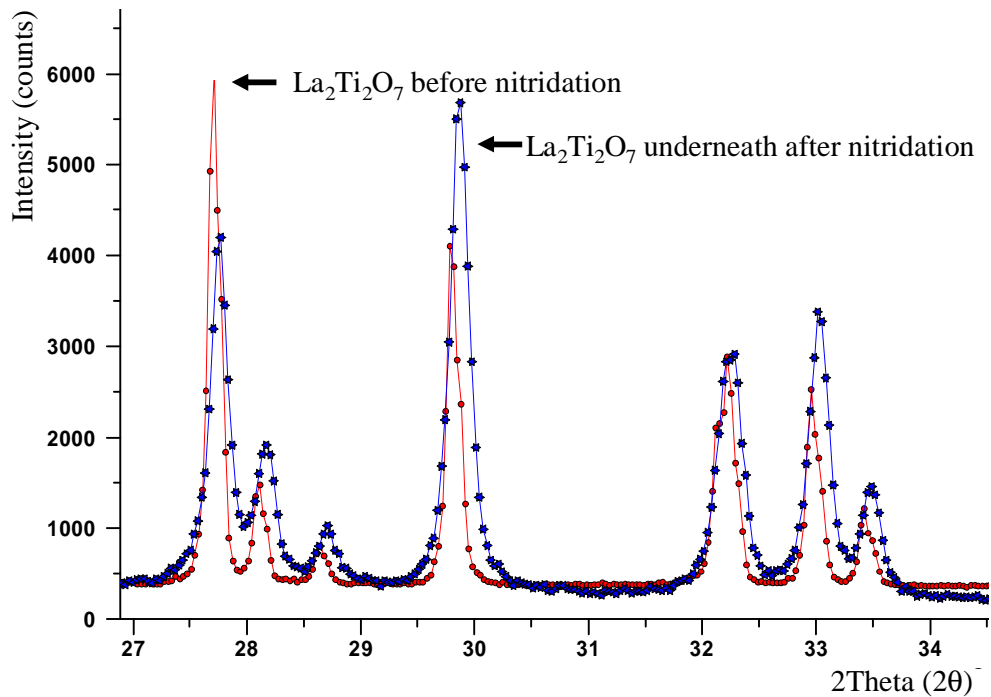
Figure 6-5 X-ray diffraction pattern of the $La_2Ti_2O_7$ underneath the surface $LaTiO_2N$ film

Figure 6-5 shows the X-ray diffraction pattern of the $La_2Ti_2O_7$ immediately underneath the oxynitride layer, the surface having been removed by careful polishing. Clearly the peaks have shifted slightly to the right (i.e. to higher θ or smaller d-spacings) compared with the normal $La_2Ti_2O_7$ peaks. It should be noted that whereas $La_2Ti_2O_7$ is white or cream and $LaTiO_2N$ is reddish brown to dark

brown, after nitridation of $La_2Ti_2O_7$ pellets, for every sample treatment, the whole of the sample appeared as dark grey. This is believed to be due to the fact that at temperatures above 500°C, ammonia decomposes into active atomic nitrogen and hydrogen, and while the active nitrogen atoms nitride the surface of the $La_2Ti_2O_7$ pellet to form the oxynitride layer, the hydrogen atoms, which are very small, can penetrate into the oxide ceramic much further than the nitrogen atoms and cause reduction of the underlying $La_2Ti_2O_7$. In such a reducing atmosphere, Ti^{4+} ions are partially reduced to Ti^{3+} ions, which normally causes samples to turn black (Canales-Vázquez *et al.*, 2005); simultaneously the oxygen combines with hydrogen and is released from the system as gaseous H_2O. Assuming overall charge balance, the reduced lanthanum titanate will then be of composition $La_2Ti^{IV}_{2-x}Ti^{III}_xO_{7-z}$ (where z is x/2). Because of the oxygen deficiency, the lattice will become smaller; and the X-ray diffraction peaks will be shifted to smaller *d*-spacings. It should also be remembered that in this case the starting $La_2Ti_2O_7$ had only been densified to a bulk density of 85%, and therefore the residual pores will significantly aid the diffusion of hydrogen through the oxide layer. Further work should therefore be directed towards studying the nitriding of fully dense $La_2Ti_2O_7$ samples.

The same procedure was used to generate thin layers of $NdTiO_2N$ on a $Nd_2Ti_2O_7$ substrate. At approximately 85% of theoretical density, samples of this oxide material were nitrided in ammonia for increasing lengths of time as described previously for $La_2Ti_2O_7$. X-ray diffraction traces of the sample (Figure 6-6) show that even after 72-hours of nitridation, the rate of formation of the $NdTiO_2N$ layer was much slower than in the lanthanum case.
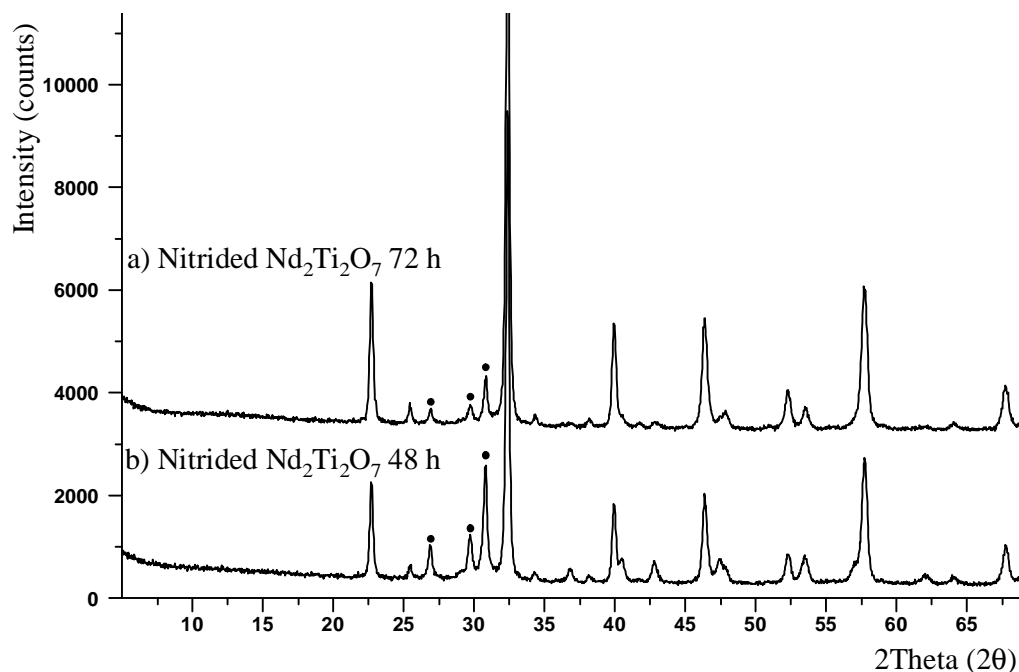
Figure 6-6 X-ray diffraction patterns of NdTiO$_2$N formed as a surface layer on dense Nd$_2$Ti$_2$O$_7$ by ammonia nitridation for increasing lengths of time at 950°C

As mentioned above, the reactivity of the rare earth elements decreases markedly with atomic number, so this observation is not surprising. The top surface and the cross-section sandwich structure of the NdTiO$_2$N film on Nd$_2$Ti$_2$O$_7$ are shown in the light micrograph of Figure 6-7. The cross sectional image shows the thickness of the NdTiO$_2$N layer to be approximately 2.3–2.7 μm, and such a thin layer would be expected to allow the X-ray beam to pass through to the oxide underneath. The grains of NdTiO$_2$N can be seen as irregular and angular (the blurry nature of this image is due to the imperfect smoothness of the specimen). As was the case with the LaTiO$_2$N, the top surface of the nitrided Nd$_2$Ti$_2$O$_7$ can be seen as a mixed colour of the normal dark brown of NdTiO$_2$N and some darkening due to reduction (see Figure 6-7).
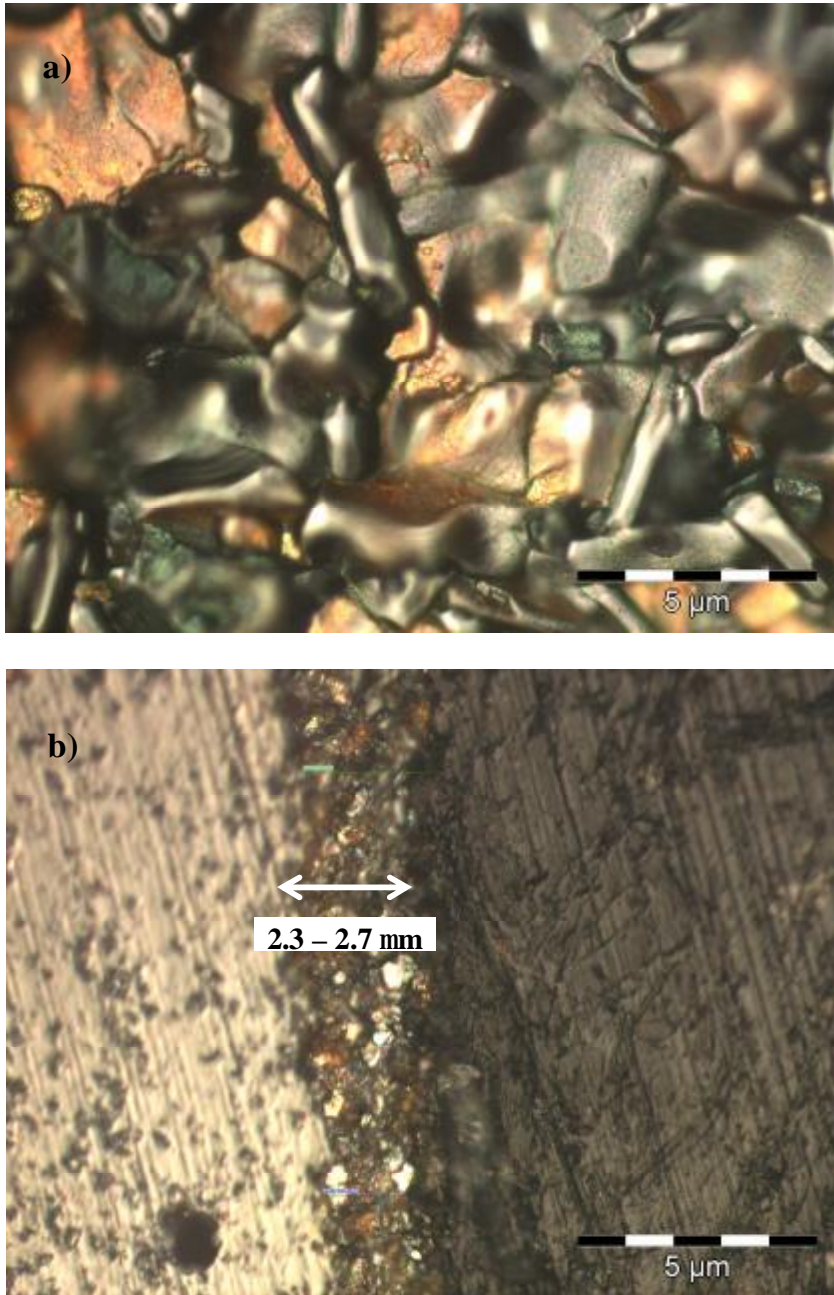
Figure 6-7 a) Top-surface and b) cross sectioned image of the NdTiO$_2$N film on a Nd$_2$Ti$_2$O$_7$ substrate

It is assumed that hydrogen had diffused into the oxide layer and caused some reduction of Ti^{4+} into Ti^{3+} with consequent loss of oxygen to balance the overall charge. Consistently with the lanthanum case, when the oxynitride layer was

polished off by about 0.08 mm, X-ray diffraction shows that the $Nd_2Ti_2O_7$ peaks shifted to smaller *d*-spacings and when the surface was polished off further (≈ 0.42 mm) the $Nd_2Ti_2O_7$ peaks are closer to their initial positions before nitriding (see Figure 6-8).
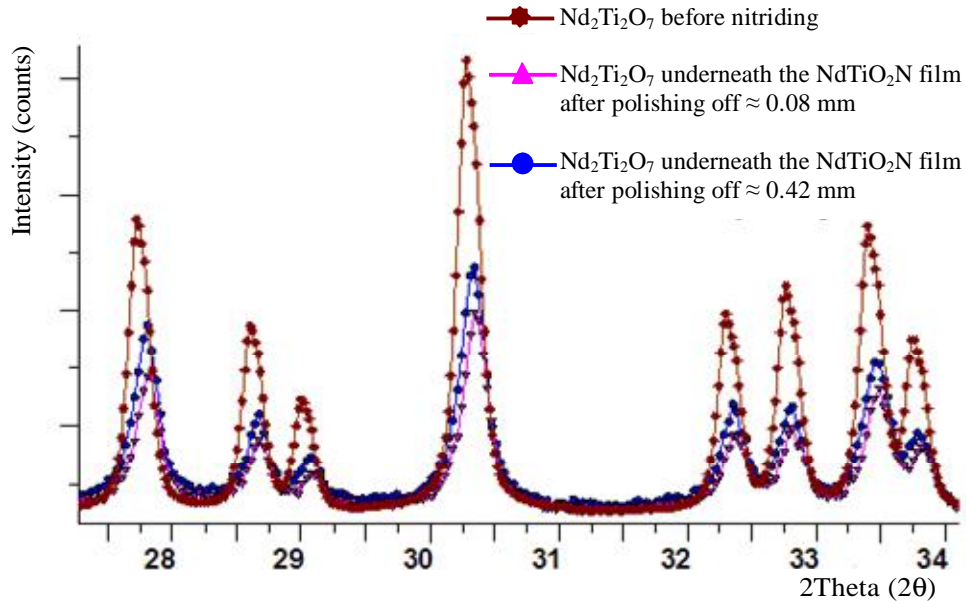
Figure 6-8 X-ray diffraction spectra of $Nd_2Ti_2O_7$ underneath the $NdTiO_2N$ film

Layers of $La_xNd_{1-x}TiO_2N$ solid solution were also prepared by reacting preprepared $(La_xNd_{1-x})_2Ti_2O_7$ pellets with ammonia in the same way as described previously for $La_2Ti_2O_7$ and $Nd_2Ti_2O_7$. Compositions were explored every 0.2 increment in x, and the mid point (x = 0.5) was also included. X-ray diffraction traces of the initial oxide samples showed that a solid solution did occur across the whole range and also confirmed the formation of the oxynitride films on these dense oxide samples after a 24-hour ammonia treatment, as shown in Figure 6-9 and Figure 6-10. Traces of oxide peaks are still just visible in the pure Nd sample (x = 0) after this nitriding time, whereas all the rest show only oxynitride peaks, indicating a substantial (> 2 μm) thickness of the oxynitride layer.
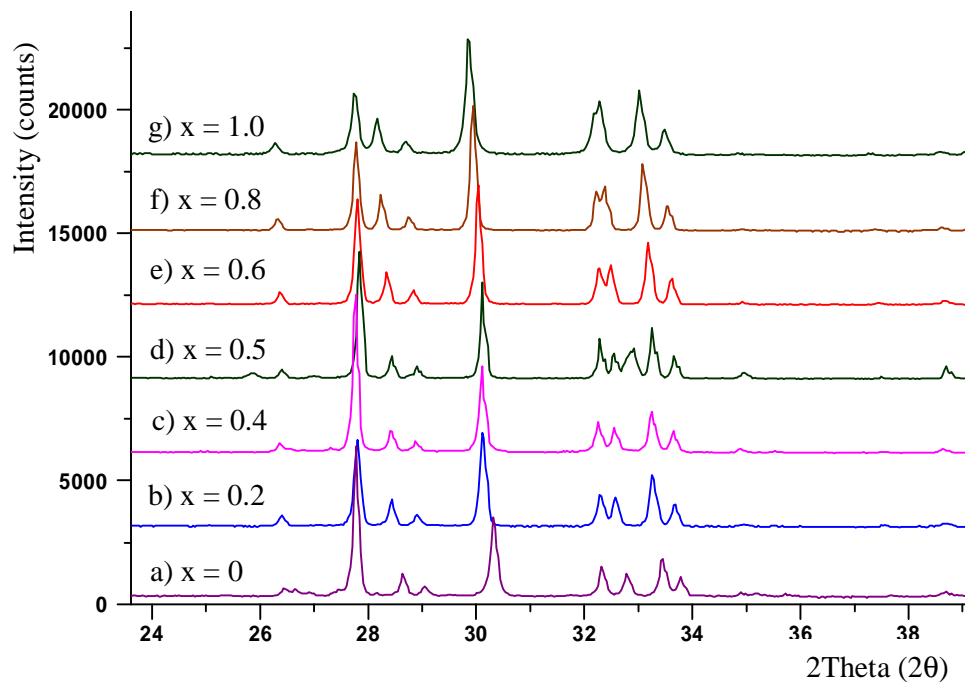
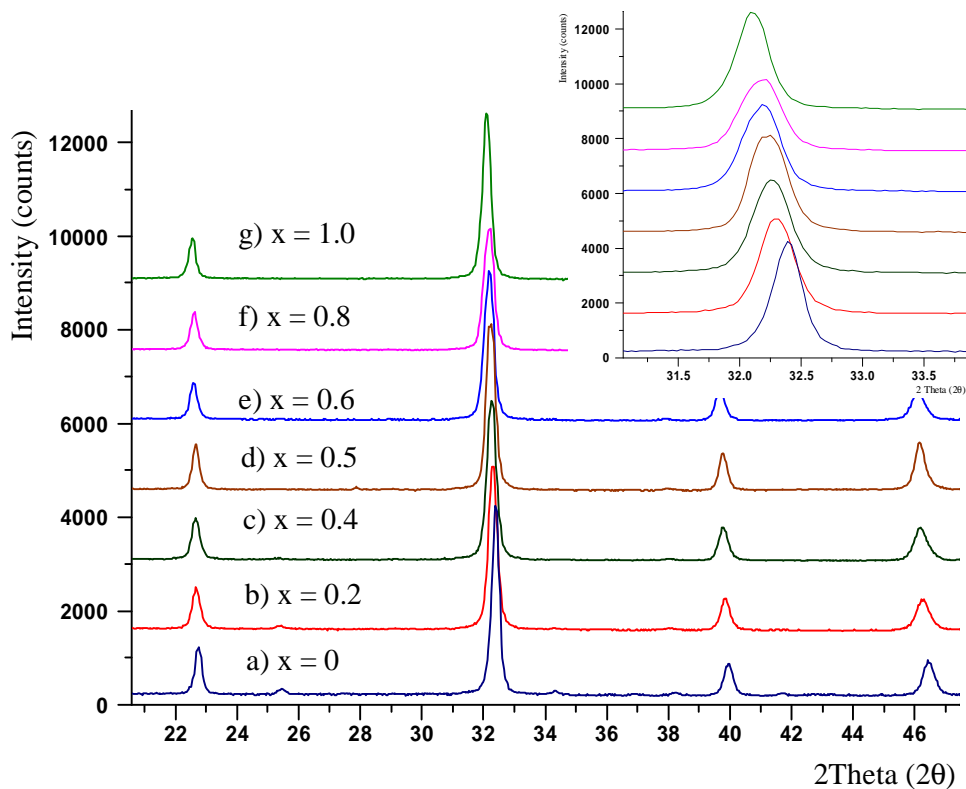Figure 6-9 X-ray diffraction traces of $(La_xNd_{1-x})_2Ti_2O_7$ pellets

Figure 6-10 X-ray diffraction patterns of films of $La_xNd_{1-x}TiO_2N$ solid solutions after ammonia treatment at 950ºC for 24 hours

SEM micrographs of the $La_{0.5}Nd_{0.5}TiO_2N$ layers (Figure 6-11) would indicate a thickness in the range of ≈ 3 μm. In contrast to the $LaTiO_2N$ samples, all Nd-containing samples have the advantage that the $NdTiO_2N$ and $La_xNd_{1-x}TiO_2N$ layers can be distinguished from the original oxides on the basis of colour. Before nitriding, both $Nd_2Ti_2O_7$ and the complete range of $(La_xNd_{1-x})_2Ti_2O_7$ samples are purple in colour but after nitriding they turned from purple through brown to dark greyish brown, with a colour variation clearly dependent on the La:Nd ratio.
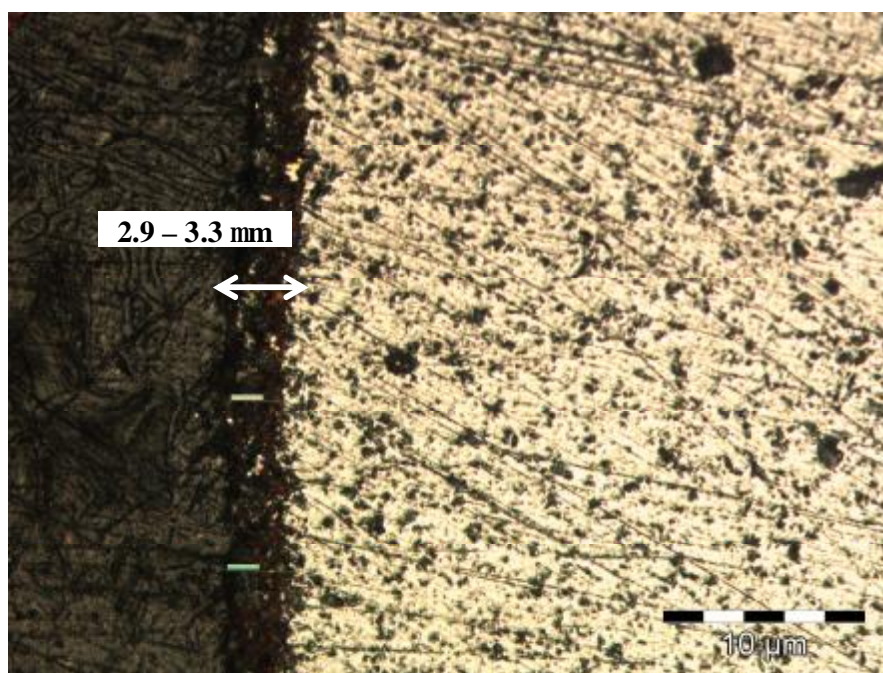
Figure 6-11 Cross section image of the $La_{0.5}Nd_{0.5}TiO_2N$ film on $LaNdTi_2O_7$ substrate

6.3 Synthesis of $ATaO_2N$ (A = Ca, Sr) oxynitride films on pre-prepared oxide samples

Attempts were also made to prepare dense $A_2Ta_2O_7$ (A = Ca, Sr), samples, which could then be subsequently nitrided in ammonia to produce surface layers of the appropriate $ATaO_2N$ oxynitrides. $Ca_2Ta_2O_7$ and $Sr_2Ta_2O_7$ pellets were prepared as

described in Chapter 3 and finally sintered in air at 1550 and 1400ºC, respectively for 3 hours to achieve high density. However, low densities (50% of theoretical) were observed at these sintering temperatures; both samples melted when higher sintering temperatures were used. 1–2 drops of 15% polyvinyl alcohol (PVA) solution were then used as a binder to help densification. After the binder eliminating step at 550ºC, the samples were sintered at 1550ºC for 3 hours. The densities of the $Ca_2Ta_2O_7$ and $Sr_2Ta_2O_7$ samples improved, as shown in Table 6-2. However, the X-ray diffraction patterns showed shifted peaks with traces of some unidentified peaks. Pure, dense samples of $Ca_2Ta_2O_7$ and $Sr_2Ta_2O_7$ were therefore not successfully prepared.

Table 6-2 Densities of densified $Ca_2Ta_2O_7$ and $Sr_2Ta_2O_7$ disks

Oxide	Calculated density (ρ_c) (g/cm^3)	Experimental density (ρ) (g/cm^3)	% ρ_c
$Ca_2Ta_2O_7$	6.45[1]	3.49	54%
$Ca_2Ta_2O_7$+PVA		5.13	79%
$Sr_2Ta_2O_7$	7.95[2]	3.81	48%
$Sr_2Ta_2O_7$+PVA		6.36	80%

[1] X-ray diffraction database ICDD number: 00-044-1008 and [2] 00-030-1304

Clearly, alternative methods (e.g. sol-gel or co-precipitation) would be needed to prepare more highly densified oxide samples, but because of time, it was not possible to pursue this. Nevertheless, the low density oxide pellets were nitrided in ammonia at 950ºC, but after reaction, they emerged from the furnace bloated and in some cases fragmented. The mechanical strength of the resulting pellets was too low for dielectric measurements to be carried out, and therefore this section of the work was discontinued

6.4 Dielectric investigation of thick film LnTiO$_2$N (Ln = La and Nd), and La$_x$Nd$_{1-x}$TiO$_2$N solid solutions

Gold electrodes were sputtered on both sides of the ≈ 10 mm diameter pellets prepared in the previous sections. A Hewlett Packard (4284 A) LCR bridge was used to measure capacitance and dielectric loss at room temperature in the frequency range 100 Hz to 1 MHz. Values for dielectric constant were then calculated as described in Chapter 3. Initially, the dielectric properties of La$_2$Ti$_2$O$_7$, Nd$_2$Ti$_2$O$_7$ and (La$_x$Nd$_{1-x}$Ti)$_2$O$_7$ solid solutions, densified to the extent of approximately 70–80% of theoretical were investigated, as shown in Figure 6-12 and Figure 6-13. Across the solid solution between the two end members, the permittivity increases, maximizing at a value of ≈ 40.
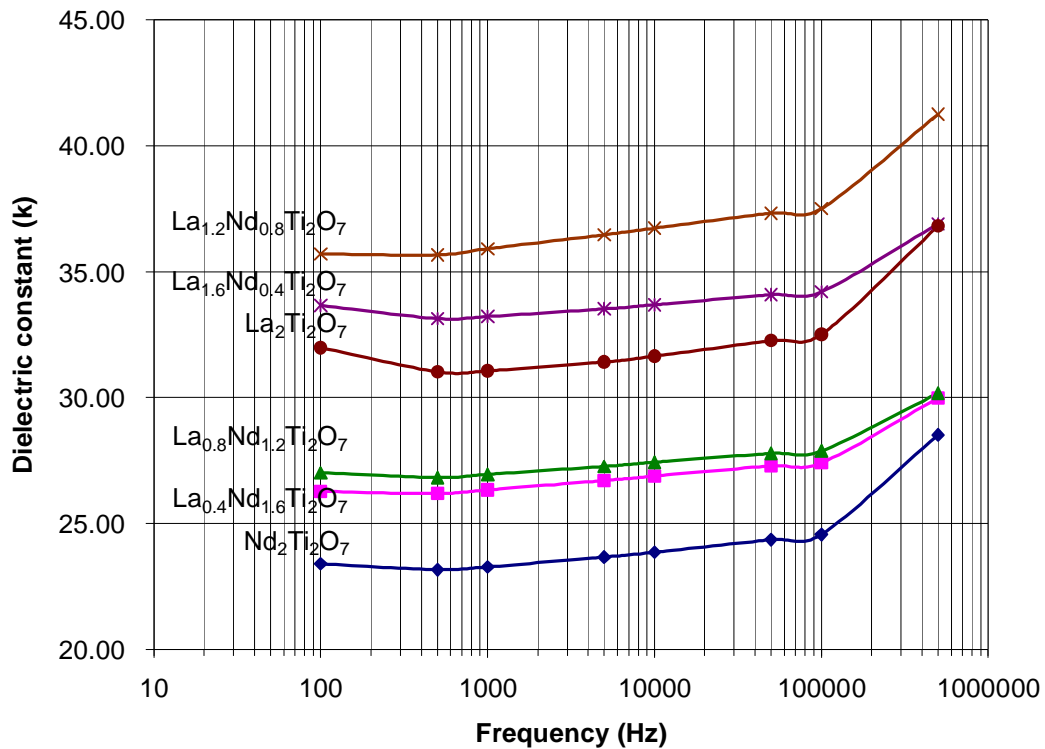

Figure 6-12 Dielectric constant of dense (La$_x$Nd$_{1-x}$)$_2$Ti$_2$O$_7$ solid solutions as a function of frequency
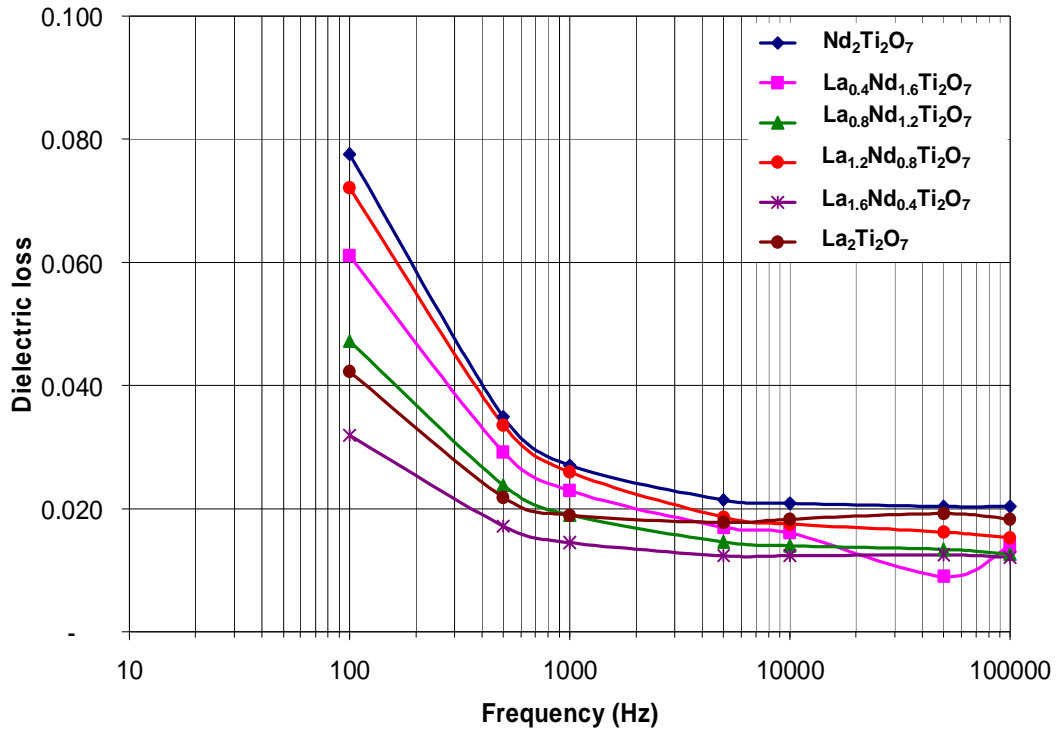
Figure 6-13 Dielectric loss of dense $(La_xNd_{1-x})_2Ti_2O_7$ solid solutions
as a function of frequency

The dielectric constant and dielectric loss of $La_2Ti_2O_7$ and $Nd_2Ti_2O_7$ and their oxide solid solutions are frequency independent at all frequencies below 100 kHz, consistent with the work of Shao *et al.* (2010). However, to explore the effect of the relatively low density, the dielectric properties of a sample of $La_2Ti_2O_7$ with high density ($\approx$ 90% of theoretical) were investigated. As already shown in Chapter 4, the dielectric constant came out as 49 with a lower dielectric loss approximately 1 order of magnitude less.

Dielectric measurements were also made on the above samples after they had been nitrided to deposit surface layers of oxynitride. Initially, the dielectric properties of oxynitride coated $La_2Ti_2O_7$ (90% of theoretical density) were studied (see Figure 6-14 and Figure 6-15). Both dielectric constant and dielectric loss

have increased after ammonia nitriding at 950ºC for 20 hours. After removing the coating from the side of the sample, the dielectric constant and the dielectric loss were greatly reduced. Other oxynitride coated samples were studied by side coat removal. It was immediately apparent that the dielectric constants of these coated materials with surface layers of $LaTiO_2N$, $NdTiO_2N$ and $La_xNd_{1-x}TiO_2N$ on respective dense oxide substrates, were approximately 10 times higher than those of their corresponding dense oxides, and these results were also associated with higher dielectric loss, as shown in Figure 6-16 and Figure 6-17. Compared with as-sintered oxides, the higher loss in the nitrided samples is believed to have been caused by the presence of Ti^{3+} ions.
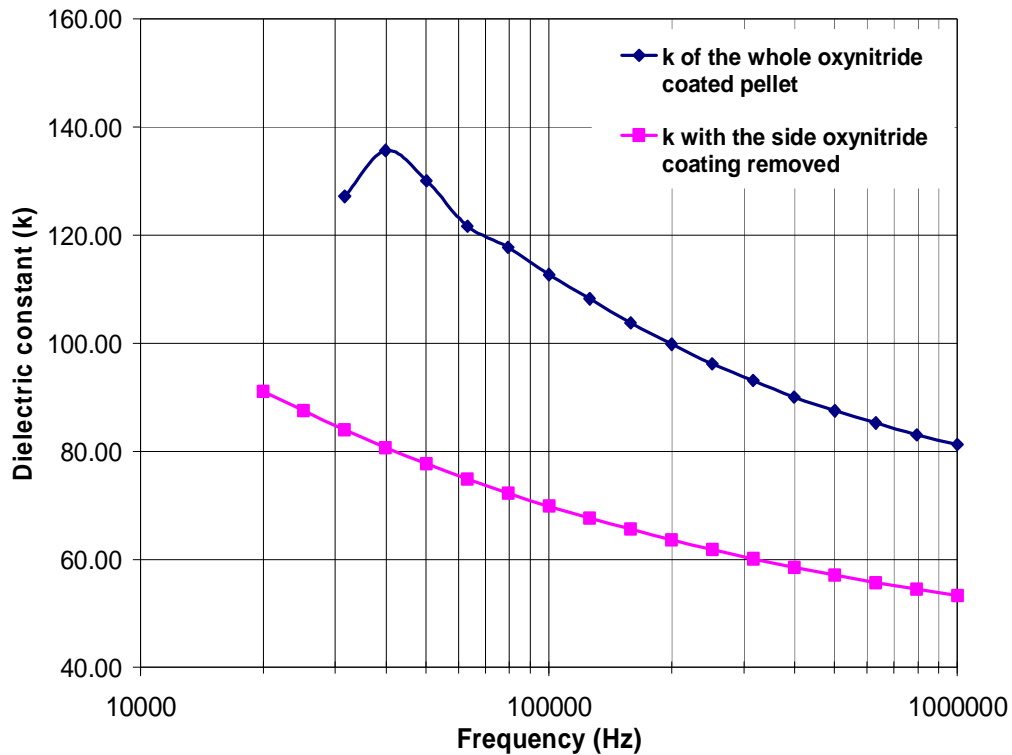

Figure 6-14 Dielectric constant of a) $LaTiO_2N$ layer coating the whole $La_2Ti_2O_7$ pellet, and b) with the $LaTiO_2N$ layer side coating removed
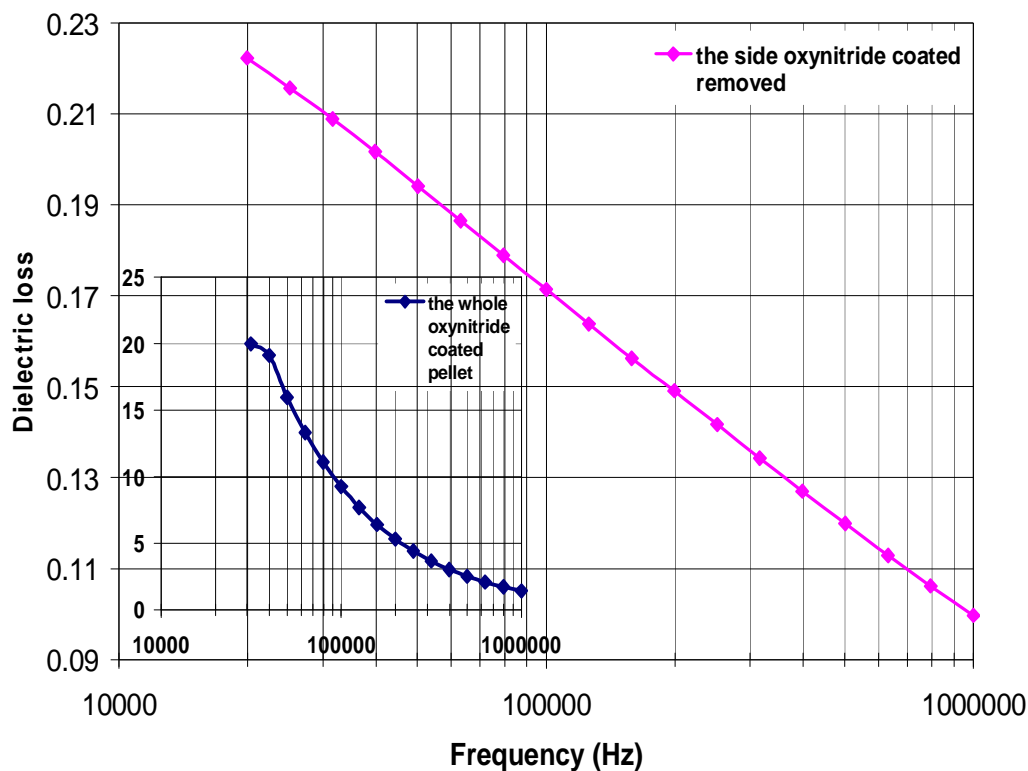
Figure 6-15 Dielectric loss of the samples with the LaTiO$_2$N layer side coating removed and the whole coating (inset)

As mentioned above for LaTiO$_2$N, after nitridation, it is believed that the (La$_x$Nd$_{1-x}$)$_2$Ti$_2$O$_7$ immediately underneath the surface oxynitride layer has been partially reduced with the simultaneous formation of some Ti^{3+} ions and the removal of some oxygen ions from the crystal lattice, resulting in a higher dielectric loss observed for these materials. The high dielectric constant values do make these oxynitrides extremely interesting for dielectric applications. However, there is a challenge to future material scientists to develop techniques for re-oxidising the sub-surface (La$_x$Nd$_{1-x}$)$_2$Ti$_2$O$_7$ whilst retaining the surface oxynitride layers in order to measure the true dielectric constant whilst maintaining low dielectric loss.
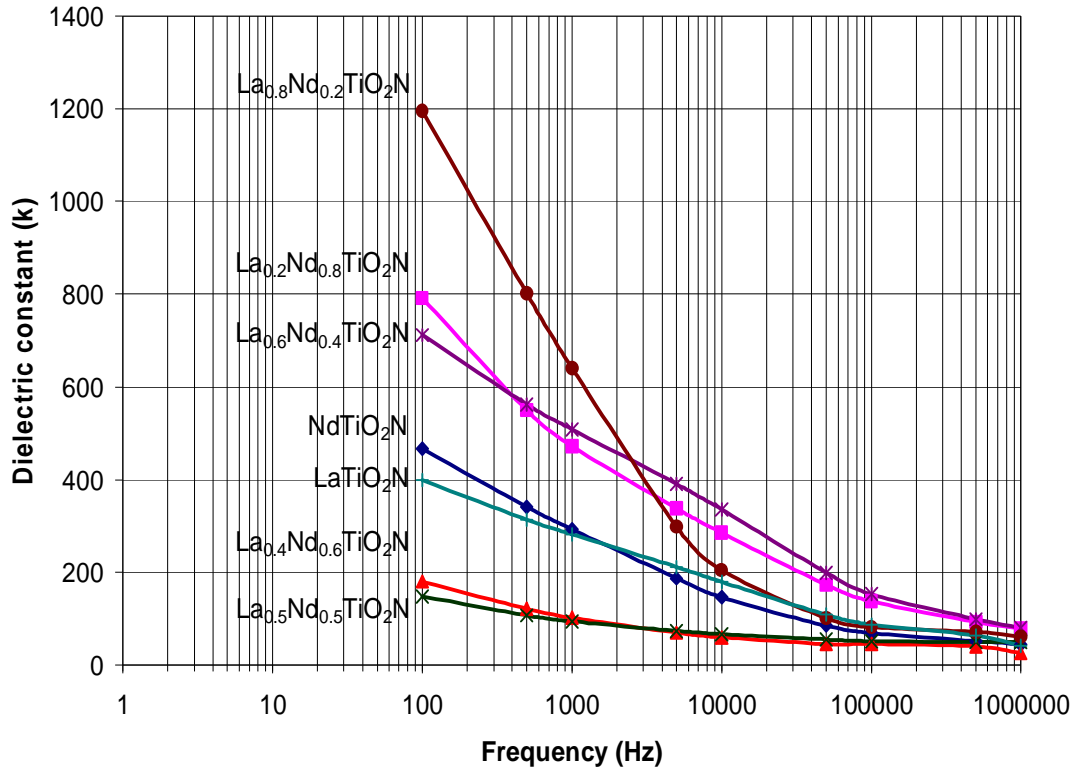
Figure 6-16 Dielectric constant of $La_xNd_{1-x}TiO_2N$ films; $0 \leq x \leq 1$
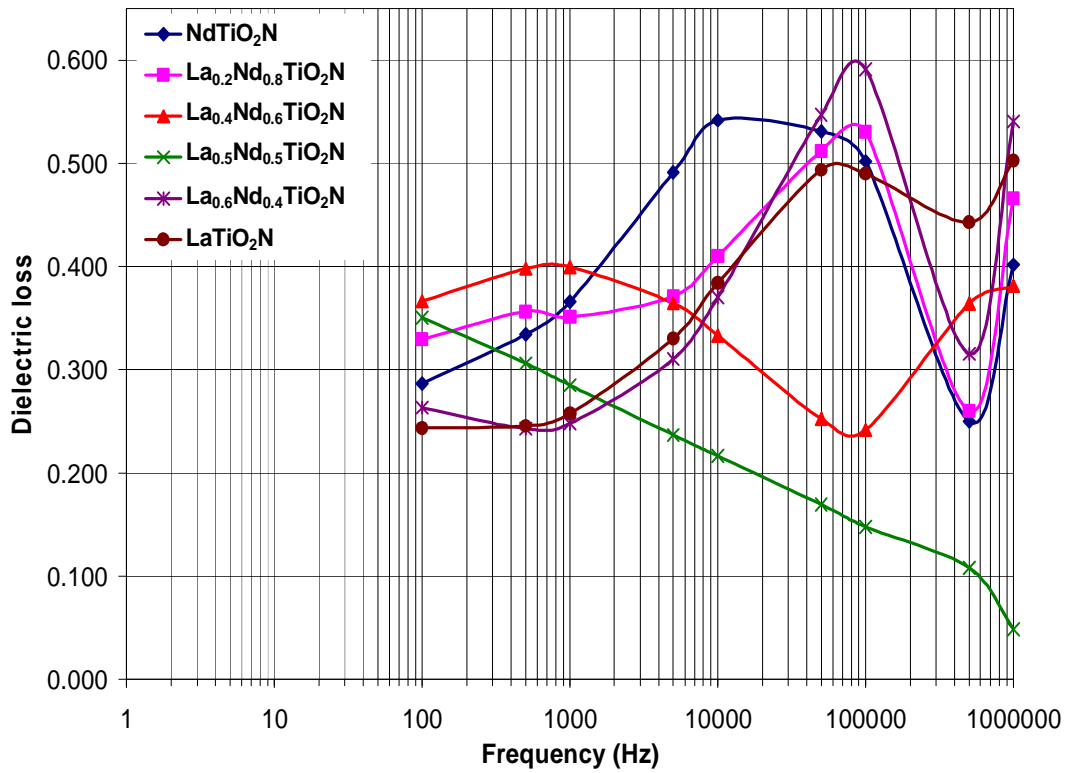

Figure 6-17 Dielectric loss of $La_xNd_{1-x}TiO_2N$ films; $0 \leq x \leq 1$

6.5 Discussions and conclusions

Surface layers of $LaTiO_2N$, $NdTiO_2N$ and $La_xNd_{1-x}TiO_2N$ were successfully deposited on the corresponding $A_2B_2O_7$ dense oxides by nitridation in flowing ammonia gas at 950ºC for up to 24 hours. X-ray diffraction, scanning electron microscopy (SEM) and optical microscopy confirmed that the correct phases had been formed, and also confirmed the existence of the surface layers of oxynitride, which were typically of thickness $\approx$ 3 μm. Dielectric measurements on the unnitrided oxide samples showed sensible permittivity data (lower than literatures values because of the reduced (85–90%) densities of the samples used) maximising in the centre of the compositional range. As expected, the presence of oxynitride layers significantly increased the measured dielectric constants of all samples, but a significantly higher dielectric loss was also observed. This is believed to be due to the reduction of the oxide material immediately below the oxynitride layer, due to the action of hydrogen from the nitriding atmosphere, which because of its small size can relatively easily permeate through the oxide and cause removal of oxygen whilst simultaneously reducing the titanium from Ti^{4+} to Ti^{3+}. In addition, there may well be an interfacial layer of slightly modified composition between the reduced lanthanum titanate and the surface oxynitride. Consequently, the dielectric properties of the nitrided oxide pellets are influenced by the more conducting contribution from this underlying reduced oxide layer. In order to avoid reduction of the oxide, alternative active nitriding agents could be used which do not involve the generation of hydrogen, the best contenders being nitrous (N_2O) or nitric (NO) oxides. However, all methods have limitations, and due to the lower temperatures of dissociation of these two oxides

the nitrogen atoms are not as active as when they are formed by dissociation of ammonia (see Chapter 2). From the above results, it can be seen that $La_xNd_{1-x}TiO_2N$ films deposited on their corresponding oxides give a promising performance in term of offering increased permittivity, but further work is needed to solve the problem of the high dielectric loss.

During the course of this work, Ebbinghaus and co-workers (2008) reported an alternative approach using single crystal oxide precursors instead of polycrystalline oxides. Thick films of the perovskite oxynitrides $LaTiO_2N$, $NdTiO_2N$, $SrNbO_2N$ and $SrTaO_2N$ were deposited as surface layers at temperature between 900ºC and 1050ºC for several hours in an ammonia flow of 50 ml/min. X-ray diffraction patterns and scanning electron microscopy revealed oxynitride layers a few micrometers in thicknesses, forming a sandwich structure on top of the unnitrided oxide. Figure 6-18 is a SEM micrograph showing a cross section of a $SrNbO_{3.5}$ crystal nitrided at 950ºC for 76 hours, clearly indicating the two surface layers of $SrNbO_2N$ with the unreacted $SrNbO_{3.5}$ in the middle. With longer reaction time, thicker oxynitride layers were formed. It should be noted that at the ferroelectric phase transition, the dielectric constant of $SrNbO_{3.5}$ is 1000 and drops to below 100 at room temperature (Akishige *et al.*, 1986 and Bobna *et al.*, 2002 cited in Ebbinghaus *et al.*, 2009). However, with only a small dependence on temperature and frequency, the dielectric constant of the $SrNbO_2N$ was observed to be as high as 5000 at 300 K; the conductivity is at least three orders of magnitude higher than that of the corresponding $SrNbO_3$ oxide (Ebbinghaus *et al.*, 2009). Thick films of $LaTiO_2N$ and $SrTaO_2N$ showed semiconductive behaviour with higher conductivities than those of the unnitrided

196

crystals (Ebbinghaus *et al.*, 2009). Based on the optical properties, nitrogen incorporation decreases the band gap and possibly results in a higher conductivity of materials. However, in this case, it would be of interest to know whether the transition metals retained their high valence state (i.e. Ti^{4+}, Ta^{5+}, Nb^{5+}) or whether some reduction (as in the present case) to lower valence state had been occurred during the long nitridation time.

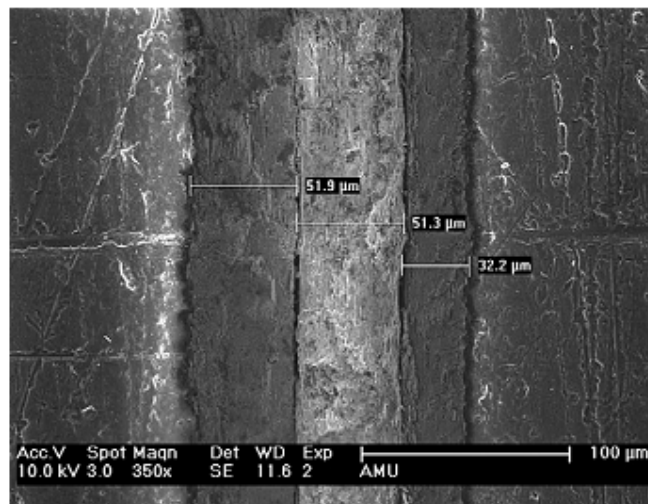Figure 6-18 SEM cross-section of a $SrNbO_{3.5}$ crystal nitrided at 950ºC for 76 hours
(Ebbinghaus *et al.*, 2009)

Compared with the nitridation of polycrystalline powders in the present study, the use of single crystals makes it easier to produce bulk oxynitride materials. The longer reaction time can increase the oxynitride layer to a certain thickness and after that the oxynitride layer will act like a barrier preventing further reaction. Nitriding a thinner slice of a single crystal may improve the thickness ratio between the oxynitride layer and the oxide underneath; as a result almost complete nitridation of a single crystal would be possible. Oxynitrides with high dielectric constant are of interest for dielectric applications; however, the high

conductivity would make these materials semiconductors with possibly high dielectric loss. For both nitrided single crystal and polycrystalline materials, an interface layer would be expected between nitrided and unnitrided layers. In the present case, it is believed that this layer is formed by the reduction of B-cation (i.e. Ti and Ta in $LnTiO_2N$ and ABO_2N, respectively) in the nitrided products and it may cause the conductive behaviour. The effect of this layer on material properties needs further study.

6.6 References

Canales-Vázquez, J., Smith, M., Irvine, J. and Zhou, W. (2005) Studies on the Reorganization of Extended Defects with Increasing n in the Perovskite-Based $La_4Sr_{n-4}Ti_nO_{3n+2}$ Series. WILEY-VCH Verlag**,** 1000-1008.

Ebbinghaus, S. G., Abicht, H. P., Dronskowski, R., Müller, T., Reller, A. and Weidenkaff, A. (2009) Perovskite-related oxynitrides - Recent developments in synthesis, characterisation and investigations of physical properties. *Progress in Solid State Chemistry,* 37**,** 173-205.

Ebbinghaus, S. G., Aguiar, R., Weidenkaff, A., Gsell, S. and Reller, A. (2008) Topotactical growth of thick perovskite oxynitride layers by nitridation of single crystalline oxides. *Solid State Sciences,* 10**,** 709-716.

Fasquelle, D., Carru, J. C., Le Gendre, L., Le Paven, C., Pinel, J., Cheviré, F., Tessier, F. and Marchand, R. (2005) Lanthanum titanate ceramics: Electrical characterizations in large temperature and frequency ranges. *Journal of the European Ceramic Society,* 25**,** 2085-2088.

Kim, Y.-I., Woodward, P. M., Baba-Kishi, K. Z. and Tai, C. W. (2004) Characterization of the structural, optical, and dielectric properties of oxynitride perovskites AMO_2N (A = Ba, Sr, Ca; M = Ta, Nb). *Chemistry of Materials,* 16**,** 1267-1276.

Le Paven-Thivet, C., Le Gendre, L., Le Castrec, J., Cheviré, F., Tessier, F. and Pinel, J. (2007) Oxynitride perovskite $LaTiO_xN_y$ thin films deposited by reactive sputtering. *Progress in Solid State Chemistry,* 35**,** 299-308.

Paul, A. F. and Robert, E. N. (1991) $La_2Ti_2O_7$ Ceramics. *Journal of the American Ceramic Society,* 74**,** 2876-2881.

Shao, Z., Saitzek, S., Roussel, P., Mentré, O., Prihor Gheorghiu, F., Mitoseriu, L. and Desfeux, R. (2010) Structural and dielectric/ferroelectric properties of $(La_{1-x}Nd_x)_2Ti_2O_7$ synthesized by sol-gel route. *Journal of Solid State Chemistry,* 183**,** 1652-1662.

Takahashi, J., Kageyama, K. and Kodaira, K. (1993) Microwave dielectric properties of lanthanide titanate ceramics. *Japanese Journal of Applied Physics, Part 1: Regular Papers and Short Notes and Review Papers,* 32**,** 4327-4331.

Wang, S. F., Hsu, Y. F., Wang, Y. R., Cheng, L. T., Hsu, Y. C., Chu, J. P. and Huang, C. Y. (2006) Densification, microstructural evolution and dielectric properties of $Ba_{6-3x}(Sm_{1-y}Ndy)_{8+2x}Ti_{18}O_{54}$ microwave ceramics. *Journal of the European Ceramic Society,* 26**,** 1629-1635.

Zhang, F. X., Lian, J., Becker, U., Ewing, R. C., Wang, L. M., Hu, J. and Saxena, S. K. (2007) Structural change of layered perovskite $La_2Ti_2O_7$ at high pressures. *Journal of Solid State Chemistry,* 180**,** 571-576.

Chapter 7 Particulate dielectric measurements of $LnTiO_2N$ (Ln = La and Nd) and $ATaO_2N$ (A = Ca, Sr and Ba) powders by impedance spectroscopy

7.1 Introduction

As a general rule, measurements of dielectric properties of ceramics are made on dense materials in the form of either bulk samples or films. Most samples are typically polycrystalline, and for the purpose of dielectric characterization, the sample is considered to be a two-phase system with a significant difference in behaviour between the grains and the grain boundary phases (Lanfredi and Rodrigues, 1999). For dense materials, factors such as the nature, amount and distribution of grain boundary phase material, the particle size and the presence of internal stresses can affect the reliability of dielectric measurements (Petrovsky *et al.*, 2006). Knowledge of dielectric properties of particulate materials is important as (in the present case) it may be difficult to produce the material in its fully dense pure state. Various approaches have been proposed to estimate the dielectric constant of samples in particulate form. Impedance spectroscopy was applied to measure the dielectric constant of powders as a two-phase system (Petrovsky *et al.*, 2006). In the present case, sample powders were dispersed in a liquid host and the impedance (Z) measured. The equivalent circuits based on mixing rules were applied to calculate the capacitance and hence the dielectric constant of the particulate phase.

Initially, due to the fact that oxynitrides are difficult to be processed into a fully dense bulk material suitable for accurate and dependable dielectric measurements, other routes have been explored for making these measurements. One option is to measure the dielectric constant of the oxynitride as a powder. Impedance spectroscopy can then be used to make dielectric measurements by suspending the powders in butoxyethanol as a liquid host and measuring the impedance as a two-phase system. Theoretical models considering the series connection of RC parallel circuits were used to analyse impedance spectra and dielectric constants were then calculated, as described in Chapter 3.

7.2 Impedance spectroscopy

In practice, there is no such thing as a resistance-free system, i.e. all media involve both resistance (R) and reactance (X) (the latter both inductive (X_L) and capacitive (X_C)) (Algilent-technologies, 2010). For example, a resistor may have inductance as an unwanted characteristic; a capacitor has unwanted resistance and an inductor may have a hidden capacitance, etc. With the combination of the primary elements and these parasitic elements, each component must be considered as a complex circuit. Resistance measurement cannot be applied for such a complex circuit. Impedance measures the ability of a circuit to resist electrical current like resistance, but it measures both resistance (R) and reactance (X) (Gamry Instruments, 2010). The elements in a component circuit can be lumped together as a simple series equivalent circuit. Impedance analysers measure resistance and reactance in series as an impedance vector (Algilent-technologies, 2010), as shown in Figure 7-1.
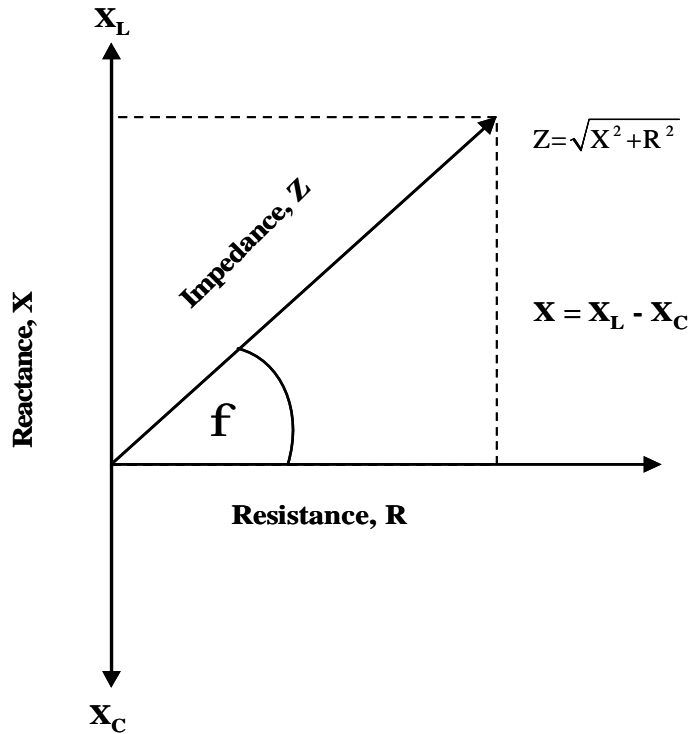
$$Z = \sqrt{X^2 + R^2}$$

$$X = X_L - X_C$$

Figure 7-1 Resistance and reactance measured as an impedance vector

Impedance is a complex number $(Z = Z' + jZ'')$. When the real part (Z') and the imaginary part (Z'') are plotted on the x and y axis by considering the equivalent circuit, a typical semicircular shape results, called a Nyquist diagram (see Figure 7-2) (Gamry Instruments, 2010). Each point on the Nyquist diagram is the impedance at a certain frequency, i.e. the low frequency data are on the right hand side of the plot and the higher frequencies are on the left. In a capacitor, resistance, inductance and resistance all behave as parasitic elements. At very low frequencies (lower than the self resonance frequency, SRF), parasitic inductance is negligible and scarcely affects the measurement at all, but at high frequency this element must be considered (Algilent-technologies, 2010).
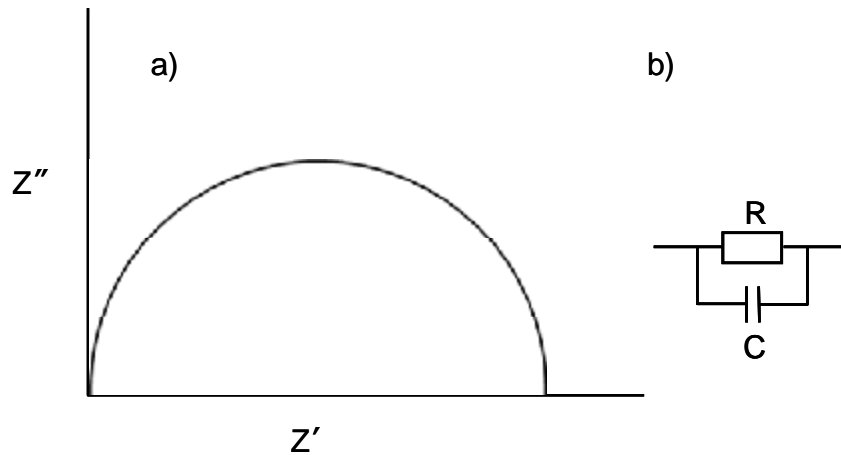
Figure 7-2 a) Nyquist diagram, and b) parallel RC circuit

Generally, either a series or a parallel circuit can be used to model this as long as the capacitance of the components exhibits a low frequency response. Nevertheless, selecting the proper equivalent circuit is critical for accurate analysis. As schematically shown in Figure 7-3, parallel resistance (R_p) is primarily determined in the case of capacitance measurement and as a result a parallel RC circuit is applied (Algilent-technologies, 2010). Also, Figure 7-4 summarises the range of impedance and resistance which can be used for equivalent circuit selection.

Additionally, from the literature (Petrovsky *et al.*, 2006, Petrovsky *et al.*, 2008a), it is generally agreed that the parallel RC equivalent circuit model is the most rational one to use to simulate the complex circuit applicable in the case of particulate dielectric measurement by impedance spectroscopy.
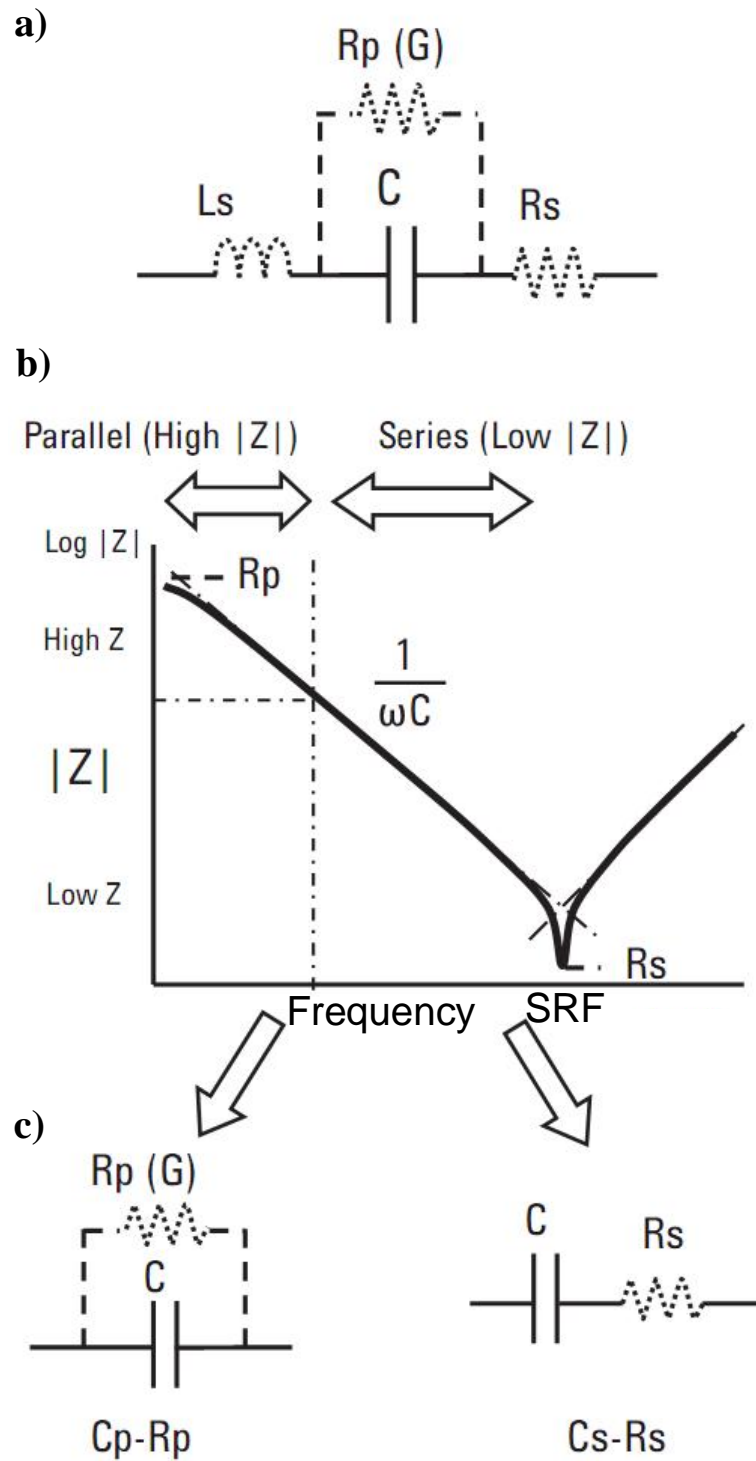
Figure 7-3 Possible equivalent circuits which can be used for modelling a capacitor
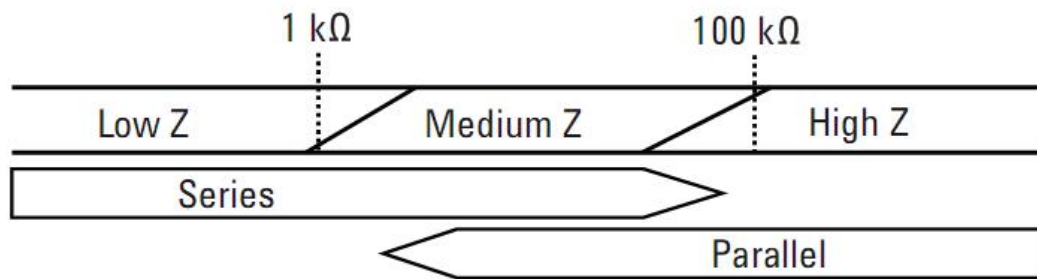(Algilent-technologies, 2010)

Figure 7-4 Range of impedance as a criterion for equivalent circuit selection
(Algilent-technologies, 2010)

7.3 Particulate dielectric measurements by impedance spectroscopy

Petrovsky *et al.* (2006) applied impedance spectroscopy to estimate the dielectric constant of powders in slurry form in a two-phase system involving powder and liquid. It is generally the case that liquids with a high dielectric constant give a more accurate estimate of the particle dielectric constant, especially for high dielectric constant materials such as ferroelectrics. However, the availability of liquids with a high dielectric constant is limited. Also, the reliability of dielectric measurements made on slurries may be affected by some factors such as size, shape, agglomeration, and sedimentation of the particles. The possible theoretical models which apply for this type of measurement, are parallel or series connections between each phase, as shown in Figure 7-5 (Petrovsky *et al.*, 2006).
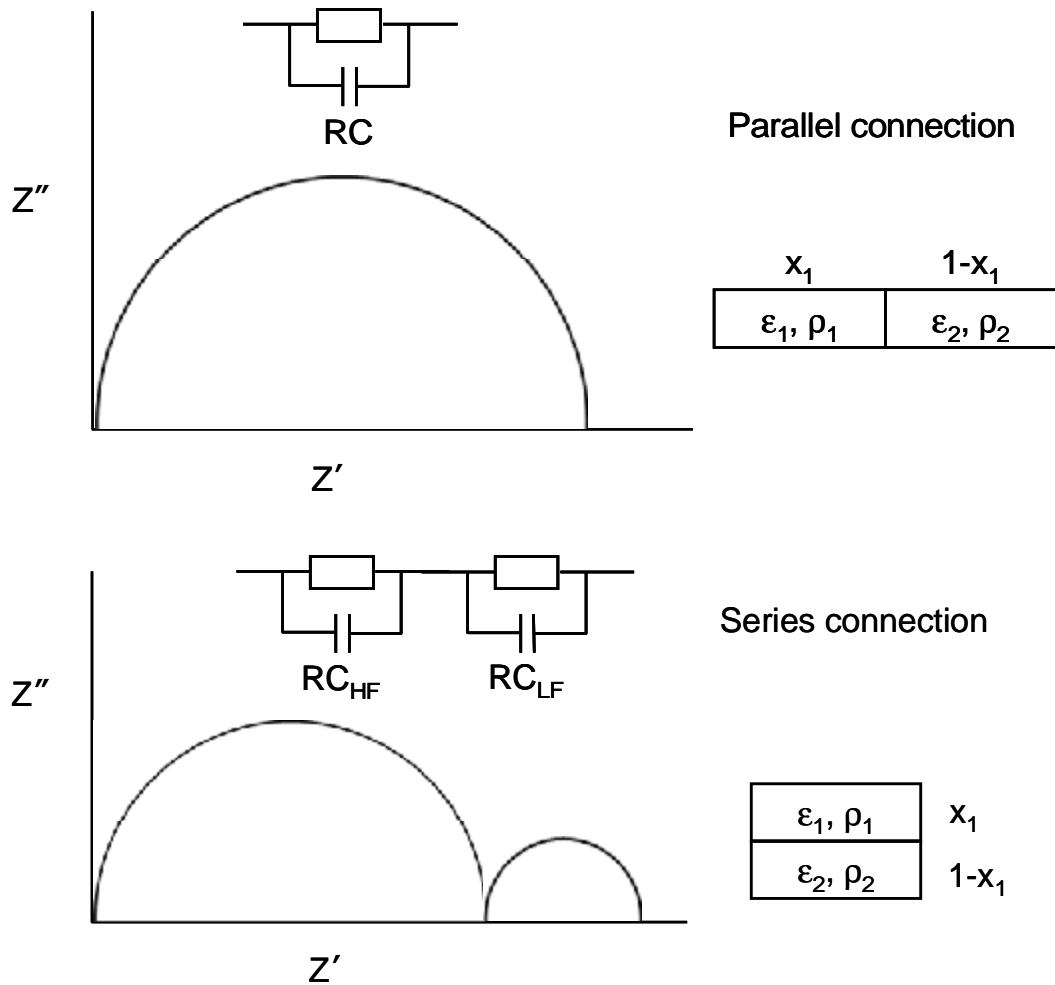
Figure 7-5 Impedance spectra of a two-phase system with parallel and series connections between phases

In case of parallel connection, impedance spectra theoretically consist of one semicircle. The effective dielectric constant of the two-phase system is expressed by Equation 7-1:

$$e_{eff} = e_1 x + e_2 (1 - x)$$

Equation 7-1

where e_{eff} is the effective dielectric constant of the slurry, e_1 and e_2 are the dielectric constants of particles and liquid host, respectively, and x is the volume fraction of powder.

For series connection, the impedance spectrum ideally show two semicircles, i.e. the first semicircle at high frequency represents the impedance data for the liquid host and the second one at low frequency is for the powder (Petrovsky *et al.*, 2006). These might overlap or partly overlap depending on the characteristics of the slurry and the difference in dielectric constants of the particles and the liquid host. The dielectric constants of the liquid host e_2 and the particles e_1 can be calculated from the measured overall dielectric constants at high and low frequency (e_{HF} and e_{LF}), by using Equation 7-2 and Equation 7-3, respectively, i.e.:

$$e_{HF} = \frac{e_2}{1-x}$$

Equation 7-2

$$e_{LF} = \frac{e_1}{x}$$

Equation 7-3

This technique was applied to measure the dielectric constant of $SrTiO_3$ powder dispersed in butoxyethanol by applying 2 parallel RC circuits individually connected in series connection to fit the impedance spectrum, and the results were in good agreement with measurements made on bulk material from previous research (Petrovsky *et al.*, 2006).

However, Nakao (2007) considered parallel and series connections of each phase as two extreme cases; a random dispersion model was proposed to compare with the parallel and series models, as shown in Figure 7-6.
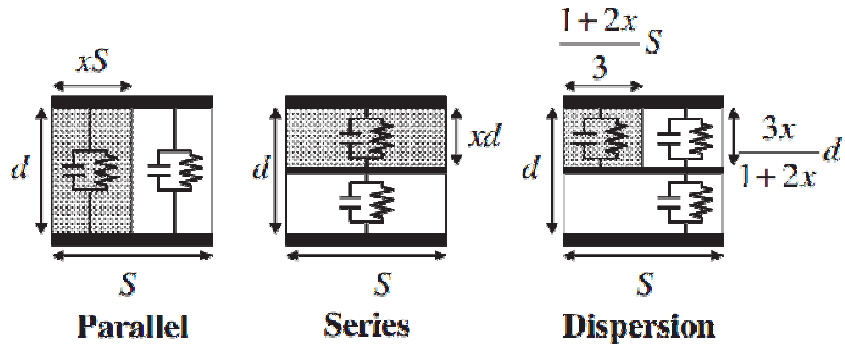
Figure 7-6 Equivalent circuit models for parallel, series and dispersion, respectively

The capacitance of the slurry in RC-RC circuit models connected in series, parallel and random dispersion are expressed by Equation 7-4, Equation 7-5 and Equation 7-6, respectively, i.e.:

$$\frac{C}{e_0} = \frac{e_1 e_2}{(1-x)e_1 + xe_2} \frac{A}{d}$$

Equation 7-4

$$\frac{C}{e_0} = \left(xe_1 + (1-x)e_2 \right) \frac{A}{d}$$

Equation 7-5

$$\frac{C}{e_0} = \frac{(1+2x)e_1 e_2 + (2-2x)e_2^2}{(1-x)e_1 + (2+x)e_2} \frac{A}{d}$$

Equation 7-6

where C is the overall capacitance, e_0 is the dielectric constant of free space, e_1 and e_2 are the dielectric constants of particles and liquid host, respectively, and x is the volume fraction of the powders.

This study confirmed that the RC-RC circuit connected in series was the model which gave the best fit of the impedance spectrum to the experimental data.

To compare the dielectric constant of powder and sintered BaTiO$_3$, Petrovsky and co-workers (2008b) investigated the dielectric constant of millimetre-size cubes and powders of BaTiO$_3$, both suspended in butoxyethanol, and the impedance measured under the same conditions. The equivalent circuit approach with 2 RC elements connected in series was used for fitting measured spectra to the calculated ones. The dielectric constants were calculated from Equation 7-7 and Equation 7-8 for high and low frequency semicircles, respectively.

$$e_{HF} = e_1^x e_2^{(1-x)}$$

Equation 7-7

$$e_{LF} = e_1 + \frac{e_2}{x}$$

Equation 7-8

where e_{HF} and e_{LF} are the effective dielectric constants for the high and low frequency semicircles, e_1 and e_2 are dielectric constants of the particles and the liquid host, and x is the volume fraction of solid loading. The results revealed that the dielectric constant of the suspended BaTiO$_3$ cubes was very similar to that of the powder. Moreover, it was not sensitive to the amount of solid loading for volume fractions higher than 10%.

Recently, Jasinski *et al.* (2010) proposed two equivalent circuit models based on a brick layer model (BLM), for mathematical fitting of impedance spectra. Only two structures could be built and the cells were divided into three-area structures; consequently two related equivalent circuits needed to be considered as depicted in Figure 7-7.
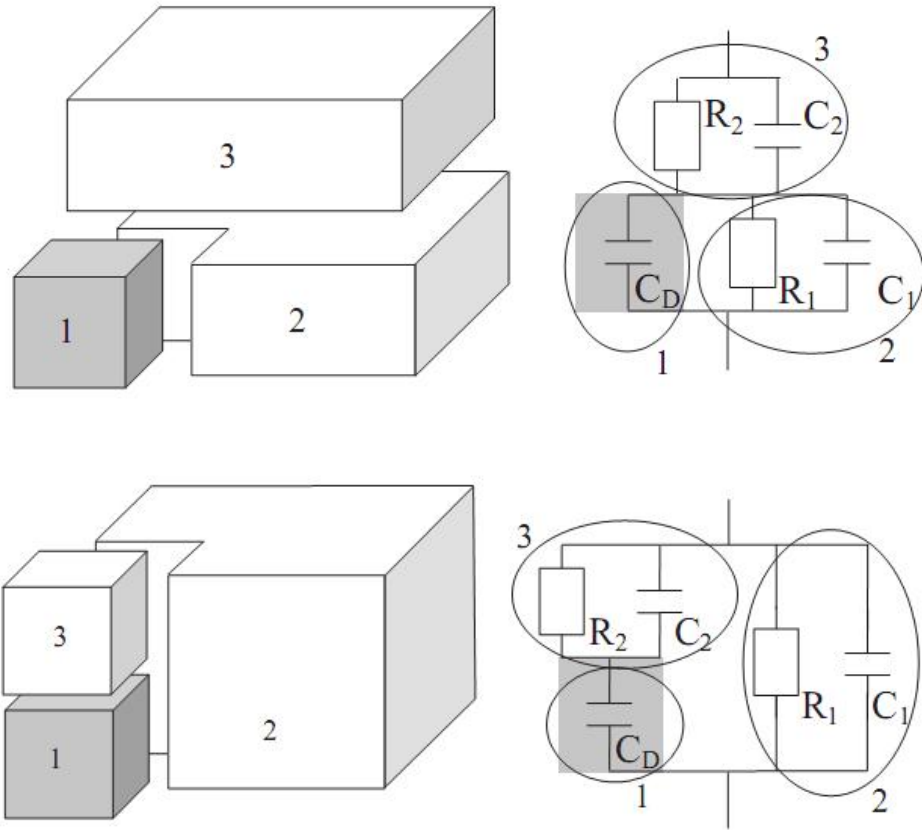
Figure 7-7 Schematic diagram of cubes suspended in liquid and their equivalent circuits

The above models are described by the following equations:

$$C_D = e_1 e_0 x^{1/3}$$

$$C_1 = e_2 e_0 \frac{1 - x^{2/3}}{x^{1/3}}$$

$$C_2 = e_2 e_0 \frac{1}{1 - x^{1/3}}$$

$$R_1 = r_2 \frac{x^{1/3}}{1 - x^{2/3}}$$

$$R_2 = r_2 (1 - x^{1/3})$$

Equation 7-9

and

$$C_D = e_1 e_0 x^{1/3}$$

$$C_1 = e_2 e_0 (1 - x^{2/3})$$

$$C_2 = e_2 e_0 \frac{x^{2/3}}{1 - x^{1/3}}$$

$$R_1 = r_2 \frac{1}{1 - x^{2/3}}$$

$$R_2 = r_2 \frac{1 - x^{1/3}}{x^{2/3}}$$

<div align="right">Equation 7-10</div>

where C is capacitance, R is resistance, ρ_1, ρ_2, ε_1 and ε_2 are resistivity and dielectric constant of particles and liquid host, respectively, and x is the volume fraction of loaded solid. The dielectric constant of $BaTiO_3$ cubes suspended in butoxyethanol was studied and the results were compared with those obtained from the simulation models (Jasinski *et al.*, 2010). The impedance spectrum of $BaTiO_3$ was fitted to a parallel RC circuit individually connected in series. The extracted R (resistance) and CPE (constant phase element) parameters from the impedance measurement were used to calculate the capacitance from Equation 7-11:

$$C = (Q)^{1/n} (R)^{(1-n)/n}$$

<div align="right">Equation 7-11</div>

where Q and n are parameters of CPE and R is resistance.

For a known capacitance, the corresponding dielectric constants for the high and low frequency spectra (e_{HF} and e_{LF}) were calculated from Equation 7-12 and Equation 7-13, respectively, i.e.:

$$e_{HF} = \frac{C_{HF}}{e_0} \mathbf{g} \frac{d}{A}$$

<div align="right">Equation 7-12</div>

$$e_{LF} = \frac{C_{LF}}{e_0} \mathbf{g} \frac{d}{A}$$

where C_{HF} and C_{LF} are the capacitances attributed to high and low frequency spectra, respectively, d is the distance between electrodes and A is the electrode surface area.

The dielectric constant measured for the $BaTiO_3$ cubes was in agreement with that determined for powder in the previous research and was not sensitive to the distribution pattern of the cubes and compositions of the liquid host. Furthermore, the results showed that the data from the simulation models provided narrower bounds for experimental data when the powder volume fraction was not less than 0.4.

The effect of liquid and powder characteristics was previously studied and the results confirmed that particulate dielectric measurement by impedance spectroscopy is a reliable method (Petrovsky *et al.*, 2008a, Petrovsky and Dogan, 2009). As shown in Figure 7-8, volume fraction of solid loading enlarges the size of the spectrum only at low frequency and different liquid hosts (varied dielectric constants) affect the shape and size of the spectrum only for high frequency spectra. The dielectric constants of $SrTiO_3$, $CaTiO_3$ and TiO_2 powders were measured with varying amounts of powder and the results showed that they remained nearly constant with powder volume fraction variation and were in reasonable agreement with the values reported for bulk materials (Petrovsky *et al.*, 2008a). So it is clearly seen that the powder volume fraction (x) only affects the shape and size of the spectrum, but the effective dielectric constant remains nearly constant provided $x \geq 0.1$, as shown in Figure 7-9.
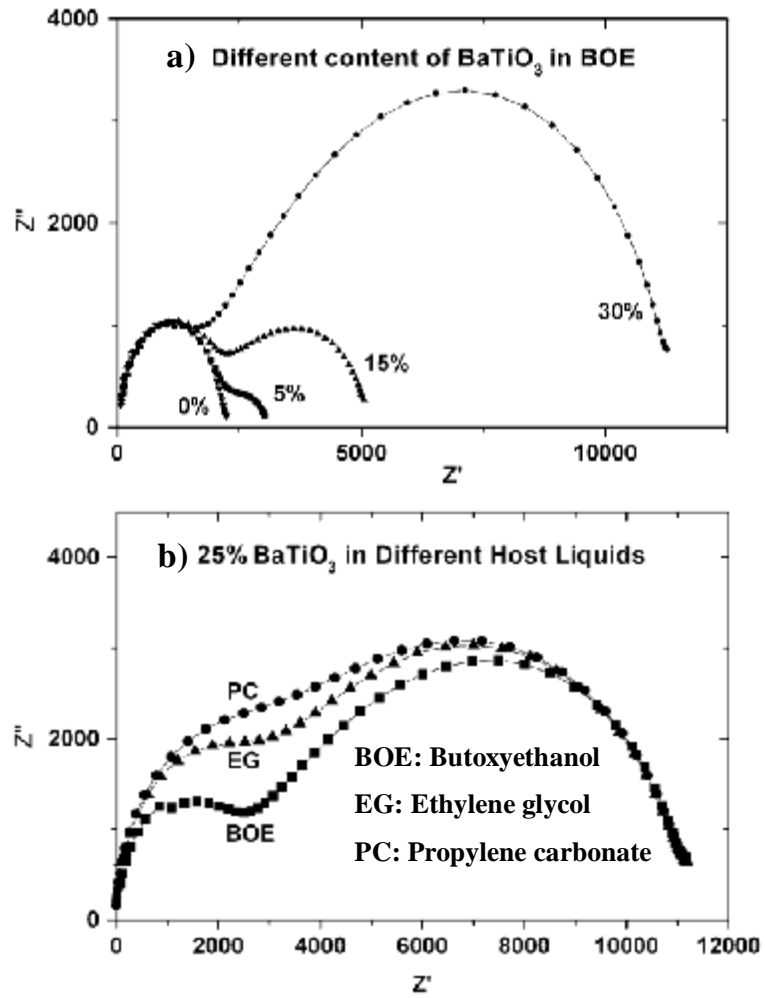
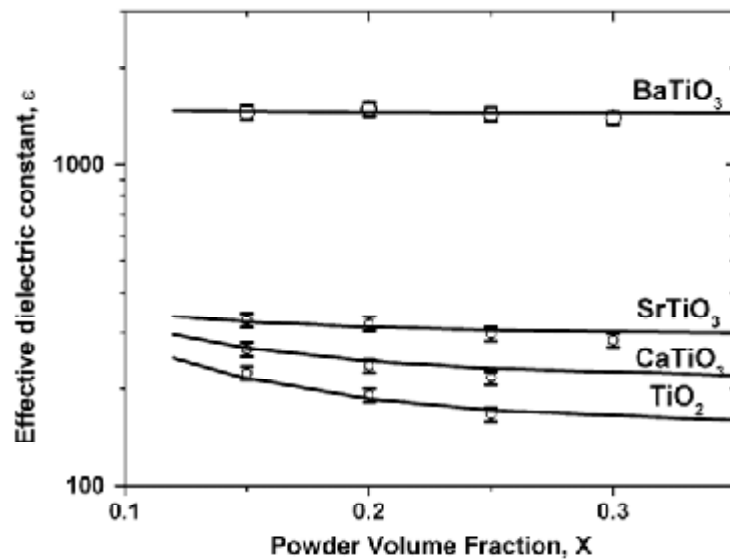Figure 7-8 Slurry characteristic effects on impedance spectra of BaTiO$_3$

Figure 7-9 Dielectric constant of different powders as a function of volume fraction

Additionally, the effect of using liquid hosts of different conductivity for particulate dielectric measurements was studied (Petrovsky and Dogan, 2009). The conductivity of the slurry was adjusted by adding acetic acid. The results showed that the dielectric constant was not affected by different resistivity of the liquid; however, the difference between the dielectric constants of the liquid host and the powder had most effect on the shape of the two impedance semicircles. The separation of the two semicircles increased with increasing dielectric constant difference.

Impedance spectroscopy allows reliable measurements to be made of the dielectric constant of particles dispersed in liquids with less effect from the slurry characteristics. Nevertheless, the only limitation of the technique is inability to also make dielectric loss measurements. Since dielectric losses for slurries are mostly related to the conductivity of the liquid host for both high and low frequency spectra, it is not possible to measure the dielectric losses of powder materials by impedance analysis (Petrovsky *et al.*, 2006).

7.4 Dielectric measurement of oxynitride powders by impedance analysis

In the present study, impedance spectroscopy was used to measure the dielectric constants of oxynitride powders. Z-View software was used to fit impedance spectra from experiments to calculation models by considering two parallel RC circuits in series connection. The obtained R and CPE values were then used to calculate capacitance and the dielectric constant of the powder. Experimental details were given in Chapter 3. $LnTiO_2N$ (Ln = La and Nd) and $ATaO_2N$ (A =

Ca, Sr and Ba) oxynitride powders were prepared by ammonolysis as described in Chapter 4. The powders were sieved to reduce effects of agglomeration and then suspended in butoxyethanol at a 20% powder volume fraction loading. In comparison, dielectric constants of the corresponding oxide ($Ln_2Ti_2O_7$ and $A_2Ta_2O_7$) powders were measured under the same conditions. Impedance spectra for suspended $ATaO_2N$ and $LnTiO_2N$ powders in butoxyethanol are presented in Figure 7-10 to Figure 7-14

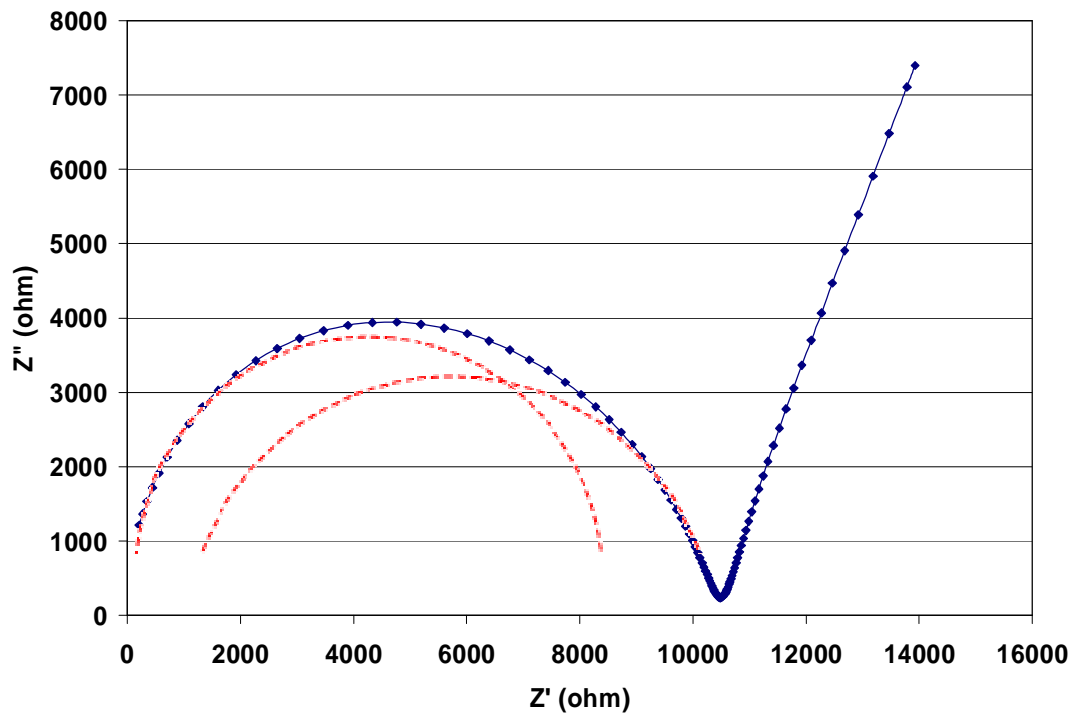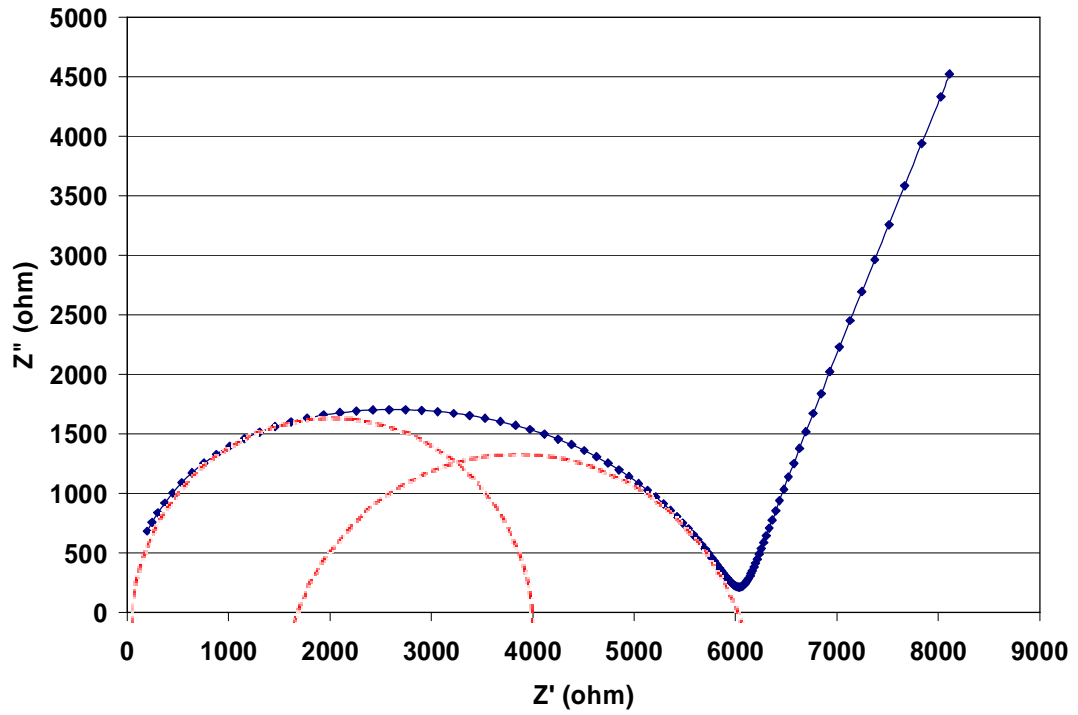Figure 7-10 Impedance spectrum of 20% $CaTaO_2N$ powder suspended in butoxyethanol

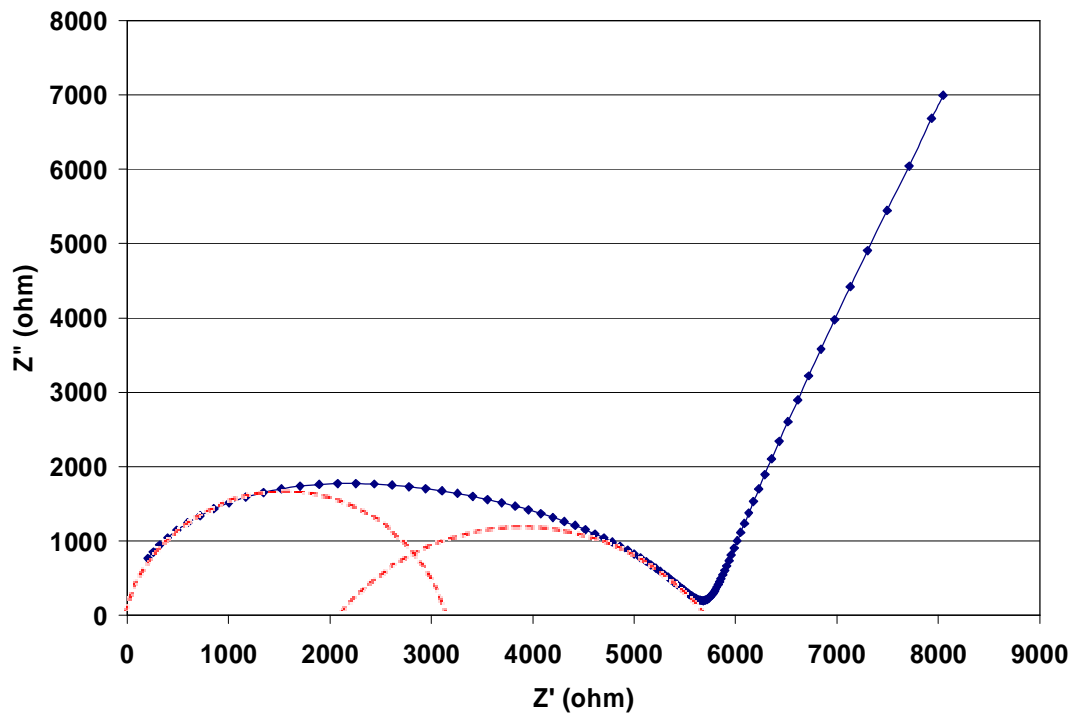Figure 7-11 Impedance spectrum of 20% SrTaO$_2$N powder suspended in butoxyethanol

Figure 7-12 Impedance spectrum of 20% BaTaO$_2$N powder suspended in butoxyethanol
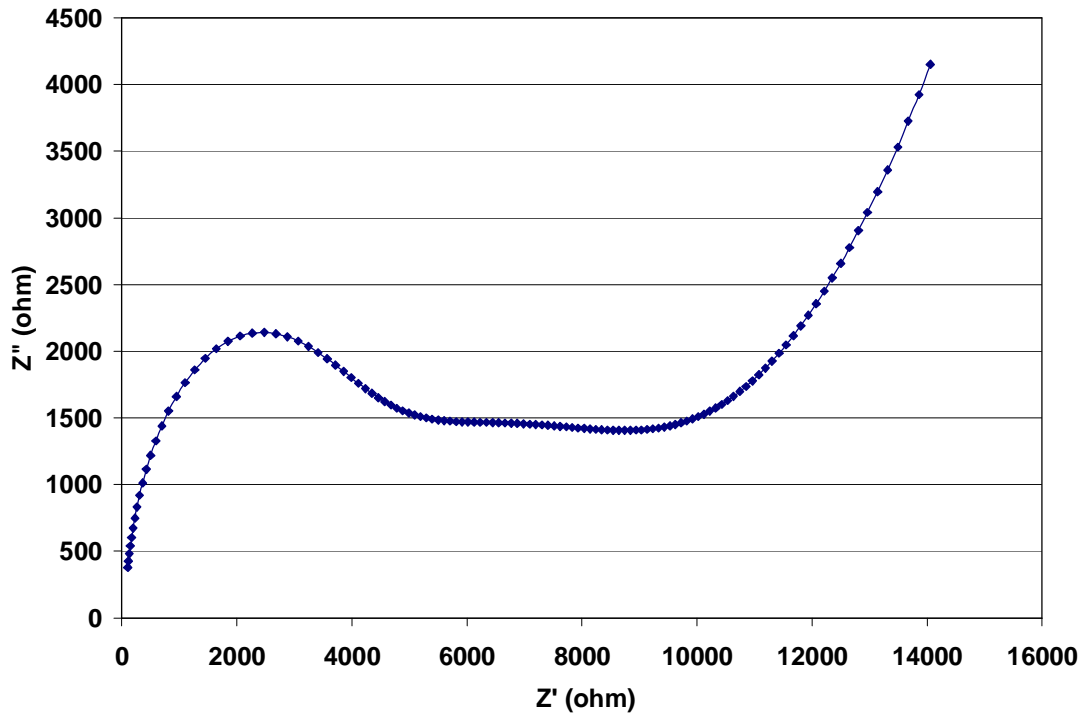
216

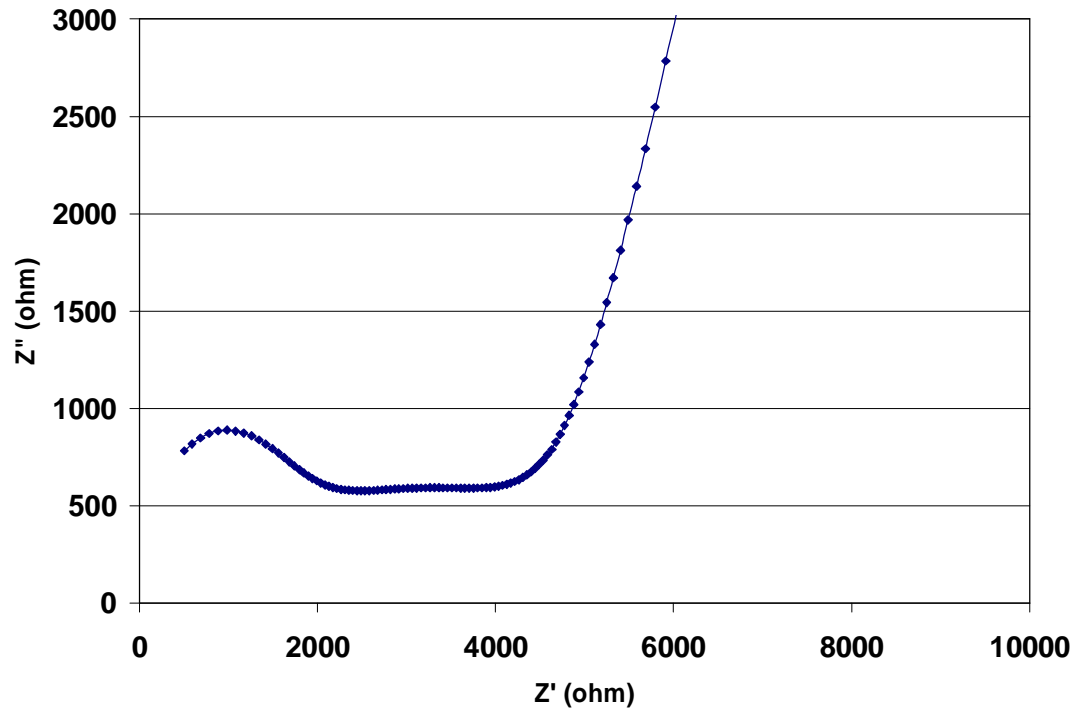Figure 7-13 Impedance spectrum of 20% LaTiO$_2$N powder suspended in butoxyethanol

Figure 7-14 Impedance spectrum of 20% NdTiO$_2$N powder suspended in butoxyethanol

None of the plots showed the perfect two semicircle spectra. Dotted lines suggest possibly overlapping semicircles. The first semicircular spectra were attributed to the high frequency response of the liquid host and the second ones to the low frequency response of the powders. It was noticed that the second semicircles at low frequency were larger in diameter than the first ones but they were depressed (i.e. the centres were below the x axis). The depression of the spectra may be caused by a non-uniform field distribution (Jasinski *et al.*, 2010). Along the radius of the electrode, the current density will certainly be disturbed near the edge of the electrode and current flow will not be perfectly normal to the surface. Therefore, CPEs were used in the equivalent circuit instead of capacitance. In the case of $LnTiO_2N$ and $Ln_2Ti_2O_7$ powders, they apparently sedimented very easily. Non-ideality with respect to particle dispersion could lead to errors in the calculation of dielectric constants. More than 20% of powder loading was then used to improve particle dispersion. Although the spectrum did not show the two ideal semicircles, the values obtained for $LaTiO_2N$, $La_2Ti_2O_7$ and $Nd_2Ti_2O_7$ were in agreement with some previous studies. The dielectric constants measured for all sample powders are shown in Table 7-1. At 0% powder loading, the dielectric constant of butoxyethanol was measured as approximately 9.8 but when increasing amounts of dielectric powders were suspended in the butoxyethanol, the dielectric constant calculated for the butoxyethanol significantly increased. The difference in dielectric constants between particles and liquid host was small and hence the two semicircular spectra were not separated.

Table 7-1 Particulate dielectric constant of $LnTiO_2N$ (Ln = La and Nd) and $ATaO_2N$ (A = Ca, Sr and Ba) and their corresponding oxide powders determined by impedance spectroscopy

Oxides	Dielectric constant	Oxynitrides	Dielectric constant
Butoxyethanol	9.8		
		$SrTaO_2N$	240
		$Ba_{0.2}Sr_{0.8}TaO_2N$	110
		$Ba_{0.4}Sr_{0.6}TaO_2N$	115
		$Ba_{0.5}Sr_{0.5}TaO_2N$	110
		$Ba_{0.6}Sr_{0.4}TaO_2N$	390
		$Ba_{0.8}Sr_{0.2}TaO_2N$	350
		$BaTaO_2N$	220
$Sr_2Ta_2O_7$	170	$SrTaO_2N$	240
$Ca_{0.4}Sr_{1.6}Ta_2O_7$	65	$Ca_{0.2}Sr_{0.8}TaO_2N$	140
$Ca_{0.8}Sr_{1.2}Ta_2O_7$	70	$Ca_{0.4}Sr_{0.6}TaO_2N$	140
$CaSrTa_2O_7$	65	$Ca_{0.5}Sr_{0.5}TaO_2N$	110
$Ca_{1.2}Sr_{0.8}Ta_2O_7$	85	$Ca_{0.6}Sr_{0.4}TaO_2N$	140
$Ca_{1.6}Sr_{0.4}Ta_2O_7$	65	$Ca_{0.8}Sr_{0.2}TaO_2N$	165
$Ca_2Ta_2O_7$	45	$CaTaO_2N$	110
$Nd_2Ti_2O_7$	43	$NdTiO_2N$	1525
$La_{0.4}Nd_{1.6}Ti_2O_7$	105	$La_{0.2}Nd_{0.8}TiO_2N$	6125
$La_{0.8}Nd_{1.2}Ti_2O_7$	114	$La_{0.4}Nd_{0.6}TiO_2N$	4664
$LaNdTi_2O_7$	69	$La_{0.5}Nd_{0.5}TiO_2N$	4584
$La_{1.2}Nd_{0.8}Ti_2O_7$	105	$La_{0.6}Nd_{0.4}TiO_2N$	16321
$La_{1.6}Nd_{0.4}Ti_2O_7$	143	$La_{0.8}Nd_{0.2}TiO_2N$	36336
$La_2Ti_2O_7$	49	$LaTiO_2N$	1100

However, many studies have shown that the particulate dielectric values are not significantly affected by the slurry characteristics and hence the impedance spectrum shape (Petrovsky *et al.*, 2006, Nakao, 2007, Petrovsky *et al.*, 2008a, b, Petrovsky and Dogan, 2009). The dielectric constants measured for $(Ca_xSr_{1-x})_2Ta_2O_7$ powders were in the range of 45–85 (except for $Sr_2Ta_2O_7$, for which k = 170). There is no previous report of measurements for $(Ca_xSr_{1-x})_2Ta_2O_7$ dielectrics apart from for bulk $Ca_2Ta_2O_7$ bulk material for which Cava *et al.* (1998) found k ≈ 24. The dielectric constant of $Ca_2Ta_2O_7$ powder here was determined as ≈ 45 which is almost twice as large as the value of Cava *et al.* However, in the Cava *et al.* experiment, the density of sintered $Ca_2Ta_2O_7$ pellets after firing at 1550ºC for 3 hours was approximately only 50% of theoretical density (see Chapter 4). At such relatively low densities, the measured dielectric constants may be very different from those of fully dense samples so it is not surprising that the dielectric constant of $Ca_2Ta_2O_7$ powder has come out as being much higher than that of bulk $Ca_2Ta_2O_7$ pellets of low density. Given the value of 45 for the dielectric constant of $Ca_2Ta_2O_7$ and the value of 170 for $Sr_2Ta_2O_7$, it is perhaps not surprising that intermediate compositions show intermediate values of dielectric constant. However, the similarity in values for all the intermediate composition is more difficult to explain.

The particulate dielectric constant measured for $La_2Ti_2O_7$ was 49, which is consistent with that of 99% dense $La_2Ti_2O_7$ (k = 48.8) reported by Paul and Robert (1991). The dielectric constant of bulk $Nd_2Ti_2O_7$ at 95–97% of theoretical density was reportedly 36 (Takahashi *et al.*, 1993) while here it was found that the particulate dielectric constant of $Nd_2Ti_2O_7$ was 43. This discrepancy is probably

due to the relatively low density of the bulk material. For other $(La_xNd_{1-x})_2Ti_2O_7$ compositions, mixed Ln^{3+} (La^{3+} and Nd^{3+}) cations substantially increased in dielectric constant from those of $La_2Ti_2O_7$ and $Nd_2Ti_2O_7$, the highest value being 143 for $La_{1.6}Nd_{0.4}Ti_2O_7$. At a 1:1 ratio of La and Nd, the particulate dielectric constant (k = 69) was higher than those of the two end members and also than that of the bulk material (k ≈ 42) reported by Takahashi *et al.* (1993). The lower value compared with other intermediate compositions may possibly due to La/Nd ordering.

For Ca- and Sr-based oxynitride compounds, all sample powders showed dielectric constants approximately 100% higher than those of their corresponding oxides. The particulate dielectric constants of $CaTaO_2N$, $SrTaO_2N$ and $BaTaO_2N$ were 110, 240 and 220, respectively. Other $Ca_xSr_{1x}TaO_2N$ and $Ba_xSr_{1x}TaO_2N$ compositions showed the dielectric constants of the order of 100–250 and 100–400, respectively. These values are much lower than the values reported by Kim *et al.* (2004), who claimed that bulk $SrTaO_2N$ and $BaTaO_2N$ have very high dielectric constants in the range 3000–5000 while $CaTaO_2N$ has a very low dielectric constant (k = 30), typical of an insulating perovskite oxide. However, the density of these bulk materials was typically 50% of the theoretical density, and hence is relatively low for reliable dielectric measurement. $LaTiO_2N$ and $NdTiO_2N$ powders exhibited very high dielectric constants of 1100 and 1525, respectively. The solid solutions of $LaTiO_2N$ and $NdTiO_2N$ gave much higher dielectric constants than those of the two end member compounds. Consistently, the dielectric constant of $LaTiO_2N$ powder is in agreement with the previous report for thin $LaTiO_2N$ films on a $SrTiO_3$ substrate (k = 1200) (Ziani *et al.*, 2008).

However, there is no previous report on other $La_xNd_{1-x}TiO_2N$ compositions or on $NdTiO_2N$, for comparison. The very large values measured for the intermediate compositions are probably due to the technical problems with the synthesis procedure, which required repeated nitridation of the samples, which in turn led to a high level of hydrogen reduction, and hence increase conductivity.

7.5 Conclusions

Impedance spectroscopy was used to characterise the dielectric properties of particulate oxynitride materials, dispersed in an appropriate liquid host. The dielectric constants of $Ca_xSr_{1-x}TaO_2N$, $Ba_xSr_{1-x}TaO_2N$ and $La_xNd_{1-x}TiO_2N$ and also $(Ca_xSr_{1-x})_2Ta_2O_7$ and $(La_xNd_{1-x})_2Ti_2O_7$ were determined by impedance measurement using these powders suspended in butoxyethanol as a liquid host. A parallel RC equivalent circuit individually connected in series was applied to extract the R and CPE parameters and finally the dielectric constants were calculated. Although the impedance spectra did not show two ideal semicircles, the measured dielectric constants of lanthanide compounds were in reasonable agreement with previous research. The particulate dielectric constants measured for $La_2Ti_2O_7$ and $LaTiO_2N$ were in the range of those reported for a bulk material (99% of theoretical density) and in thin film form deposited on $SrTiO_3$, respectively. However, the dielectric constants of $CaTaO_2N$, $SrTaO_2N$ and $BaTaO_2N$ particles are significantly different from those reported by Kim *et al.* (2004); it is believed that this discrepancy is because the low density of the bulk samples may seriously affect the empirical dielectric measurements. The error in oxynitride particulate dielectric constant measurements is considered to be below 10%.

7.6 References

Cava, R. J., Krajewski, J. J. and Roth, R. S. (1998) Low temperature coefficient bulk dielectrics in the $Ca_2Nb_2O_7$-$Ca_2Ta_2O_7$ system. *Materials Research Bulletin,* 33**,** 527-532.

Jasinski, P., Petrovsky, V. and Dogan, F. (2010) Impedance spectroscopy of BaTiO3 cubes suspended in lossy liquids as a physical model of two-phase system. *Journal of Applied Physics,* 108.

Kim, Y.-I., Woodward, P. M., Baba-Kishi, K. Z. and Tai, C. W. (2004) Characterization of the structural, optical, and dielectric properties of oxynitride perovskites AMO_2N (A = Ba, Sr, Ca; M = Ta, Nb). *Chemistry of Materials,* 16**,** 1267-1276.

Lanfredi, S. and Rodrigues, A. C. M. (1999) Impedance spectroscopy study of the electrical conductivity and dielectric constant of polycrystalline $LiNbO_3$. *Journal of Applied Physics,* 86**,** 2215-2219.

Nakao, Y. (2007) Dielectric constant evaluation of dielectric powders by complex impedance analysis with model of RC-RC parallel circuits connected in series. *Japanese Journal of Applied Physics,* 46**,** 7008-7012.

Paul, A. F. and Robert, E. N. (1991) $La_2Ti_2O_7$ Ceramics. *Journal of the American Ceramic Society,* 74**,** 2876-2881.

Petrovsky, V. and Dogan, F. (2009) Fundamentals of Impedance Spectral Analysis Applied to Determine Permittivity of Dielectric Particles. *Journal of the American Ceramic Society,* 92**,** 1054-1058.

Petrovsky, V., Manohar, A. and Dogan, F. (2006) Dielectric constant of particles determined by impedance spectroscopy. *Journal of Applied Physics,* 100**,** 014102-014104.

Petrovsky, V., Petrovsky, T., Kamlapurkar, S. and Dogan, F. (2008a) Characterization of Dielectric Particles by Impedance Spectroscopy (Part I). *Journal of the American Ceramic Society,* 91**,** 1814-1816.

Petrovsky, V., Petrovsky, T., Kamlapurkar, S. and Dogan, F. (2008b) Physical Modeling and Electrodynamic Characterization of Dielectric Slurries by Impedance Spectroscopy (Part II). *Journal of the American Ceramic Society,* 91**,** 1817-1819.

Takahashi, J., Kageyama, K. and Kodaira, K. (1993) Microwave dielectric properties of lanthanide titanate ceramics. *Japanese Journal of Applied Physics, Part 1: Regular Papers and Short Notes and Review Papers,* 32**,** 4327-4331.

Ziani, A., Le Paven-Thivet, C., Le Gendre, L., Fasquelle, D., Carru, J. C., Tessier, F. and Pinel, J. (2008) Structural and dielectric properties of oxynitride perovskite LaTiO$_x$N$_y$ thin films. *Thin Solid Films,* 517**,** 544-549.

Other reference resources:

Algilent-technologies (2010, September 25th) Impedance measurement handbook: A guide to measurement technology and techniques. 4th ed. Retrieved from http://cp.literature.agilent.com/litweb/pdf/5950-3000.pdf

Gamry Instruments (2010, September 19th) Application note: Basic of Electrochemical Impedance Spectroscopy. Retrieved from http://www. gamry.com/App_Notes/EIS_Primer/Basics_Of_%20EIS.pdf

Chapter 8   Discussion and conclusions

It is well established that nitrogen incorporation increases the dielectric constant of SiO_2, even though the reason for this is not entirely clear. The combined effects of a higher dielectric constant for oxynitride materials compared with oxides and the flexible ion substitution of perovskite type materials was expected to provide considerable scope for developing new materials with good dielectric properties. In the present study, $LnTiO_2N$ (Ln = La and Nd), $ATaO_2N$ (A = Ca, Sr and Ba) and their solid solutions were synthesised by ammonia nitridation of the corresponding oxide precursors at high temperatures for several hours, and the existence of $La_xNd_{1-x}TiO_2N$, $Ca_xSr_{1-x}TaO_2N$ and $Ba_xSr_{1-x}TaO_2N$ solid solutions were confirmed by X-ray diffraction. However, other rare earth titanium oxynitrides ($RTiO_2N$; R = Ce, Sm, Dy, Yb and Y), and solid solutions of $Ca_xBa_{1-x}TaO_2N$ could not be prepared. In the present study, all the oxynitride compositions prepared had perovskite structures with overall compositions ABX_3, where A and B represent the 12- and 6-coordinated cations, and X is either oxygen or nitrogen. However, different cations have their own structural preferences and in particular the size of different cations has a significant influence on structural stability. Typical alternative oxynitride structures are scheelite, pyrochlore, perovskite and fluorite structures, and these occur depending on the difference between the sizes of the A- and B-cations (Tessier and Marchand, 2003). For example, the rare earth (R)-titanium oxynitrides of Sm, Dy and Y were reported as having a pyrochlore structure of composition $R_2Ti_2O_{5.5}N$ (Dolgikh and Lavut, 1991 cited in Tessier and Marchand, 2003).

The crystal structures of $LnTiO_2N$ (Ln = La and Nd) and their solid solutions were determined as orthorhombic by Rietveld refinement. Clarke *et al.* (2002) and Logvinovich *et al.* (2009) reported a triclinic structure for $LaTiO_2N$ (by neutron diffraction), but in the present case X-ray diffraction could not distinguish the multiple overlaps of the principle reflections generated by the triclinic cell, especially due to the low crystallinity of the samples, which resulted in additional broadening of the reflections. The structures of Nd-rich $La_xNd_{1-x}TiO_2N$ compositions were determined as orthorhombic in space group *Pnma* and La-rich compositions were refined (as done by Yashima *et al.* (2010)) in orthorhombic space group *Imma*. It is believed that future more detailed studies may show that the correct space group for the La-rich composition is triclinic $P\bar{1}(I\bar{1})$ as determined by Clarke *et al.* (2002) for $LaTiO_2N$. The structures of $Ca_xSr_{1-x}TaO_2N$ and $Ba_xSr_{1-x}TaO_2N$ changed from tetragonal to orthorhombic and tetragonal to cubic with increasing Ca and Ba substitution, respectively. A systematic variation in a-, b- and c- axis lengths and small but almost constant octahedral distortion were observed with increasing cation substitution for all the $La_xNd_{1-x}TiO_2N$, $Ca_xSr_{1-x}TaO_2N$ and $Ba_xSr_{1-x}TaO_2N$ series. When a cation of smaller ionic radius substitutes in the A-cation sites, the bond distances between the transition metal (M) and the (O,N) anions remain almost constant but the bond angles are forced to assume smaller values and as a result, the crystal structure tends to change from higher to lower symmetry (Aguiar *et al.*, 2008). As in the case of $Ca_xSr_{1-x}TaO_2N$ and $Ba_xSr_{1-x}TaO_2N$ compositions, the structures changed from the higher symmetry tetragonal to the lower symmetry orthorhombic and from cubic to tetragonal, respectively. However, in the case of the $La_xNd_{1-x}TiO_2N$ series,

lanthanum and neodymium ions are very similar in size (1.06 and 0.99 Å, respectively) so the cation substitution has no significant effect on Ti–(O,N)bond angles, and hence no structural transition is observed by X-ray diffraction.

With regard to the cubic perovskite structure, the structural distortion in the $La_xNd_{1-x}TiO_2N$, $Ca_xSr_{1-x}TaO_2N$ and $Ba_xSr_{1-x}TaO_2N$ solid solution series was expected to give rise to a high polarisation and hence a high dielectric constant should be observed. In order to measure the dielectric constant of a bulk material, a fully dense sample is necessary. Attempts were made to prepare fully dense samples of $LaTiO_2N$, $NdTiO_2N$, $CaTaO_2N$ and $BaTaO_2N$ by hot-pressing and spark plasma sintering. However, neither of these techniques could provide a pure oxynitride phase of high density. The dielectric loss of densified $LaTiO_2N$, $CaTaO_2N$ and $BaTaO_2N$ was much higher than acceptable levels (> 0.01), and in fact the samples exhibited conductivity due to the presence of trace amounts of conducting phases—a fine dispersion of nitride particles in the grain boundaries.

Due to the difficulty of achieving oxynitride densification, an alternative procedure was devised which involved taking dense $(La_xNd_{1-x})_2Ti_2O_7$ bulk samples and nitriding in ammonia to form a dense oxynitride layer on the surface of the corresponding oxide. In addition, it was also expected that the good dielectric properties of $La_2Ti_2O_7$ combined with the anticipated high dielectric constant of the oxynitride material with negligible mismatch between the dielectric film and the substrate would provide an improved material. X-ray diffraction confirmed the formation of oxynitride layers of approximately 3 μm thickness on the surface of the oxide pellets. The oxynitride layer significantly increased the overall dielectric constant of the pellet but at the same time resulted

in increasing dielectric loss compared with the original oxide compounds. In ammonia nitridation, nitrogen acts as the nitriding agent but the hydrogen simultaneously generated acts as a reducing agent. While the nitrogen is incorporated to form the oxynitride layer, the hydrogen removes oxygen from the oxide precursor and simultaneously reduces titanium from 4+ to 3+. The increasing dielectric loss observed is therefore believed to be due to the formation of reduced compositions of the type $La_2Ti_{2-x}^{IV} Ti_x^{III} O_{7-z}$ (where z is x/2) underneath the oxynitride layer. Both X-ray diffraction and the colour of nitrided pellet provided the strong evidence for the $Ti^{4+} \rightarrow Ti^{3+}$ reduction with oxygen lost to balance the charge. These chemical changes have a deleterious effect on the dielectric measurements. A bulk oxynitride material in the form of a single crystal will obviously give a higher dielectric constant than an oxynitride layer deposited on the oxide bulk material. However, it is not easy to synthesise a single crystal of an oxynitride compound because oxynitrides decompose at the high temperatures needed for crystal growth. Nitridation of a single crystal of oxide is sensible route to give a single crystal of an oxynitride material. Ebbinghaus *et al.* (2008) nitrided single crystals of oxides with compositions $A_2B_2O_7$ (A = alkaline earth or rare earth and B = transition metals) and X-ray diffraction confirmed the formation of thick films of perovskite oxynitrides of $LaTiO_2N$, $NdTiO_2N$, $SrNbO_2N$ and $SrTaO_2N$ on the original single crystals in thicknesses of micrometers. The dielectric constants and conductivities of $LaTiO_2N$, $SrNbO_2N$ and $SrTaO_2N$ films on the corresponding oxide single crystal were significantly higher than before nitriding. This work is significant, and suggests that if the nitridation time is further prolonged, it may finally yield a

completely reacted crystal (i.e. 100% oxynitride single crystal). Nevertheless, for dielectric measurements, this may be what as happened in the polycrystalline samples in the present case. A highly reactive nitridation for a shorter time would be preferable in order to minimise the hydrogen effect. Alternatively, a nitrogen source such as NO and N_2O (i.e. hydrogen-free) may be necessary to eliminate the deleterious effect of hydrogen if prolonged nitridation is required.

Because of the difficulties experienced in preparing bulk or thin layers of oxynitride samples, alternative dielectric measurement methods have been explored to obtain the true value of the dielectric constant. Impedance spectroscopy was used to measure the dielectric constant of particles suspended in an appropriate liquid and behaving as a two-phase system. Previous research has confirmed that this is a reliable technique for particulate dielectric measurement (Petrovsky *et al.*, 2006, Petrovsky *et al.*, 2008a, b, Petrovsky and Dogan, 2009, Jasinski *et al.*, 2010). It has established that the measured dielectric constant of the powder is not influenced by the volume fraction of powder loading, or by choice of host liquid and slurry characteristics. For $La_xNd_{1-x}TiO_2N$ and the corresponding oxide compounds, sedimentation occurred, and therefore a high volume fraction of powder was used so that the powder suspension improved. The measured particulate dielectric constants for $La_2Ti_2O_7$ (k = 49) and $LaTiO_2N$ (k = 1100) powders were in good agreement with literature values for 99% dense bulk material (k ≈ 48–49) and thin films (k ≈ 1100–1200), respectively. The similar dielectric constants measured for $Nd_2Ti_2O_7$ and $NdTiO_2N$ powders were approximately 43 and 1500, respectively. The value for $Nd_2Ti_2O_7$ powder is higher than that previously reported for 95% dense bulk material (k ≈ 36), but this

would be low because of the rather low density. However, the particulate dielectric constant measured for all the $La_xNd_{1-x}TiO_2N$ solid solution compositions is far too large to be believable. Based on previous research (Petrovsky *et al.*, 2008a, Jasinski *et al.*, 2010), at a volume fraction of 0.2–0.3, it is expected that the dielectric constant of the liquid host butoxyethanol is in the range 15–30 and the ratio of the resistances of particle and liquid is approximately in the range 1–5. However, dielectric measurements on these samples gave very high values for dielectric constant of the liquid host and the ratio of resistance. Due to technical problems in the laboratory, these samples needed to be repeatedly nitrided in ammonia for many cycles, and since hydrogen concentration increases with nitridation time, the repeated nitridation in the case of $La_xNd_{1-x}TiO_2N$ powders may cause a very high hydrogen concentration in the sample, in turn generating a high proportion of electron traps (Green *et al.*, 2001), resulting in the observed high values in dielectric measurement. In future work, the ammonia nitridation should in principle be carried out at low temperature for much shorter times to reduce the hydrogen content in the product (Green *et al.*, 2001), and the particulate dielectric measurements on the $La_xNd_{1-x}TiO_2N$ compositions repeated. The dielectric constants of suspended $Ba_xSr_{1-x}TaO_2N$ and $Ca_xSr_{1-x}TaO_2N$ powders in butoxyethanol were also determined by impedance spectroscopy. The results show that the dielectric constant of these powders were in the range 100–400, which are much lower than those compacted powders reported by Kim *et al.* (2004). These measurements were made on 50% dense samples, which is too low for a reliable dielectric measurement and it is believed that the present results give more accurate values for these materials.

The very large values for dielectric constant measured for compositions in the $La_xNd_{1-x}Ti_2O_2N$ series raised the question of whether, just as with the occurrence of Ti^{3+} in the sub-surface regions of oxynitride layers deposited on $La_2Ti_2O_7$ and $Nd_2Ti_2O_7$, there was also some Ti^{3+} in the oxynitride itself, and indeed whether this was true of all the oxynitrides prepared in this study. Evidence for the presence of Ti^3+ in the sub-surface oxide was provided both by colour and also the observation of shifts in X-ray reflections, which when this layer was removed, caused the reflections to move back to their normal positions. For all the oxynitrides prepared here, the colour was never white, and most often was dark grey, this often being modified by the intrinsic colour of some of the ionic species present. Examination of the positions of X-ray lines for evidence of shifts to lower *d*-spacings did not prove positive. In general, lines occurred at their expected positions, even though because all samples were prepared in the same way, it could be argued that if every sample contained Ti^{3+}, then every sample would look the same. However, the very high dielectric constants observed for compositions in the $La_xNd_{1-x}Ti_2O_2N$ series suggested that there might be higher concentrations of Ti^{3+} present, in which case some difference in X-ray line positions might have been observed, but in fact this was not the case. Further scrutiny of line positions for samples of other compositions nitrided for increased lengths of time also failed to detect any line shifts. It is possible that bearing in mind the stronger bonding in oxynitrides compared with oxides, less Ti^3+ can be accommodated during ammonia nitriding, and this does not readily show up on X-ray spectra, even though present in sufficient amount to significantly change the conductivity of the sample and hence give a high dielectric loss. Overall it

would therefore seem the most likely explanation that just as Ti^{3+} was incorporated into oxide titanates during ammonia nitriding, some Ti^{3+} was also introduced into the corresponding oxynitrides. However, it is noticeable that compositions in the $(Ba,Sr)TaO_2N$ and $(Ca,Sr)TaO_2N$ series gave much more sensible measured values of dielectric constant than compositions in the $(La,Nd)TiO_2N$ series. Despite certain technical problems which required the latter samples to be subjected to much longer nitriding times, it could be argued that the first two series were not as amenable to Ti^{3+} incorporation. Because of limitations of time it was not possible to explore these issues further, but clearly this is a fruitful area for future study.

For solid-gas reaction between ammonia and oxide precursor powders, the reaction mainly occurs at the surface of the powder and achieving through-nitriding is difficult; a rotating tube furnace with the sample in the form of loose powder could help in mixing the powder thoroughly during the nitriding treatment in order to obtain a homogenous oxynitride product. Even though ammonia gas is relatively highly reactive, it introduces a high concentration of hydrogen in the oxynitride product which causes errors in dielectric measurements. Other nitrogen sources such as NO and N_2O therefore need to be considered. Alternatively, nitridation by microwave heating might increase the nitriding reactivity, allowing shorter nitriding time than a conventional electrical furnace and also minimise hydrogen effects.

The work described in this thesis has shown that it is extremely difficult to prepare good quality, pure, dense samples of oxynitrides in a condition which would allow measurement of their dielectric properties. However, no results have

been obtained which might suggest that the original principle, i.e. that nitrogen incorporation increase the dielectric constants of oxides, is incorrect, and therefore, there still remains the challenge of finding better ways of producing good quality oxynitride samples. In addition, the desirability of having a final perovskite structure is also believed to be a good research objective, both because of the established large dielectric constants demonstrated in the case of perovskite oxides, and also because of the chemical/structural flexibility exhibited by this structure. In an attempt to achieve an improved result with a simple preparation procedure, an experiment was designed to prepare a barium titanium oxynitride by nitriding $BaTiO_3$ in flowing ammonia gas at 1000°C for 16 hours. The resulting powder was very light bluish green in colour compared to the white $BaTiO_3$ powder before nitriding; X-ray diffraction showed no trace of a possible oxynitride product, but only $BaTiO_3$ and a small amount of Ba_2TiO_4. However, the observed colour change would suggest that some chemical change had occurred. There may be scope for repeating experiments of this type, with small amounts of other, higher valency cations present which would enable the nitrogen to be incorporated whilst still retaining charge balance.

As discussed in earlier chapters, an alternative way of carrying out the nitridation step is by using oxides such as NO or N_2O. These gases avoid the simultaneous generation of hydrogen which appears to be a key problem in the case of Ti- and Ta-based oxynitride perovskites because it encourages these element to change to lower oxidation states, resulting in increased conductivity (and hence increased dielectric loss). However, this is unknown territory, and a preliminary study

would be necessary to determine whether perovskite oxynitrides could indeed be produced using these gases as the nitriding agent(s).

The original intention of this work was to produce dense bulk samples of oxynitrides, and therefore no thought was given as to whether it would be possible to produce these compounds by conventional thin (or thick) film techniques. However, whereas it is relatively simple to produce binary or even ternary nitrides by these methods, it is not as easy to produce quaternary (or more complex) oxynitrides with precise control of the final composition. In addition, evidence from the oxide perovskite field has shown that it is often useful to have small amounts of additional metal cations present in order to develop the best properties, and this would further complicate the synthesis procedure. However, this is another field for exploration which the present work has opened up.

In summary therefore, it is believed that there is still scope for future work on oxynitrides as dielectric materials, and especially those which have the perovskite structure. The present work has mainly shown the difficulties associated with working with these compounds, but also has shown that oxynitrides with high dielectric constant can be produced, and the challenge remains to make these materials in good quality form whilst also minimising dielectric loss. It is believed that further research may open up new ways in which these objectives can be realised.

References:

Aguiar, R., Logvinovich, D., Weidenkaff, A., Rachel, A., Reller, A. and Ebbinghaus, S. G. (2008) The vast colour spectrum of ternary metal oxynitride pigments. *Dyes and Pigments,* 76**,** 70-75.

Clarke, S. J., Guinot, B. P., Michie, C. W., Calmont, M. J. C. and Rosseinsky, M. J. (2002) Oxynitride perovskites: Synthesis and structures of $LaZrO_2N$, $NdTiO_2N$ and $LaTiO_2N$ and comparison with oxide perovskites. *Chem. Mater.,* 14**,** 288-294.

Ebbinghaus, S. G., Aguiar, R., Weidenkaff, A., Gsell, S. and Reller, A. (2008) Topotactical growth of thick perovskite oxynitride layers by nitridation of single crystalline oxides. *Solid State Sciences,* 10**,** 709-716.

Green, M. L., Gusev, E. P., Degraeve, R. and Garfunkel, E. L. (2001) Ultrathin (< 4 nm) SiO_2 and Si-O-N gate dielectric layers for silicon microelectronics: Understanding the processing, structure, and physical and electrical limits. *Journal of Applied Physics,* 90**,** 2057-2121.

Jasinski, P., Petrovsky, V. and Dogan, F. (2010) Impedance spectroscopy of BaTiO3 cubes suspended in lossy liquids as a physical model of two-phase system. *Journal of Applied Physics,* 108.

Kim, Y.-I., Woodward, P. M., Baba-Kishi, K. Z. and Tai, C. W. (2004) Characterization of the structural, optical, and dielectric properties of oxynitride perovskites AMO_2N (A = Ba, Sr, Ca; M = Ta, Nb). *Chemistry of Materials,* 16**,** 1267-1276.

Logvinovich, D., Bocher, L., Sheptyakov, D., Figi, R., Ebbinghaus, S. G., Aguiar, R., Aguirre, M. H., Reller, A. and Weidenkaff, A. (2009) Microstructure, surface composition and chemical stability of partly ordered $LaTiO_2N$. *Solid State Sciences,* 11**,** 1513-1519.

Petrovsky, V. and Dogan, F. (2009) Fundamentals of Impedance Spectral Analysis Applied to Determine Permittivity of Dielectric Particles. *Journal of the American Ceramic Society,* 92**,** 1054-1058.

Petrovsky, V., Manohar, A. and Dogan, F. (2006) Dielectric constant of particles determined by impedance spectroscopy. *Journal of Applied Physics,* 100**,** 014102-014104.

Petrovsky, V., Petrovsky, T., Kamlapurkar, S. and Dogan, F. (2008a) Characterization of Dielectric Particles by Impedance Spectroscopy (Part I). *Journal of the American Ceramic Society,* 91**,** 1814-1816.

Petrovsky, V., Petrovsky, T., Kamlapurkar, S. and Dogan, F. (2008b) Physical Modeling and Electrodynamic Characterization of Dielectric Slurries by

Impedance Spectroscopy (Part II). *Journal of the American Ceramic Society,* 91**,** 1817-1819.

Tessier, F. and Marchand, R. (2003) Ternary and higher order rare-earth nitride materials: Synthesis and characterization of ionic-covalent oxynitride powders. *Journal of Solid State Chemistry,* 171**,** 143-151.